Chiral spin structures in ultrathin magnetic films

Chiral spin structures in ultrathin magnetic films

PROEFSCHRIFT

ter verkrijging van de graad van doctor aan de Technische Universiteit Eindhoven, op gezag van de rector magnificus, prof.dr.ir. F.P.T. Baaijens, voor een commissie aangewezen door het College voor Promoties, in het openbaar te verdedigen op dinsdag 7 januari 2020 om 13:30 uur.

door

Franciska Chrétien Ummelen

geboren te Roermond

Dit proefschrift is goedgekeurd door de promotoren en de samenstelling van de promotiecommissie is als volgt:

voorzitter:	prof.dr.ir. G.M.W. Kroesen
1e promotor:	prof.dr.ir. H.J.M. Swagten
2e promotor:	prof.dr. B. Koopmans
co-promotor:	dr.ir. R. Lavrijsen
leden:	prof.dr. M. Kläui (University of Mainz)
	prof.dr. C.H. Marrows (University of Leeds)
	prof.dr. A. Fiore
adviseur:	dr. D. Ravelosona (CNRS C2N)

Het onderzoek dat in dit proefschrift wordt beschreven is uitgevoerd in overeenstemming met de TU/e Gedragscode Wetenschapsbeoefening.

Chiral spin structures in ultrathin magnetic films

Franciska Chrétien Ummelen

A catalogue record is available from the Eindhoven University of Technology Library. ISBN: 978-90-386-4905-4

This work is part of the research programme of the Foundation for Fundamental Research on Matter (FOM), which is part of the Netherlands Organisation for Scientific Research (NWO).

Contents

1

General introduction

Chiral magnetic textures posses many unique qualities and are envisaged to be the building blocks of future data storage technology. This thesis is dedicated to the understanding of the physical interactions governing such structures. In this general introduction we will first clarify the term 'chirality', a concept at the heart of many exciting scientific phenomena. In particular, we discuss how it manifests itself in the field of thin film magnetism and spintronics, where its importance was only recently realized. We will introduce one specific spintronics device, the 'racetrack memory', in more detail. For its further development chiral magnetic structures are paramount, and hence the work presented in this thesis is directly of relevance for this device. Also the role of data storage technology in present-day society is discussed, providing the motivational context for our research efforts. The chapter concludes with an outline of the remainder of this thesis.

1.1 Chirality and magnetic thin films

A chiral object refers to something that is unequal to its mirror image. The most obvious example from everyday life is a hand: a left hand cannot be translated or rotated in such a way that it becomes a right hand*. Figure 1.1(a) illustrates this principle. Intuitively, it would be expected that structures with opposite

*This actually is the etymological origin of the word chiral, as $\chi\epsilon\iota\rho$ is Greek for hand.

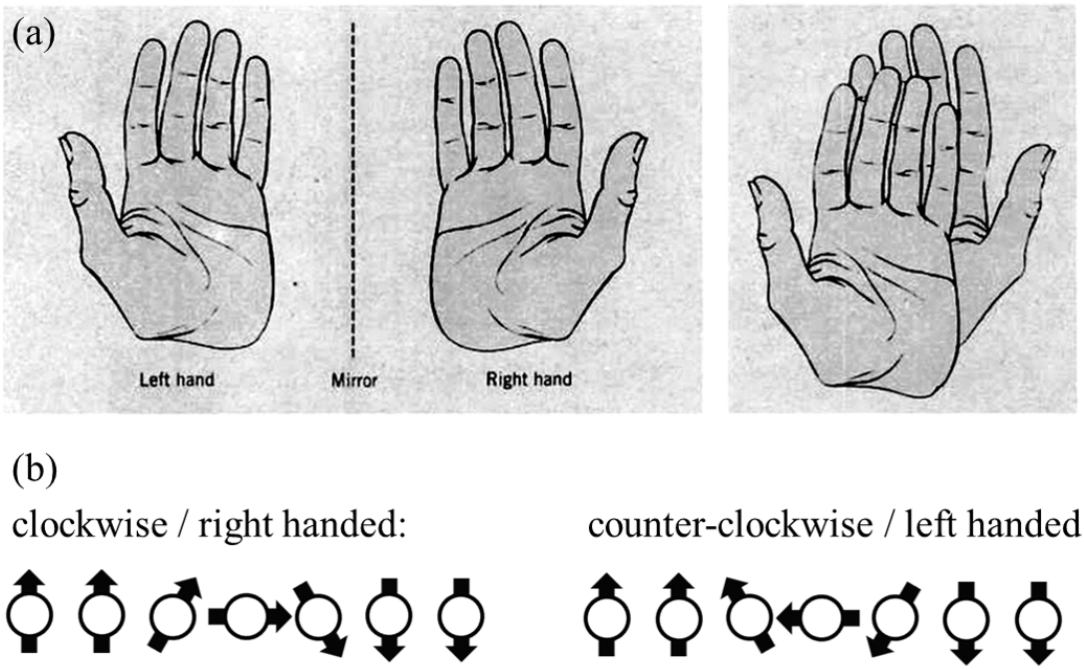

Figure 1.1: (a) Illustration of the concept of chirality using a human hand: a hand is not superimposable on its mirror image. From Ref. [3]. (b) Two chains of spins with different chirality: clockwise/right-handed rotation and counter-clockwise/left-handed rotation.

chirality are equally likely to occur, but it turns out that sometimes one specific chirality dominates. This seemingly simple concept is at the center of some of the most fundamental problems in science. The most well-known example is found in chemistry, where solutions of chiral molecules rotate the polarization plane of light. An example from particle physics is the breaking of mirror symmetry for radioactive decay. This chiral phenomenon on the smallest imaginable scale is believed to be related to the big question of why there is more matter than antimatter in our universe [1]. In biology a similar mystery exists: why do amino acids only occur in their left-handed form, and why does the double helix of our DNA always spiral in a right-handed fashion [2]?

The work presented in this thesis belongs to the field of magnetism and spintronics. Spintronics involves controlling both the charge and spin property of electrons. Here spin refers to an intrinsic form of angular momentum and its associated magnetic dipole moment. Why the angular momentum of an electron corresponds to

a magnetic moment can be understood in a semi-classical picture. When an electron is treated as a charged particle, spinning of this particle around its own axis implies a movement of charge, which is known to generate a magnetic field. The orientation of the magnetic moment depends on the direction of the spinning, and throughout this thesis spins will be visualized as arrows indicating this orientation. In a magnetic material localized, uncompensated spins are present, together giving rise to a macroscopic magnetic moment, which we will also visualize using arrows.

Also in this research area a puzzling but exciting chirality-related phenomenon exists. Figure 1.1(b) schematically shows two chains of spins in which the rotation with respect to neighbouring spins is opposite. These senses of rotation are referred to as right-handed versus left-handed or clockwise versus counter-clockwise. These two configurations are examples of spin structures with a different chirality. In the midst of the previous century it was discovered that for crystals that had a structure lacking inversion symmetry, it is possible that these two configurations can have a different energy, so one sense of rotation is preferred. Following this discovery it was conjectured that some form of symmetry breaking is a condition for this preference to exist: when looking at Fig. 1.1(b) it cannot be imagined that the two configurations would have a different energy without some additional ingredient. In recent years, it was realized that the symmetry could be broken by creating a thin[†] magnetic layer for which the top and bottom interface are not identical. This is currently still followed by a huge research effort to measure and control chiral spin structures in thin film material systems.

Magnetic thin films were already heavily researched before it was realized that they could host chiral spin structures [4]. The possibility to grow them posed various new opportunities in materials science. Multilayered material stacks that do not occur in nature could be created. An interesting example is two magnetic layers separated by a non-magnetic layer; we will come back to this specific stack in the next section. Further, by choice of an appropriate seed layer, the crystal structure and grain sizes in the magnetic layer can be tuned. Also, in thin films a lot of

[†]In this thesis, 'thin' refers to a thickness of less than the exchange length, the minimum length over which the magnetization can twist in order to minimize dipolar interactions. When the film thickness is smaller than this exchange length, the magnetization can be presumed to be constant over the thickness of the film.

atoms are located at the interface compared to atoms which are inside the bulk, so interfacial interactions that are normally negligible can suddenly be studied and exploited. For certain material stacks this has the consequence that spins prefer to be oriented perpendicular to the interface, referred to as perpendicular magnetic anisotropy (PMA).

Magnetic thin films can comprise many magnetic domains, which are uniformly magnetized regions in which all spins point in the same direction. At the border between such domains, narrow regions exist where the magnetization gradually rotates. Such a spin structure is called a domain wall (DW), and in Fig. 1.2(a) an artist's impression of of a DW in a film with PMA is depicted. Inside a DW the newly discovered chiral interaction comes into play. There are several ways that the spins can be rotated with respect to each other: in the plane of the DW or perpendicular to the plane of the the DW and and in a clockwise or counter-clockwise sense. The chiral interaction determines which option is favoured, and thereby heavily influences the energy and dynamical properties of the DW. In samples with a strong chiral interaction, all the DWs have the same sense of rotation, and are referred to as chiral DWs.

When the chiral interaction is strong enough, and if the other material parameters also allow for it, exotic chiral spin structures can be formed: magnetic skyrmions. These are whirls in the magnetization, such as schematically depicted in Fig. 1.2(b). Depending on the experimental conditions, either densely packed arrays of these structures are formed, or isolated skyrmions can occur. Skyrmions may be as small as several nanometers, and their peculiar spin configuration gives rise to a large stability and a distinctive current-induced motion. In all respects, they are appealing entities to study.

The chiral interaction in magnetic materials is called the Dzyaloshinskii-Moriya interaction (DMI). Measuring the DMI has proven to be a challenging task, and is a major theme in the research community. Also, the controlled manipulation of magnetic skyrmions is still in its infancy. Further, DMI is not only of interest because of the fascinating physics involved, but also because it is believed to have a great potential for applications. The next section focusses on the applications of magnetic thin films in data storage technology and the role of DMI. Also one of the

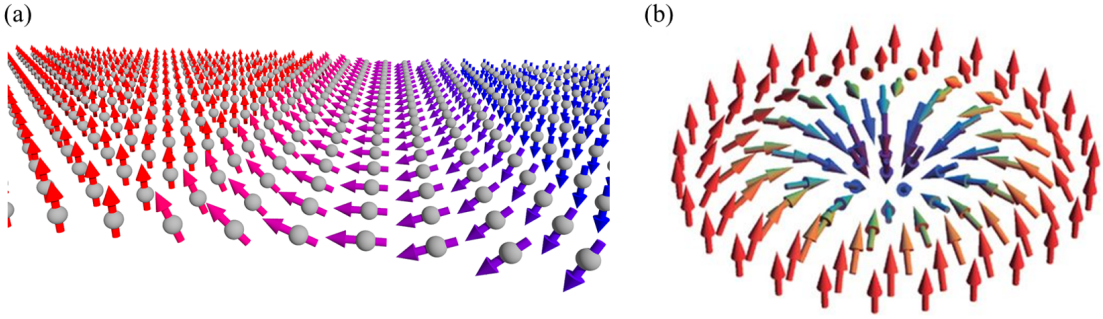

Figure 1.2: Artist's impressions of two chiral spin structures that can be found in ultra thin magnetic films: (a) a chiral DW and (b) a magnetic skyrmion. Adapted from Ref. [5] and Ref. [6], respectively.

most promising concepts for future data storage devices, the racetrack memory, is introduced.

1.2 Spintronics and Racetrack memory

The field of spintronics emerged in 1988 when giant magneto-resistance (GMR) was discovered [7, 8]. This phenomenon occurs in a thin film multilayer in which two magnetic layers are separated by a non-magnetic conductive layer. It refers to a giant change in electrical resistance depending on the mutual orientation of the magnetization between neighbouring layers. This allowed for the development of a sensitive magnetic sensor, leading to a radical miniaturization of hard disk drives. Closely related sensing devices, in which the non-magnetic conductive layer is replaced by an insulating layer[‡], are still used to read out hard disks up to this day.

Nowadays, still much of the research done in the field of spintronics is motivated by improving data storage technology. The importance of this subject to society is evident when considering some recent data regarding information and communication technologies (ICT) [9]. The increasing number and importance of 'smart' devices, which store and process data and are connected to the internet, is clearly noticeable in everyday-life. The expectation is that by 2020, 6 billion smart phones

[‡]In these devices, the electrons tunnel between the magnetic layers, and the change in resistance depending on the orientation of the magnetization is referred to as tunneling magneto-resistance.

will be online, together with 20 billion other devices, forming the so-called 'internet of things'. This development will be accompanied by an increase in energy consumption. This is not only because these devices need power to operate, but mainly because they require network services and data centres, which will consume considerable amounts of energy. The data centres, for instance, used up 194 TW h in 2014, which was about 1 % of the total global energy consumption. All aspects of ICT together are estimated to account for approximately 10 % of the current global energy consumption [10], and the worst case scenario prediction is that this will increase to 51 % 2030 [11]. Improving data storage technology is therefore vital.

A great benefit of magnetic storage is that it is non-volatile, meaning that no energy is required to preserve the data when a device is turned off. A novel memory device with potential for low energy consumption, is the racetrack memory, which was introduced in 2003. This is basically a shift register in which bits of information move through a thin magnetic strip. In Fig. 1.3(a) the red-blue colour coding indicates up and down domains[§], which are separated by DWs. When the up domains are assigned a value 0 and the down domains a value 1 (or vice versa) they can be seen as bits of information. This magnetically encoded information is moved through the racetrack by an electrical current, such that only one stationary read and write head are necessary to access all the data in the entire track. The absence of mechanically moving parts is beneficial, because it increases robustness, lowers heat generation, and removes a limitation to the operation speed. As can be seen in the schematic representation in Fig. 1.3(a), the track can be folded into the third dimension which allows for a drastic increase in storage density per surface area (the expensive part in current-day semiconductor processing), which is also beneficial from an applications point of view.

Since its introduction, the racetrack memory has undergone several key improvements [14]. Not only was there a development in materials such that much smaller bit sizes could be achieved, also the mechanism by which the DWs were moved changed drastically. Originally, a torque was exerted on the DW by electrons that

[§]In principle, data could also be encoded by domains with their magnetization laying in-plane, but nowadays research is mainly focussed on materials with PMA because of their extremely narrow DWs, and hence potential small bit size.

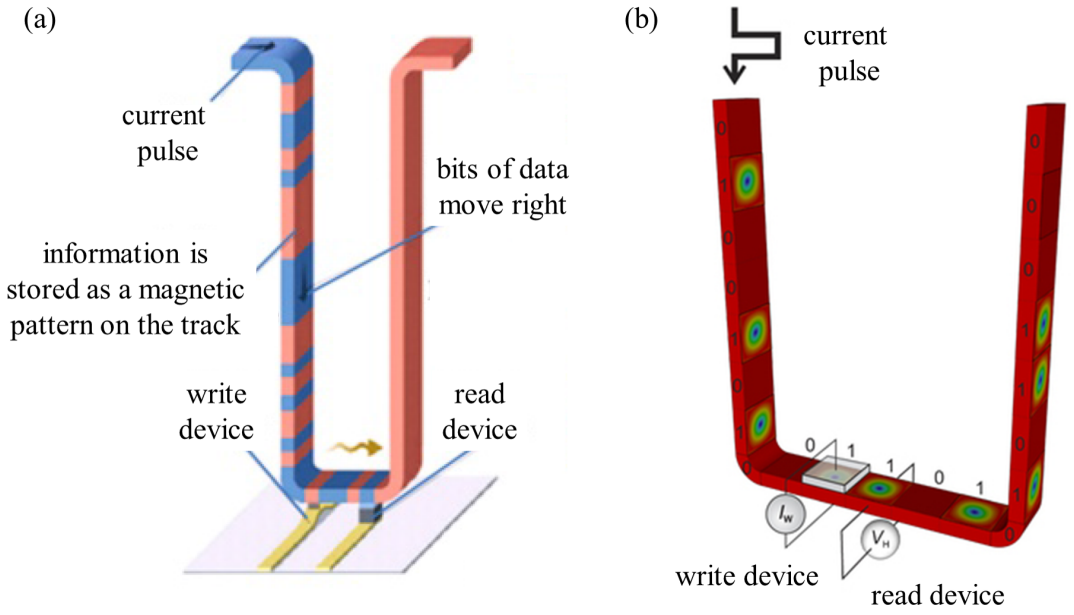

Figure 1.3: Racetrack memory based on (a) DWs or (b) magnetic skyrmions. Adapted from Ref. [12] and Ref. [13], respectively.

flow through the magnetic layer when a current is applied. Later spin currents generated in adjacent layers were used, which lead to significantly larger DW velocities [15]. However, this new mechanism only works if the spins in all DWs rotate in the same fashion, either clockwise or anti-clockwise. This makes the control of chiral interactions in magnetic thin layers technologically relevant. With respect to the energy consumption, it is important that the DWs are minimally hindered by pinning and defects, such that they can be moved using small current densities. To achieve this, it has been proposed to instead of encoding zeros and ones as up and down domains, encoding them as the presence or absence of a magnetic skyrmion, as depicted in Fig. 1.3(b). Because a skyrmion is not in contact with the racetrack edge (opposed to a DW), and has the freedom to move around possible defects, it is expected to be less prone to pinning. Therefore the critical current density required to move a skyrmion is orders of magnitude smaller than for DWs. For this version of the racetrack memory, control of chiral interactions is even more paramount. Not only does it determine whether the skyrmions can be moved by spin currents from adjacent layers, it also determines their stability, size, and direction in which they are pushed by currents.

The development of the racetrack memory is progressing steadily. Currently, the fasted observed DW motion amounts to around one kilometer per second [16]. Also several groups have already reported proof-of-principle experiments in writing and moving skyrmions in a racetrack. However, the contemporary industrial standard for data storage technology are truly impressive with respect to scale and reliability. Whether or not racetrack memories will really be able to compete and end up in our daily-used computers, smart phones or data centres, only time will tell. Nevertheless it provides a great motivation to research the wonderful physics of chiral spin structures.

1.3 This thesis

This thesis is divided into two parts. Part I concerns the effect of the DMI on magnetic DWs. This parts starts with a background chapter, comprised of a short description of the energies that affect magnetic DWs, the state of the art regarding DMI, and a more detailed introduction to the contents of this part of the thesis. This is followed by chapters presenting original work performed during this PhD project. Chapter 3 describes a phenomenon that can be exploited to measure the DMI. Chapter 4 demonstrates how that same phenomenon can be used to create a purely field-driven racetrack memory. Chapter 5 focusses on the configurations DWs take in magnetic strips under the influence of magnetic fields, and the role of the DMI. In Chapter 6 DW motion driven by the precession torque exerted by a magnetic field is explored theoretically. This is a mechanism fundamentally different from traditional field-driven or current-induced DW motion. The part ends with a brief summary of the results and the relation between them.

Part II involves the even more exotic topics of magnetic skyrmion bubbles and their current-induced motion. Again, this part starts with a background chapter with a brief overview of the relevant theoretical concepts followed by the recent developments in this research field. Also a detailed introduction to the experimental chapters that follow is given. Next, in Chapter 9, an unexpected response of skyrmion bubbles to an electrical current is investigated and we attempt to interpret this. In Chapter 10 it is investigated how skyrmion bubbles behave when restricted to small geometries. Part II also ends with a summary and outlook.

The research presented in this thesis is largely of an experimental nature, and hence various experimental techniques and equipment are instrumental for this work. For the fabrication of samples sputter deposition, electron beam lithography, and focussed ion beam irradiation are employed. The measurements are based on the magneto optical Kerr effect (MOKE), particularly using a Kerr microscope. These are all well-established techniques, so in order to let the reader focus on the exciting physics and experiments, the experimental methods are described in Appendix A instead of in a chapter of the main text.

Part I

Domain walls & Dzyaloshinskii-Moriya interaction

2

Background on part I: domain walls and Dzyaloshinskii-Moriya interaction

Part I of this thesis focusses on magnetic DWs that are manipulated by external magnetic fields. We study these spin structures in ultrathin magnetic films sandwiched between high-SOC materials, the fabrication of which is discussed in Appendix A. First, we introduce the energy terms that govern the magnetic state in such systems and how these affect magnetic DWs, which is essential to appreciate the experimental chapters that follow. Special attention is paid to the DMI, which introduces chirality to these systems. Subsequently, the state of the art regarding this chiral interaction is presented: key discoveries from literature and complex unsolved problems that motivated the research in this thesis are discussed. Last, it will be announced what can be expected from the experimental chapters that follow.

2.1 Basic theory

In this section the various energy contributions that determine the spin configurations in magnetic thin films with perpendicular magnetic anisotropy (PMA) are discussed. They can be summarized in the following equation for the total energy, E, in a volume, V:

$$E = \int_V \left(\underbrace{\frac{A}{|\mathbf{M}|^2} (\nabla \mathbf{M})^2}_{\text{exchange}} \underbrace{- \mathbf{M} \cdot \mu_0 \mathbf{H}_\mathrm{a}}_{\text{Zeeman}} \underbrace{+ K_\mathrm{eff} \sin^2 \theta}_{\text{anisotropy}} \underbrace{+ D \left[\mathbf{M} (\nabla \cdot \mathbf{M}) - (\mathbf{M} \cdot \nabla) \mathbf{M} \right]}_{\text{DMI}} \right) \mathrm{d}V. \tag{2.1}$$

The first term represents the direct exchange interaction favouring parallel alignment of neighbouring spins, a key ingredient for every ferromagnetic material. Here A is the exchange stiffness and $\mathbf{M}$ is the magnetization. The second term represents the Zeeman energy, which describes that it is energetically favourable for the magnetization to align with an external applied magnetic field, $\mathbf{H_a}$, and μ_0 is the vacuum permeability. The third term represents the effective uniaxial anisotropy* with K_eff the effective perpendicular magnetic anisotropy constant. The last term represents the DMI, an antisymmetric exchange contribution that occurs in systems with broken inversion symmetry and high spin-orbit coupling. It favours orthogonal alignment of neighbouring spins with a preferred rotational sense, with D the DMI constant.

2.1.1 Magnetic anisotropy

We now first examine the third term further. This term describes how the magnetization prefers to be oriented along a certain axis, which is termed the so-called easy axis of magnetization. This anisotropy can have multiple underlying causes. The contribution that is most important for systems studied in this thesis, is a result of spin-orbit coupling (SOC). Considering a single, semiclassical atom in which an electron orbits a nucleus, the concept of SOC can be understood intuitively. Seen from the frame of reference of the electron, it is the nucleus that is in motion, and because the nucleus possesses electrical charge it generates a magnetic field, which in turn affects the spin of the electron. Similarly, the spin is also coupled to orbital angular momentum in the much more complex situations in solid state physics. This can lead to a preferential direction of the magnetization with respect to the crystalline structure of the material or to an interface with

*Other symmetries and higher order contributions to the anisotropy do exist, but are omitted from this discussion because they can be neglected for the materials used in this thesis.

another material. In this thesis, ultrathin layers of Co grown on top of Pt are studied, of which the interface induces a magnetic anisotropy perpendicular to the thin film.

Another important contribution to the effective anisotropy comes from the demagnetizing field, $\mathbf{H}_\mathrm{d}$, which promotes flux closure inside a magnetic medium and minimizes dipolar stray fields. This contribution is determined by the magnetization configuration and the demagnetization tensor, $\mathcal{N}$, where the latter follows from the geometrical shape of the magnetic medium:

$$\mathbf{H}_\mathrm{d} = -\mathcal{N}\mathbf{M} = -\begin{pmatrix} N_x & 0 & 0 \\ 0 & N_y & 0 \\ 0 & 0 & N_z \end{pmatrix} \mathbf{M}. \tag{2.2}$$

Here a smaller dimension corresponds to larger demagnetization factor and the trace of $\mathcal{N}$ is equal to one. For the thin films studied in this thesis, where the film thickness is much smaller than the sample width or length, $N_z \approx 1$. In case of homogeneously magnetized thin film, the effective anisotropy (as is used in Eq. 2.1) can therefore be expressed as

$$K_\mathrm{eff} = \underbrace{\frac{K_{\mathrm{S},1} + K_{\mathrm{S},2}}{t}}_{\text{interface}} - \underbrace{\frac{1}{2}\mu_0 M_\mathrm{S}^2}_{\text{demag.}}, \tag{2.3}$$

where t is the magnetic film thickness, M_S is the saturation magnetization, and $K_{\mathrm{S},1}$ and $K_{\mathrm{S},2}$ are the anisotropy contributions of both interfaces of the magnetic layer. This means that K_eff can be tuned by the layer thickness, the choice of materials and the structure at the interfaces, making it a convenient parameter to control in order to achieve the right balance to stabilize the spin structures we want to study.

2.1.2 Dzyaloshinskii-Moriya interaction

The fourth term of Eq. 2.1, describing the DMI, introduces chirality to the system, and is therefore the central theme of the work in this thesis. DMI was first

introduced for low-symmetry crystals by Igor Dzyaloshinskii and Toru Moriya [17, 18]. DMI is of importance to a wide variety of material systems: spin-glasses [19], cuprates [20], molecular magnets [21], and multiferroic materials [22]. Here we will only focus on one particular class of systems with DMI: ultrathin ferromagnetic layers interfaced with high SOC materials. This may seem like an unexpected material class to study DMI, because one of the prerequisites for the interactions to exist is inversion asymmetry. However, it was realized by Albert Fert that at an interface the symmetry is reduced, which also allows for DMI [23]. In literature, DMI induced by this type of inversion symmetry breaking is often referred to as interfacial DMI. However in this thesis we will simply refer to this as DMI, as it is the only type we study. The technological relevance was soon realized and over the last decade DMI has gained huge interest, leading to the rapid development of measuring techniques and applications.

We will now give an intuitive argument for why the DMI can exist at all, and why broken inversion symmetry is a prerequisite. Figure 2.1(a) schematically shows two neighbouring spins ($\mathbf{S_i}$ and $\mathbf{S_j}$) and a adjacent heavy metal (HM) atom (which introduces strong SOC), a typical situation in which DMI can arise. The DMI vector, $\mathbf{D_{ij}}$, is directed perpendicular to the plane of these three sites. The energy associated with the DMI between two spins can be expressed as

$$E_{\mathrm{DMI},\ ij} = \mathbf{D_{ij}} \cdot (\mathbf{S_i} \times \mathbf{S_j}) \,. \tag{2.4}$$

This implies that when only the DMI is considered, neighbouring spins would point perpendicular to each other, and the sense of rotation is determined by the direction of $\mathbf{D_{ij}}$. This seems like a rather counterintuitive phenomenon, but Fig. 2.1(a) demonstrates that it is not necessary for the two senses of rotation to have the same energy. In situation I two spins are shown and the right spin is rotated counter-clockwise with respect to the left spin. Then two operations are performed that do not change the energy of the system: a rotation of the whole system and inversion of all spins, leading to situation II and III, respectively. The spins in situation III at the same angle to one another as in situation I, but now rotated in a clockwise fashion, so with opposite chirality. When ignoring the HM atom, the chirality is the only difference between situation I and III, and

we can conclude that the same energy should be associated with both chiralities. However, when the HM atom mediates the interaction between $\mathbf{S_i}$ and $\mathbf{S_j}$, it is no longer possible to create situations that are identical except for their chirality using operations that conserve the energy of the system, so the two chiralities are allowed to have a different energy. Also note that if a second, identical HM atom would be introduced on the opposite side of the two spins, situation I and III would again be identical except for their chirality, and no energy difference is allowed.

Real systems are obviously more complex than the three atoms sketched in Fig. 2.1(a). To evaluate the total DMI, the energy from Eq. 2.4 has to be summed over all pairs of neighbouring spins. The result can be translated to a DMI energy, D, in units of $\mathrm{mJ\,m^{-2}}$, as done for instance in Ref. [24]. This constant can be either positive or negative, setting the chirality of spin structures in the system. When experimentally assessing the DMI strength, this is the parameter that is determined, or the closely related interfacial DMI constant, D_s, in units of $\mathrm{pJ\,m^{-1}}$, in which the dependence on the magnetic film thickness is eliminated by $D_\mathrm{s} = D \times t$. Further, the contributions of all relevant interfaces have to be included to obtain the net DMI in the sample. In a perfectly symmetrical stack, where top and bottom interface of the magnetic layer are identical, these contributions exactly cancel out and there is no net DMI. Alternatively, as both signs of the DMI can occur depending on the combined materials, samples can be designed such that the contributions of the two interfaces add up instead of cancel out. This is referred to as additive DMI, which is often used when engineering material stacks with strong DMI.

2.1.3 Magnetic domain walls

In Chapter 1 magnetic DWs were already introduced as the transition region between two magnetic domains. This transition region is a frustration to the system, with respect to both the exchange energy and the magnetic anisotropy: the spins here are not aligned perfectly with their neighbours and they also do not point along the easy axis. Considering only the exchange interaction, the DW should be as wide as possible, minimizing the discrepancy between neighbouring

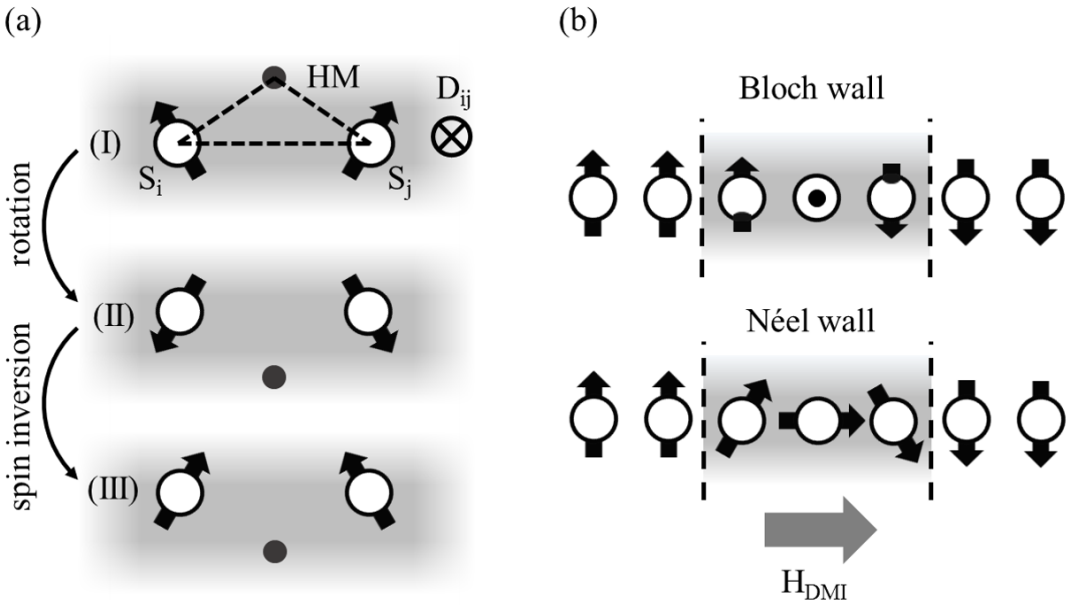

Figure 2.1: (a) Using only the energy conserving operations of rotation and spin inversion, it is not possible to obtain a version of the depicted system of two spins ($\mathbf{S_i}$ and $\mathbf{S_j}$) and a heavy metal (HM) atom which only difference to the original system is the sense of spin rotation. (b) Side views of two types of DW. The DMI promotes the formation of a Néel wall with its chirality fixed by the sign of $\mathbf{D}$. The DMI can be treated as a magnetic field, $\mathbf{H}_{\mathrm{DMI}}$, that is only present inside the DW.

spins. Considering only magnetic anisotropy, the DW should be as narrow as possible, minimizing the number of spins that are not aligned with the easy axis. Therefore the width of the DW, λ, and the associated energy, σ_0 are determined by the competition between these two contributions via the well-known equations

$$\lambda = \sqrt{A/K_{\mathrm{eff}}} \quad \text{and} \quad \sigma_0 = 4\sqrt{AK_{\mathrm{eff}}}. \tag{2.5}$$

The situation is complicated significantly in systems exhibiting DMI and in the presence of in-plane magnetic fields. In that case the internal structure of the DW becomes of importance, which can be a Bloch configuration, a Néel configuration (both illustrated in Fig. 2.1), or an intermediate form. The in-plane field gives a contribution to the Zeeman energy depending on how the magnetization inside the DW is oriented with respect to this field. To describe the effect of the DMI on

a DW, we use the continuous form as was presented in Eq. 2.1, explicitly worked out for an infinitely extended thin film in the xy plane, with no variation in the magnetization along the z direction[†]:

$$E_{\mathrm{DMI}} = D\left(m_z\frac{\partial m_x}{\partial x} - m_x\frac{\partial m_z}{\partial x} + m_z\frac{\partial m_y}{\partial y} - m_y\frac{\partial m_z}{\partial y}\right). \tag{2.6}$$

Now consider the situation that the magnetization is constant along the y direction, but a DW is present along the x direction, as drawn in Fig. 2.2(a), and evaluate Eq. 2.6. The last two terms vanish because there is no variation in the y direction. In the case of a Bloch wall $m_x = 0$ and the first two terms vanish as well, so $E_{\mathrm{DMI}} = 0$. For a Néel wall, the first two terms both give a positive (negative) contribution to E_{DMI} when the chirality is left-handed (right-handed) in case D is positive. So when $D \neq 0$ a Néel configuration minimizes E_{DMI}, and the chirality is determined by the sign of D.

A third contribution influencing the DW structure comes from magnetostatic interactions. When the film is patterned i.e. when it is not considered an infinitely extend plane, these typically tend to align the magnetization along the longest axis of the magnetic body. Similarly to how this favours in-plane magnetization in a film, inside a DW it favours the magnetization to lay along the length of the DW (when the strip is wide compared to the the domain wall width), corresponding to a Bloch wall.

To compare the DMI with the other effects influencing a DW, it is convenient to treat all contributions as corresponding effective fields. The magnetostatic interactions favouring a Bloch configuration can be expressed as a demagnetizing field, H_K, which depends on the sample geometry in a complex way as described in Ref. [25]. We define the x component of the in-plane magnetic field, H_x to be along the same axis as the DMI field (see Fig. 2.2(a) for a sketch of the sample geometry and the coordinate system). The DMI field, with strength H_{DMI}, is only present inside the DW where a splay between neighbouring spins is present:

[†]This is an accurate description when the film thickness is less than the exchange stiffness length, $l_{\mathrm{ex}} = \sqrt{\frac{A}{\mu_0 M_{\mathrm{S}}}}$.

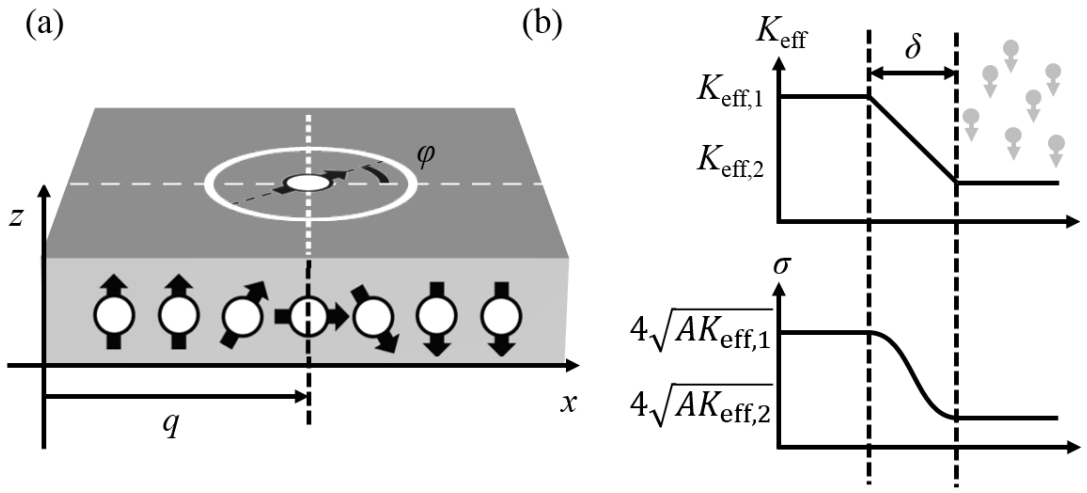

Figure 2.2: (a) Definition of q and φ in the 1D model. (b) A transition in the effective anisotropy (for instance created by ion irradiation) poses an energy barrier for DWs.

$$H_{\text{DMI}} = \frac{D}{\mu_0 M_{\text{S}} \lambda}. \tag{2.7}$$

The total energy of a DW, σ, in the geometry sketched in Fig. 2.2(a) is now given by:

$$\sigma = \underbrace{\sigma_0}_{\text{Eq. 2.5}} + \lambda \mu_0 M_{\text{S}} \left(\underbrace{H_K \cos^2 \varphi}_{\text{demag.}} - \pi \left(\underbrace{H_{\text{DMI}}}_{\text{DMI}} + \underbrace{H_x}_{\text{Zeeman}} \right) \cos \varphi - \underbrace{\pi H_y \sin \varphi}_{\text{Zeeman}} \right). \tag{2.8}$$

Minimizing the DW energy now gives the internal magnetization angle inside the DW, φ, as depicted in Fig. 2.2(b). This parameter is paramount for the mechanisms, speed, and direction of DW motion, to which we will come back in Chapter 8. Moreover, in samples where the material parameters are not uniform, σ is position dependent. A sudden transition in σ poses an energy barrier for a DW, which is the topic of the next section.

2.1.4 Domain walls at an anisotropy transition

The discussion up to here has concerned thin films with uniform material parameters. However, it is possible to create samples with, for instance, non-constant K_{eff}. This parameter can be controlled by changing the film thickness, by an electric field, or by focused ion beam (FIB) irradiation [26], and the latter is used in various instances in this thesis as it allows for abrupt changes in K_{eff} to be induced using the focused ion beam resolution. At an abrupt transition from a low K_{eff} to a high K_{eff} region, a DW is pinned because of the corresponding transition in DW energy, see Fig. 2.2(b) for a sketch of such an energy landscape.

To calculate the exact pinning strength due to the change in anisotropy, a one-dimensional (1D) model can be used. In this model it is assumed that the magnetization is constant along the y and z direction, while along the x direction the profile of the DW is fixed [27]. This means that only two parameters that can vary remain: the position of the DW along the x direction q and the in plane angle φ. This simplifies the situation such that the DW pinning strength can be calculated analytically, which is done in Ref. [26], resulting in

$$H_{\text{depin}} = \underbrace{\frac{K_{\text{eff},1} - K_{\text{eff},2}}{2\mu_0 M_{\text{S}}}}_{\text{step height}} \times \underbrace{\frac{2\lambda}{\delta} \tanh \frac{\delta}{2\lambda}}_{\text{step width}} . \tag{2.9}$$

$K_{\text{eff},1}$ and $K_{\text{eff},2}$ are the effective anisotropy constants in region 1 and 2, respectively, δ is the width of the K_{eff} transition region, and λ is the DW width as defined in Eq. 2.5. The strength of the pinning is expressed as the pinning field, H_{depin}, the magnetic field strength that is required for the DW to overcome the energy barrier.

The intuitive interpretation of Eq. 2.9 is that the pinning strength becomes larger when the energy barrier sketched in Fig. 2.2(b) becomes steeper. The barrier becomes steeper if (I) the difference between the two constant levels ($K_{\text{eff},1} - K_{\text{eff},2}$) increases or (II) the width of the K_{eff} transition region is reduced (relative to DW width). Because it is the Zeeman energy (which scales with the size of the magnetization, as can be seen in Eq. 2.1) that makes a DW depin upon the application of a magnetic field, a larger M_{S} also leads to a smaller H_{depin}.

2.1.5 Magnetization dynamics

Last, we briefly touch upon the basics needed to describe the dynamics of spin structures. Dynamics in the field of magnetism is generally described by the Landau-Lifshitz-Gilbert (LLG) equation [28]:

$$\frac{\partial \mathbf{M}(t)}{\partial t} = \underbrace{-\gamma\mu_0 \mathbf{M} \times \mathbf{H}_{\text{eff}}}_{\text{precession}} + \underbrace{\frac{\alpha}{M_{\text{S}}} \mathbf{M} \times \frac{\partial \mathbf{M}(t)}{\partial t}}_{\text{damping}} . \tag{2.10}$$

The precession term describes how the magnetisation precesses around an effective field $\mathbf{H}_{\text{eff}}$, in which the contributions of the exchange, anisotropy, external magnetic field, dipolar fields and DMI are incorporated. Here γ is the gyromagnetic ratio, which amounts to $1.76 \times 10^{11}\,\text{rad}\,\text{s}^{-1}\,\text{T}^{-1}$. The damping term describes how the magnetisation relaxes towards its equilibrium position along the effective field. Here α is the damping constant, which describes the rate of this relaxation. The LLG equation can be expanded with terms that describe spin transfer torques, and this will be discussed in part II of this thesis. Also, the LLG equation can be combined with the aforementioned 1D model, which provides a powerful tool to study and understand the dynamics of DWs.

2.2 State of the art on DMI

Here we will introduce some of the key findings, measuring techniques, applications, and unsolved questions regarding DMI. Please note that due to the vastness of the field this is by no means a complete overview. Also note that discussion regarding the role of DMI in current-driven DW motion and stabilization of magnetic skyrmions is postponed to Part II of this thesis.

2.2.1 Experimental techniques

There are several methods to obtain the DMI strength, and on the coming pages the following key categories are discussed: static imaging of spin structures, asymmetric DW motion, asymmetric nucleation, tilted edge states, asymmetric spin wave propagation, and spin torque efficiency. For each category one or more ex-

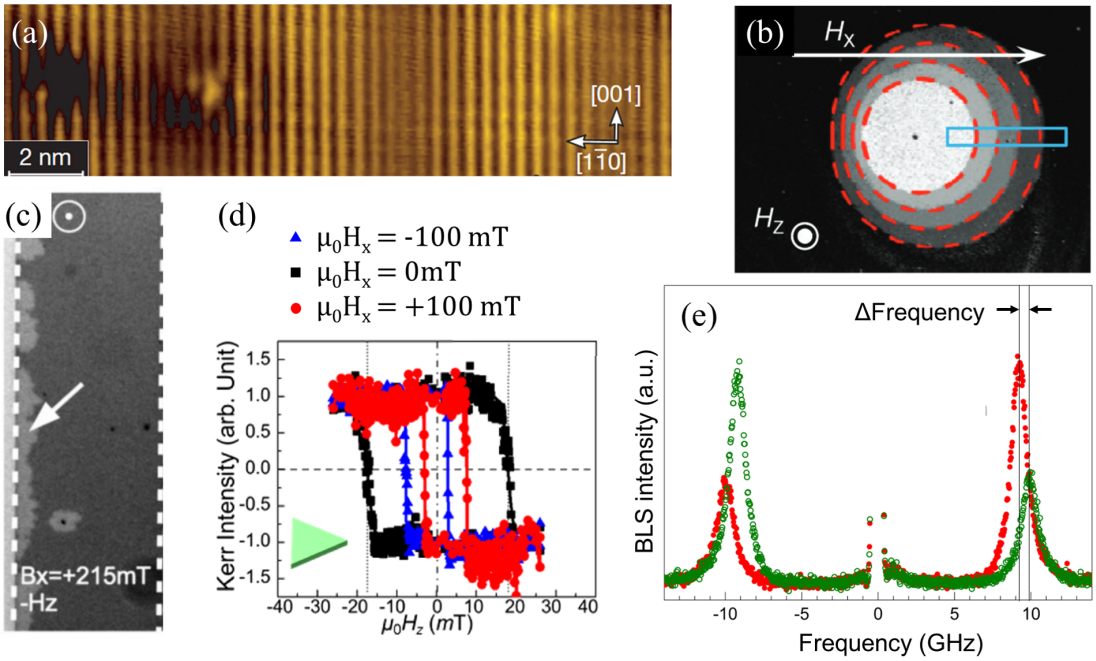

Figure 2.3: Various experimental techniques to determine D. (a) SP-STM image of Mn on W showing a spin spiral structure. From Ref. [29]. (b) Combination of 4 Kerr microscope images of an asymmetrically expanding magnetic bubble in the presence of an in-plane magnetic field. From Ref. [30]. (c) From Ref. [31]. (d) Asymmetric hysteresis loops obtained in an asymmetric geometry in the presence of an -in-plane magnetic field. Adapted from Ref. [32]. (e) Frequency shift observed using BLS. From Ref. [33].

amples of corresponding experimental techniques are introduced, and an overview is shown in Fig. 2.3. Also the most distinctive pro (+) and con (-) for every category is listed.

Static imaging of spin structures

The typical size of magnetic domains and the internal angle φ inside DWs are determined by the balance of the different energy contributions, including the DMI. Direct observation of the magnetic structure thus contains information on the DMI. Spin-polarized scanning tunnelling microscopy on manganese on a tungsten substrate resulted in the first experimental evidence of DMI in thin layers [29], the key measurement is shown in Fig. 2.3. It was revealed that the spins formed spirals, meaning that neighbouring spins were tilted with respect to one another,

as sketched in Fig. 2.1. Other techniques that are used for imaging of static chiral structures are nitrogen vacancy magnetometry [34], magnetic force microscopy [35], and scanning electron microscopy with polarization analysis [36].

+ Details of the magnetic configuration are measured directly instead of being inferred from other observations.

– Often restricting measurement conditions are required, depending on the specific imaging technique that is used. For example no magnetic fields are allowed or no capping layer is allowed.

Asymmetric domain-wall motion

The measurement of DW dynamics can also give information about the DMI, as the dynamics depend on the DW energy. When the displacement of a DW is measured instead of the internal spin structure inside DWs, techniques with a lower spacial resolution than in the previous section can be used. Kerr microscopy is an example of a powerful tool to image domain structures (for an introduction to this technique, see Appendix A) and deduce their dynamics. When studying DW motion, the DMI can be treated as an effective in-plane field inside the DW. The first work using this principle was by Je et al. [30]. They realized that the velocity of a moving DW depends on its energy, and that the DW energy in turn depends on the in-plane magnetic field and DMI field experienced by the DW. In Fig. 2.3(b) a combination of four consecutive images of a out-of-plane field-driven expansion of a magnetic bubble in the presence of an in-plane field is shown. The result is asymmetric bubble expansion (ABE): on the left side of the bubble the DMI field and the in plane field counteract each other, whilst on the right side they enhance each other. The DW velocity is measured as function of externally applied in-plane field, and a clear minimum in the obtained curve is observed. It was reasoned that at this applied in-plane field the DMI field was exactly canceled, hence D could be directly calculated using Eq. 2.7.

+ Measurements can be performed using widely available equipment.

– Additional influences on the DW velocity (like chiral damping or complex creep behaviour) complicate the interpretation of the data.

Asymmetric nucleation

Also the out-of-plane field required to nucleate a bubble domain of opposite magnetization inside a uniformly magnetized film depends on the DW energy. Hence, the dependence of this nucleation field on the in-plane magnetic field can be used to deduce the DMI strength [37]. In larger structures, it can be observed how switching of the magnetization commences on one side of the sample (see Fig. 2.3(c)), and how this asymmetric nucleation (AN) is affected by in-plane magnetic fields [31].

+ Requirements on both spacial and time resolution are low.

– Nucleation of a magnetic domain usually starts at a defect. Therefore, random defects can influence the measured DMI value.

Tilted edge states

At the physical edge of a film, the spins are tilted away from the z direction due to the DMI [38]. This can be exploited to determine the DMI strength: in geometrically asymmetric structures the coercive field is altered in the presence of an in-plane magnetic field, resulting in an asymmetric hysteresis loop (AH), see Fig. 2.3(d) [32].

+ DMI can be derived from (easily measurable) hysteresis curves.

– This method only works if the material parameters are not changed at the edges, and the edges are straight and virtually defect-free. This poses strict requirements for the quality of the structures created by lithography.

Asymmetric spin wave propagation

Another approach to measure the DMI is based on asymmetric spin wave propagation. A spin wave refers to the collective motion of spins in a magnetic material. Because the DMI favours a certain sense of rotation between neighbouring spins, it will cause spin waves of opposite chirality to have different energies. Brillouin light scatttering (BLS), which excites and probes these spin waves optically, is a widely used technique to probe this effect [33, 39–41] (for example, see Fig. 2.3(e)), but it can also be done using spin-polarized electron energy loss spectroscopy [42] or by all-electrical propagating spin wave spectroscopy [43].

+ The value of A is not required to derive a value for D. As A is tricky to access experimentally, it usually poses the largest uncertainty in the D values obtained by other methods.

– As spin waves with opposite chiralities are located at opposite interfaces, differences between these interfaces can also lead to a difference in energy between these spin waves. In particular, a difference in the interfacial anisotropy contributions is difficult to distinguish from the DMI.

Spin torque efficiency

Last, the torque exerted on a DW by a spin current depends on the DW configuration (e.g. a Bloch or Néel configuration), as will be explained in Chapter 8. By probing the strength of this torque as a function of an applied in-plane magnetic field, the DW configuration as a function of magnetic field can be deduced, from which a value for the DMI can be derived [44, 45].

+ Most of the envisioned devices base on chiral spin structures are operated by spin torques. This method is therefore suitable to study material stacks that are directly of interest for applications.

– Electrical current introduces many additional phenomena in a magnetic material, complicating the interpretation of the data.

2.2.2 Unsolved issues

In literature, a large spread in measured DMI values is reported [41]. Even when the same material stacks are investigated, regularly contrasting DMI strength are obtained (sometimes even with an opposite sign), if the samples are grown in different labs. There are several reasons for these discrepancies, some of which are related to the applied measurement techniques. For instance, not all techniques measure at the same scale: some probe the DMI very locally, whilst others measure an average over a larger area. A large spacial inhomogeneity of the DMI has been reported in some cases, which makes the results dependent on the measuring scale of the applied measurement technique [34, 35]. Moreover, the interpretation of the data is often not straight forward. Unexpected effects that are difficult to distinguish from the intrinsic DMI, like chiral damping, can play a role [46, 47].

Table 2.1: Overview of experimentally obtained values for D_s in multilayers with Co as the magnetic layer. Several experimental techniques are used: asymmetric nucleation (AN), Brillouin Light Scattering (BLS), Asymmetric Hysteresis (AH), Asymmetric Bubble Expansion (ABE), and spin-orbit torque efficiency (SOT efficiency). Based on Ref. [32].

	Material stack (thickness in nm**)**	**Ds** (pJ m^{-1})	**Technique**	**Ref.**
I:	Pt (3) / Co (0.6) / AlO_x (2)	1.32	AN	[31]
II:	Pt (4) /Co (1-2) / AlO_x (2)	1.43	BLS	[40]
III:	Pt (4) /Co (1.3-1.8) / AlO_x (2)	1.37	BLS	[48]
IV:	Ta (4) / Pt (4) / Co (1.3-1.8) / AlO_x (2)	2.18	BLS	[48]
V:	Ta (4) / AlO_x (1.95) / Co (1.15) / Pt (4)	-1.63	AH	[32]
VI:	Ta (4) / Ir (4) / Co (1.25-3) / AlO_x (2)	0.84	BLS	[49]
VII:	Pt (3) / Co (0.7) / Ir (0-1.3) / Pt (1)	-0.56 to 0.84	ABE	[50]
VIII:	Ta (5) / Pt (2.5) / Co (0.3) / Pt (1.5)	0.04	ABE	[30]
IX:	Pt (4) / Co (0.36) / Pt (1)	0.05	SHE	[44]
X:	Pt (4) / Co (0.6) / Pt (0.4) epitaxial	0.01	ABE	[50]

To summarize what is already known about the DMI for material stacks similar to the ones studied in this thesis, and to illustrate some typical unsolved issues, Table 2.1 gives an overview of reported DMI strengths (here D_s is listed instead of D, to make a fair comparison between stacks with different magnetic layer thickness), measured using various techniques.

Stack I, II, and III seem to show comparable values for D_s in Pt/Co/AlO_x samples, obtained by different experimental techniques. Pt/Co interfaces appear at many

instances in this thesis, but we cannot simply assume that they give this reported contribution to the DMI. Intuitively, the Co/AlO_x interface should not contribute to the DMI because it does not contain a heavy metal, but recent theoretical work has shown that oxides can also contribute to the DMI [51]).

It is remarkable that the D_s found for stack IV is significantly larger than for the previous stacks, while the relevant interfaces consist of the same materials. These samples are grown in the same lab as stack III, and measured using the same technique, with the only difference the presence or absence of a Ta buffer layer below the actual material stack. A Ta seed layer is known to improve the crystalline orientation of the subsequent layers [52]. The different results for stack III and IV demonstrate that besides the choice of materials also the structure at the interface is of utmost importance for the DMI.

Imagine flipping a sample containing chiral magnetic structures up side down, and observing the magnetization through the substrate. If before the magnetization inside the DWs was directed from down domains towards up domains, now it points from the up domains towards the down domains. In other words, the chirality of the DWs is now opposite. When instead of flipping over a sample, a sample with the inverted material stack is grown, it is therefore expected to have an equal but opposite DMI strength. Stack V shows that an inverted material stack indeed results in a D_s with the opposite sign (note that we use the convention that a positive D corresponds to left-handed chirality and a negative D to right-handed chirality).

Stack VI shows that introducing a thin layer of Ir between a Co/Pt interface, inverts the sign of the DMI, indicating that Co/Pt and Co/Ir interfaces induce DMI with an opposite sign. The results on VII, on the contrary, show that Pt/Co and Ir/Co have a DMI with the same sign.

Last, some typical results on nominally symmetrical Pt/Co/Pt stacks are shown. Because here the net DMI is caused purely by differences in the interface structure, different signs of the DMI can be found for very similar samples. The DMI in such a symmetric stack could therefore be controlled by subtle interface engineering, for instance by varying the deposition temperature and pressure as was done in Ref. [53].

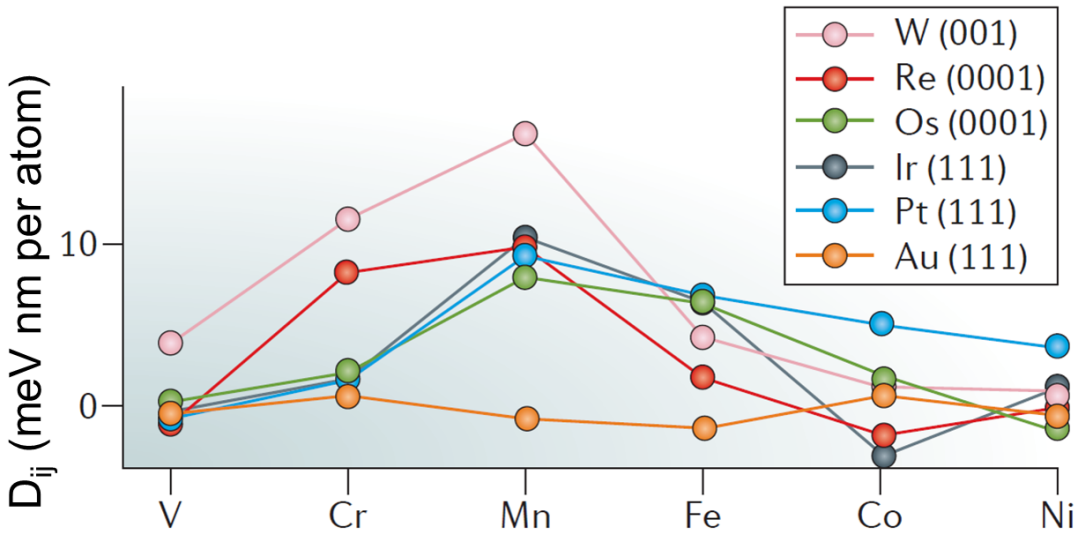

Figure 2.4: *Ab initio* calculation of the DMI for various combinations of *3d* metals on top of *5d* metals. Adapted from Ref. [51] and [54].

2.2.3 Understanding DMI

The precise physical origin of this elusive interaction remains controversial, though some interesting progress has been made over the last couple of years. Experimentally, researchers are looking for correlations with other material parameters. Convincing correlations with proximity-induced magnetic moments [55] and the Heisenberg exchange [39] have been found.

Ab inito calculations can be helpful in the search of the precise origin of DMI. An example hereof is that they have proven that the DMI in thin films is really an interfacial phenomenon [24]. Also, they can provide an overview of the DMI for a large number of material combinations in order to find trends. Figure 2.4 shows the DMI between spins of *3d* metals on top of *5d* metal substrates determined by *ab initio* calculations [51]. A clear optimum in DMI strength around Mn is visible, irrespective of which heavy metal is used (with Au as an exception, which seems to induce negligible DMI at all possible interfaces). This is a surprising trend, considering that the key ingredients for DMI (high SOC and inversion asymmetry) do not depend on which transition metal is used. It is concluded that the *3d*/*5d* band lineup is an additional essential ingredient. Further, theoretical calculations can give guidance in which materials to use for creating a stack with

additive DMI. The calculation of an opposite sign of D_{ij} for Pt/Co and Ir/Co has inspired the creation of Pt/Co/Ir multilayer with a large net DMI [56]. However, as mentioned before, there have also been experimental observations indicating that Pt/Co and Ir/Co interfaces have the same sign of D_{ij}, in sharp contrast with the *ab initio* calculations. Calculated systems will always be a simplification of the complex atomic structure in real samples, making it challenging to really get to the bottom of the physics of DMI in real samples.

2.2.4 Applications

Regardless of its origin, DMI poses exciting possibilities from an applications point of view, in particular regarding the racetrack memory, as introduced in Chapter 1. Traditionally, at a certain driving field, the internal magnetization of the DW itself starts to precess which sharply decreases the DW velocity, which is known as Walker breakdown. When DMI is introduced to a system, it stabilizes the internal structure of the DW, allowing for larger driving fields, and hence larger DW velocities before Walker breakdown occurs [57, 58]. Also the fact that in plane magnetic fields can be used to selectively increase or decrease the velocity of specific DWs created the possibility for new design schemes for memory devices [59–61]. In Part II, applications related to the more exotic effects of DMI will be discussed.

2.3 Content part I

In the first part of this thesis, we are contributing to this research field in the following ways. In Chapter 3 we explore an alternative method to measure DMI, by studying the depinning of DWs from an anisotropy barrier in the presence of in-plane magnetic fields. This method is suitable to measure weak DMI in perpendicularly magnetized samples. What is especially interesting about this method, is that also the DMI in the low anisotropy region, created by FIB irradiation, is reflected in the results.

In Chapter 4 it is shown that the DMI-induced asymmetric DW depinning from the previous chapter cannot only be used to measure the DMI, but also to manipulate DW motion. It is shown that multiple DWs in a single strip can synchronously be

moved in one direction, which is traditionally not possible using magnetic fields only. This proof-of-principle experiment shown in this chapter are in essence a prototype of an alternative form of the racetrack memory that can be operated exclusively by a magnetic field instead of currents.

In Chapter 5 we examine the geometrical shape of DWs in long strips with a typical width of several micrometres. It turns out that in the presence of DMI, the observed DW shapes are non-trivial. The importance of this observation is twofold. It implies that the DMI strength can, in principle, be deduced from the DW shape, which provides again an alternative measurement technique to determine the value of the DMI. Secondly, it is important to keep in mind that the DW geometry may be strongly affected by the DMI when designing actual memory devices in which multiple DWs are packed closely together.

Last, in Chapter 6 we investigate a completely new principle to achieve DW motion. Because the investigated mechanism is fundamentally different from previously explored mechanisms for DW motion, this chapter exclusively focuses on the theoretical basis and numerical calculations; no experimental results are shown. By combining the LLG equation with the 1D model we show that via the precession term from Eq. 2.10, an in-plane field can exert a torque on a DW, leading to DW motion. Again, the DMI is a vital ingredient. It determines in which direction the in-plane field has to be applied to move the DW, and it makes it possible to move multiple DWs synchronously in the same direction.

3

Asymmetric domain-wall depinning induced by Dzyaloshinskii-Moriya interaction

DMI is currently the focus point of many research efforts in the spintronics community. Its possible applications and fundamental new physics motivates us to understand, measure and manipulate this interaction. Using an elegant, alternative approach, we show that by depinning a DW from an anisotropy barrier in PMA nanowires in the presence of a static in-plane field, the presence of DMI can be detected. This is experimentally demonstrated, and clear effects are observed even though a sample with small DMI is used. The technique presented could be used to obtain both the sign of the DMI constant and its quantitative value. [*]

3.1 Introduction

The DMI is relevant for spintronics in several ways. By the stabilization of a Néel type DW, it enables DW motion at higher velocities, which could improve the so-called racetrack memory [63, 64]. Moreover, it was recently observed that in systems with strong DMI a novel type of spin structure can form: the magnetic skyrmion [65–67]. These vortex like structures can be extremely small, stable and

[*] This Chapter has been published in *IEEE Transactions on Magnetics* [62]

movable by low current densities, and are expected to be the building block for the next generation of memory devices [68, 69].

As introduced in Chapter 2, various techniques to measure DMI have recently been explored: (I) the aforementioned effect of in-plane external fields on DW motion, (II) influencing domain nucleation with in-plane fields [31], (III) Brillouin light scattering [39, 40, 70], and (IV) scanning nanomagnetometry [71]. In all these studies, the emphasis lies on structures with strong DMI, which is understandable as this is desirable with respect to applications involving skyrmions. But, in experiments regarding the asymmetric DW motion under the influence of in-plane magnetic fields [30], it becomes clear that also a small DMI can have a large impact on the behavior of the system. However, the investigated DWs can take on peculiar shapes of which the theoretical understanding (and hence deducing a reliable DMI strength) remains a challenge [46].

In this chapter, we will show that depinning of DWs from an anisotropy barrier can be influenced by applying an in-plane magnetic field, and that this influence differs for up-down and down-up DWs. This does not only prove the presence of DMI in our system with low asymmetry, but also is a neat example of how even a small DMI can have a significant effect on the behavior of DWs. We present a plausible intuitive interpretation of the observations, and discuss how a quantitative value for the DMI can be obtained using our experimental technique.

3.2 DMI and depinning

We study microstrips with PMA, which contain a middle region with reduced magnetic anisotropy (for the experimental realization of such a system, see the next section). Figure 3.1 shows the situation schematically. Sweeping a perpendicular field (H_z) can result in a situation where the region with reduced anisotropy has an opposite magnetization from the rest of the strip. The in-plane angle, φ (see Fig. 3.1), is expected to be $\pm\pi/2$ (corresponding to a Bloch wall), which follows from magnetostatics [27]. The width of the DWs is determined by a competition between the magnetic anisotropy and exchange interaction and corresponds to a DW energy, σ, of $\sigma = 4\sqrt{AK_{\text{eff}}}$, with A the exchange constant and K_{eff} the effective anisotropy constant. Therefore the anisotropy boundaries pose an energy

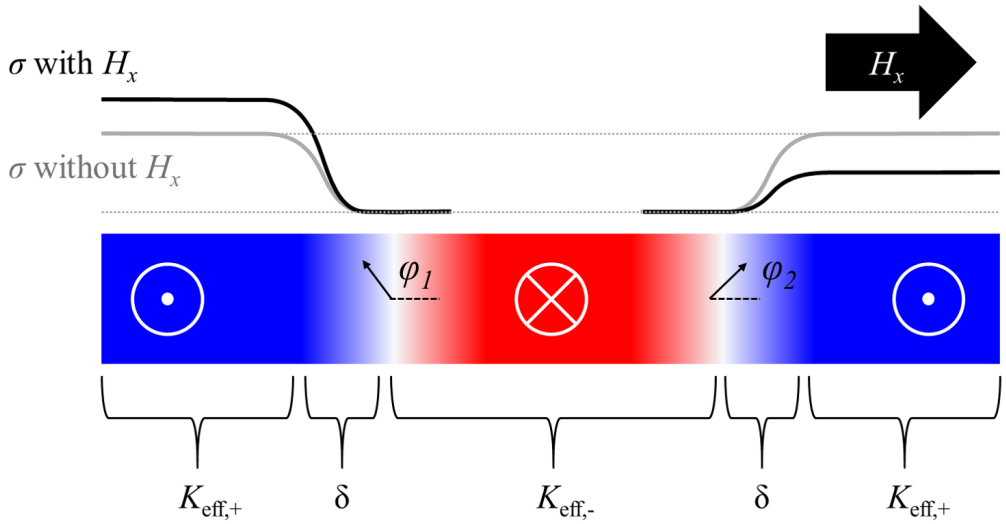

Figure 3.1: Schematics of the top view of a magnetic strip with PMA. The middle part with reduced anisotropy ($K_{\text{eff,+}} < K_{\text{eff,-}}$), and the regions where the anisotropy transition occurs (which is assumed to occur in a linear way), indicated by δ ,and the definition of the in-plane angle φ are shown. In the presence of DMI and an in-plane field, the energy landscape is different for the up-down and down-up DW.

barrier and the DWs are pinned [26]. The height of the energy barrier determines the strength of the perpendicular field that is required to depin the DW (H_{depin}).

Now we take the effect of the DMI into account. We assume that the DMI is negligible in the area with reduced anisotropy; in our structures the DMI is induced at the interfaces, and as the reduction of anisotropy is caused by a reduction of the interface quality an accompanying reduction in the DMI strength is expected (note that this not verified experimentally, and this assumption is further discussed in section 3.4). DMI is a chiral interaction which favors Néel walls ($\varphi = 0 \vee \varphi = \pi$), so the DWs will take this configuration (or an intermediate form between the Bloch and Néel configuration, depending on the strength of the DMI) when they enter the pristine regions. However, the favoured in-plane angle is different for the two DWs in our system, as an up-down DW and a down-up DW need to have a different φ in order to have the same chirality. The height of the energy barrier at the anisotropy step is still the same for both DWs. Adding an in-plane magnetic field along the strip (H_x) lifts this degeneracy: for one DW H_x and the DMI favor the same in-plane DW angle, while for the other DW they favor the opposite one. As a result, there will be a difference in how easily the energy barrier is overcome,

i.e. there will be a difference in H_{depin}. This is a measurable quantity, and will be the focus point of the experimental results that will be presented.

3.3 Experimental results

For this study, we prepared magnetic strips with a lateral dimension of 1 µm patterned on a silicon wafer using a typical e-beam lithography and lift-off process. The patterned strips, which are deposited using DC magnetron sputtering, consist of the following material stack: Ta (5 nm) / Pt (4 nm) / Co (0.6 nm) / Pt(4 nm), which is expected to have a certain DMI value [30]. A region with reduced PMA is created in the middle of the strips by irradiation with highly energetic Ga^+ ions, resulting in samples that are similar to the ones studied by Haazen *et al.* [72]. In Fig. 3.2 an image of five typical strips is shown, and the Ga^+ irradiated area (labeled Ga^+) and the two non-irradiated regions (labeled I and II) are indicated. In the magnetically soft region, a domain with opposite magnetization is nucleated by an external perpendicular field H_z, and two DWs are created and pinned at the edge of the irradiation boundaries, which is the situation shown in Fig. 3.2(a). When the perpendicular field H_z is increased, at a critical field, i.e. H_{depin}, the DWs are depinned from the irradiation boundaries and propagate through regions I and II towards the ends of strips.

Measurements are performed using polar Kerr microscopy, visualizing the z component of the magnetization (M_z), and a homebuild three dimensional magnet, which can apply fields up to 40 mT. Figure 3.2(b) shows the contrasting behavior of up-down and down-up DWs that occurs when in-plane fields are applied along the strips. For all strips, region II is switched at a certain H_z, while the DW adjacent to region I remains pinned. When H_z is increased further, eventually the DWs of region I depin as well. Now H_z is swept in the other direction; when negative values are reached, the Ga^+ irradiated region again switches first, but now region I of the strips switches first, while the DWs of region II stay pinned.

To obtain more quantitative data about this phenomenon, we measure hysteresis loops (the magnetic field is swept along the z direction). Two measurements are taken per magnetic strip: one for region I, and one for region II. A step in the hysteresis loops corresponds to the depinning of the DW from its anisotropy

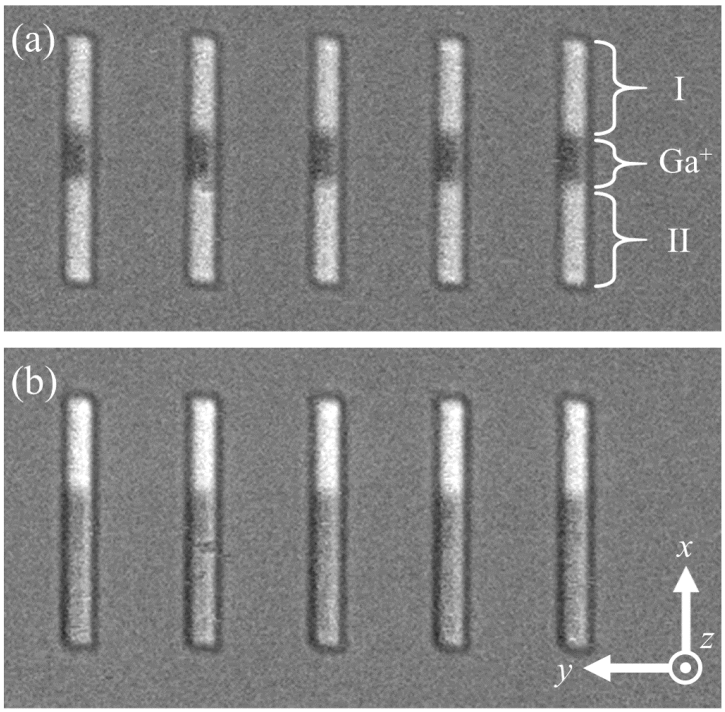

Figure 3.2: Kerr microscope image of 5 typical 1 µm × 10 µm Pt/Co/Pt nanostrips. (a) After saturation, a magnetic field is applied in the z direction and the magnetization in the middle region of each strip is switched because of the lower anisotropy here. In each strip, two DWs are created and pinned at the anisotropy barrier. (b) An in-plane field in the x direction affects the two DWs in the same strip differently. In this picture it can be seen that the DWs at region II have already depinned and propagated through the rest of the strip, while the DWs at region I are still pinned. Definition of the axes is included in the lower right corner.

barrier. This routine is repeated for various strengths of H_x. A typical result is shown in Fig. 3.3(a), where it can be seen that the loop obtained in region I is shifted in the (positive) H_x direction with respect to the loop obtained in region II. This means that when H_z is swept from negative to positive, the DW at region II is the first to depin, while when the z field is swept from positive to negative the DW at region I is the first to depin. In Fig. 3.3(b) the results obtained with the in-plane field in the opposite direction are shown, and it can be seen clearly that the loops for region I and II are now shifted in the opposite direction.

We now plot the difference in depinning field between the region I and II DWs, ΔH_{depin}, versus H_x, see Fig. 3.4. The ΔH_{depin} shows an almost linear dependence

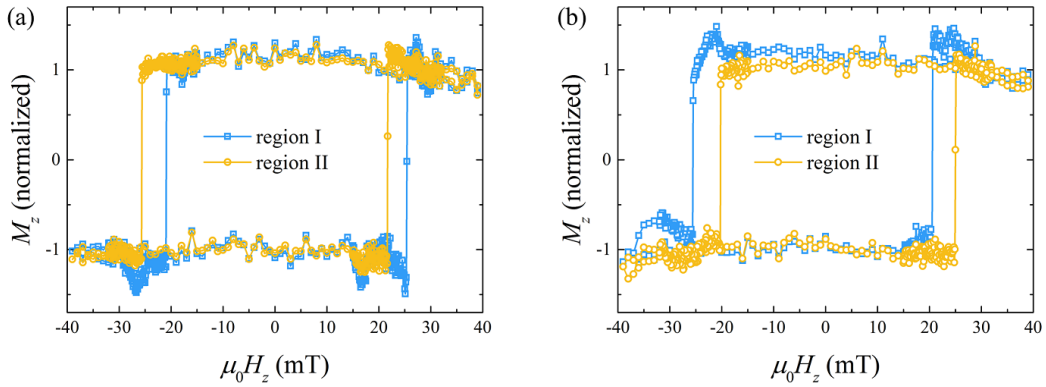

Figure 3.3: Typical hysteresis loops obtained in region I and II of one strip when (a) $\mu_0 H_x = +39\,\mathrm{mT}$ (b) $\mu_0 H_x = -39\,\mathrm{mT}$.

on H_x. This behavior is consistent with the interpretation in section 3.2. A larger the in-plane field means a larger difference in energy barrier, so a larger difference in depinning field is also expected. The results are reproducible for different samples.

3.4 Discussion & Conclusion

The experimental findings correspond well to the interpretation given in section 3.2. The energy landscape should be symmetrical in the absence of an in-plane field, and we indeed see in Fig. 3.4 that there is no significant shift at zero field. Following the theory that was developed in the context of asymmetric DW motion (see again Eq. 2.8) it is expected that the asymmetry in depinning field is proportional to the in-plane field, up to the field strength that is equal to the effective DMI field [57]. At this field the shift versus in-plane field curves are expected to saturate. This is not observed, indicating that the DMI field is larger than 40 mT. Measurements with a modified setup that can reach higher fields should be performed to confirm this. The saturation field gives a quantitative value for the difference in DMI between the irradiated and non-irradiated regions. If the DMI in the irradiated region vanishes completely, this means that both the sign and strength of the DMI in the structure as deposited can be determined. However, the vanishing of DMI by ion irradiation that is assumed here is not trivial; it is possible that the two interfaces of the magnetic layer are influenced in a dif-

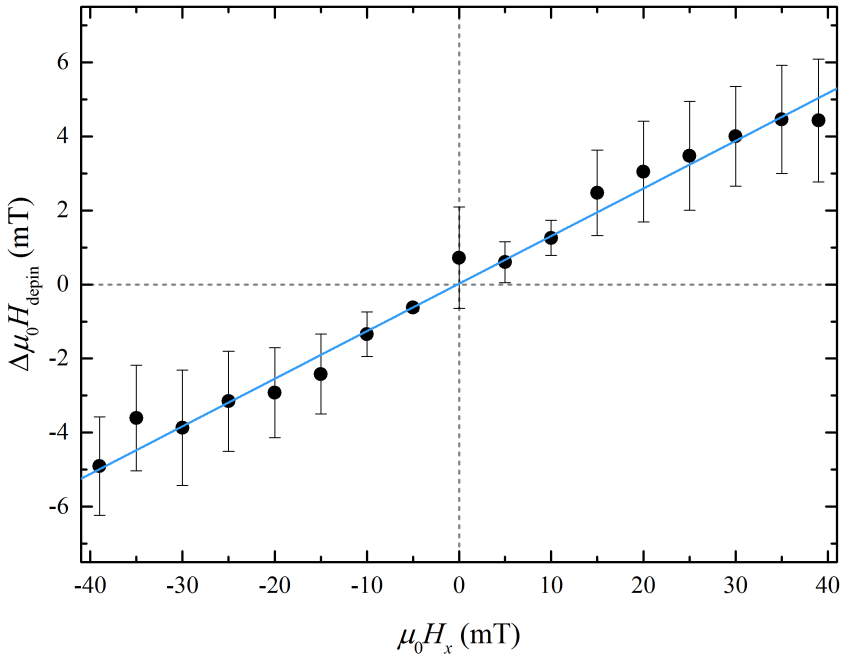

Figure 3.4: $\Delta H_{\mathrm{depin}}$ (the difference between the depinning fields for region I and II) as a function of the static magnetic field in the x direction for a typical sample. Each point represents an average over ten microstrips.

ferent way, resulting in an asymmetry [73]. This is an issue that requires further research.

An electromagnet is used to apply the external in-plane field during the measurements. We note that a possible out-of-plane leakage field from the in-plane magnet cannot explain our observations. Such a leakage field would indeed shift the hysteresis loops, but the shift would be the same for region I and II of the wires. When considering only the *difference* in depinning field between region I and region II DWs, we are not susceptible to this experimental error. Another consideration is that the depinning fields do not have to be identical for all DWs as they depend on random local irregularities that can cause additional pinning. The fact that all region II DWs have a lower depinning field than the region I DWs in Fig. 3.2 could be explained by a structural asymmetry that was unintentionally created during ion irradiation process. However, this cannot explain the in-plane

field dependence; when the in-plane field is reversed, the region II DWs have a *higher* depinning field than the region I DWs. This makes us confident that the observed effect should indeed be explained by a combination of the in-plane field and the presence of DMI.

In conclusion, we observe that in-plane magnetic fields affect the depinning field of an up-down and down-up DW in our sample stacks in the opposite way. An explanation is that the DMI field is parallel to the applied field for one DW, and antiparallel to the applied field for the other DW, resulting in a different energy barrier at the anisotropy transition. The in-plane field at which the difference between up-down and down-up DWs seizes to increase is equal to the DMI field, providing an easy method to determine the DMI constant, especially in the case of small DMI.

4

Racetrack memory based on in-plane-field controlled domain-wall pinning

Magnetic DW motion could be the key to the next generation of data storage devices, shift registers without mechanically moving parts. Various concepts of such so-called 'racetrack memories' have been developed, but they are usually plagued by the need for high current densities or complex geometrical requirements. We introduce a new device concept, based on the DMI, of which the importance in magnetic thin films was recently discovered. In this device the DWs are moved solely by magnetic fields. Unidirectionality is created utilizing the recent observation that the strength with which a DW is pinned at an anisotropy barrier depends on the direction of the in-plane field due to the chiral nature of DMI. We demonstrate proof-of-principle experiments to verify that unidirectional DW motion is achieved and investigate several material stacks for this novel device including a detailed analysis of device performance for consecutive pinning and depinning processes. [*]

[*] This Chapter has been published in *Scientific Reports* [74]

4.1 Introduction

Driven by the ever increasing demand for denser and faster data storage media, novel memory devices are being explored by the spintronics community. One of these novel devices is the so-called racetrack memory, a magnetic strip in which information is stored as magnetic domains that can be transported along the strip [75], without the requirement of any mechanically moving components. Over the years, various versions of this device have been developed; made of in-plane or out-of-plane magnetic strips [76, 77], based on the spin transfer torque or on spin-orbit torque [63, 78] and in single layers or in exchange coupled stacks [16]. What is a common factor in all these racetrack versions is that an electrical current needs to run through the strip in order to move the domains, or equivalently the DWs. A racetrack based on DW motion driven by magnetic fields is considered unfeasible, because these fields drive up-down and down-up DWs in opposite direction, resulting in annihilation of the stored information. This is unfortunate, because field driven devices posses some beneficial properties: they are unhindered by Joule heating, which poses a major problem when driving large currents through small wires [79], electrical contacts are not required, when designed cleverly power consumption might be small [80], and their lifetime is not limited by electromigration [81].

Over the last decade, several creative approaches to circumvent this seemingly unsurmountable problem have been put forward. One of them is a DW ratchet created by saw tooth shaped anisotropy profile or asymmetric notches [82, 83]. Drawbacks of such ratchet compared to the conventional racetrack are that the information can only be moved in one direction, and the complex structural modulation makes it unlikely to be implemented in industry. Another interesting idea is to make use of the precession torque that a magnetic field exerts on the magnetic moments inside the DW [84, 85], as will be discussed in detail in Chapter 6. However, this mechanism of DW motion has not yet been demonstrated in materials with PMA.

Another approach is the so-called bubblecade memory [59]. Recently it was observed that field-induced growth of reversed domains becomes asymmetrical in the presence of in-plane magnetic fields [30, 46, 86]. Based on these experiments it

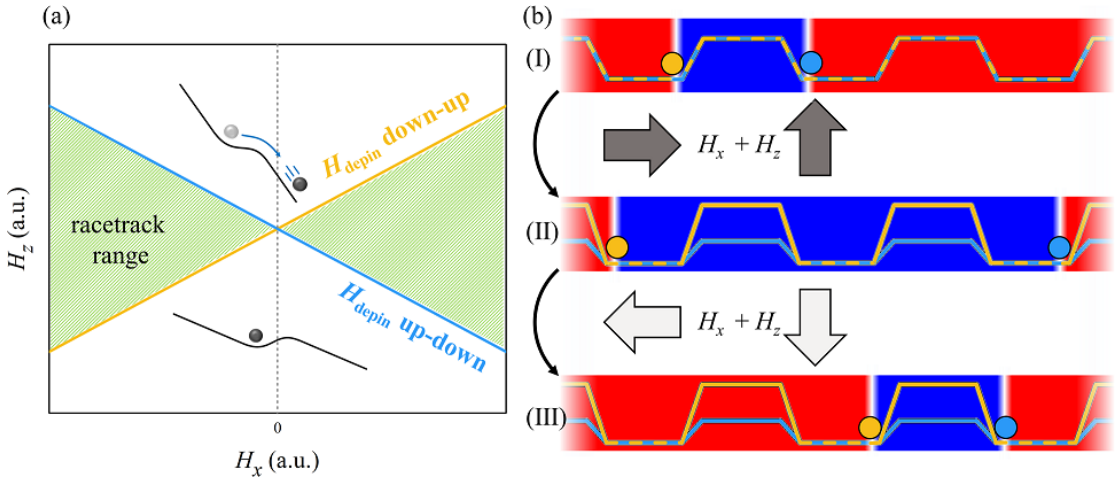

Figure 4.1: Device concept. (a) Schematic graph of the change in H_{depin} (both for UD and DU DWs) as a function of H_x. For $H_z < H_{\text{depin}}$ a DW stays pinned at an anisotropy barrier while for $H_z > H_{\text{depin}}$ it will move past it, as indicated by the black inset cartoons. (b) Some initial magnetic configuration is shown in situation I (red=down, blue=up) together with a schematic energy landscape for the DWs, which are represented by circles (DU=yellow, UD=blue). H_x lowers the energy barriers for one type of DW, which is subsequently moved by an H_z pulse, and the system ends up in the configuration shown in situation II. A following H_x and H_z pulse with opposite signs move the other type of DWs in the same direction, ending up in the configuration shown in situation III.

was shown that magnetic bubbles could be moved unidirectionally by expanding and shrinking them asymmetrically. The underlying physical phenomenon is the DMI, which stabilizes chiral Néel walls, leading to a difference in DW energy (and hence a difference in DW velocity) when parallel or antiparallel in-plane magnetic field are applied. This antisymmetric type of exchange interaction is intensively researched because of its importance for spin-orbit torque driven DW motion [63, 87] and for the formation of magnetic skyrmions [69, 88].

In this work, an alternative physical design is proposed for a purely magnetic-field-driven racetrack memory. We were inspired by the results from Chapter 3 that a combination of an in-plane magnetic field and DMI causes a significant asymmetry in the DW depinning field at an anisotropy barrier [62]. Based on this particular phenomenon, we have designed magnetic tracks with an effective DMI, combined with a lateral modulation of the PMA using local ion irradiation. It is demonstrated that unidirectional motion of multiple DWs is achieved for alternat-

ing in-plane and out-of-plane field combinations, fully in line with the underlying physics of DMI-induced depinning asymmetry. In the following, experimental data proving the device concept will be gathered emphasizing the decisive role of the direction of the additional symmetry-breaking in-plane magnetic field. Moreover, several material combinations with different strengths of DMI will be explored, yielding significant, sometimes unexpected changes in effective DW movement. Our data include a careful analysis of the success rate of the observed unidirectional motion. This is an important step towards a further understanding of the physics processes and, though many technical challenges remain regarding scaling down and the control of orthogonal magnetic fields, the potential implementation in future memory devices.

4.2 Device concept

In systems with PMA, a step in the magnetic anisotropy forms a pinning site for DWs [26]. The magnetic field directed perpendicular to the sample plane (z direction) necessary to overcome such energy barrier, H_{depin}, is determined by the difference in DW energy in the low and high anisotropy regions and by the width of the barrier. Recently it was demonstrated that an additional in-plane magnetic field, H_x, influences H_{depin} in systems with DMI [62]. Because of the chiral nature of DMI, the change in H_{depin} is different for up-to-down (UD) and down-to-up (DU) DWs. Figure 4.1(a) schematically shows this dependence for the two types of DWs (although in actual experiments the behaviour will be more complex). It can be seen that for a certain value of H_x there exist a range of H_z (the green-shaded region in Fig. 4.1(a)) resulting in depinning of UD walls but not of DU walls (or vice versa, depending on the sign of the DMI). Because of the symmetry of the situation, at $-H_x$ DU walls will now move while UD walls remain pinned for the same range of H_z. DW motion driven by H_z will always be such that either the up or the down domains grow, which implies that UD and DU walls are driven in opposite directions. Utilizing the influence of H_x, one can keep UD walls pinned when up domains are expanded, and keep DU walls pinned when down domains are expanded.

In Fig. 4.1(b) it is schematically shown how this can lead to directional motion

of multiple DWs in a strip with block-shaped anisotropy profile. In this device, every transition from low to high anisotropy, forms a pinning site. Situation I shows an initial magnetic configuration, which we want to shift coherently to the right through the strip. In the first step, a positive H_z is applied, which expands the up domains, while $+H_x$ is applied such that DU walls are pinned and UD walls are free to move as long as the fields are applied. The configuration after this first step is shown in situation II. The second step is the application of a negative H_z field, which expands down domains while $-H_x$ changes the DW energy landscape such that only the UD walls are pinned. This results in the configuration which is shown in situation III, in which both DWs have shifted to the right with respect to their initial configuration.

4.3 Proof of principle

To experimentally test this device concept, 70 µm long, 1 µm wide Ta (5 nm) / Pt (4 nm) / Co (0.6 nm) / Pt (4 nm) strips with multiple 2 µm long regions of reduced anisotropy are produced. Reducing the anisotropy locally is achieved by irradiation by a focussed ion beam, and for this particular sample a dose of 0.5 µC cm^{-2} was used. During the measurements, the strips are first saturated with a positive H_z field, and by applying a short negative H_z pulse, some randomly located inverted domains are created.

Now the steps as described in the previous section are performed. Experimentally, we apply a 0.5 ms H_z pulse together with a constant in-plane field. It was decided to always start with pulses in the $-z$ direction, to carry out each step twice and to repeat the complete procedure five times. See Appendix B.1 for details on how the magnetic configuration of a strip is extracted from the raw experimental data (e.g. it is discussed how up and down domains can be identified automatically and how a specific DW is traced through subsequent images). The magnetic state of a typical strip during each cycle is shown in Fig. 4.2(a). The situation after the nucleation of random domains is shown in cycle 1, where the blue and red regions represent up and down domains, respectively. The white shading indicates the regions along the strip with lower magnetic anisotropy. The magnetic configuration after each field pulse (in this measurement $-H_z$ fields are combined with $+H_x$ fields) is

shown. By reading the figure from bottom to top it can be seen how the magnetic domains move in time, and in general it can be seen that both UD and DU walls are successfully moved to the right. To complete the proof-of-principle, it is shown that coherent movement to the left is possible as well. Experimentally this is done by now combining positive H_x fields with positive H_z fields, and the results are shown in Fig. 4.2(b).

In order to verify our interpretation of the observation, two additional experiments were performed. Figure 4.2(c) shows the same experiment, but now using in-plane fields transverse to the strips instead of parallel to the strips. No unidirectional motion was observed, excluding unintentional asymmetry created during sample fabrication as the source of unidirectionality. Instead, it nicely corresponds to the interpretation based on DMI, where a transverse field is not expected to create a difference between UD and DU DWs. A second control experiment was performed, in which an unirradiated sample is investigated. For typical H_z fields that were used before ($\sim 10\,\mathrm{mT}$), the DWs are now propagated over such a large distance that they reach the end of the strip within one field step. We repeated the experiment with a factor two smaller H_z fields, of which the results are shown in Fig. 4.2(d). Interestingly, we do not observe an asymmetric DW velocity, which is in agreement with earlier observations [46]. This shows that unidirectional motion shown in (a) and (b) is created by asymmetric depinning and not by asymmetric DW velocity, as is the case in the bubblecade memory [59].

4.4 Device optimization

In Fig. 4.2 it can be seen that sometimes a DW that is supposed to propagate remains pinned, and vice versa. It is of importance to optimize the H_x and H_z field strengths that are used during the procedure to achieve a minimal amount of errors. Figures 4.3(a to c) show the measured success rate at various field combinations for the device that was used for the proof-of-principle measurements. To obtain these percentages, measurements have been performed on five strips simultaneously. The center-to-center distance of these strips is $5\,\mu\mathrm{m}$, which we have calculated to be sufficient to make dipolar fields emanating from neighbouring strips negligibly small. For each combination of field strengths, the DWs are

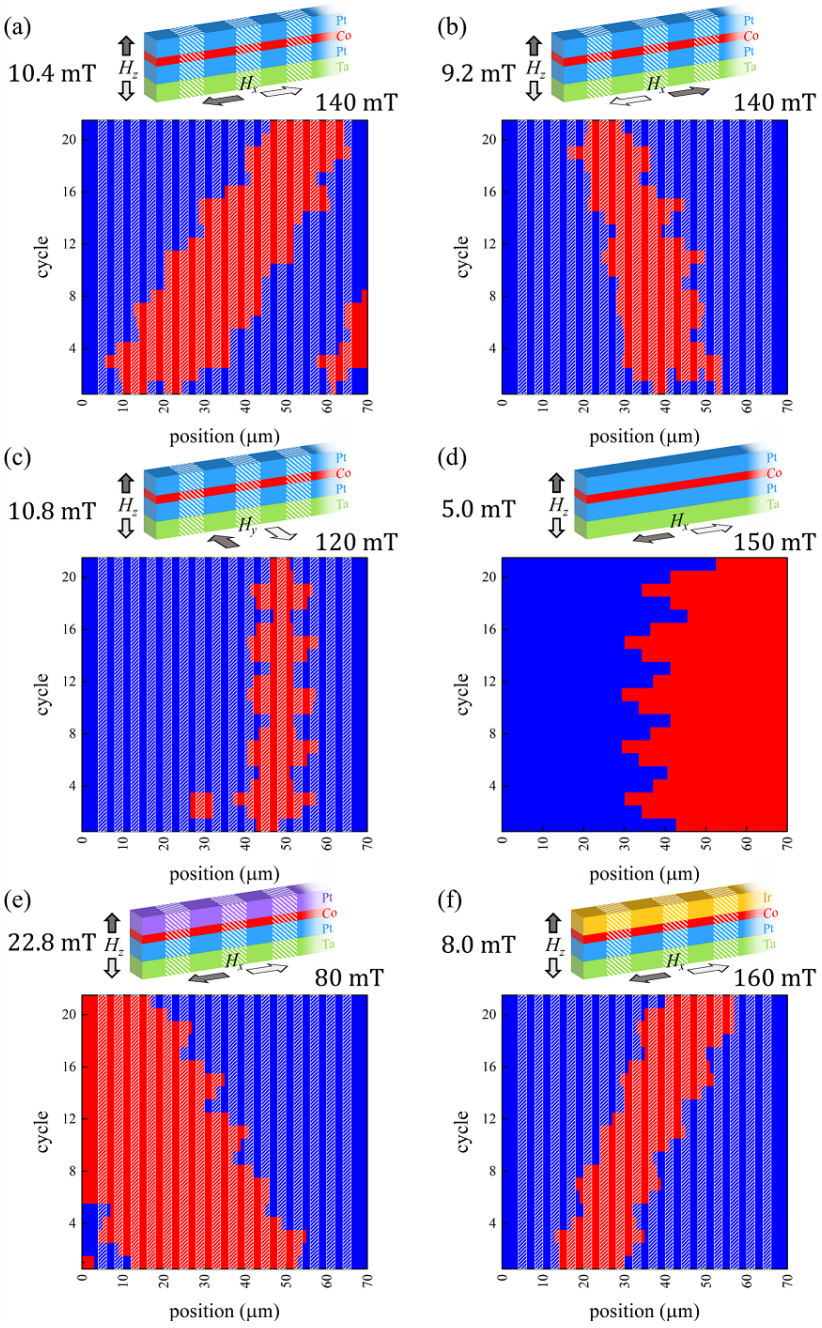

Figure 4.2: Magnetic configuration (red=down, blue=up) of a strip for every cycle in the propagation sequence. (a) DWs successfully being moved to the right. (b) DWs successfully being moved to the right by changing the sign of combined fields. (c) In-plane fields are applied transverse to instead of along the strips. (d) Unirradiated strip. (e) Sample with top Pt layer grown under higher argon pressure. (f) Sample with top Pt layer replaced by Ir.

propagated 20 times. Though is is not possible to give an exact number because for each measurement a different number of DWs is randomly nucleated, each percentage shown here is based on approximately 200 events. Figure 4.3(a) shows the measured probability that a DW remains pinned when it is supposed to remain pinned, which is high for small fields. Figure 4.3(b) shows the measured probability that a DW moves when it is supposed to move, which is high when large fields are used. To shift the domains coherently, it is required that both the pinning and moving step are successful. This probability is computed by the multiplication of the pinning probability with the moving probability, and the result is shown in Fig. 4.3(c). The plot shows two green regions with success rates of $\sim 60\%$. Note that the existence of these regions is not trivial; if the UD and DU depinning fields are not influenced differently, the pinning probability equals one minus the moving probability, of which the product can never exceed 25% !

To ensure that the physics is ruled predominantly by DMI, it is investigated how the behaviour of the device changes when the DMI is increased. Because this increases the asymmetry between UD and DU walls, this is expected to improve the reliability of the proposed field-driven racetrack as the field range with a high total success rate should be expanded. We have investigated two alternative sample stacks: (i) a sample for which the top Pt layer is grown at a different pressure and (ii) a sample for which the top Pt layer is replaced by an Ir layer. These stacks are chosen because DMI is affected by both interface engineering by altering the growth kinetics [46] and by variation of the used materials at the interfaces [50]. Because these new stacks are structurally less symmetrical than the Pt/Co/Pt sample that was used up to now, the DMI (and therefore the success rate of the racetrack) is expected to be increased. The DMI was not measured independently for the samples used in this work, but studies on similar samples, grown in the same lab, can be found in literature [32, 46].

One typical evolution of the magnetic structure for a sample with a Pt top layer grown at an argon pressure of 1.12 Pa instead of 0.29 Pa is shown in Fig. 4.2(e). The success rate at various field combinations is shown in Fig. 4.3(d). The maximum success rate is comparable to the one obtained for the standard Pt/Co/Pt sample, though it is reached at significantly higher H_z fields. The most striking difference can be seen when comparing Fig. 4.2(a) to Fig. 4.2(d): while the same

field polarities are used, the direction of the DW motion is surprisingly opposite! For Pt/Co/Pt samples both observations of a dominant DMI contribution from the bottom interface as from the top interface have been reported [30, 44, 50], suggesting a sensitive dependence on the interface quality. When the growth pressure is increased the growth kinetics, and therefore the interface quality, changes. It was observed that increasing the growth pressure for the top Pt layer drastically increases the magnetic surface anisotropy (which also explains why a larger difference in anisotropy could be created and higher H_z fields were required), which suggests that the interface quality is improved. Therefore we speculate that the change in direction of DW motion might be due to a sign change in effective DMI by a change in the dominant interface, which would be a surprisingly large effect of such a subtle modification of the material stack. However, because also the irradiated regions play a role in our racetracks, caution should be taken with this conclusion. It has been reported that ion irradiation affects the structural properties of the top and bottom interfaces in a Pt/Co/Pt sample differently [73], so it is not unlikely that the DMI is affected.

Large effective DMI strengths have been observed for Pt/Co/Ir stacks [32, 56]. In contrast to symmetric stacks where the DMI contributions of both interfaces (partially) cancel each other, this system could have an enhanced total DMI, because opposite signs of the DMI are expected for Pt/Co and Ir/Co interfaces [24, 50, 89] (though recently conflicting observations were reported [49]). We conclude our study on the field-driven racestrack concept with measurements on a Ta (5 nm) / Pt (4 nm) / Co(0.8 nm) / Ir (4 nm) sample. Figure 4.3(e) shows the success rate at various field combinations for strips irradiated with a dose of 0.2 $\mu C\,cm^{-2}$. Large regions with a success rate of 80-90 percent are observed, a clear and significant improvement with respect to the Pt/Co/Pt samples, underlining the importance of DMI for these devices.

The choice for the extremely low irradiation dose used on this sample is necessary because for the slightly higher dose of $0.4\,\mu C\,cm^{-2}$ the nucleation field in the irradiated regions drops below the depinning fields. This triggered us to repeat the test of a device without irradiation for this material stack. Surprisingly, the results, shown in Fig. 4.3(f), are completely different from the unirradiated Pt/Co/Pt sample in Fig. 4.2(d). Though the latter is a single measurement instead of a phase

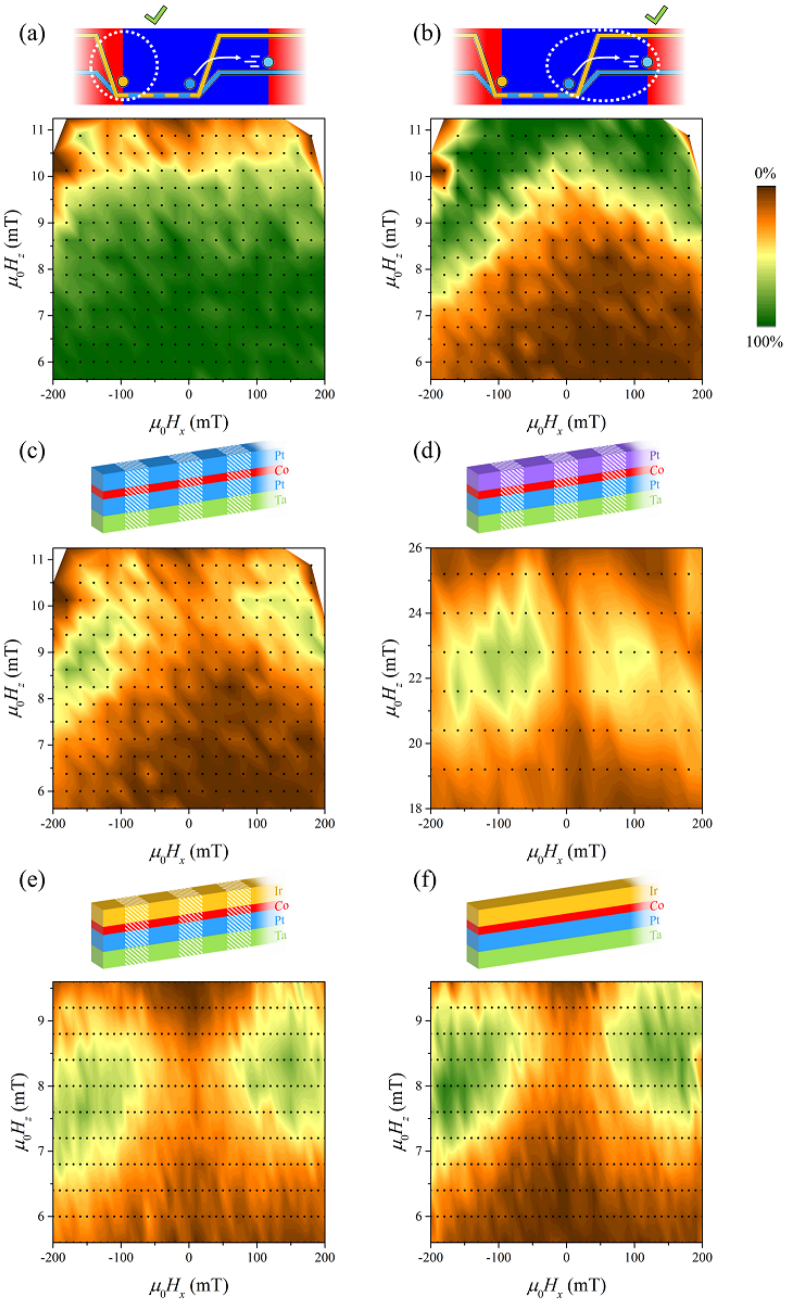

Figure 4.3: Success rate (indicated by colour scale) as a function of H_x and H_z. (a) Probability of a successful pinning step. (b) Probability of a successful depinning step. (c) Probability that a complete procedure (both pinning and moving) is successful for this sample. (d) Probability that a complete procedure is successful for a sample with the top Pt layer grown at a higher pressure. (e) Probability that a complete procedure is successful for an irradiated Pt/Co/Ir sample. (f) Probability that a complete procedure is successful for an unirradiated Pt/Co/Ir sample.

diagram, it can be seen clearly that there is no unidirectional DW motion. For the Pt/Co/Ir sample however, the success rate is considerable, and the maximum occurs at similar fields as for the irradiated Pt/Co/Ir sample. As no anisotropy profile is created in this sample, the unidirectional displacement must be due to an asymmetry in DW velocity, similar to the principle behind the bubblecade memory [59]. This means that when analyzing the irradiated Pt/Co/Ir sample, two DMI related phenomena have to be considered: both the asymmetry in DW velocity and in depinning field play a role, making this particular device very interesting.

In order to unravel the physical origin behind these contributions, we further investigate the difference between the irradiated and unirradiated sample. First it is verified that DW motion follows the creep law in both irradiated and unirradiated samples, and that the DW velocity is not significantly altered by irradiation, see Appendix B.2. Figure 4.4 shows boundaries at which the probability of moving and staying pinned are 50 percent, both for DWs that are supposed to move and supposed to pin. The curves for the irradiated sample are clearly shifted towards higher depinning fields by an amount of 0.49 ± 0.06 mT. This makes sense; when barriers are introduced, higher fields are required for DW propagation than when there are no barriers. Interestingly, the slopes of the graphs are identical within the margin of error for the irradiated and unirradiated sample. This seems to indicate that apparently no additional asymmetry with in-plane field is created by the irradiation, in striking contrast to the Pt/Co/Pt case. An explanation could be that the effect is simply very small at this small irradiation dose. However, the irradiation seems to have a positive effect on the performance of the device, as the maximum success rate is clearly higher for the irradiated sample. In-depth analysis of the data, see Appendix B.2, shows that the transition between the situation in which a DW moves or pins becomes more abrupt after irradiation. The reason for this is that without irradiation only the probability that a DW reaches the barrier position plays a role, but for the irradiated sample this probability has to be combined with the probability that the DW can depin from this barrier. When the field range for which only one type of wall can move past a barrier (the green-shaded range in Fig. 4.1 stays equally large, this more abrupt transition leads to a higher maximum success rate.

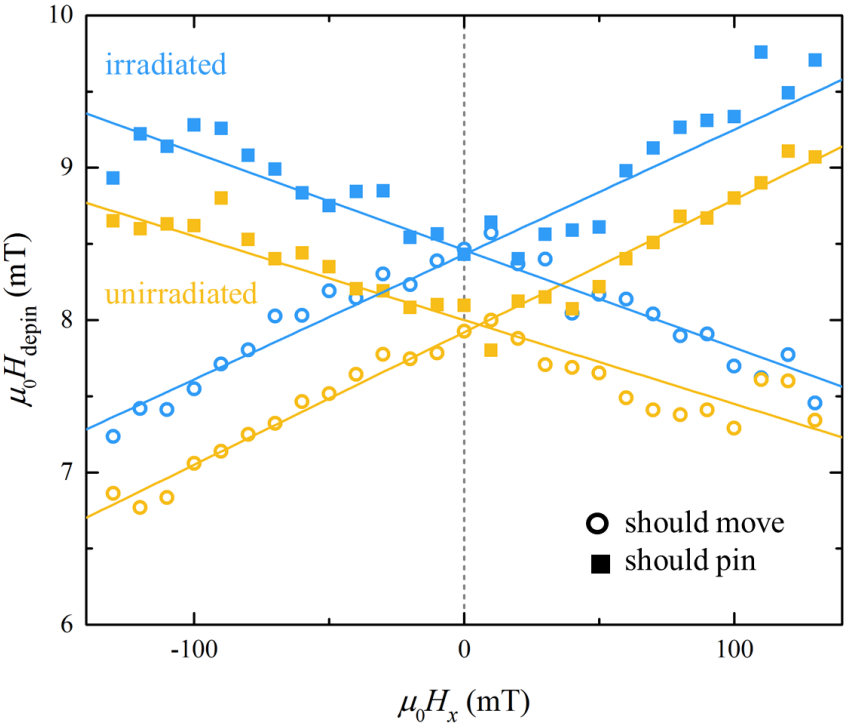

Figure 4.4: Boundaries for which a DW has a 50 percent probability to depin, for both the irradiated and unirradiated Pt/Co/Ir sample and for both DWs that are suppose to remain pinned and for DWs that are supposed to move.

4.5 Discussion

The results of the device optimization lead to an unexpected conclusion: by varying the material stack, we have created two types of devices, both of them function, but have a different underlying principle. The Pt/Co/Pt devices are based on a difference in depinning field for UD and DU walls, as explained before. The Pt/Co/Ir samples, however, get their unidirectionality from a difference in velocity between UD and DU walls, similar to the principle behind the bubblecade memory, but now using DWs instead of magnetic bubbles. The Pt/Co/Ir sample has the highest success rate of the devices investigated so far. This does not automatically mean that the difference in velocity is the best basis for a field-driven racetrack. When material stacks with larger differences in depinning field for UD and DU

walls are designed, also a larger success rates are expected. Therefore both types of devices are interesting candidates for future memory applications.

The size of the regions with reduced anisotropy in the investigated samples is 2 µm. This choice was made to enable Kerr microscope imaging, but does not reflect the fundamental limits of the device. One may wonder whether the use of a focussed ion beam significantly increases the minimal bit size, but this is not the case. First, the width of the created anisotropy boundary is 22 nm, but could be further reduced by switching from Ga ions to, for instance, He ions [90]. Secondly, the actual limiting factor is the minimal distance between two DWs at which they do not interact with each other by dipolar fringe fields, which is considerably more than 22 nm [91, 92], just as in a traditional racetrack device. Finally, we note that for the simple anisotropy profile we need to create, a *focussed* ion beam is not essentially required. The ion irradiation could be done through a mask [93], greatly reducing the sample fabrication time.

Another concern could be the DW velocity that poses a fundamental limit to the operation speed of the device. This velocity is related to H_z which unfortunately cannot be increased arbitrarily, because it is required to be in a specific range in order to make the device function, see Fig. 4.1(a). For the samples investigated, this is in the creep regime and the velocities are in the order of $10 \times 10^{-3}\,\mathrm{m\,s^{-1}}$. To improve the speed, a different material stack and irradiation dose, resulting in a higher depinning field, could be used. Moreover, the theoretical possibility to have this type of racetrack operating with higher DW velocities (and smaller sample dimensions) is demonstrated by micromagnetic simulations, see Appendix B.3.

One advantage of the proposed device over conventional current-driven racetracks is the creation of discrete positions at which the DW can be located (how it can be achieved that the DWs certainly end up at these anisotropy barriers is discussed in Appendix B.3). In studies on current-induced DW motion, asymmetric DW depinning in the presence of in-plane fields was also observed [72, 94]. This implies that the advantageous pinning sites tunable by in-plane fields that were investigated in this work, could be extended to current-driven devices.

Though the development towards devices that are of interest for industry should

be possible in theory, as discussed above, this will certainly not be trivial. An example of a technical issue is the quality of the strip edges. These will have to be very smooth for nanoscale devices to prevent them from forming pinning sites that dominate over the pinning by barriers induced by irradiation, which makes the lithography challenging. Another example is making a sample design in which magnetic fields can be applied locally, which is necessary in applications where it is desirable to control the DWs of only one strip situated within a large array of strips. However, these issues are beyond the scope of this work.

Finally, the rather elementary devices shown in this chapter are purely meant to demonstrate the proof-of-principle of this DMI-based racetrack memory, and therefore have the geometry of simple strips. However, extension to a second dimension can open up new possibilities: DWs could be selectively moved through a grid by using magnetic fields in the y direction as well, or operators for DW logic could be designed using this concept of DW motion.

In summary, we have presented a technique to achieve unidirectional DW motion based on the chiral dependence of the depinning field on in-plane fields. Proof-of-principle measurements were shown and a number of material stacks were investigated to explore the possibilities and requirements of this novel device.

4.6 Methods

Both Ta (5 nm) / Pt (4 nm) / Co (0.6 nm) / Pt (4 nm) and Ta (5 nm) / Pt (4 nm) / Co (0.8 nm) / Ir (4 nm) were deposited on a SiO_2 (100 nm) substrate in a UHV magnetron sputtering facility. The 1 µm × 70 µm strips were created by standard electron beam lithography and lift-off techniques. The 2 µm long regions of lower magnetic anisotropy were created by focussed- ion-beam irradiation using a FEI Nova Nanolab 600 dualbeam system. All measurements are performed using an Evico Kerr microscope and home-built electro magnets.

5

Domain-wall configurations in Pt/Co/Pt

Novel data storage devices such as the racetrack memory rely on the synchronous motion of magnetic DWs through narrow wires. The geometrical configuration of these DWs is of relevance both for the interaction between different domains or DWs, and for the interpretation of DW velocity measurements. In this work we study DW configurations in magnetic strips under the influence of magnetic fields, using the archetype Ta/Pt/Co/Pt material stack with PMA and a non-zero DMI. Several configurations, besides a straight DW with a minimal length, are observed. When applying only magnetic fields perpendicular to the sample, a curvature of the DW is observed. This observation is linked to DW pinning at the sample edges and we propose a model for its dependence on the field strength. Furthermore, the influence of in-plane magnetic fields is studied. Fields directed along the strip are found to increase or decrease the aforementioned curvature, while fields directed transverse to the strip result in tilting of the DW. This is explained by a difference in DW velocity depending on the relative orientation of the DW and the in-plane field direction, which is caused by the DMI. We discuss the possible causes for the observed DW shapes without providing definitive conclusions, as a universal understanding is still lacking.

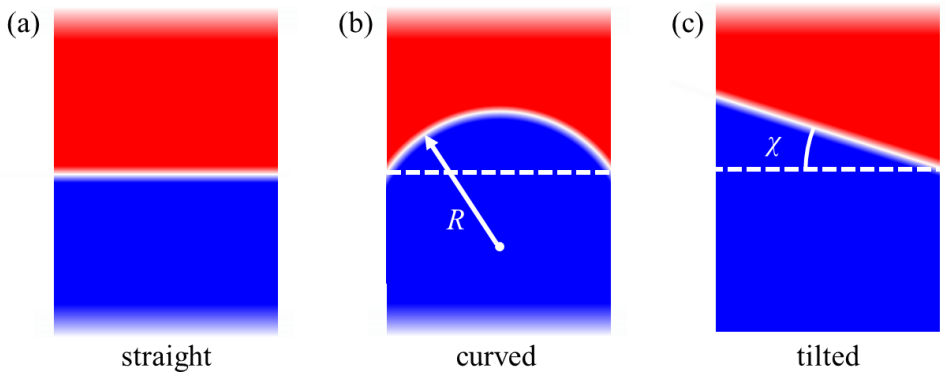

Figure 5.1: Three typical DW shapes encountered in this work: (a) a straight DW, (b) a curved DW with a curvature radius R, and (c) a tilted DW with tilt angle χ.

5.1 Introduction

Systems with PMA are of great interest for data storage applications: their narrow DWs enable the realization of small bit sizes and can be moved with high velocity by applying spin-orbit torques [63, 75, 76, 95]. Though the DWs can be of sub 10 nm width, bit sizes on that scale have not been realized yet experimentally in a racetrack device. One major obstacle is the interaction between neighbouring DWs by dipolar fringe fields, which is now stimulating the development racetrack memories based on (synthetic) antiferromagnets [16]. Naturally, the geometrical configuration of the DWs influences this interaction.

The behaviour of DWs in PMA materials has also been studied extensively to probe the DMI. The DMI favors the formation of Néel-type DWs with a fixed chirality and can be modeled as an effective field [57]. The DW energy is at its maximum when an in-plane magnetic field is applied that exactly cancels this effective DMI field, and hence the DW velocity is minimal under these conditions. Various groups have therefore studied the asymmetrical expansion of magnetic bubbles in the presence of in-plane fields to extract the DMI strength via this principle [30, 50, 96]. However, there are still features in such measurements that cannot be described by the current models [46], precluding the extraction of the DMI strength.

In this work, we also study PMA materials under the influence of out-of-plane and in-plane magnetic fields, and we also pay particular attention to observations

that could be related to the DMI. However, instead of studying a large, expanding bubble, we study DWs in micro patterned strips. This introduces a new aspect to the problem, namely the DW interactions with the edge of the structure. We study the geometrical shape of the DWs in these structures and observe various non-trivial configurations: besides a straight DW that spans the strip transversely (Fig. 5.1(a)), we also observe curved DWs (Fig. 5.1(b)) and tilted DWs (Fig. 5.1(c)), depending on the strength and direction of the applied magnetic field. This curvature and tilt angle are experimentally easily accessible, and could provide a useful means to determine the DMI, when correctly linked to theory. We present a simple model based on DW velocity measurements and considering that the edge of the structure poses additional pinning sites for DWs, it allows to explain qualitatively our observations.

5.2 Domain-wall velocity

The samples studied in this work are Ta (4 nm) / Pt (4 nm) / Co (0.6 nm) / Pt (4 nm) stacks deposited by magnetron sputter deposition, in the shape of small strips that are created by standard electron beam lithography and lift-off techniques. The growth conditions are chosen such that the samples have an effective anisotropy (K_{eff}) of 1.3 MJ m^{-3} (using $M_{\text{S}} = 1.4$ MA m^{-1} and a nominal thickness of the Co layer of 0.6 nm) and the DW velocity is expected to be asymmetrical under the influence of in-plane magnetic fields, see Appendix C.1. In these PMA samples, DWs can be moved by magnetic fields directed perpendicular to the sample surface, which we define as the z direction. In this section, the velocity of DWs under the influence of magnetic fields is studied. This is necessary for the interpretation of the geometrical DW configurations that are discussed later on.

Figure 5.2(a) shows the measured DW velocity as a function of H_z. The DW was imaged using a Kerr microscope for a 25 µm wide strip. The blue line is a fit to the creep law [97], while the yellow line is a fit assuming the system is in the depinning regime [98], see Appendix C.2 for the precise form of the fit functions. These fits enable us to extract the depinning field and depinning temperature, which are found to be 100 mT and 5800 K, respectively. These values are consistent with

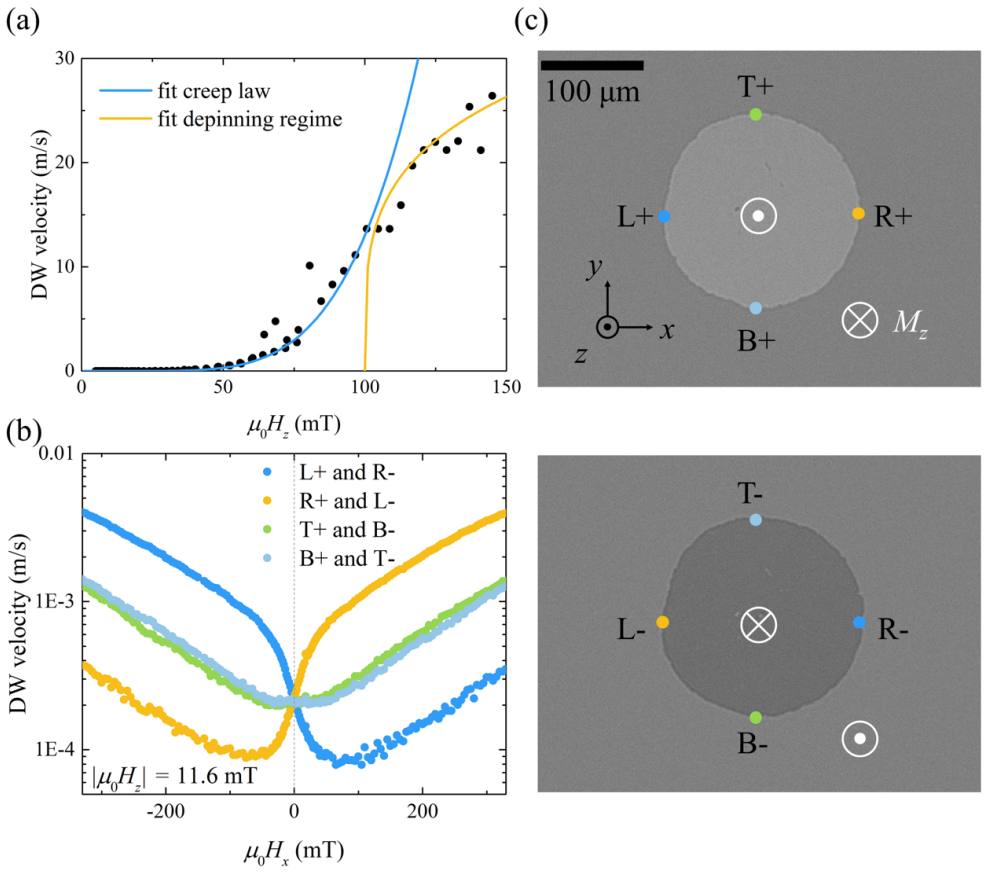

Figure 5.2: (a) DW velocity as a function of applied magnetic field in the z direction. The lines indicate fits with the theoretical curves for creep (blue) and depinning behaviour (yellow). (b) DW velocity as a function of in-plane magnetic field. The data for left moving DWs when a positive H_z is applied (L+) is combined with the data for right moving DWs when a negative H_z is applied (R-). For the top (T) and bottom (B) part of the bubble, the data are combined in a similar way. In (c) two typical Kerr microscope images of bubbles in the full sheet sample are shown, together with the definition of the colour coding that is used in (b).

literature [97], which confirms that the sample behaves as a regular Pt/Co/Pt stack.

The material stack is further investigated by measuring the expansion of magnetic bubbles under the influence of in-plane fields, oriented in the x direction, in an unpatterned sample. The results are shown in Fig. 5.2(b) where the labels L, R, T, and B refer to the most left, right, top, and bottom point of the bubble. Figure 5.2(c) shows typical Kerr microscope images of a bubble, on which these labels are

defined graphically. For point T and B (at these positions the DW is parallel to the applied in-plane field direction) the results are overlapping curves, while the results for point R and L do not overlap. The current theory [30] predicts velocity versus H_x curves that are symmetrical around a certain magnetic field (from which the DMI strength can be deduced), but the measured curves for point R and L have no symmetry axis. This is in agreement with earlier measurements on similar samples [46], but complicates the interpretation of the results. Some explanations have been put forward, based on chiral damping [47] and variation of the DW width with in-plane field [99], but a model that can completely account for curves like the ones in Fig. 5.2(b) is still lacking (though very recent work including an orientation dependence of the DW elasticity yields promising results [100]).

5.3 Characterisation of the domain-wall shape

Up to now, only the velocity of the DWs was considered, and next we will concentrate on their geometrical configuration. We start with the simplest case where $H_x = H_y = 0$, followed by a study of the influence of H_x, and finally a study on the influence of H_y. Because of the uniaxial anisotropy that prefers all magnetic moments to align with the z axis, and the exchange interaction which favours parallel alignment of neighbouring magnetic moments, there is an energy cost associated with the creation of a DW. This energy is calculated as $\sigma_0 = 4\sqrt{AK_{\text{eff}}}$, as was discussed in Chapter 2, where A is the exchange stiffness constant. Therefore it is intuitively expected that inside a strip, a DW spans the strip in such way that its length is minimized: straight and perpendicular to the length of the strip.

Figure 5.3(a) shows Kerr microscope images of DWs in 25 µm wide strips after being propagated by different driving fields H_z. For large driving fields, a straight DW is indeed observed, as expected. For the small driving fields this is no longer the case: the DW bulges outward in the direction of DW propagation.

A comparable observation was done by Wunderlich *et al.* [101]. In that work it is described how a DW is pinned when moving from a narrow strip into the junction of a Hall cross. If the DW would propagate further as a straight entity, it would need to have a great increase in length (and hence in energy), so instead it is pinned at the entrance of the cross and expands as an arc of a circle, until a

semicircle is formed and it is possible again to propagate along the opposite edges. Further it was reported by Cayssol *et al.* that edge roughness in a magnetic strip can lead to DW pinning in a similar fashion [102]. The strips we study are created with lift-off techniques, so some edge roughness is certainly expected, which could lead to the observed DW curvature.

However, the model as presented in these works does not explain the dependence of the curvature on the strength of H_z. We therefore extend that model by introducing a dependence of the pinning strength on the DW curvature. Intuitively, this can be understood as follows: if a straight DW moves away from a pinning site (or equivalently into the centre of a Hall cross) its length becomes 'infinitely' longer, so the energy barrier that pins the DW is infinitely high. Alternatively, for a DW shaped like a semicircle, there is no additional DW length created at the edges when the DW moves, and therefore there is no energy barrier. One can imagine that for curvatures that lay in between these two extremes, the pinning strength has an intermediate value and depends on the curvature. These situations are all sketched in Fig. C.1. The model with this extension is worked out mathematically in Appendix C.3. The resulting relation between the radius, R of the circle arc the DW forms and H_z is as follows:

$$R = \frac{w}{2\sin\left(\arctan\left(\frac{\sigma_0}{2\mu_0 M_S H_z w}\right)\right)}, \tag{5.1}$$

where w is the strip width, μ_0 the vacuum permeability, and M_S the saturation magnetization.

We extract the DW profiles from the Kerr microscope images, and fit these to a circle using the Pratt method [103]. The curvature (which is defined as $1/R$) is plotted as a function of H_z in Fig. 5.3(b). Though the data points are scattered, it is clear that the curvature decreases with H_z, which is consistent with what is seen by eye in Fig. 5.3(a).

The blue line in Fig. 5.3(b) shows a calculation of the curvature as a function of H_z using equation 5.1 and the following material parameters: $M_S = 1.4$ MA/m, $A = 1.5 \times 10^{-11}$ A/m, and $K_{\text{eff}} = 1.3\,\text{MJ m}^{-3}$. The qualitative behaviour matches

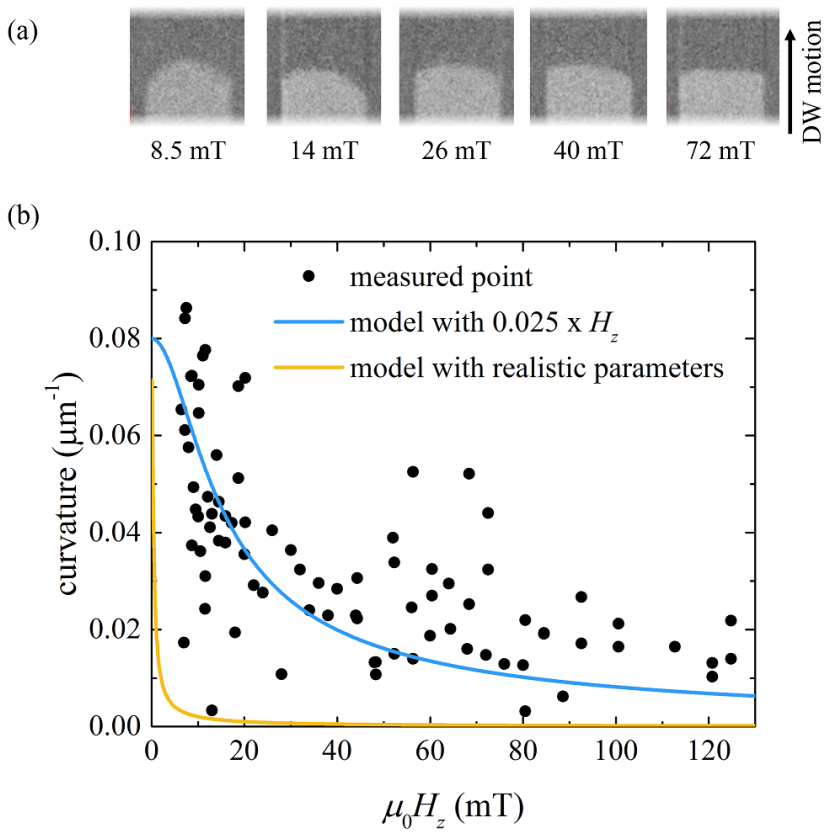

Figure 5.3: (a) Kerr microscopy images of DW configurations in 25 μm wide Ta/Pt/Co/Pt strips for various field strengths. (b) DW curvature as a function of H_z extracted from Kerr microscope images. The blue line is a calculation using equation 5.1. For this calculation realistic material parameters, as mentioned in the main text, are used. Due limitations of the model, the magnetic fields have to be multiplied by a factor 0.025 for the model to match the experimental data (the yellow curve shows the results without this fudge factor).

the experimental data well, but quantitatively there is a significant difference: the magnetic field to achieve a certain curvature according to the model is a factor 0.025 smaller than what is necessary experimentally. This is not surprising: the model does not include any thermal effects, while it was shown in the previous section that for almost all investigated magnetic fields the system is in the creep regime, in which thermal effects are extremely important. Also, only pinning at the edges is considered, while it is well known that for polycrystalline Co layers there is also significant pinning within the 'bulk' of the film [104]. We expect these to be the most important directions for improving the quantitative predictions of

the model, but here we limit ourselves to showing the basic idea of how increasing H_z can cause a decrease in DW curvature.

Next, the influence of an in-plane field applied along the strip is investigated. Figure 5.4(a) shows Kerr microscope images taken during this experiment. The same material stack as before was used, but now a 50 µm wide strip was studied (see Appendix C.5) and a fixed $\mu_0 H_z = 20\,\mathrm{mT}$ field was used to drive the DW motion. The DW profile is clearly affected by the in-plane field: its profile becomes more curved or more flattened depending on the in-plane field direction.

This asymmetric behaviour seems directly related to the DMI, but the interpretation is not trivial. Here we will briefly discuss three alternative interpretations that are worked out in detail in Appendix C.4. A natural first attempt to describe our observations is to include the influence of the DMI and H_x in the DW energy following Eq. 2.8, and then apply Eq. 5.1 again to calculate the DW curvature. However, in that case the influence of H_x turns out to be negligible for realistic parameters. This discrepancy probably arises because we do not account for the creep behaviour of our system.

Another explanation for the discrepancy between the model and our experimental observations could be that the DW does not expand like a circle arc, as is assumed during the derivation of Eq. 5.1. Based on the velocity measurements of Fig. 5.3(b) this assumption should indeed be revisited. The correct DW equilibrium shape can be calculated using the Wulff construction [105]. However, this analysis also leads to the conclusion that the influence of H_x should be much smaller than what is observed experimentally.

Alternatively, one could treat the combination of an in-plane and out-of-plane field as an effective out-of-plane field, $H_{z,\,\mathrm{eff}}$. The in-plane field alters the DW velocity, and we define $H_{z,\,\mathrm{eff}}$ as the out-of-plane field that would lead to the same velocity in absence of any in-plane fields. This $H_{z,\,\mathrm{eff}}$ can then be inserted into equation 5.1 instead of H_z. The results of this analysis are opposite of the experimental observations: it is calculated that the DW becomes more curved under the influence of an in-plane field that slows it down, but in practice it straightens. We therefore believe that the three approaches discussed here cannot account for the observed influence of H_x on the DW curvature, but all approaches

are worked out in Appendix C.4 such that the reader can assess this for him or herself.

As mentioned before, for DW velocity measurements under the influence of H_x, results are obtained that cannot be explained by a modification of the DW energy in the creep law only. It is plausible that the same ingredient required to solve this problem is missing in our analysis of the DW configurations inside the strips. Irrespective of its physical origin, asymmetric DW velocity can intuitively explain how an H_x field can affect the DW curvature. Suppose some DW curvature arises by pinning at the edges, as described before. The orientation with respect to the applied in-plane field, and so the DW velocity, now varies along the DW. When the field is applied such that the middle part of the DW moves faster than the parts at the edges, the curvature will increase. When the in-plane field results in a slower moving middle part of the DW with respect to the parts at the edges, the wall will become flatter. This provides a qualitative interpretation of the trend observed in Fig. 5.4(b).

Last, the influence of in-plane fields applied transversely to the magnetic strips, H_y, is investigated, again using 50 µm wide Ta/Pt/Co/Pt strips. It has been shown by micromagnetic simulations that a combination of strong DMI and an in-plane field transverse to the strip could lead to a tilted configuration of the DW [45, 106], and it has been suggested that measurements of the tilt angle χ (graphically defined in Fig. 5.1(c)) could provide a tool to extract the DMI strength. The theoretical χ versus H_y curves, calculated following the approach from literature (which in principle is minimizing the sum of the Zeeman, DMI, and DW energies) are shown in Fig. 5.5(c) for three different DMI strengths. Experimentally, a clear tilting of the DW is indeed observed, as can be seen in the Kerr microscope images in Fig. 5.5(a). The χ increases with increasing in-plane field strength, and its sign depends on the sign of the in-plane field. To make this more quantitative, Fig. 5.5(b) shows the extracted χ as a function of in-plane field, also see Appendix C.6 for additional discussion.

Though there are similarities between the calculated and measured curves, their agreement is inadequate to determine the DMI strength by comparing them. Firstly, the calculated values of χ are much smaller than the experimentally ob-

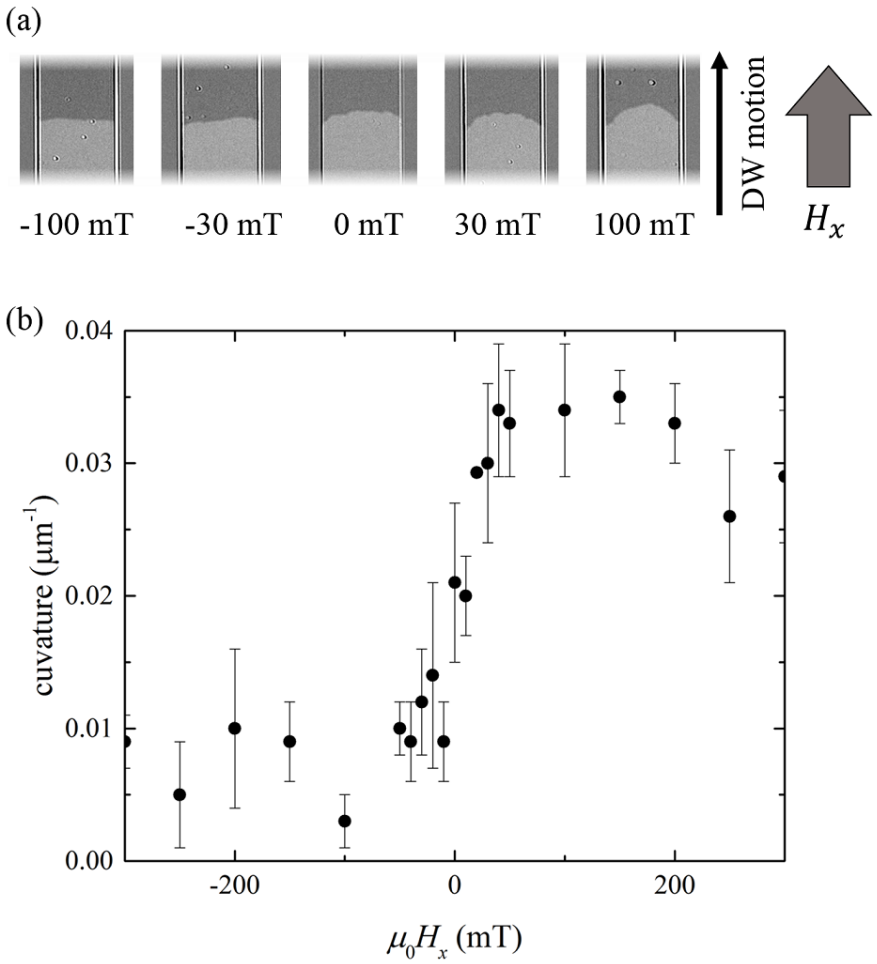

Figure 5.4: Influence of of longitudinal in-plane magnetic fields on the DW configuration. (a) Kerr microscopy images of a DW for various in-plane field strengths. (b) Curvature as extracted from Kerr microscopy images as a function of in-plane field strength.

served ones. This could be solved by using a larger DMI strength for the calculations, but that would not be realistic for the investigated material stack. Also the shapes of the curves are qualitatively different: while in the experiment from $H_y = \pm 50\,\mathrm{mT}$ onward the tilt angle is saturated and does not increase anymore, the model predicts a much more gradual increase in tilt angle with field.

In recent work by Kim *et al.* [107], also a clear tilt of DWs is observed in strips subjected to in-plane fields. They use a material stack in which the sign of the DMI is known and conclude that the direction of the tilting is opposite to what

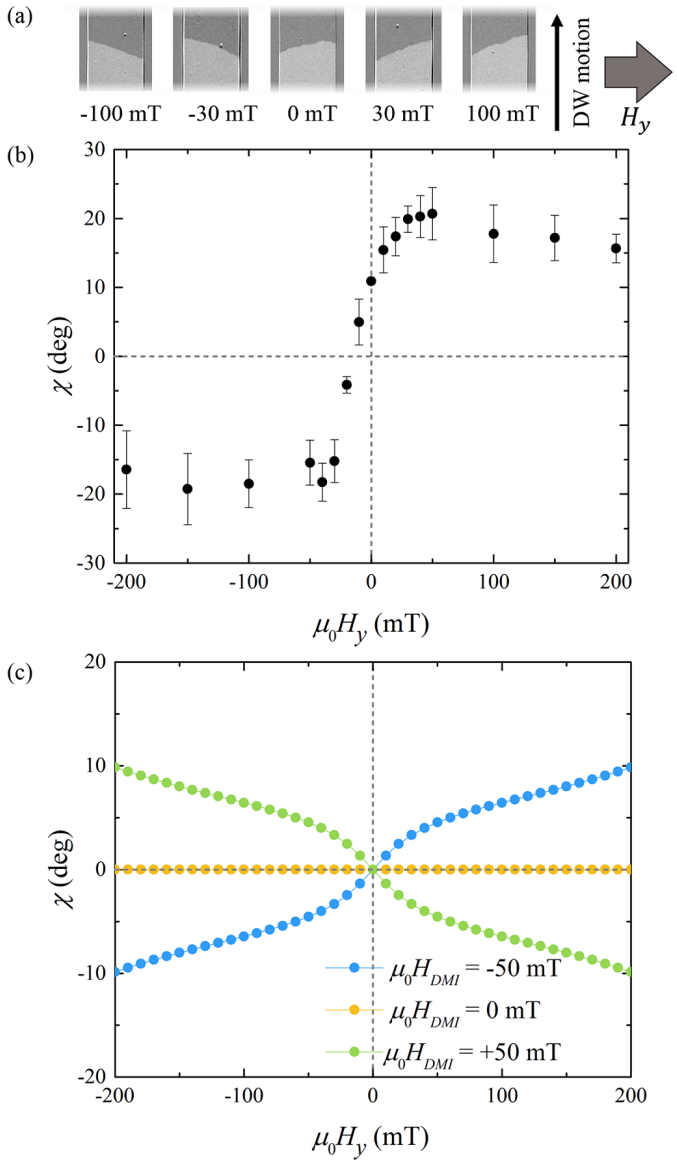

Figure 5.5: Influence of in-plane fields perpendicular to the strips. (a) Kerr microscopy images of a DW for various in-plane field strengths. (b) DW tilting angle as extracted from Kerr microscopy images as a function of in-plane field applied perpendicular to the strip. (c) Theoretical curves of the DW tilting angle as a function of in-plane field, for different values of the DMI strength. Here the convention that a negative value of H_{DMI} corresponds to a left handed configuration is followed.

would be expected for the energy minimization as proposed in the theoretical papers. However, they find a convincing correlation between asymmetry in the DW velocity and the DW tilting. When a curvature (or other kind of irregularity)

arises in the DW, a relatively fast movement towards one of the edges could lead to tilted configuration. The asymmetry in velocity as measured in Fig. 5.2(b) agrees with the sign of the tilt angles measured in Fig. 5.5(b) following this interpretation. We therefore cannot exclude that our measured tilt angles where influenced by this effect, plausibly it is even dominant in determining the DW configuration. Our measurements therefore do not lead to a straightforward extraction of the DMI strength. Nevertheless, we believe measuring χ still has potential, if the DWs could be prepared such that they certainly reach their energetically optimal configuration, uninfluenced by dynamics.

5.4 Discussion and Conclusion

Using patterned Ta/Pt/Co/Pt samples and magnetic fields, various non-trivial DW configurations have been observed. The interpretation of the observations is based on the measured DW velocity and additional DW pinning at the edges of a patterned structure. The model for curvature we presented has limitations. Most importantly, thermal effects are not incorporated, while DW motion is described by the creep law in the studied regime. Though this model does not capture the detailed behaviour of the DW or achieve good quantitative agreement with the experimental data, it is able to describe the general effect of a magnetic field on the DW configuration, and understand this intuitively.

Both the effect of perpendicular and in-plane magnetic fields were studied, and the latter turns out to be intimately related to asymmetric DW velocity measurements that are conducted in unpatterned samples. The observed DW curvature and tilt angle are directly measurable and may provide a convenient route to extract the DMI strength in the future. However, first a deeper understanding of the experimental observations is required. We are currently following the approach presented in Ref. [108] where edge pinning is modelled as a counter field present at the strip edges, which can be included in the creep law. This improved theoretical modeling is still in progress.

6

Precession-torque-driven domain-wall motion in out-of-plane materials

DW motion in magnetic nanostrips is intensively studied, in particular because of the possible applications in data storage. In this work, we will investigate a novel method of DW motion using magnetic field pulses, with the precession torque as the driving mechanism. We use a one dimensional (1D) model to show that it is possible to drive DWs in out-of-plane materials using the precession torque, and we identify the key parameters that influence this motion. Because the DW moves back to its initial position at the end of the field pulse, thereby severely complicating direct detection of the DW motion, depinning experiments are used to indirectly observe the effect of the precession torque. The 1D model is extended to include an energy landscape in order to predict the influence of the precession torque in the depinning experiments. Although preliminary experiments did not yet show an effect of the precession torque, our calculations indicate that depinning experiments can be used to demonstrate this novel method of DW motion in out-of-plane materials, which even allows for coherent motion of multiple domains when the DMI is taken into account. [*]

[*] This Chapter has been published in *AIP Advances* [85]

6.1 Introduction

Ever since the proposal of the racetrack memory [75] there has been much interest in the topic of DW motion [57, 64, 72]. The conventional approaches to drive DWs use spin-polarized currents [64, 72] or magnetic fields [57, 109]. As magnetic fields typically cannot provide coherent DW motion, thus resulting in loss of data in data storage devices, spin-polarized currents are generally used to drive DWs in magnetic racetracks [14, 16]. A disadvantage, however, is that the large currents that are necessary can cause breakdown of devices due to Joule heating [79].

In this work we will describe a novel method of DW motion, where magnetic fields are used in such a way that coherent DW motion is possible. The field is applied along a hard axis, i.e. perpendicular to the magnetization in the domains, with the resulting precession torque as the driving mechanism behind the DW motion. This has already been demonstrated for in-plane materials [84], and in this work we will explore the use of this method in out-of-plane (OOP) materials. This is especially interesting for the use in data storage devices, as OOP materials can provide much larger storage densities than IP materials [14]. As no current is sent through the nanowires when using this method, the chance of device breakdown is expected to be lower than for current-driven devices. Therefore, this method of DW motion can be interesting for applications where device lifetime is important.

We will first introduce this new method of DW motion and show that it can be used to drive DWs in OOP materials using a simple model. Then the key parameters that influence the DW motion will be explored, focussing on modelling the depinning experiments that can be used to verify this method of DW motion. The preliminary experiments we performed will be discussed as well, followed by a review of some challenges for this new method of DW motion, including how coherent DW motion can be achieved using the DMI.

6.2 Theory

To explain how the precession torque can drive DW motion we start with the Landau-Lifshitz-Gilbert (LLG) equation [28, 110], the most general description of

magnetization dynamics:

$$\frac{\mathrm{d}\mathbf{M}}{\mathrm{d}t} = -\gamma\mu_0\mathbf{M}\times\mathbf{H}_{\mathrm{eff}} + \frac{\alpha}{M_{\mathrm{s}}}\left(\mathbf{M}\times\frac{\mathrm{d}\mathbf{M}}{\mathrm{d}t}\right). \tag{6.1}$$

Here, $\mathbf{M}$ is the local magnetization, γ the gyromagnetic ratio, μ_0 the vacuum permeability, $\mathbf{H}_{\mathrm{eff}}$ the effective field the magnetization experiences, α the Gilbert damping factor and $M_{\mathrm{s}} = |\mathbf{M}|$. The first term describes the precession of the magnetization around the effective field, while the second term describes the damping that causes the eventual alignment of $\mathbf{M}$ with $\mathbf{H}_{\mathrm{eff}}$.

In Fig. 6.1 the working principle of precession-torque-driven DW motion is depicted. We start with a down domain and an up domain, separated by a Bloch DW. When an in-plane field H_{IP} is applied perpendicular to both the spins in the domains and the spins in the DW, the spins will experience a torque according to the precession term in the LLG equation. In the domains, both the anisotropy and the exchange energy prefer the spins to point in the same direction, while in the DW the anisotropy and the exchange energy are in competition. As a result of this the precession torque has a larger effect on the spins in the DWs than on the spins in the domains, which results in a rotation of the spins in the DW in the direction depicted by the small arrows in Fig. 6.1(a). In Fig. 6.1(b) it can be seen that this rotation of the spins effectively moves the DW to the right, which is the essence of precession-torque-driven DW motion.

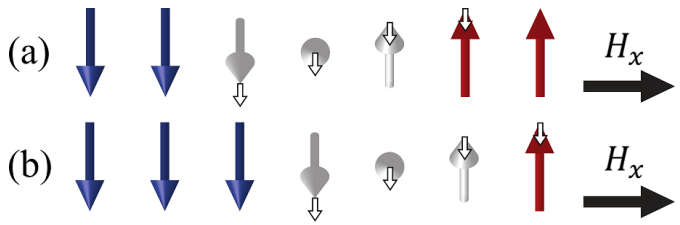

Figure 6.1: (a) H_{IP} exerts a torque on the spins in the DW, causing the spins to rotate in the direction indicated by the small arrows. (b) The rotation of the spins causes an effective movement of the DW to the right.

6.3 Results

The DW motion can be described by deriving a one dimensional (1D) model, starting with the LLG equation [111]. In this model, the DW is defined by two

collective coordinates, the DW position q and the internal DW angle φ, as defined in Fig. 6.2(a). By integrating the LLG equation over an infinitely long nanowire with a fixed DW profile [26], two equations are obtained that describe the two collective coordinates:

$$\alpha\dot{q} - p\lambda\dot{\varphi} = \frac{\gamma\lambda}{2M_\mathrm{s}}\left(\frac{\partial E}{\partial q}\right), \tag{6.2}$$

$$p\dot{q} + \alpha\lambda\dot{\varphi} = \frac{\gamma\lambda\mu_0}{2}\left[\pi\left(H_x\cos\varphi + H_y\sin\varphi\right) - H_\mathrm{D}\sin 2\varphi\right]. \tag{6.3}$$

Here, p determines the polarity of the DW, with $p = +1$ for an up-down DW and $p = -1$ for a down-up DW. λ is the DW width, H_D is the anisotropy field of the DW, the sign of which determines whether Bloch or Néel walls are favored, and $\frac{\partial E}{\partial q}$ describes the energy landscape of the DW, including a possible magnetic field in the z-direction.

The parameters that are used in these simulations are realistic parameters for a Pt/Co/Pt stack [72], with $\alpha = 0.1$, $K_\mathrm{eff} = 0.4875\,\mathrm{MJ\,m^{-3}}$, $\lambda = 5.7\,\mathrm{nm}$ and $\mu_0 H_\mathrm{D} = 23\,\mathrm{mT}$. Using Eq. 6.2 and Eq. 6.3 the displacement of a DW due to a field pulse can be numerically calculated, as shown in Fig. 6.2(b) and 6.2c. In these figures the position of the DW during (grey area) and after (white area) a 10 ns field pulse is calculated for various field pulse strengths (Fig. 6.2(b)) and various values of α (Fig. 6.2(c)). It can be seen that after several nanoseconds the DW velocity decreases, which is due to the damping term in the LLG equation. This term causes the spins in the DW to eventually align with H_IP, which reduces the torque ($\tau \propto \mathbf{M} \times \mathbf{H}_\mathrm{IP}$) and therefore impedes the DW motion, eventually causing the DW motion to stop. This is the reason there is a larger displacement for larger H_IP (larger torque) and for lower α (it takes longer for the spins to align with the applied field, which results in a large torque for a longer time). Furthermore, when H_IP is turned off there is an effective field in the y-direction, dominated by the demagnetization field of the DW. This creates a torque in the opposite direction of the torque generated by H_IP, which causes the DW to move back to its initial position. In the outlook we will discuss how this backward motion can be eliminated, e.g. using pinning sites.

For the parameters we used, the DW displacement after a single field pulse is in

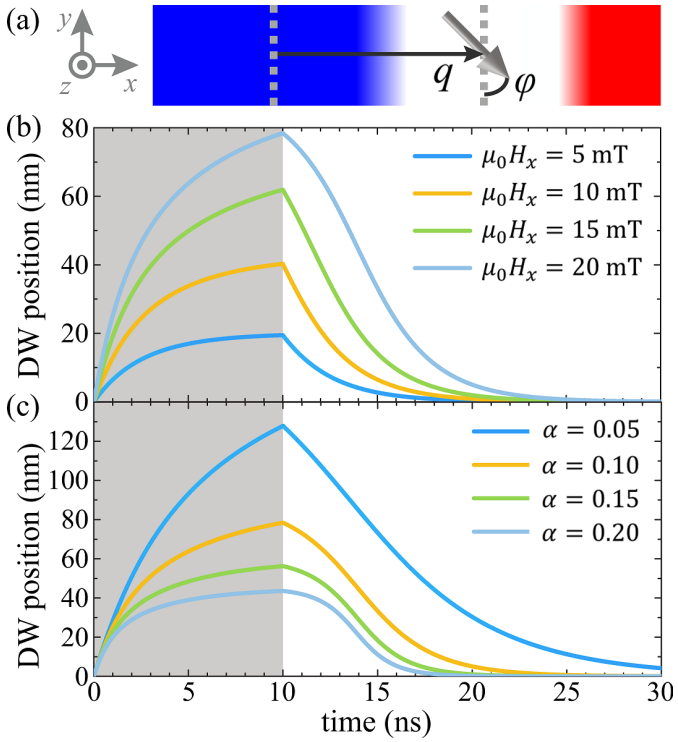

Figure 6.2: (a) Top view of the DW, with q the displacement of the DW and φ the internal DW angle. (b) DW displacement due to a 10 ns in-plane field pulse for various values of H_{IP} ($\alpha = 0.1$) and (c) for various values of α ($\mu_0 H_{\mathrm{IP}} = 20\,\mathrm{mT}$).

the order of 100 nm. Combined with the fact that the DW moves back to its initial position after the pulse ends, this makes it difficult to detect the effect of the precession torque directly. With depinning experiments it is possible to overcome these complications, and detect the effect of the precession torque indirectly. For these experiments, Ga^+-irradiation can be used to create an energy barrier for the DW [26]. This energy barrier can be overcome using a z-field, with the depinning field H_{dep} representing the critical z-field for which the DW depins. The precession torque can assist the depinning, and thus lower the depinning field. The energy landscape is incorporated in the 1D model via the $\frac{\partial E}{\partial q}$ term in Eq. 6.2, and also includes a z-field, which causes the energy landscape to tilt. In Fig. 6.3(a) the energy landscape is shown for $H_z < H_{\mathrm{dep}}$. Assuming a constant effective anisotropy in the irradiated (non-irradiated) region of K_{eff} ($K_{\mathrm{eff},0}$), and a linear transition region with width δ, the derivative of the energy of the system with respect to the DW position is given by [26]

$$\frac{\partial E}{\partial q} = \frac{2\lambda}{\delta} \frac{(K_{\text{eff},0} - K_{\text{eff}}) \sinh\left(\frac{\delta}{\lambda}\right)}{\cosh\left(\frac{2q}{\lambda}\right) + \cosh\left(\frac{\delta}{\lambda}\right)} - 2\mu_0 M_\text{s} H_z. \tag{6.4}$$

In Fig. 6.3(b) and 6.3(c) it can be seen how an in-plane field pulse can cause the DW to depin for a z-field lower than the depinning field. The information is presented in a phase diagram, where the two degrees of freedom (q, φ) are plotted against each other, in Fig. 6.3(b) for various values of H_IP, in Fig. 6.3(c) for various values of the rise time of the IP field pulse. In both cases, initially the DW is positioned in the local energy minimum. The in-plane field then causes the DW to move to the right (in the direction of the energy barrier), and causes φ to increase towards the equilibrium angle φ_eq (indicated by the horizontal dashed line in Fig. 6.3(c)) determined by H_IP and H_D. When the in-plane field is strong enough (and the rise time is short enough), the DW will overcome the barrier before φ reaches φ_eq, and the DW depins. When φ reaches φ_eq before that, the DW will move back due to the energy landscape. Eventually the DW will reach the equilibrium position (q_0, φ_eq) via the spiralling motion visible in Fig. 6.3(b) and 6.3(c). The dependence of depinning on the rise time of the IP field pulse, as seen in Fig. 6.3(c), is related to the effective field, determined by H_D and H_IP. A long rise time results in an effective field that only slowly moves away from the direction of H_D, the initial direction of the DW magnetization. This way, the magnetization can follow the effective field, and the torque is reduced ($\tau \propto \mathbf{M} \times \mathbf{H}_\text{eff}$). Thus, to maximize the torque the field should reach its maximum value as quickly as possible, corresponding with a short rise time. For long rise times the total DW displacement decreases, similar as for low in-plane fields and high damping parameters.

Experimentally, it is the depinning field that can be measured, e.g. with a Kerr microscope. Therefore, the 1D model is used to calculate how much the depinning field will change for various IP field strengths, the result of which is shown in Fig. 6.4(a). As expected, a stronger in-plane field corresponds to a larger change in the depinning field. More surprisingly, for both positive and negative in-plane fields there is a reduction of the depinning field. This is due to the fact that the torque generated by the in-plane field is in opposite directions at the start of the pulse and at the end of the pulse. Therefore, either at the start of the pulse or

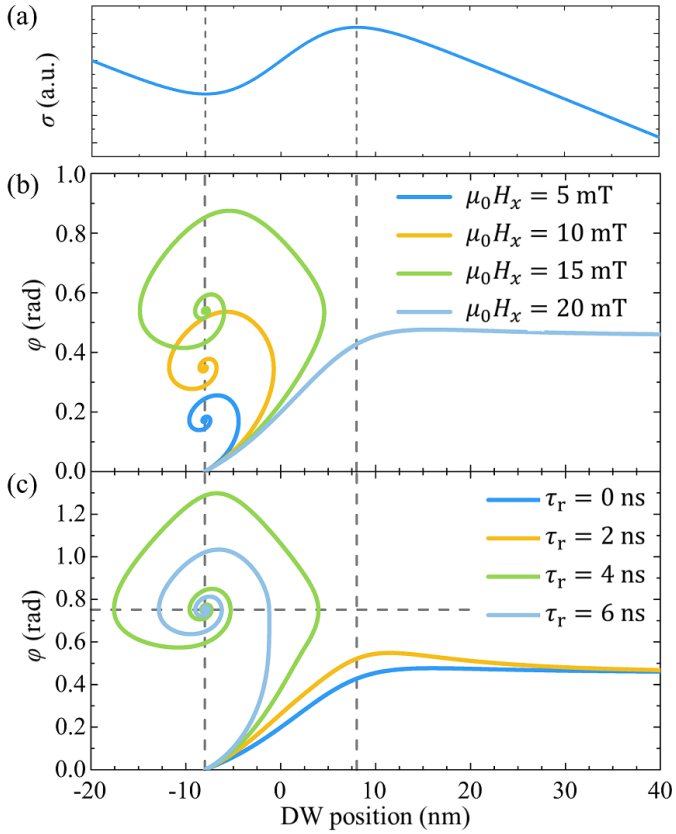

Figure 6.3: (a) DW energy landscape due to Ga^+-irradiation with $H_z < H_{\text{depin}}$. (b) (q,φ) diagrams for various values of H_{IP}. The dashed vertical lines indicate the local minimum (left) and local maximum (right) in the energy landscape ($\tau_{\text{r}} = 0\,\text{ns}$). (c) (q,φ) diagrams for various values of the rise time τ_{r} ($\mu_0 H_x = 20\,\text{mT}$).

at the end of the pulse the torque is in the right direction to assist the depinning of the DW. In Fig. 6.4(b) the dependence of the change in depinning field on the damping parameter is shown, for $\mu_0 H_{\text{IP}} = 5\,\text{mT}$. It is clear that the change in depinning field decreases for larger α, in correspondence with the result from Fig. 6.2(b).

We have performed preliminary experiments where we tried to show the effect of the precession torque on DW motion. The IP fields in the experiments were generated by sending a 10 ns current pulse through a gold waveguide. On top of this waveguide an insulating SiO_2 layer was deposited, followed by Ta (5 nm) / Pt (4 nm) / Co (0.6 nm) / Pt (4 nm) nanostrips (1 µm × 10 µm). The middle part of the nanostrips was irradiated with Ga^+-ions to introduce the DW energy barriers,

and a Kerr microscope was used to determine the depinning fields. Although our calculations show that a change in depinning field of about 0.6 mT is expected for $\mu_0 H_{\mathrm{IP}} = 5\,\mathrm{mT}$, in these preliminary experiments no change could be detected. A possible explanation could be the value of α, as we saw earlier that α has a large influence on the DW motion. TR-MOKE measurements of α [112] show a field dependent value of α, with $\alpha \approx 1$ for the fields used in the experiments and a decreasing α for higher fields. This field dependence can be explained by extrinsic contributions to the damping that disappear for high fields, such as inhomogeneous broadening[112]. As visible in Fig. 6.4(b) these high values of α make it more difficult to detect the effect of the precession torque in depinning measurements.

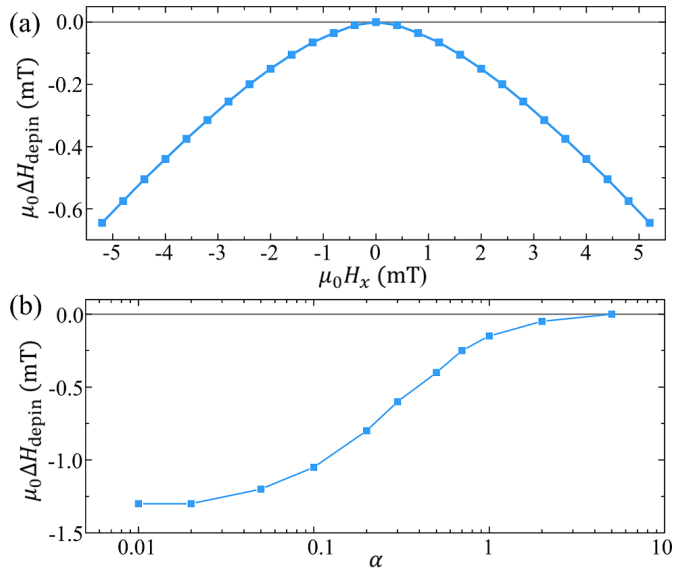

Figure 6.4: (a) Calculated change in depinning field due to in-plane field pulses. (b) Dependence of the change in depinning field at $\mu_0 H_{\mathrm{IP}} = 5\,\mathrm{mT}$ on α.

6.4 Outlook

Although we have shown theoretically that the precession torque can be used to drive DWs in OOP materials, there are still several issues that complicate the potential use in data storage devices. First, in a potential racetrack memory the reversal of the DW motion after the end of an in-plane field pulse inhibits any

effective DW motion. A way to overcome this is the use of pinning sites [84]. As the depinning from a pinning site depends on the rise or fall time of the field pulse, it is possible to adjust the rise and fall time in such a way that the DW depins during the rise time, but stays pinned at the next pinning site during the fall time, thus preventing the backward motion of the DW. A second issue we have not yet discussed is coherent motion of multiple DWs. To ensure coherent DW motion, a fixed chirality of the DWs is essential. The chirality defines whether the magnetization rotates in a clockwise or counterclockwise direction throughout the DW in the positive x-direction. The DMI, an anti-symmetric exchange interaction that prefers neighboring spins to be at an angle [17, 18], favors Néel walls with a fixed chirality, which means that using materials with high DMI can ensure coherent DW motion with the precession torque. In Fig. 6.5 the direction of DW motion for both down-up (left) and up-down (right) DWs can be seen for both chiralities, with the IP field now along the y-axis, perpendicular to the spins in the DWs. Indeed, as long as the chirality is fixed the DWs will move in the same direction, regardless of polarity, which ensures the required coherent DW motion.

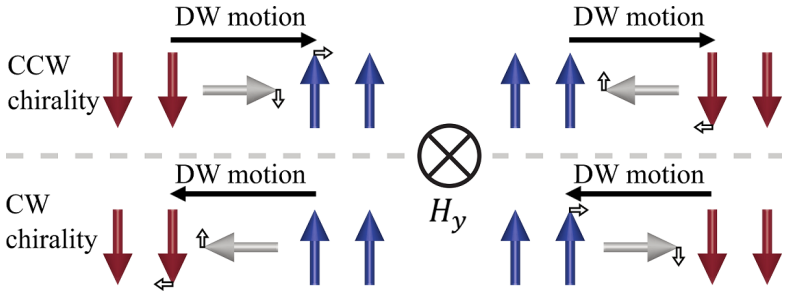

Figure 6.5: Direction of DW motion for clockwise (CW) and counterclockwise (CCW) chiralities, for both polarities.

To conclude, we have used a 1D model to show that the precession torque can be used to drive DWs in OOP materials. Because of the backward motion of the DW at the end of the pulse, it is challenging to directly detect the DW motion experimentally. Therefore, we focussed on depinning experiments, for which the 1D model was extended with an appropriate energy landscape. This enabled us to predict the change in depinning fields as a result of the in-plane field pulses, with a dependence on H_{IP}, α and the rise and fall time of the field pulse. Although we have not been able to measure the effect of the precession torque experimentally,

possibly due to a high α, our calculations indicate that it is feasible to use depinning experiments to observe the effect of the precession torque in OOP materials.

7

Summary & outlook part I

This first thesis part, *viz.* Chapter 2 to 6, focussed on magnetic DWs in Pt/Co/X stacks with perpendicular magnetic anisotropy, and in particular on the DMI in such systems. The DMI forces a DW (partially) into a chiral Néel configuration, which changes the DW energy and creates an asymmetry in its reaction to in-plane magnetic fields. In literature the DW velocity is extensively investigated in relation to DMI. We investigated whether other features of a DW, in particular its pinning at an anisotropy barrier and its geometrical configuration, are also affected by the DMI, and if so, whether these effects can be exploited to measure the elusive DMI strength. Further, we looked into new possibilities that chiral DWs offer for DW dynamics, and presented two new methods to achieve field-driven unidirectional DW motion.

Chapter 3 shows a study on magnetic micro wires that are partially irradiated with Ga^+ ions, which creates anisotropy barriers that act as pinning sites for DWs. The pinning strength is found to be controllable by a magnetic field directed along the length of the wires, which is directly related to the DMI. It is shown that the DMI strength in the as-grown sample stack can be deduced from the pinning strength measured as a function of that in-plane field, assuming that the DMI is fully suppressed in the irradiated part of the strip. This could be a valuable addition to other methods for DMI determination, because it is suitable for measuring small DMI strengths and the experiments can be performed using widely available equipment. If the DMI of the pristine stack is already known, this measurement technique also poses the exciting possibility to probe the DMI in the irradiated

stack. Our expectation would be that for high irradiation doses the interfaces become so ill defined and alloy-like that the DMI vanishes. However, it is known that ion irradiation affects the two interfaces of a magnetic layer differently [73, 113], so it is conceivable that for low doses the asymmetry of the system, and hence the net DMI, is enhanced. A measurement of the DMI as a function of irradiation dose is therefore far from trivial and to our knowledge not reported in literature. This future line of research could result in the new possibility to controllably modify the DMI locally.

In Chapter 4 similar strips containing many irradiated regions are studied. It is demonstrated that using the chiral change in pinning strength by in-plane magnetic fields, as discovered in the previous chapter, a unidirectional motion of all DWs in the strip can be achieved. In essence, this is a prototype of a racetrack memory fully operated by magnetic fields. Though current-driven DW motion has many technological advantages, there are some niche applications for field driven memories conceivable. However, before considering applications, the material stack needs to be optimized, as the demonstrated reliability in this proof-of-concept study is still too low for industry. The next step in this line of research would be to replace the polycrystalline Co layer by an amorphous CoFeB, to reduce random pinning sites. Following our interpretation a larger DMI should lead to a greater reliability, so the DMI will have to be optimized for this new magnetic layer.

Up to this point we have treated DWs as if they traverse the magnetic strips in a straight and perpendicular way. When a DW is 'pushed' against an engineered anisotropy barrier this is a reasonable assumption, but when the strip does not contain such barriers this becomes less trivial. In Chapter 5 we focussed on geometrical configuration of magnetic DWs in unirradiated microstrips under the influence of magnetic fields. When solely driven by an out-of-plane field, we observe a curved DW. We explain this curvature by pinning at the edges of the strip, and extend an existing model from literature to explain the dependence of the curvature on the field strength. When an in-plane field is added, this influences the DW configuration in a chiral way. A field directed along the strip increases or decreases the curvature, and a transverse field results in a tilted DW. We relate the observed geometries to the familiar chiral dependence of the DW velocity on in-

plane fields. This implies that the DMI can be deduced from this geometrical DW configuration. However, we were not able to model the geometrical configuration such that it satisfactorily describes the experimental observations. We expect that this is related to the reported unexpected features in DW velocity measurements, impeding the interpretation of these measurements. These unexplained features have been reported to vanish when using sufficiently large driving fields, such that the DW motion is in the flow regime instead of the creep regime. The next step in this investigation would therefore be to increase the out-of-plane field strength that drives our DW, and validate that the DMI can be deduced from the observed DW geometries. Another important direction to investigate is what happens when the size of the studied magnetic strips is reduced. If similar geometrical DW shapes are observed on a smaller scale, it would be of great technological importance.

Though the previous chapters have shown that in-plane magnetic fields greatly influence the properties of a DW, they are not used to actually move the DW. In Chapter 6, the last chapter of part I, we theoretically explored the possibility to use an in-plane field to move a DW in an out-of-plane material. The idea is based on the well-known principle that spins precess around an (effective) magnetic field. When a field is applied in-plane, but perpendicular to the spins inside a DW, these spins should precess around that field. Subsequently, the spins constituting one half of the DW are rotated towards the z axis, while the spins of the other half are rotated away from the z axis, thereby effectively moving the DW. Using a one dimensional model it is demonstrated that DW motion via this principle is indeed expected, and the effect of the magnetic field strength, the damping, and the rise time (the time needed for the magnetic field to go from zero to the set value) are investigated. The results show that for the motion to be significant, a small damping constant is required, but also a shorter rise time than so far used in our experiments. A natural next step in this project would therefore be an optimized proof-of-principle experiment on materials with a low damping constant, such as yttrium–iron–garnet. Theoretically, the next step would be to explore the effect of DMI. This would be a distinct addition to the effective field experienced by the DW, and could lead to new interesting physics. Moreover, the direction of the DW motion depends on the DW chirality, making the DMI is an essential ingredient for DW motion via this principle.

Part II

Skyrmions & current-induced effects

8

Background on part II: skyrmions and current-induced effects

In this part, we will address some of the most exotic and recently discovered phenomena in thin film magnetism. First, magnetic skyrmions are discussed, which were already briefly mentioned in Chapter 1. We will discuss how these magnetic textures are defined, and examine what determines the size and stability of skyrmions of the type studied in this thesis. Then the spin-transfer torque and the spin Hall effect are introduced, two essential concepts for the current-induced motion of DWs and skyrmions. The similarities and difference between DW and skyrmion motion are highlighted. Then we portray the state of the art by showing a selection of recent experimental results from literature. With regard to the skyrmions, several types of thin film samples that host magnetic skyrmions at room temperature are shown, and techniques to generate these skyrmions are discussed. With regard to current-induced effects, we give a very brief historical overview of how the present understanding of current-induced effects in perpendicular materials has developed. Then we discuss the state of the art regarding current-induced skyrmion motion. We conclude this chapter with a detailed content of the chapters to come.

8.1 Basic theory

8.1.1 Definition of a magnetic skyrmion

In general, a skyrmion is a topological defect in a continuous field that has particle-like properties. Examples are found, for instance, in elementary particle physics [114] and liquid crystals [115], but also in condensed matter physics and magnetism. In the latter, a magnetic skyrmion refers to a whirl of spins, as was intuitively introduced and depicted in Chapter 1. In this section magnetic skyrmions are described in a more formal way, based on the winding number, w.

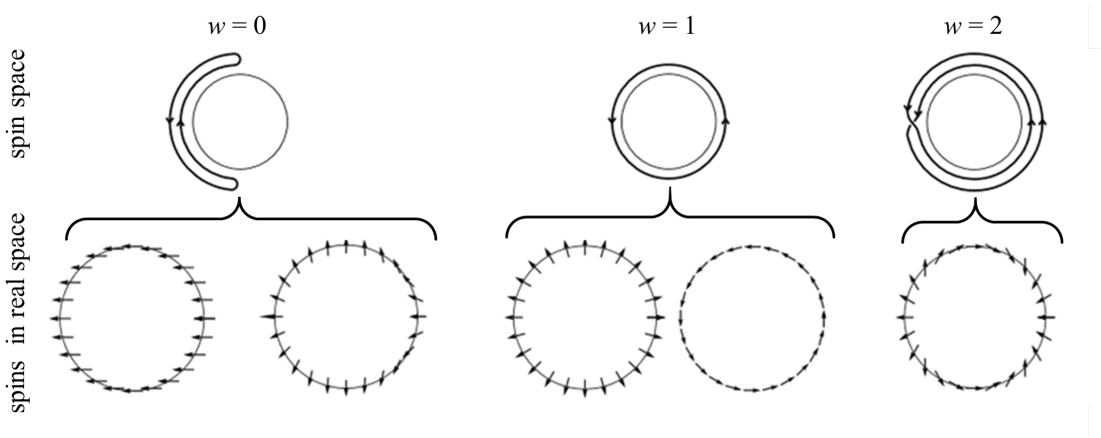

Figure 8.1: Examples of spin structures and there corresponding paths though order parameters space for various winding numbers. Adapted from Ref. [116].

We start by giving an intuitive description of the concept of winding numbers. Besides the normal, physical space, a spin configuration space that consists of all possible directions of an individual spin can be defined. The dimensionality of this spin space depends on the magnetic system that is studied: for systems with a strong in-plane anisotropy it is a one-dimensional circle representing all possible in-plane angles, and for systems without a restriction to one plane or axis (like the ones studied in this thesis) it is the surface of a sphere representing all possible polar and azimuthal angles. The winding number is now the number of times that the spin space is wrapped when sampling the physical space.

In Fig. 8.1 various examples are shown for a circle of spins with strong in-plane anisotropy, because this situation is most straightforward to depict graphically. By tracking the in-plane spin angle when following the circle in real space, the

corresponding path through spin space can be drawn. For $w = 0$ two possible examples are shown. The first is the uniform ferromagnetic state, which is mapped onto a single point in spin space, and is therefore referred to as topologically trivial. Also a non-uniform magnetic state that does not wrap spin space completely is shown. This magnetic configuration can be continuously deformed into the uniform state (or put otherwise: its path in spin space can be shrunken into a single point), and is therefore also topologically trivial. The examples shown for $w = 1$ are magnetic vortices, spin structures that are often used as example in textbooks on magnetism [117], but have only been observed satisfactorily in 2000 [118]. For these structures spin space is wrapped completely, and the path cannot be shrunken into a single point. The consequence is that these structures cannot be deformed continuously into the uniform magnetic state, hence they are topologically stable. This is equivalent to how the twist in a Möbius strip cannot be removed without breaking the strip. All spin structures with a winding number unequal to zero possess such topological stability. Lastly, more complex spin structures corresponding to higher winding numbers can also be envisioned, and an example is shown for $w = 2$.

The same principles as discussed above apply for the material systems treated in this thesis. The mathematical definition of the winding number for such magnetic films with spherical spins is

$$w = \frac{1}{4\pi} \iint \left(\frac{\partial \mathbf{m}}{\partial x} \times \frac{\partial \mathbf{m}}{\partial y} \right) \cdot \mathbf{m} \, \mathrm{d}x \, \mathrm{d}y, \tag{8.1}$$

where $\mathbf{m}$ is the normalized local magnetization. For a derivation of Eq. 8.1 we refer to Ref. [122]. A magnetic skyrmion is now defined as a spin structure for which $w = \pm 1$ (the sign depends on whether the magnetization at infinity is up or down). A more visual meaning of $w = 1$ is that the magnetic structure can be continuously deformed into a 'hedgehog' when projected onto a sphere, as illustrated in Fig. 8.2. Because also in this dimensionality $w = 0$ holds for the uniform magnetic state, skyrmions are topologically protected*. Besides skyrmions, also other

*In practice, this does not imply that a skyrmion is infinitely stable. In a real sample, a skyrmion can disintegrate at the sample edge or a defect. Also, the discrete atomic nature of a real sample and the unavoidable variations in material parameters ensure that the energy re-

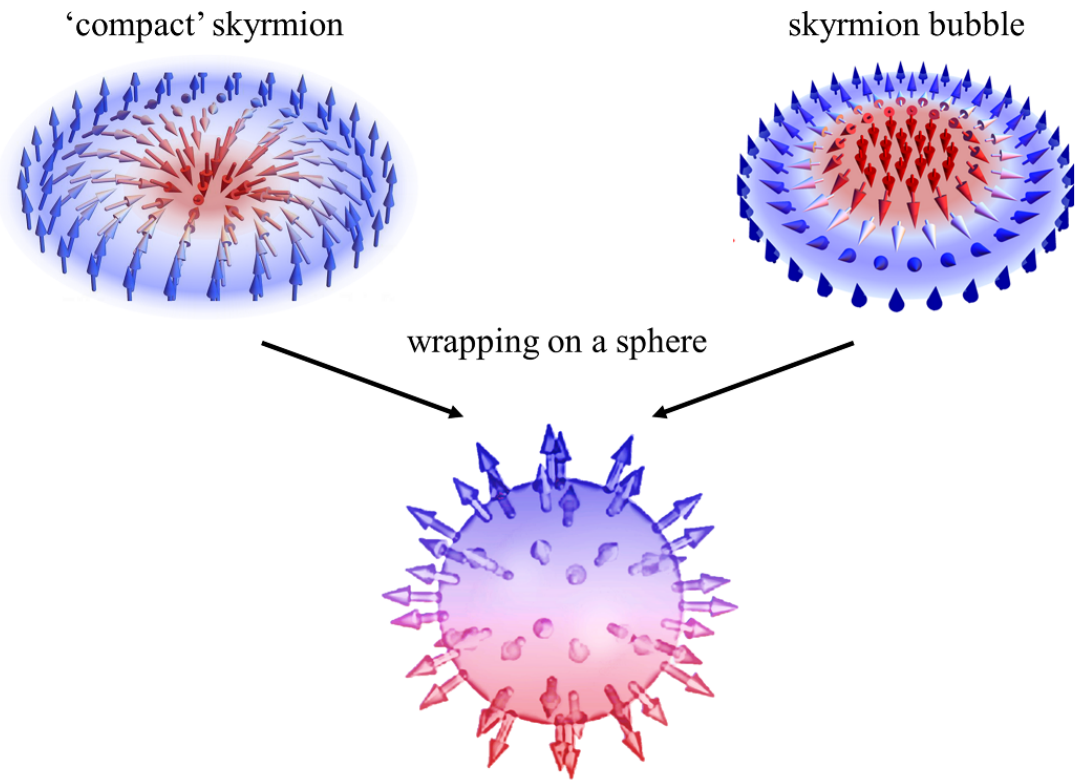

Figure 8.2: Schematic visualization of a compact skyrmion and a skyrmion bubble, which differ by the absence or presence of a plateau of constant magnetization at their centre. Both magnetic textures can be wrapped on a sphere in the same fashion. Adapted from Refs. [119], [120], and [121].

interesting spin textures characterized by other winding numbers, for instance antiskyrmions ($w = -w_{\text{skyrmion}}$) and biskyrmions ($w = 2$), have been observed and are investigated [123–125].

Note that $w = \pm 1$ is a broad definition, so a skyrmion does not always resemble the 'compact skyrmion' depicted in Fig. 8.2. The way the spins should rotate inside the whirl is not specified, the skyrmion can have any size, and its shape does not need to be circular. Especially regarding the size, experimental observations are diverse, ranging from a few nm to tens of µm. Though these larger textures fully meet the winding number criterion, they do not fit well with the vision of skyrmions as the exciting new building blocks for data storage. This brings up the question whether

quired for skyrmion annihilation is not infinite. In fact, to what degree the topological protection contributes to the stability of physical skyrmions is unclear.

there should be an additional criterion to define a skyrmion. Some researchers argue that structures with a large domain of constant magnetization at their core (see the 'skyrmion bubble' in Fig. 8.2) should not be called a skyrmion, but there is no consensus on this matter. This is a case of semantics rather than of physics, but to avoid confusion we will refer to spin structures with a large domain of constant magnetization at their core as 'skyrmion bubbles'.

The radial cross section of a skyrmion resembles a DW. However, whether this DW is in a Bloch or Néel configuration and whether its chirality is left-handed or right-handed is not captured by the winding number. In thin film multilayers it is the interfacial DMI that can ensure that all skyrmions in a sample have the same chirality. Just as for DWs, the interfacial DMI always favours a Néel configuration, with its handedness depending on the sign of D.

8.1.2 Stability of skyrmion bubbles

The spin structures that will be studied in the experimental chapters that follow are all of the skyrmion bubble type. Therefore we will elaborate on what determines their size and stability in this section. Because in skyrmion bubbles the size of the core is large compared to the width of the surrounding DW, these spin structures can be described using the so-called 'thin wall model'. In this model, the energy of a circular domain in a film with perpendicular magnetic anisotropy, E_{sk}, is calculated compared to the energy of uniform magnetized film. The geometry is sketched in Fig. 8.3(a) and the total energy is calculated by

$$E_{\mathrm{sk}} = \underbrace{\sigma t 2\pi R}_{\mathrm{DW}} + \underbrace{2\mu_0 M_{\mathrm{S}} H_z t \pi R^2}_{\mathrm{Zeeman}} - \underbrace{\mu_0 M_{\mathrm{S}}^2 \pi t^3 I\,(d)}_{\mathrm{dipolar}}. \tag{8.2}$$

Here t is the film thickness, H_z is the magnetic field strength in the direction perpendicular to the film, and σ is the DW energy as defined in Eq. 2.8. The first term is associated with the energy of a DW covering a circle with radius R. The second term represents the change in Zeeman energy when introducing a circle with radius R with opposite magnetization into the film.

The last term represents the change in energy due to long-range dipolar stray

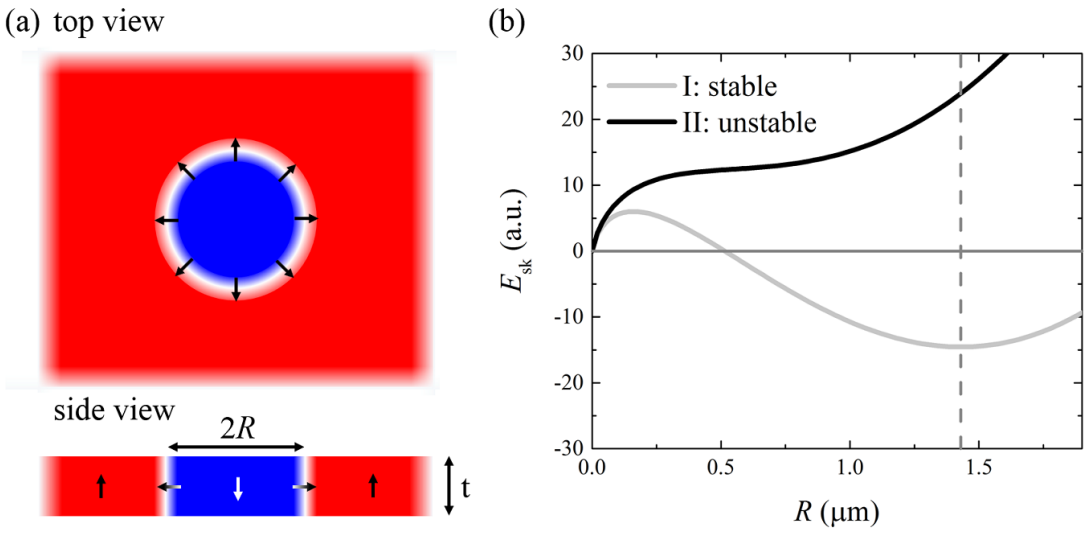

Figure 8.3: (a) Geometry of the thin wall model. (b) Examples of energy versus bubble radius curves calculated using the thin wall model.

fields when introducing the circular domain. The field energy[†] was only treated as a uniaxial term in the magnetic anisotropy in part I of this thesis, and its long-range contribution was ignored. However, for the stabilization of skyrmion bubbles this is an essential ingredient. This stray field energy increases with the inverted magnetic volume, and grows as either t, M_S or R is increased. The factor $I(d)$ is defined as:

$$I(d) = -\frac{2}{3\pi} d \left[d^2 + (1 - d^2) \frac{E(u^2)}{u} - \frac{K(u^2)}{u} \right], \tag{8.3}$$

where $d = 2R/t$, $u^2 = d^2/(1 + d^2)$, and $K(u)$ and $E(u)$ are the complete elliptic integrals of the first and second kind, respectively. So $I(d)$ is a geometrical factor depending on the ratio between the circle radius and the film thickness. For a mathematical background on the precise form of this expression, we refer to Ref. [27].

This model enables us to calculate the energy associated with the presence of a magnetic bubble as a function of its radius, for a certain set of conditions and material parameters (the applied magnetic field, film thickness, magnetic anisotropy,

[†]Also referred to as magnetostatic energy or demagnetization energy.

exchange interaction, interfacial DMI, and the saturation magnetization). Figure 8.3(b) shows two examples of such calculated curves. Curve I is calculated with parameters that are typical for our experiments, and shows a minimum at $R = 1.3\,\mu m$, indicating that bubbles of that size are stable. For the calculation of curve II the same parameters are used, only the stray field term in Eq. 8.2 is reduced (in Chapter 10 the relevance of reducing this particular term will become clear). This results in a curve without a minimum, meaning that bubbles are not stable under these conditions. The model also allows for the calculation of the energy barriers associated with creating or annihilating a bubble, and for the calculation of the influences of different material parameters on the bubble size and stability.

8.1.3 Current-induced effects in magnetic films

Sending an electrical current through a magnetic material can affect the magnetic texture in a wide range of ways. For instance, it is well-known that an electrical current generates a magnetic field, which can influence the magnetization. Also, the simple fact that heat is generated (Joule heating) gives rise to phenomena that are so exotic that a completely new field, known as spin caloritronics, is dedicated to them [126]. However, the most important principle for the work presented in this thesis is that the spins of the current-carrying electrons can exert a torque on the local magnetization: the spin-transfer torque (STT). Here we introduce this physical phenomenon, and later we will come back to its relevance for DW and skyrmion motion.

Itinerant spins tend to align with the local magnetization, so when flowing through a uniform magnetic medium an electrical current becomes spin polarized. When these electrons then pass through a region in which the direction of the magnetization is different, their spin will follow the local magnetization due to the exchange force [127]. Conservation of angular momentum dictates that the localized spins must undergo an equal and opposite change in angular momentum, as illustrated in Fig. 8.4(a). The STT was first introduced for a system of two uniform, ferromagnetic layers separated by a non-magnetic spacer (like in Fig. 8.4(a)) [128], and was later extended to the case of continuously varying magnetization, corre-

sponding to a magnetic DW. In that case, the torque exerted on the localized spins results in a movement of the DW in the flow direction of the itinerant electrons. The effect of the STT on the magnetization can be formally described as [111]:

$$\left(\frac{\partial \mathbf{m}}{\partial t}\right)_{\text{adiabatic STT}} = -\left(\mathbf{u}\cdot\nabla\right)\mathbf{m}, \tag{8.4}$$

which can be included into the LLG equation (Eq. 2.10) as an additional term. Here $\mathbf{m} = \mathbf{M}/M_{\text{S}}$, and $\mathbf{u}$ is the spin drift velocity in the direction of the electron flow, with its magnitude $|\mathbf{u}| = \frac{g\mu_{\text{B}}PJ}{2eM_{\text{S}}}$. Here g is the Landé factor, μ_{B} the Bohr magneton, P the spin polarization, J the current density, and e the elementary charge.

In the derivation of Eq. 8.4 it is assumed that the itinerant spins can follow the local magnetization adiabatically. In real systems this assumption is often invalid, hence early theoretical work based on this equation resulted in a poor agreement with experimental results [129]. When the magnetization cannot be followed adiabatically and the itinerant spins become significantly misaligned with the local magnetization, this causes an additional torque, referred to as the nonadiabatic STT. This torque is directed perpendicular to the formerly introduced adiabatic STT, and therefore appears as yet another additional term in the LLG equation:

$$\left(\frac{\partial \mathbf{m}}{\partial t}\right)_{\text{nonadiabatic STT}} = \beta\mathbf{m}\times\left(\mathbf{u}\cdot\nabla\right)\mathbf{m}. \tag{8.5}$$

The strength of the nonadiabatic STT is characterized by a phenomenological parameter β, of which the precise physical origin is still topic of debate and research.

Also in non-magnetic materials interesting current-induced effects can occur. In materials with strong spin-orbit coupling, a spin current is generated perpendicular to the direction of the flow of the electrical current, as illustrated in Fig. 8.4(b). This is called the spin Hall effect (SHE). The SHE has three contributions: asymmetric scattering, the side-jump mechanism, and the intrinsic spin Hall effect [132]. Asymmetric scattering occurs when electrons encounter an charged impurity. The impurity creates an electric field, and a relativistic transformation of this field leads to a magnetic field in the rest frame of the electron. This results

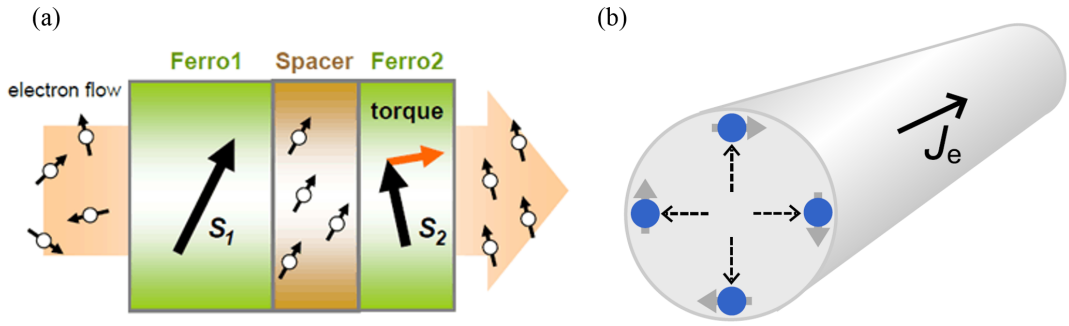

Figure 8.4: (a) Spin-transfer torque illustrated. (b) Electrons in a heavy metal are deflected in the direction perpendicular to the electron flow (J_e) depending on their spin, known as the spin Hall effect. From Ref. [130] and [131].

in a spin-dependent force on the electron, and hence in a spin current transverse to the current flow. The side-jump mechanism also occurs at an impurity and can be derived by treating the electron as a wave packet. During a scattering process the centre of this wave packet undergoes a spin-dependent lateral displacement, because of a change in momentum. The intrinsic contribution is based on the precession of the spins about the momentum-dependent magnetic field related to the band structure of the material. Which mechanism is dominant depends on the specific material parameters, temperature, and the type and amount of impurities. We realize that the description of the SHE sources that is given here is rather limited, as an in-depth treatment is beyond the scope of this thesis. For a comprehensive discussion on the SHE the reader is referred to Ref. [132].

Though the three contributions to the SHE are fundamentally very different, they all rely on spin-orbit coupling. Heavy metals exhibiting strong spin-orbit coupling can therefore be exploited as a source of spin currents. By interfacing a magnetic thin film with a heavy metal layer it is possible to inject a vertical spin current into the magnetic layer with the orientation of these spins in plane and perpendicular to the current direction. If the magnetization is not aligned with the injected spins, a torque will be exerted. This can lead to magnetization dynamics like precession of the magnetization, DW motion or even switching of the magnetization.

8.1.4 Skyrmions & currents

Because the spin texture of a skyrmion is similar to that of a DW, it is not surprising that they are affected by the same current-induced phenomena. Indeed, it has been shown theoretically, that just as for DWs, skyrmions can be moved by either the STT from an in-plane spin-polarized current, or by a vertical spin current injected by, for instance, the SHE [69]. However, in the case of skyrmions, their topology leads to additional effects [133]. Their motion can be described using Thiele's equation, which is in essence a balance of forces that act on the magnetic texture [134]:

$$\mathbf{G} \times (\mathbf{v_s} - \mathbf{v_d}) + \mathcal{D}(\beta \mathbf{v_s} - \alpha \mathbf{v_d}) + \mathbf{F}_{\text{pin}} = 0. \tag{8.6}$$

Here $\mathbf{v_d}$ is the drift velocity of the skyrmion, $\mathbf{v_s}$ is the velocity of the conduction electrons, $\mathbf{F}_{\text{pin}}$ is the pinning strength, $\mathcal{D}$ is is the dissipative force tensor, and $\mathbf{G}$ is the gyromagnetic coupling vector. When driven by the SHE instead of a planar spin current, this equation is adapted to by setting $\mathbf{v_s}$ to zero and adding the term $4\pi\mathcal{B} \cdot j_{\text{hm}}$ on the left side of the equation [135]. Here j_{hm} is the current density through the heavy metal, and $\mathcal{B}$ quantifies the efficiency of the torque and depends on the precise spin structure. The essential assumption that is necessary to derive Thiele's equation is that the magnetic texture is rigid, also when it is translated [136]. As will become apparent in the following chapters, this assumption is not valid for the magnetic textures we study, and hence Eq. 8.6 is not used. Therefore we do not review all the quantities that are introduced above, but only discuss what general behaviour can be expected of skyrmions based on an equation of this form.

The big difference between DW and skyrmion motion is the first, gyrotropic term of Eq. 8.6, which is zero for DWs. This is because $\mathbf{G}$ is directly proportional to the winding number as defined in Eq. 8.1. The term leads to a velocity component perpendicular to the current direction. This is referred to as the skyrmion Hall effect, a name that reminds one of the original Hall effect describing a transverse component of the velocity for an electrically charged particle in the presence of a magnetic field. Several types of Hall effects have been introduced over the years

(spin Hall effect, quantum Hall effect, anomalous Hall effect etc.), but what is unique about the skyrmion Hall effect is that it is based on topological charge.

When examining DW motion driven by a planar STT, it is found that the velocity as a function of current density heavily depends on the ratio between α and β. In particular, when $\beta = 0$, below a certain critical current density, no DW motion will occur at all, an effect known as intrinsic pinning. For skyrmions it was shown theoretically that there should be no intrinsic pinning, and the relation between velocity and current density is completely independent of the ratio between α and β [137]. Interestingly, when transverse skyrmion motion is impeded, for instance by the physical edge of the sample, calculations show that the velocity versus current relation becomes similar to those of DWs, including the dependence on α/β [138].

Lastly, a skyrmion is in principle able to to move around a pinning site due to its geometry, whereas a DW is not. Therefore it is expected that devices based on magnetic skyrmions require a lower minimum current density to operate (when high speed is not essential), and will therefore have a lower power consumption. To what extend a skyrmion is affected by pinning is strongly dependent on the ratio between skyrmion diameter and the size of magnetic inhomogeneities in the material [139]. Material stacks that have a higher level of homogeneity or host skyrmions that are significantly smaller than their typical grain size have to be developed in order to fully exploit this special feature of magnetic skyrmions.

8.2 Experimental state of the art

8.2.1 Magnetic skyrmions

The first experimental observation of magnetic skyrmions was done in 2009 on a non-centrosymmetric MnSi crystal [65]. Soon also observations in thin films followed: a single atomic layer of Fe on top of Ir (111) was the first in that category [88]. These observations where done using neutron scattering and spin-polarized scanning tunnelling microscopy (SP-STM), both performed at low temperatures. An example of such a skyrmion lattice observed in a thin film at low temperature is shown in Fig. 8.5(a). This sparked a great research effort to stabilize skyrmions at room temperature in multilayer stacks in which the SHE could be exploited.

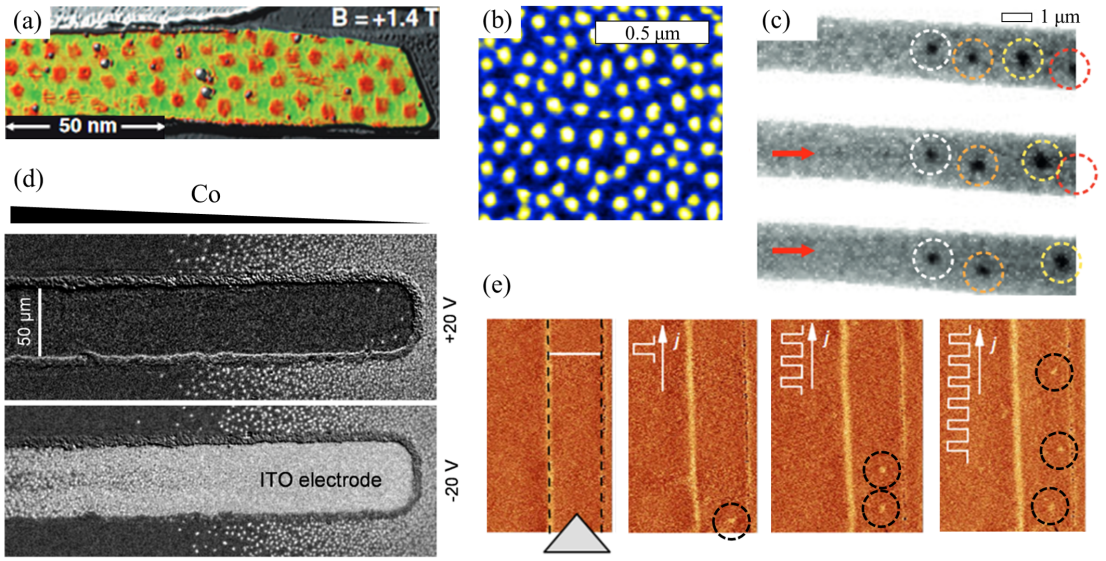

Figure 8.5: Experimental observations of magnetic skyrmions in thin film samples. (a) PdFe bilayer on a Ir(111) surface at $T = 8\,\mathrm{K}$ imaged by SP-STM. From Ref. [143]. (b) Magnetic skyrmions at room temperature in a Ir/Fe/Co/Pt stack observed with magnetic force microscopy. From Ref.[144]. (c) Skyrmions at room temperature in a Pt/Co/Ta multilayer of 15 repetitions, imaged by magnetic transmission soft X-ray microscopy. The current-induced direction of motion is consistent with the SHE (red arrows indicate current direction). From Ref. [140]. (d) Skyrmion bubble stabilization in Pt/Co/AlO_x by precise control of the Co thickness or an applied electric field. From Ref. [145]. (e) Skyrmions are nucleated an moved in a Pt/Ni/Co/Ni/Au/Ni/Co/Ni/Pt strip by current injected by a sharp electrical contact (indicated as a triangle in the first image). From Ref. [146]. Individual skyrmions are emphasized by dotted circles.

This was a challenging task, as the essential ingredient for skyrmion stabilization, the DMI, was far from understood. Nevertheless, a few years layer several groups managed to stabilize skyrmions at room temperature in sputtered transition metal stacks [56, 140–142].

There are several types of thin-film samples that are suitable for hosting magnetic skyrmions. In general, creating a large interfacial DMI is beneficial. Especially in material stacks where the top and bottom interface of the magnetic layer induce additive DMI, large net DMI values can be obtained, as was discussed in Chapter 2. Skyrmions have been successfully stabilized in such stacks [56, 144], see for instance Fig. 8.5(b). Dipolar stray fields can also aid the stabilization of skyrmions. However, increasing dipolar stray fields is achieved by increasing the magnetic vol-

ume, whereas increasing the magnetic layer thickness dilutes the interfacial DMI. To combine strong DMI with strong dipolar stray fields, a multilayer consisting of many repetitions of magnetic and heavy metal layers can be designed [56, 140], see for instance Fig. 8.5(c). Another approach showing skyrmions in a magnetic multilayer is by tuning the thickness of the magnetic layer to find conditions in which skyrmions are stable [145]. In particular, at a certain thickness the interfacial perpendicular anisotropy is precisely compensated by the demagnetization field that favours in-plane magnetization, and near such a transition the ratio between the different material parameters varies greatly. Figure 8.5(d) shows an example.

Under some conditions skyrmions are created spontaneously and form a lattice, as is the case in Fig. 8.5 (a), (b), and (d). Under other conditions skyrmion are metastable, meaning that a uniform magnetic state can exist, but if by some means a skyrmion is injected into the system, it will remain stable. This last category is especially interesting, as it provides the opportunity to study individual, isolated skyrmions. In turn, this asks for a means to controllably inject skyrmions in such systems. The most widely used approach is the use of inhomogeneous (spin) currents that result in the creation of skyrmions [88, 146, 147], as for instance shown in Fig. 8.5(e). Other possibilities include laser-induced heat pulses [148, 149], a local magnetic field [150], or moving skyrmions from regions where they spawn spontaneously to a region where they are metastable.

8.2.2 Current-induced effects

The current-induced motion of magnetic DWs has been investigated extensively, motivated by its potential for future spintronic technologies. In particular, when research efforts shifted towards perpendicularly magnetized materials, unexpected experimental observations followed. In 2009 Miron *et al.* measured current-driven DW motion in the direction against the electron flow [151]. This could not be understood by an STT from the spin-polarized current flowing though the magnetic material, and alternative effects needed to be considered. One explanation that was explored was a negative P or β parameter leading to DW motion against the electron flow. This explanation was discarded, but interestingly almost a decade later the existence of such a negative STT was demonstrated experimentally [152].

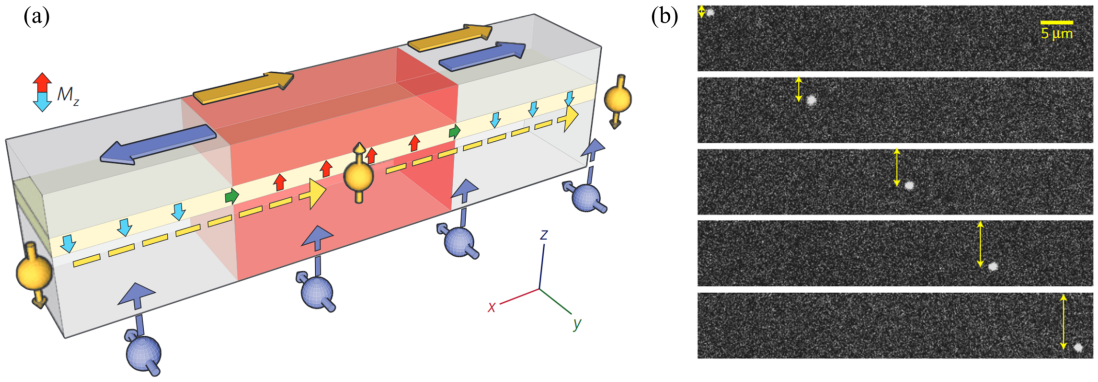

Figure 8.6: (a) Current-induced effects in perpendicular materials. The STT from the spin-polarized current flowing through the magnetic layer drives the DWs along the electron flow (yellow electrons and arrows). The vertical spin current injected due to the SHE exerts a torque on Néel walls, but its direction depends on the DW chirality (purple). From Ref. [72]. (b) Snapshots of skyrmion motion at $j = 2.8 \times 10^5\,\mathrm{A\,cm^{-2}}$ through a magnetic strip. Besides the motion along the current direction (parallel with the length of the strip), the skyrmions also exhibit a transverse displacement, as emphasized by the yellow arrows. From Ref. [135].

However, the current interpretation of Miron's results is that the DW motion is driven by the spin Hall effect (SHE). This is a plausible explanation because the experiments were performed on a material system containing a heavy metal layer, and when the direction of the torque depends on the spin configuration inside the DW, all directions of motion are conceivable, including against the electron flow.

The importance of the SHE in perpendicular materials was confirmed by additional experiments [72], and Fig. 8.6(a) shows the present view of different (spin) currents important for DW motion in perpendicular materials. Of course, also in perpendicular materials a current gets spin polarized (indicated by the yellow spins) when flowing through a magnetic material and exerts a torque on DWs. This torque will typically (when $P > 0$ and $\beta > 0$) drive the DW in the direction of the electron flow, as indicated by the yellow arrows. Whether this traditional effect or the SHE is dominant depends on the specific material system [153].

The orientation of the spins injected by the SHE is in-plane and perpendicular to the current direction, as indicated by the blue spins. When the localized magnetic moments are directed along the same axis no torque is exerted. For the geometry of a strip in which DWs divide the length of the strip into smaller magnetic domains

(as typically is the case for a racetrack memory), this means the SHE cannot affect a Bloch wall. It does exert a torque on Néel walls, but for a multitude of DWs to move in the same direction, they all need to have the same chirality. Figure 8.6(a) shows two DWs with opposite chirality and as indicated by the blue arrows these are driven in opposite directions. Homochiral Néel walls will only form in thin films when a sizable interfacial DMI is present. The DMI is therefore an essential ingredient for DW motion driven by this mechanism, and in turn the SHE now provides a tool to measure the DMI. If the efficiency of the torque on a DW is measured as a function of the applied longitudinal magnetic field, the DW configuration as a function of this field and hence the DMI can be deduced [44].

Currently, the general consensus is that the SHE is the dominant contribution for DW motion in typical multilayer stacks in which skyrmions are stable. Several studies have shown evidence of current-induced DW motion and interpret this as SHE-driven [140, 145, 147]. The experimental skyrmions in thin film multilayers are still hindered considerably by pinning sites, resulting in larger critical currents to initiate the skyrmion motion than is theoretically predicted.

What is distinctively different for skyrmion dynamics, compared to DWs, is the prediction of an additional velocity component perpendicular to the current direction, called the skyrmion Hall effect, as discussed in subsection 8.1.4. Recently, two groups were able to observe the skyrmion Hall effect experimentally [135, 154], and a typical observation is shown in Fig. 8.6(b). From theory it was already known that the size of the skyrmion Hall effect should depend on the skyrmion diameter and the damping constant, but from the experiments it followed that it also strongly depends on the driving force. Although the two groups ascribe this dependence to different physical phenomena, they both report that the skyrmion Hall effect is more pronounced at higher skyrmion velocities.

8.3 Contents part II

In this thesis part we experimentally investigate magnetic skyrmion bubbles. Precisely tuning the magnetic layer thickness allows us to stabilize skyrmion bubbles in material stacks similar to those investigated in part I of this thesis. Only the thickness of the magnetic layer is altered; the used materials, substrate, and de-

position process all remain unchanged. Skyrmion bubbles with diameters in the order of a micrometre can also be imaged using the same experimental technique as was employed in part I: Kerr microscopy.

In Chapter 9, we will show that we are indeed able to stabilize skyrmion bubbles in our samples, and characterize their basic properties (e.g. their diameter and the range of applied fields for which they are stable). We then study their current-induced behaviour. Though there is no sign of the skyrmion Hall effect, the direction of motion observed for various investigated heavy metal layer thicknesses is completely unexpected. Inverting the spin-current injected by the SHE does not lead to a reversal in the direction of motion, which conflicts with the prevailing view of the SHE as dominant driving mechanism. Therefore the influence of all possible current-induced contributions, as introduced in section 8.1.3, has to be reconsidered for this case. Additional experiments in which the layer thicknesses, the current direction, and current density are varied, as well as additional measurements of the DMI are performed to disentangle the contributions from the spin Hall effect, Joule heating, and the various types of spin-transfer torque exerted by a planar polarized current. The provisional conclusion is that the observed skyrmion bubble motion is governed by a negative spin-transfer torque.

In Chapter 10 we continue our investigation on skyrmion bubbles in confined geometries. In order to progress, some technical improvements are necessary. First, extremely precise layer thickness control has to be achieved such that a varying magnetic layer thickness is no longer required. After homogenous films containing skyrmion bubbles are created, it becomes possible to pattern these into devices. Because of the extreme sensitivity of skyrmion bubble stability to changes in material parameters, high-quality device edges are required. The method for device patterning as followed in part I will no longer suffice, so we optimize our lithography process. We then demonstrate skyrmion bubble stabilization in confined geometries. We show that this confinement forces the skyrmion bubbles, that tend to move around disorderly in unpatterned films due to thermal fluctuations, into certain preferential positions. Different physical mechanisms that could possibly govern the responds of the skyrmion bubbles to the physical edge of the geometries and to each other, are considered. We find that for these relatively large skyrmion bubbles, dipolar stray fields give the dominant contribution. Last,

we explore an alternative method of sample fabrication. Using our expertise on FIB in these material stacks, we manage to stabilize skyrmions in geometries written by FIB, imbedded in a ferromagnetic layer. By independently switching the magnetization outside the FIB geometries, we can control the dipolar stray fields.

9

Anomalous direction for skyrmion bubble motion

Magnetic skyrmions are localized topological excitations that behave as particles and can be mobile, with great potential for novel data storage devices. In this Chapter, the current-induced dynamics of large skyrmion bubbles is studied. When skyrmion motion in the direction opposite to the electron flow is observed, this is usually interpreted as a perpendicular spin current generated by the spin Hall effect exerting a torque on the chiral Néel-type skyrmion. By designing samples in which the direction of the net generated spin current can be carefully controlled, we surprisingly show that skyrmion bubble motion is always against the electron flow, irrespective of the net vertical spin-current direction. We find that a negative bulk spin-transfer torque is the most plausible explanation for the observed results, which is qualitatively justified by a simple model that captures the essential behaviour. These findings demonstrate that claims about the skyrmion chirality based on their current-induced motion should be taken with great caution.

Magnetic skyrmions are swirling spin textures that are currently the focus of many research efforts [54]. In such a whirl the magnetization direction in the centre is opposite to the magnetization direction at the edge, while in-between the magnetization direction rotates gradually with a certain chirality. The interaction that favours this chiral rotation is the DMI [17, 18], which plays an important role

in the creation and stabilization of magnetic skyrmions. This interaction is only present in systems with strong spin-orbit coupling (SOC) and structural inversion asymmetry (SIA), which occurs in certain crystals lacking inversion symmetry or in ultrathin multilayers near interfaces. In both type of systems with SIA, skyrmions have been observed experimentally [56, 65–67, 140], and here we will focus on the latter. We observe a unique motion of skyrmion bubbles, that cannot be described by conventional physical effects.

In order to become a viable candidate for future data carriers, the movement of skyrmions should be controlled, preferably by electrical current. Figure 9.1 schematically shows a typical stack like we investigate in this Chapter —an ultrathin ferromagnetic (FM) layer in between two heavy metal (HM) layers —and the current-induced effects that can propagate a skyrmion. Electrons moving in the plane of the sample through the magnetic layer become spin polarized, and exert a bulk spin-transfer torque (STT) on the skyrmion (indicated in yellow). This torque results from angular momentum conservation [111, 155], and in principle always leads to movement in the direction of the electron flow. The spin Hall effect (SHE) occurs in a heavy metal where a spin accumulation is generated perpendicular to the charge current (indicated in blue). If there is a magnetic material adjacent to this heavy metal the injected spins can exert a torque on the magnetization texture [72, 156]. This can lead to fast and efficient motion either along or against the electron flow, depending on the sign of the spin current and the orientation of the magnetization. In practice, heavy metal layers are generally present in material stacks that contain skyrmions, as they are also required to induce a sizable DMI. Also, bulk STTs are widely believed to be relatively small in ultrathin layers [157]. Therefore it is not surprising that the SHE is considered to be the dominant driving mechanism in experimental reports on current-induced skyrmion motion, especially when motion against the electron flow is observed.

For the creation of samples that contain skyrmions, the approach of Schott *et al.*, in which a wedge of magnetic material is investigated, is used [145]. In such samples, the skyrmions typically appear at small ($\sim 0.5\,\mathrm{nm}$) magnetic layer thicknesses, at the onset ferromagnetism. Further, we systematically vary the vertical spin current injected by the SHE. Its size and sign are controlled by the thicknesses of the HM layers adjacent to the FM layer, by which we are able to control the ex-

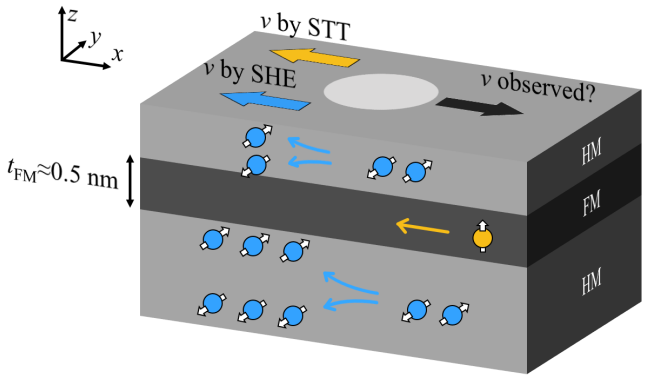

Figure 9.1: Schematic view of the studied geometry: a thin FM layer sandwiched between HM layers in which a skyrmion bubble is stabilized. Also the spin currents that can cause a torque on the skyrmion are depicted: a vertical spin current caused by the SHE and an in-plane spin current from conduction electrons that become spin polarized when flowing through a magnetic material.

pected direction of motion. In striking contrast, we observe an unexpected, unique skyrmion motion that cannot be explained by either the SHE or the traditional bulk STT. In similar atomically thin magnetic layers, depinning measurements on magnetic domain walls (DWs) could only be explained by a *negative* spin transfer torque [152]. Using a qualitative model, we show that this novel ingredient is a plausible explanation for the observed anomalous skyrmion motion.

9.1 Sample design

The perpendicular spin current density, J_S, induced by the SHE in a heavy metal layer is determined by $J_S = \theta_{SH} J$, where θ_{SH} is the spin Hall angle and J the charge current density in the heavy metal. If the thickness, t, of the heavy metal layer is comparable to spin diffusion length, λ_{sf}, J_S is reduced by a factor $1 - \text{sech}\,\frac{t}{\lambda_{sf}}$ [158]. This implies that in a Pt/Co/Pt sample the net injected spin current can be controlled by varying the thicknesses of both Pt layers [72]. For the main experiment, samples will be grown in which one of the Pt layers gradually varies in thickness. We choose to vary the top Pt layer thickness, so that the bottom Pt layer remains constant, which limits changes in properties determined by the subsequent interfaces, like the magnetic anisotropy or DMI. The thickness vari-

ation is chosen such that both the situation in which the dominant contribution from the SHE comes from the bottom Pt layer, and the situation in which the dominant contribution comes from the top Pt layer can be studied. For purely SHE-driven motion, the direction of motion is expected to be opposite in these two regimes. Also, it is expected that between these two regimes there is a thickness combination (probably when the thicknesses of both Pt layers are comparable) for which the spin currents coming from the top and bottom exactly cancel out. This will be referred to as the cancellation point, and here SHE-driven motion cannot occur.

Before we show these results on controlling the direction of the net spin current, it is important to demonstrate how to stabilize skyrmion bubbles in the sample. Following the approach by Schott *et al.*, the thickness of a magnetic layer is gradually varied. This results in a large variation of material parameters (especially the saturation magnetisation, M_S, the effective magnetic anisotropy constant, K_{eff}, and DMI are expected to vary with thickness) in one sample, allowing access to the narrow parameter window in which skyrmion bubbles can be stabilized [145]. The used material stack is Ta (5 nm) / Pt (4 nm) / Co (0 - 0.8 nm) / Pt (4 nm), schematically shown in Fig. 9.2(a).

The remanence as a function of the Co layer thickness is obtained using polar MOKE measurements and is shown in Fig. 9.2(b). In the graph two regimes can be identified: for Co thicknesses above 0.5 nm the sample has an out-of-plane easy axis and the remanence is 100 percent. For thicknesses below 0.4 nm the remanence is zero, because the ferromagnetic-paramagnetic transition is approached and the ferromagnetic state disappears. When the remanence turns to zero around 0.4 nm Co thickness, the magnetization and out-of-plane easy axis do not disappear immediately (though the values of M_S and K_{eff} are significantly reduced, see Appendix D.1): a small regime exists in which at zero applied magnetic field multiple small out-of-plane magnetized domains appear, and the up and down domain are equal in size. This results in a measured remanence of zero, since in this measurements we average over a large area on the sample containing many up and down domains. Using Kerr microscopy a labyrinth structure is observed at remanence in this thickness regime, but when a small magnetic field (~ 0.1 mT) is applied circular, micron-sized domains spontaneously form, see Fig. 9.2(c). These

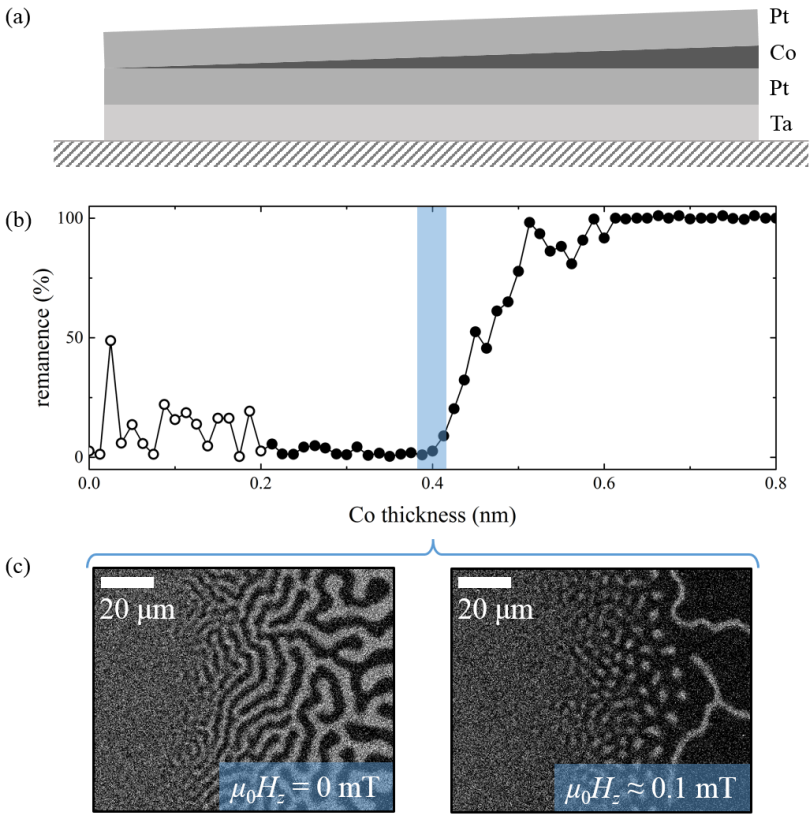

Figure 9.2: (a) Schematic representation of the studied sample. (b) Remanence of the sample as a function of the Co thickness. A transition where the PMA disappears is observed. The non-zero points below 0.2 nm (indicated by open circles) have no physical meaning. They occur because at these thicknesses only noise is measured, leading to problems in the algorithm determining the remanence. (c) Magnetic domain structures observed by Kerr microscopy at the transition, both with and without the application of a small perpendicular magnetic field.

are the skyrmion bubbles that will be studied in the remainder of this Chapter, and the thickness at which they occur will be referred to as the skyrmion transition.

In Appendix D.2 the characterization of the skyrmion bubbles is shown (here also the results for Pt/Co/Ta and Pt/Co/Ir samples are shown), and the general conclusions are the following: for all investigated stacks the diameter of the bubbles is of the order of 1 µm, the field at which they are stabilized is of the order of 0.1 mT and the Co thickness range in which they are stable is only 0.01 nm wide. This last value seems extremely low, but around the ferromagnetic-paramagnetic transition, the material parameters vary extremely rapidly with effective Co thickness.

Because for the stabilization of skyrmions a delicate balance between material parameters is required, it is not surprising that they are only stable in a very narrow thickness range. Despite the narrow stability range, the skyrmion transition was reproducibly found in all material stacks investigated, indicating that this method is a reliable way to create skyrmion bubbles, even in a sample stack in which the magnetic layer is interfaced with the same material on both sides. This is a non-trivial result, as the DMI, which is believed to be essential in the stabilization of skyrmions, is typically small in such nominal symmetric samples (though not necessarily zero, because differences in growth can also lead to asymmetry [46, 50]).

Based on this successful stabilization, a sample to investigate the role of the SHE on skyrmion bubble motion is designed. This is a Pt (4 nm) / Co (0-0.6 nm) / Pt (0-10 nm) sample in a double wedge geometry, schematically shown in Fig. 9.3(a). In one direction the Co thickness is varied, which is necessary to hit the narrow thickness range in which the skyrmion bubbles are stable. In the other direction, the thickness of the top Pt layer is varied, which ensures a gradually varying SHE induced spin current along the sample. It is important to note that for the analysis later on it is assumed that the spin Hall angle is the same for the top and bottom Pt layer, and independent of the Pt layer thickness. This may seem crude, but experiments presented in Appendix D.3 show that the net direction of of the injected spin current is opposite for samples with a bottom Pt layer of 4 nm and a top Pt layer of 2 nm and vice versa. Moreover, earlier experiments on very similar samples grown with the same deposition tool show that for Pt layers of equal thickness the spin currents cancel out [72], which justifies the assumption.

9.2 Results

To perform the electrical experiment, metallic probes are landed at either side of the skyrmion bubbles at each Pt thickness we want to investigate for current injection. The probes are typically placed 200 µm apart and placed such that the conventional current runs in the direction of increasing Co thickness. See Appendix D.4, D.5, and D.6 for details on the velocity determination, the calculation of the current densities, the reasoning behind the choice for this current direction,

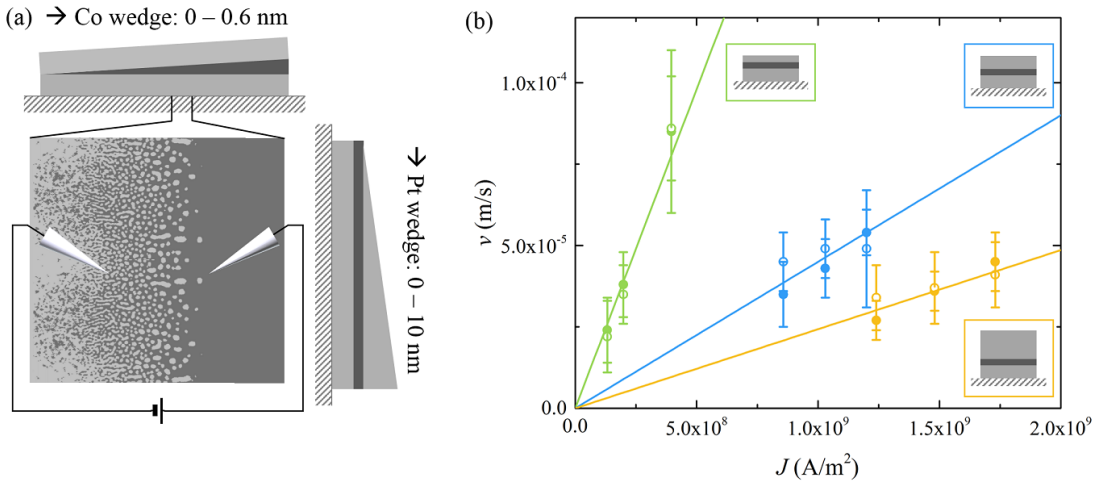

Figure 9.3: (a) Schematic representation of the double wedge sample and the application of current. (b) Measured skyrmion bubble velocity at various thicknesses of the top Pt layer: 1.5 nm (green points), 4.5 nm (blue points) and 7.5 nm (yellow points). At each thickness three current densities are used, and skyrmion bubbles of both polarities (indicated by the open and closed points) are investigated. The lines are linear fits fixed through the origin. The large error bars are a consequence of the rapidly varying material parameters along the Co wedge, see Appendix D.4 for further explanation.

and a discussion about the homogeneity of the current. At each Pt thickness 6 measurements are performed: three different current densities are investigated for both skyrmion bubble polarities (so both the case that the magnetization in the centre of the skyrmion bubble points in the $+z$ direction while the magnetization of the surroundings points in the -z direction and vice versa). Figure 9.3(b) shows three typical measurements of the average velocity, v, as a function of the applied current density through this sample. Of the three data sets, the green points represent the situation in which the top Pt layer is much thinner than the bottom layer (1.5 nm), blue shows the situation where the Pt thicknesses are comparable (4.5 nm) and yellow shows the situation where the top layer is much thicker than the bottom layer(7.5 nm). All measured velocities are positive, corresponding to movement along the charge current direction. This indicates that no cancellation point or reversal of movement direction is observed.

These observations are surprising, because they seem incompatible with motion driven by the SHE alone: as explained in the introduction, in that case the direction of motion would be opposite for the situation with a bottom Pt layer that is

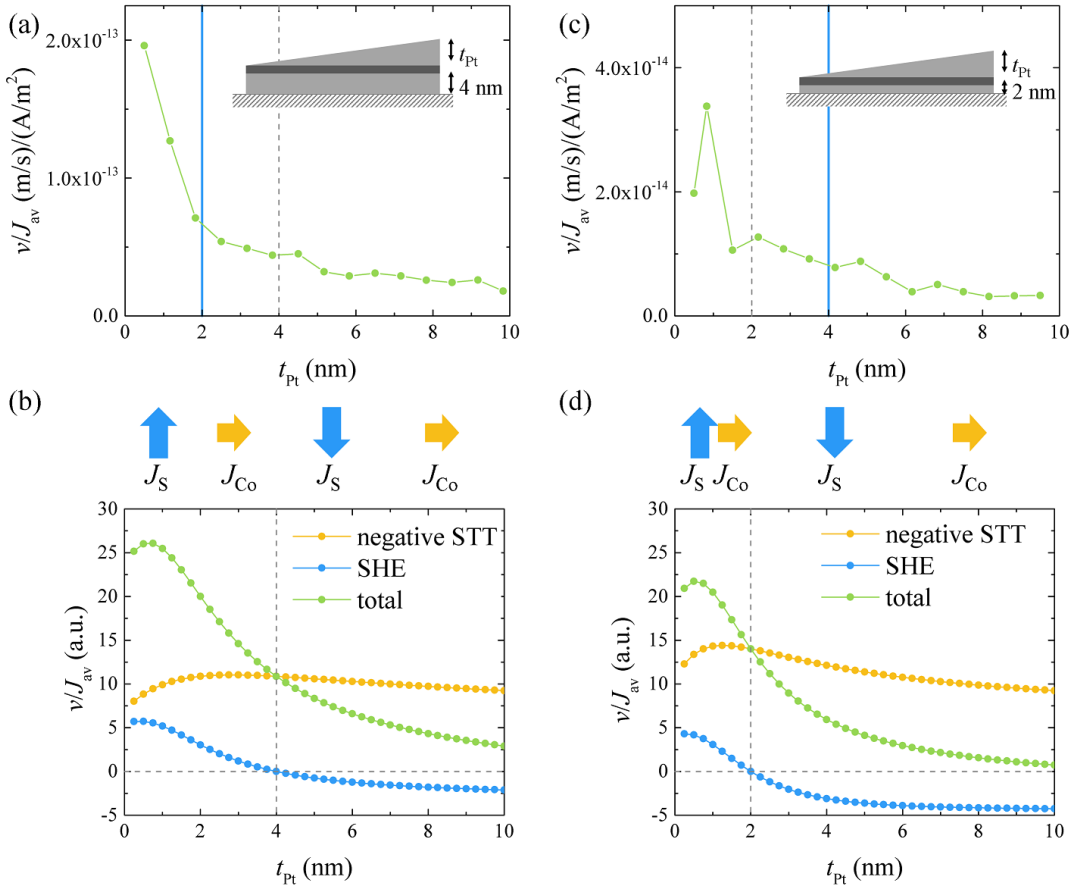

Figure 9.4: Velocity per (average) current density as a function of the top Pt layer thickness for the sample with (a) a 4 nm thick bottom Pt layer (c) a 2 nm thick bottom Pt layer. (b+d) Calculation of the layer specific current densities using the Fuchs-Sondheimer model for the same material stacks which are used experimentally.

thicker than the top Pt layer and vice versa. The conventional bulk spin-transfer torque also does not provide an explanation, as it predicts motion in the direction of the electron flow only. However, Je *et al.* [152] already encountered a similar observation in an experiment on DWs and how efficient they are depinned by current. They explained their results by the presence of a hitherto never observed *negative* bulk spin transfer torque. We will now investigate if this is also a plausible explanation for our observations. To do this, we will use a simple, qualitative model which includes both this negative bulk spin transfer torque and the SHE to predict how the skyrmion velocity will change along the double wedge sample, and compare this to the experimental results.

Experimentally it is found that v is proportional to J_{av} within the margins of error. Such a linear relation is expected for motion in the flow regime. For the small current densities used here, the observed motion is not expected to be in flow regime. However, we will use this linear approximation, as from the few measurement points per Pt thickness it is not possible to fit a more complex relation accurately. Using the well-known one dimensional model for DW motion, we find that the velocity as a result of the STT (either positive or negative) is proportional to the current density in the magnetic layer, J_{Co}, and the velocity as a result of the SHE is proportional to the net injected spin Hall current density, $J_{\mathrm{S},net}$, see Appendix D.7. Here pinning and thermal effects are not considered and current densities from 0-2.0 $\times$ 10^9 A m^{-2} are investigated (which corresponds to the current densities that are used experimentally). Moreover, in case both effects are present, it is found that the velocity v is equal to the sum of the velocities that would have been caused by the individual contributions, so $v = C_1 J_{\mathrm{Co}} + C_2 J_{\mathrm{S},net}$, where C_1 and C_2 are proportionality constants. Dividing by the average current density in the whole stack, J_{av}, transforms this equation to the form: $v/J_{\mathrm{av}} = C_1 J_{\mathrm{Co}}/J_{\mathrm{av}} + C_2 J_{\mathrm{S},net}/J_{\mathrm{av}}$. The benefit of this form is that v/J_{av} is experimentally accessible (for each Pt thickness, the velocity per average current density, v/J_{av}, can be determined by a linear fit through the data points, and the results are plotted in Fig. 9.4(a)), while $J_{\mathrm{Co}}/J_{\mathrm{av}}$ and $J_{\mathrm{S},net}/J_{\mathrm{av}}$ can be estimated using the Fuchs-Sondheimer model. Calculations using parameters from Cormier *et al.* [157] and assuming that θ_{SH} is equal for the the top and bottom Pt layer (see earlier discussion), are shown in Fig. 9.4(b), where $J_{\mathrm{Co}}/J_{\mathrm{av}}$ is indicated by the yellow points and $J_{\mathrm{S},net}/J_{\mathrm{av}}$ by the blue points. For $J_{\mathrm{Co}}/J_{\mathrm{av}}$ we see only a small variation with Pt thickness, related to scattering at the outer surfaces. For $J_{\mathrm{S},net}/J_{\mathrm{av}}$ a different behaviour is observed, as expected. There is a cancellation point when the top Pt layer has the same thickness as the bottom layer (indicated by the dashed, gray line). The values for C_1 and C_2 are not trivial to calculate: one can imagine that they depend on several parameters that are difficult to access. Examples are the spin Hall angle, the configuration of the DW (Bloch, Néel, or something in between), the spin polarization, the damping parameter and the nonadiabaticity, β (in Appendix D.7 it is shown how these parameters appear in the one dimensional model for DW motion). Moreover, the general view is that the bulk STT becomes smaller for thinner magnetic layers [153, 157]. Why

this effect would become large and negative for atomically thin layers, as was indicated by the experiments of Je *et al.* is unclear, which makes it impossible to calculate how large this contribution is. We therefore empirically try to add the contributions together for different values of C_1 and C_2. It turns out that when taking $C_2 = 1.5C_1$ (the resulting curve is shown in green in Fig. 9.4 (b) and (d)), the qualitative behaviour of the experimental data can be fairly well reproduced. This includes the fact that the skyrmion bubble velocity is always in the direction of the charge current for the layer thicknesses investigated and that the velocity decreases for larger top Pt layer thicknesses.

9.3 Alternative interpretations

We will now consider three alternative explanations for the observed results, and show that each of them falls short. First, we consider gradients in the material properties caused by the wedge geometry of the sample combined with Joule heating is as the source of motion. As the material parameters vary rapidly around the skyrmion bubble transition, it is conceivable that there is a gradient in the energy of the skyrmion bubbles, resulting in a force on the skyrmion bubbles. If this force would drive the motion and if the heating by the current would be necessary to overcome pinning, the direction of motion would indeed not depend on the Pt thickness. This interpretation can be tested by measurements with currents applied in other directions and by inverting the current direction (because Joule heating does not depend on the direction of the current, the direction of motion should neither). Supplementary video 1 and 2 (available online [159]) show the sample from Fig. 9.2 with the probes positioned such that the current flows along constant Co thickness. The skyrmion bubbles move in the direction of the current for this measurement configuration as well, so not along the direction in which the material parameters vary. The two movies show the two polarities of the current, and inverting the current direction also leads to an inverted direction of motion of the skyrmion bubbles. Therefore, this experiment rules out the wedge geometry and Joule heating as the source of the observed motion.

Also, one may wonder whether a possible inversion of the sign of the DMI at the same Pt thickness where the expected inversion of the net spin current occurs

could explain the measurements without the need of a negative STT. After all, reversion of both of these effects would result in DW or skyrmion motion in the same direction. First, though the net spin current is tuned by the thicknesses of the Pt layers, the DMI is an interface effect, hence it is not expected to vary upon variation of the top layer thickness (assuming the interface remains constant). If through some subtle effects the DMI would vary, it would be purely coincidental if a change in sign would occur at the same thickness as the cancellation point of the spin current. Moreover, this scenario would show as a minimum in v/J_{av} versus t, because a cancellation point for the spin currents would still be expected at which there would be no motion at all. This is not observed (see Fig. 9.4 (a+c)), which excludes this scenario.

Last, considering the short λ_{sf} in Pt ($\approx 1.2\,\mathrm{nm}$ [160]), the net difference in injected spin current decreases rapidly with increasing Pt layer thicknesses, hence a possible difference in interface transparency might impede controlling the net spin current direction. Therefore, it is verified that the net spin current is opposite for a Pt (4 nm) / Co (0.6 nm) / Pt (2 nm) and a Pt (2 nm) / Co (0.6 nm) / Pt (4 nm) stack, see again Appendix D.3. We therefore also study a double wedge sample with a bottom Pt layer of 2 nm, in which a reversal of the net spin current direction should certainly occur. The measured results are shown in Fig. 9.4(c). The positions with Pt thickness combinations for which we have checked that the net spin current has the opposite direction are indicated by the vertical blue lines in Fig. 9.4(a) and (c). In both cases, a positive velocity is measured, meaning that although the spin current is opposite, the skyrmion motion is actually in the same direction. Please note that this could still be explained by the SHE alone in case the DMI has an opposite sign in the two samples, but additional experiments presented in Appendix D.8 render this explanation unlikely: there is no indications of a DMI with opposite sign in the Pt (2 nm) / Co (0.6 nm) / Pt (4 nm) sample, though the DMI is significantly smaller as compared to the inverted layer composition. The results on the double wedge with a bottom Pt layer of 2 nm turn out to be very similar to the results for the sample with the 4 nm Pt layer: there is no point at which the direction of motion reverses and all observed velocities are positive and the observed velocities per current density are larger for thin top Pt layers than for thick top Pt layers. In Fig. 9.4(d) calculations using the Fuchs-Sondheimer

model are shown, using the same material parameters as in Fig. 9.4(b), except for that now the bottom Pt layer thickness is set to 2 nm. Again, there is a fair qualitative agreement between the calculations and the experimental results. All this suggests that a combination of the SHE and a negative bulk STT is so far the only plausible explanation for the observed skyrmion bubble motion.

9.4 Discussion and outlook

The results in this paper show that additional current-induced effects, besides spin-orbit torques and traditional bulk spin-transfer torques, can play a role in skyrmionic systems. The most likely explanation for our observation is the existence of a negative bulk spin-transfer torque, for which there have previously been indications in a study on chiral DWs in atomically thin Co films [152]. There are various sorts of bulk STTs: there is an adiabatic and a non-adiabatic term, as well as higher order contributions. We will now briefly discuss how likely these terms are to cause the negative STT we observe. The higher order contributions become increasingly important for narrow DWs, which might explain why the effect is, up to now, only observed in atomically thin films. However, the underlying physical mechanism for this contribution is momentum transfer, which should never result in motion against the electron flow [161]. For the standard adiabatic and non-adiabatic terms it is theoretically possible to drive a domain wall or skyrmion against the electron flow, when the spin polarization in the magnetic layer or the nonadiabaticity becomes negative [162]. However, why these bulk effects would dominate over the SOT induced effects in atomically thin layers remains unclear. Therefore, the origin of this negative STT is a subject on which further investigation is certainly required. Using giant magnetoresistance measurements we have searched for signs of a negative spin polarization, but so far none were found, see Appendix D.9.

We will now discuss the chirality of the studied skyrmion bubbles. The observation of skyrmion bubbles by itself does not imply the presence of DMI, as dipolar stray fields can be sufficient for their stabilization [163]. Usually it would be concluded from current-induced motion opposite to the electron flow that a chiral Néel wall must be present to enable SHE-driven motion. However, as this paper

shows that the observed motion cannot be explained by the SHE alone we cannot draw this conclusion. Additional experiments to measure the DMI are discussed in Appendix D.10. Though the results are not fully conclusive, they certainly suggest the presence of DMI, but not strong enough to enforce a complete Néel configuration. Also, the results in Fig. 9.4 show that, though the SHE cannot account for the observed behaviour on its own, it is undoubtedly an essential ingredient. To account for the direction of the torque exerted by the SHE as modeled in Fig. 9.4, a (partially) left-handed Néel configuration is required. This suggests that the bottom Pt/Co interface induces the dominant contribution to the DMI.

Irrespective of the precise origin of the observed effect, there are some practical implications. As mentioned before, the DMI is intensively investigated, but remains difficult to measure. Because it is directly related to the chirality of the skyrmions it helps to stabilize, the direction of skyrmion motion under influence of the SHE reveals the sign of the DMI. When skyrmion motion is observed —especially in the direction against the electron flow for which up to now no other mechanism than the SHE was considered likely —its direction is often used to deduce the sign of the DMI and compare this with the expectation for the used material stack. Now knowing that there is an alternative effect that can lead to skyrmion motion against the electron flow as we have demonstrated here, this type of analysis becomes unreliable. We would therefore advise to always do additional measurements to determine the chirality of skyrmions if this is of importance, such as direct imaging of the magnetization orientation inside the DWs or checking the presence of the skyrmion Hall effect [71, 135].

9.5 Methods

The material stacks used in this work are all grown on thermally oxidized SiO_2 substrates. Before the deposition, the substrates are cleaned using acetone and isopropanol in a ultrasonic bath. For further cleaning, they are exposed to an oxygen plasma for 600 s. Deposition is done by d.c. sputtering using a argon plasma of approximately 0.01 mbar, in a system with a base pressure of approxi-

mately 10×10^{-7} mbar. The thickness variations/wedge geometries are achieved by gradually covering the sample with a mask during the deposition.

To control the thickness of the deposited layers, calibration samples have been grown prior to the samples studied in this chapter. On these calibration samples material is deposited for a known amount of time (typically 300 s). Afterward the thickness of the deposited layer is measured by atomic force microscope, from which the growth rate can be calculated with a typical uncertainty of 10 percent.

The data in Fig. 1(b) was obtained from hysteresis loops that are measured using a polar MOKE setup. All other measurements are performed using a Kerr microscope from Evico magnetics [164]. A Picoprobe tungsten probe tip with point diameter of 2 µm and a Keithley 2400 SourceMeter are used for current injection. The data is analysed using a MATLAB script, of which the principles are explained in Appendix D.4.

10

Controlling skyrmion bubble confinement by dipolar interactions

Large skyrmion bubbles in confined geometries of various sizes and shapes are investigated. Two fundamentally different cases are studied: (I) when there is no magnetic material present outside of the small geometries and (II) when the geometries are embedded in films with a uniform magnetization. It is found that the preferential position of the skyrmion bubbles can be controlled by the geometrical shape, which turns out to be a stronger influence than local variations in material parameters. In addition, the direction of the magnetization outside of the small geometries can be used to manipulate these preferential positions. We show by numerical calculations that the observed interactions between the skyrmion bubbles and structure edge, including the overall positioning of the bubbles, can be explained by considering dipole-dipole interactions only.[*]

10.1 Introduction

Magnetic skyrmions are whirls in the magnetization in which neighbouring spins are rotated with respect to each other with a specific chirality. They cannot be removed by continuous deformation of the magnetization without creating a singularity, which provides a topological barrier that makes them robust against

[*] This Chapter is under review at *Applied Physics Letters*. An eprint is available on arXiv [165].

annihilation. They are predicted to be less hindered by pinning sites or defects than magnetic domain walls (DWs), and their size can be in the order of nanometers. These properties make them suitable for data storage. For the envisioned skyrmion racetrack memory [68, 69, 166], the skyrmions are required to be present in small geometrically confined structures, instead of infinite sheets of material. Therefore, the interaction between skyrmions and the edge of the magnetic structure is crucial. In fact, this interaction is necessary to prevent skyrmions from being expelled from the track, it can stabilize skyrmions in absence of an external magnetic field [140, 141], assist in their formation [138, 167], and by reducing the width of the track it could be possible to reduce the size of the skyrmion and hence to achieve larger data storage densities [54].

In the research field on skyrmions, usually a distinction is made between a 'compact skyrmion' and a 'skyrmion bubble'. These objects share many properties, but the latter has typically a much larger size and has a constant magnetization at its core [54]. Numerical and experimental work on compact skyrmion confinement show that there is indeed a repulsive interaction between skyrmions and sample edges that is a result of tilting of the magnetic moments at the edge, which is caused by the Dzyaloshinskii-Moriya interaction (DMI) [38, 168]. For skyrmion bubbles, dipolar interactions are paramount in their stabilization, and because near the sample edge these stray fields will change, it is intuitively expected that the edges will influence the skyrmion bubbles via this mechanism. Though this has been realized before [135], to our knowledge it has never been studied in any detail. In this work, first we study skyrmion bubbles in confined (I) isolated circular, square and triangular geometries and explore to what extend the position of these skyrmion bubbles can be controlled by the sample shape. It is observed that the skyrmion bubbles are repelled by the structure edges and arrange themselves in configurations reflecting the symmetry of the confining geometry. Next, we study (II) these small geometries containing skyrmion bubbles when embedded in uniformly magnetized films, and show that by controlling the dipolar stray fields emanating from this uniform magnetized region, we can manipulate the position of the skyrmion bubbles. Finally, we calculate theoretically how skyrmion bubble stability changes in the vicinity of an edge due to a change in dipolar interactions and calculate the preferred positions of skyrmion bubbles in some shapes consid-

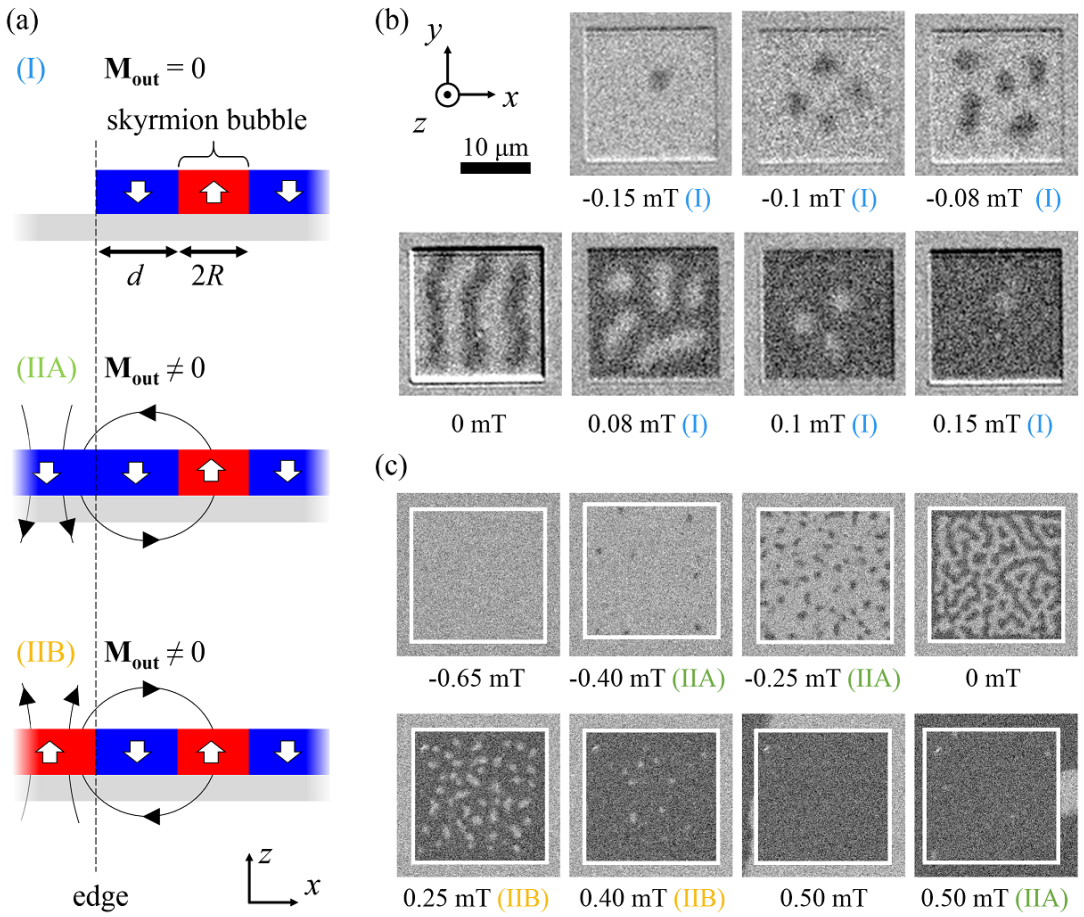

Figure 10.1: (a) Schematic representation of the three investigated edge types: I with no magnetic material outside the skyrmion containing geometry, II with the material outside the geometry magnetized (A) antiparallel to the skyrmion bubble core (B) parallel to the skyrmion bubble core. (b+c) Kerr microscope images of 20 µm wide square structures for (b) a sample created by EBL (c) a sample created by FIB. Because the edge of the FIB structure is not visible, its location is indicated by a white frame. Below each image the applied perpendicular magnetic field and the corresponding edge type are indicated.

ering dipolar interactions only. The observed behaviour matches well with these calculations, indicating that dipolar interactions are the main factor determining the positions of skyrmion bubbles with respect to edges and to each other.

10.2 Observations

A Ta (5 nm) / Pt (4 nm) / Co (t_{Co}) / Ir (4 nm) stack is used as a basis for the samples studied in this work. The two different heavy metal layers adjacent to the magnetic layer are known to induce a large interfacial Dzyaloshinskii-Moriya interation [56], which ensures that any DWs that are formed will be of the Néel type and will have a fixed chirality. By careful tuning of the Co layer thickness, t_{Co}, a balance between the DW energy and dipolar energy can be found, such that skyrmion bubbles can be stabilized using a small external magnetic field [145, 169, 170]. Skyrmion bubbles are studied in circular, triangular, and square shapes of sizes ranging from 4 µm to 20 µm. In the case of circular symmetry, no dependence on the azimuthal coordinate is expected, in contrast to the triangular and square shapes. The different structure sizes enable us to investigate up to which dimensions the edges influence the skyrmion bubbles, and down to which dimensions skyrmion bubbles can be stabilized. Here we only show the key results for a few of these structures that clearly demonstrate the investigated bubble-edge interaction. Additional results are included in Appendix E.3.

Two different fabrication processes, one based on electron beam lithography (EBL) and one based on Ga^+ focussed ion beam irradiation (FIB), are used (fabrication details are discussed in Appendix E.2). In the case of FIB we start off with a film with perpendicular magnetic anisotropy, in which no skyrmion bubbles can be stabilized. The FIB irradiation then lowers the anisotropy locally, such that skyrmion bubbles can be stabilized in the irradiated regions only. The two methods lead to two distinct situations at the edge of the structures. The EBL samples correspond to edge type (I), with no magnetic material outside the structure. The FIB samples correspond to edge type (II), with magnetic material outside of the investigated structures that has a homogeneous magnetization. In Fig. 10.1(a) schematic side views of a skyrmion bubble near the edge is shown for these different edge types.

Figure 10.1 also shows Kerr microscope images of a 20 µm wide square created (b) by EBL and (c) by FIB for various applied magnetic fields. The behaviour as a function of magnetic field is comparable for both samples: at remanence a labyrinth domain structure forms, for small fields densely packed skyrmion bubbles

occur, for increasingly larger fields only a few individual skyrmion bubbles remain, until the uniform state is reached. The skyrmion bubbles in the EBL structure have different dimensions than in the FIB structure (the average radii are 1.34 µm and 0.7 µm, respectively) and the magnetic field at which these states occur is different for the two samples, suggesting a difference in the material parameters. Additionally, bubbles are observed at $t_{\mathrm{Co}} = 0.7 \pm 0.1$ nm and $t_{\mathrm{Co}} = 0.6 \pm 0.1$ nm. Both samples show a property that is useful for our study: for the FIB sample it can be seen that at $\mu_0 H_z = 0.50$ mT the magnetization outside the irradiated structure switches. This coercive field is larger than the field for which the skyrmion bubbles are stabilized ($\mu_0 H_z \approx 0.25$ mT). This makes it possible to study the behaviour of the skyrmion bubbles both when the magnetization outside the shape points parallel and antiparallel to the magnetization at the skyrmion core. For the EBL sample the dimensions of the bubbles and stripes are comparable to the size of the structure itself, and they do not seem to be distributed randomly throughout the structure. The stripes at remanence seem to align with the edges of the structure [171], and for fields where skyrmion bubbles are stabilized, these bubbles seem to be distributed such that the space in the structure is packed optimally.

First, edge type (I) is explored by investigating the EBL sample. Observations on triangular shapes, which are highly anisotropic, of three different sizes are shown in Fig. 10.2. Because the skyrmion bubbles exhibit thermal motion, spontaneous creation and annihilation, Kerr microscope movies are used to study their temporal variation, instead of singular pictures. From these movies 100 consecutive frames are analysed, extracting the bubble positions and sizes. The system is reinitialized after every measurement. In Fig. 10.2 the positions of the skyrmion bubbles in the triangles for all 100 frames are indicated by semitransparent red dots, the size of which corresponds to the average size of a skyrmion bubble. The benefit of this representation is that if a bubble is detected at a certain spot multiple times, this spot becomes brighter red, and hence the preferential positions of the bubbles become visible.

Figure 10.2(a) shows the results for the triangle with sides of 8 µm, which is the smallest triangular structure in which we succeeded to stabilize skyrmion bubbles, at a field of 0.05 mT. Only one bubble is visible in each frame of the movie, and this

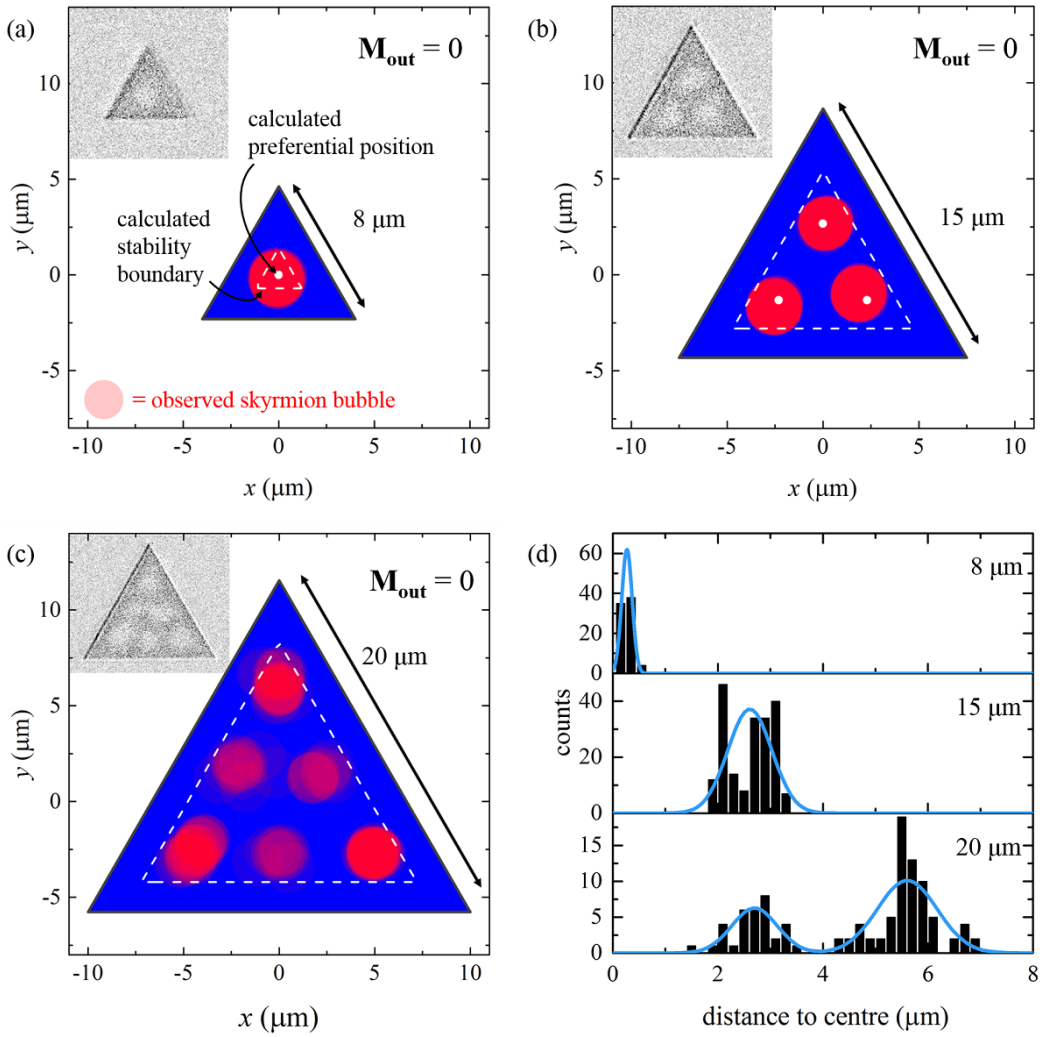

Figure 10.2: Experimentally detected positions of skyrmion bubbles in EBL-fabricated triangles with sides of (a) 8 µm (b) 15 µm (c) 20 µm in 100 frames of a 15 frames per second video. The sized of the red circles corresponds to the average bubble size. Insets show typical Kerr microscope images of the system. Dotted white lines indicate the stability region discussed in section 10.3 and white dots indicate the theoretically calculated bubble positions, which will be discussed later as well. (d) Histograms showing the number of detected skyrmion bubble as a function of the distance to the structure centre for all three triangles, together with Gaussian fits through the data.

bubble is always positioned at the centre of the triangle, as evidenced by the bright red spot. Figure 10.2(b) shows a triangle with sides of 15 µm at a field of 0.06 mT. Three preferential positions are observed, which follow the triangular symmetry of the sample structure. However, the symmetry in the measured preferential

positions is not perfect, suggesting that local variations in material parameters also influence the preferential positions. In earlier works it was found that such local variations in material parameters were dominant in determining the equilibrium positions of skyrmions [172, 173], but our results clearly indicate that the shape of the structures is the dominant influence for the magnetic structures investigated here. Last, Fig. 10.2(c) shows the results for the triangle with 20 µm wide sides at a field of 0.05 mT. Though in this case semitransparent spots dispersed throughout the structure are observed, which indicates that the skyrmion bubbles are now less strictly confined and move around more freely, six positions that are most preferred are clearly visible. In Fig. 10.2(d) these visual observations are quantified as the the number of observed skyrmion bubbles as a function of the distance between the centre of the triangle and the centre of the bubble. For the 8 µm structure, there are only counts in the close vicinity to the centre of the triangle. The small deviation from 0 can be explained either by an energy minimum due to local variation in material parameters or by the uncertainty in the detection of the structure edge during image analysis. For both the 15 µm and 20 µm triangle, the peaks in the histograms correspond to a triangular distribution, showing that the bubbles are well confined by the sample shape.

Next, the FIB sample (in particular the circle with a diameter of 8 µm) is studied under influence of a 0.25 mT field, both for the situation that the magnetization outside of the FIB structure points antiparallel (edge type (IIA)) and parallel (edge type (IIB)) to the magnetization at the core of the skyrmion bubbles. Kerr microscope movies are analysed in the same way as in the previous section and the results are plotted in Fig. 10.3(a) and (b). Because inside the structure containing the skyrmion bubbles the conditions are identical, it is remarkable that there is such a distinct difference between the preferential positions in (a) and (b). This difference is also apparent in Fig. 10.3(c), which shows histograms with the number of observations as a function of the distance to the structure edge for both the situation in (a) (green) and (b) (yellow). For situation (b) there are no observations closer than 1.9 µm from the edge, which suggests a repelling force between the skyrmion bubbles and the structure edge. The fact that in Fig. 10.3(a) there is a preferential spot in the middle of the structure that is not there in Fig. 10.3(b) suggests that the interactions between the bubbles and the edge and the inter-

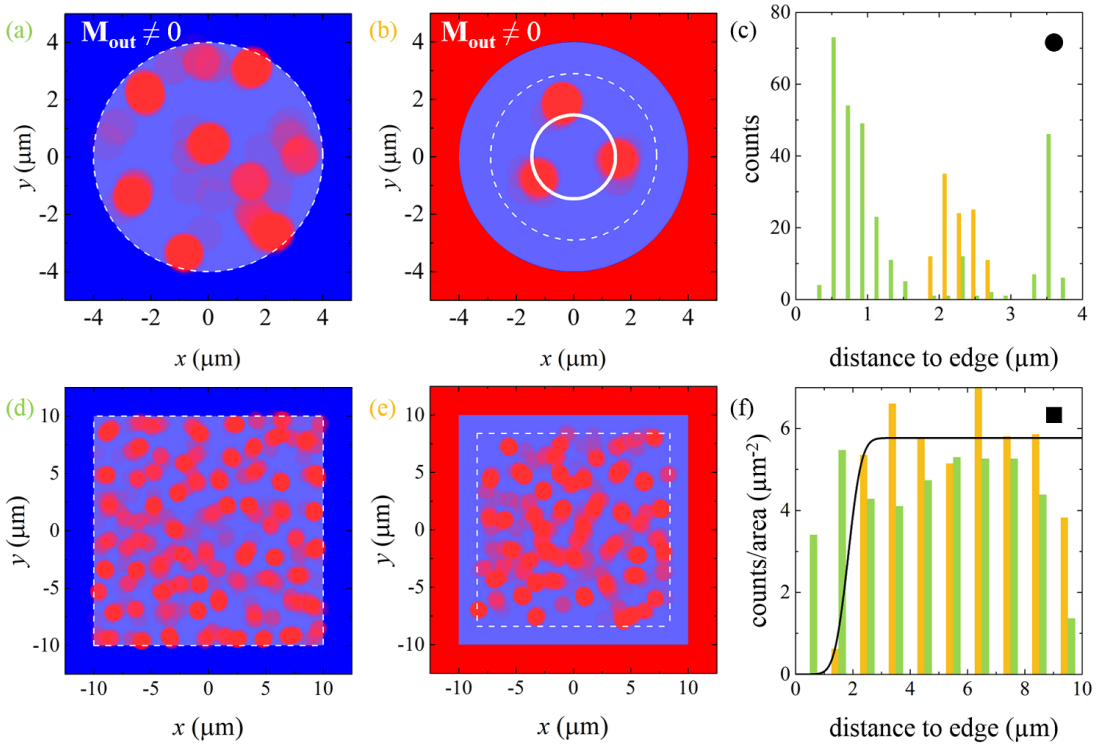

Figure 10.3: Skyrmion bubble positions detected in the FIB circle (the irradiated region is indicated by a lighter shade of blue) with a 8 µm diameter when the magnetization outside the structure points (a) antiparallel to (b) parallel to the magnetization at the core of the bubbles. We used 100 frames of a 10 frames per second Kerr microscope video. (d+e) Likewise for the 20 µm wide square. Dotted white lines indicate the stability region discussed in section 10.3, the white solid line indicates the expected bubble positions. (c) and (f) show histograms of the number of detected bubbles for the situation shown in (a (green)+b (yellow)) and (d (green)+e (yellow)), respectively.

bubble interactions are dominant over structural imperfections in determining the preferential spots. However, the data also suggests some influence of local variations in material properties, because if they were negligible the skyrmion observations would be distributed evenly along circles, because of the symmetric nature of the structure.

For the 20 µm sized squares, from which some raw images are shown in Fig. 10.1(c), the observed skyrmion positions are shown in Fig. 10.3(d) and (e), again for the situation that the magnetization outside the shape is aligned antiparallel or parallel to the cores of the skyrmions, respectively. The preferential positions seem to be distributed randomly through the FIB structure, indicating that the influence

of the structure shape is no longer of relevance for this ratio between the structure size and skyrmion bubble size. However, in the vicinity of the edge the skyrmion bubbles can clearly be controlled by the magnetization outside the structure. Figure 10.3(f) quantifies the visual observations from Fig. 10.3(d) (green) and (e) (yellow): the number of bubbles counted per unit area is plotted as a function of the distance to the structure edge. For the green bars, the counts per area are indeed approximately constant as a function of the distance to the edge. For the yellow bars this is not the case: a fit with an error function (black curve) reveals that the number of detected bubbles rapidly drops to zero around 1.8 µm away from the edge. Thus again we observe a repelling force between the skyrmion bubbles and the structure edge that can be switched on and off by controlling the magnetization direction in the surroundings of the structure.

10.3 Interpretation

We will now discuss which mechanisms could be behind the observed interaction between skyrmion bubbles and the structure edge. Strong DMI has been reported for Pt/Co/Ir samples in literature, suggesting that edge canting could play a role, just as for compact skyrmions. A problem with this interpretation for our observations is the length scale: the onset of this interaction is when the skyrmion and edge state 'touch', so typically over the distance of the DW width and edge state width. These are in the order of tens of nanometers for the material stacks used here, see Appendix E.1, while it is observed experimentally that the distance between the edge and skyrmion bubbles is in the order of micrometers. Therefore DMI-induced edge states cannot explain why our skyrmion bubbles are repelled by the structure edge.

We use a combination of the thin wall model and numerical calculations of the dipolar energy for bubbles near a sample edge to show that dipolar interactions are a plausible explanation for the observed results. The effect of a sample edge on a single bubble is calculated by simulating a single bubble in a semi infinite plane and calculating the total energy of the system as a function of the distance between the bubble and the edge. Figure 10.1(a) shows the dipolar fields that are involved for the three investigated edge types. Situation IIA shows the edge of

a FIB structure where the magnetization beyond the edge is directed opposite to the magnetization at the bubble core. The stray fields emanating from beyond the edge help stabilize the bubble, and the dipolar energy should in principle be the same as for a bubble in an infinite film. Situation IIB shows a skyrmion bubble near the edge of a FIB structure, but now with the magnetization beyond the edge pointing in opposite direction. The stray fields emanating from beyond the edge now increase the bubble energy. For edge type I, which corresponds to the the EBL samples, there is no magnetic material and hence no stray field from beyond the edge. The bubble energy is now increased with respect to the energy of a bubble in an infinite film, because the dipolar fields that lower its energy are partially missing. Figure 10.4 shows numerical calculations of how the dipolar energy varies as a function of the distance, d (also indicated in Fig. 10.1(a)) between the bubble and the edge for these three situations (see the Methods section for details on this calculation).

The stability and size of a skyrmion bubble can be calculated using the 'thin wall model' [27, 145]. Here the energy of a circular domain in an infinite film is calculated with respect to the uniformly magnetized state. The size and stability of this circular domain is determined by the balance between the Zeeman energy, the DW energy and the dipolar energy. We determine the relevant material parameters experimentally, and within the margins of error a combination can be found resulting in stabilization of skyrmion bubbles with sizes as observed by Kerr microscopy, see Appendix E.1. Note that the uncertainties in the experimental values are much larger than the range for which skyrmion bubbles can be stabilized, so this calculation is qualitative in nature. Near an edge, a bubble will experience a reduction in dipolar stray fields, which can be calculated using the thin wall model. For our material parameters, the dipolar term may be reduced by about 8 percent before the skyrmion bubble is no longer stable (see the inset in Fig. 10.4(b), where the energy minimum disappears at this reduction). From the numerical calculations in the main figure, it can now be determined at what distance to the edge the dipolar field of influence is reduced by this amount. For the FIB edge this amounts to 1.15 bubble diameter and for the EBL edge 0.58 bubble diameters. The regions in which no skyrmion bubbles should be stable are indicated by dashed white lines in Fig. 10.2 and 10.3. Indeed, there are no ob-

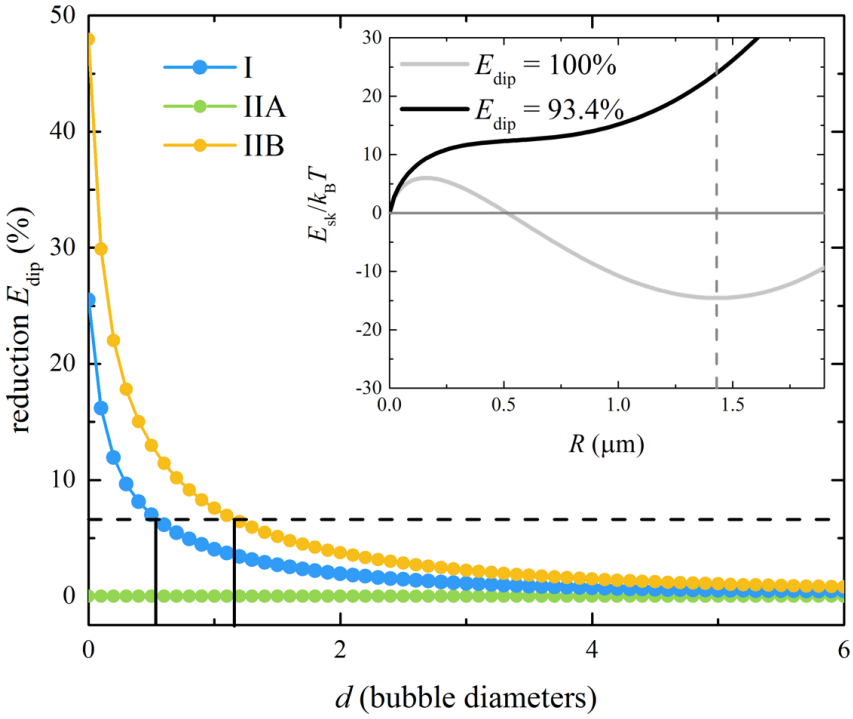

Figure 10.4: Reduction in total bubble energy with respect to the situation of a single bubble in an infinite film for the three investigated types of edges. Inset shows thin wall model calculations of the total skyrmion bubble energy, E_{sk}, as a function of its radius, R, both for standard and reduced dipolar energy contribution. Subsequently, the straight black lines indicate at what energy reduction and distance to the edge, d, skyrmion bubbles become unstable. For clarification, R and d are indicated in Fig. 10.1.

servations beyond these limits, demonstrating that dipolar interactions are likely responsible for the observed long range repulsion. Also, the same type of calculations can be used to predict the preferred skyrmion bubble positions in some of the geometries (again, see Appendix E.3 for details). These positions are indicated in white dots or lines in the data plots, and agree well with the experimentally observed bubble positions.

10.4 Conclusion and outlook

We have investigated skyrmion bubbles in confined geometries created by two different techniques, which enables us to study how the bubbles are influenced by different types of structure edges. We show that dipolar interactions are the most plausible explanation for the observed repulsion between the bubbles and the edge, which is a fundamentally different mechanism than what causes such repulsion for compact skyrmions. We have shown that ion beam irradiation can be used to confine bubbles in a novel way. The bubble-edge repulsion can be controlled by switching the magnetization outside the skyrmion-containing structures, posing exciting possibilities for future experiments and applications.

11

Summary & outlook part II

The second part of this thesis, comprising Chapter 8 to 10, focussed on magnetic skyrmion bubbles. These entities have gained major attention within the research community over the last years, due to their desirable properties for data storage technology. Several types of material stacks have been reported to host magnetic skyrmions. We studied Pt/Co/X stacks in which the Co thickness is tuned very precisely. These material stacks are similar to the ones studied in part I of this thesis, providing us with valuable prior knowledge of properties like the magnetic anisotropy, saturation magnetisation, response to ion irradiation, and DMI-related behaviour. First, we have shown that we can reproducibly produce samples in which skyrmion bubbles are stabilized. Two attributes specific for skyrmions and skyrmion bubbles are investigated: their current-induced motion and their interaction with physical sample edges.

In Chapter 9, current-induced behaviour is investigated. Though we study micrometre sized skyrmion bubbles, their current-induced behaviour is predicted to be the same as for compact skyrmions, because of their topological similarity. We do observe an extremely low critical current density required to initiate skyrmion bubble motion, as predicted. The direction of motion is always along the direction of the current flow, so the skyrmion Hall effect is not observed. Surprisingly, reversing the direction of the spin current injected by the SHE, does not lead to a reversal of the direction of skyrmion bubble motion. This is in contrast to other experimental reports, in which the SHE is identified as the main driving mechanism for their skyrmions, and sometimes even presented as proof of their chiral nature. We explore alternative mechanisms for the observed motion, and based on our experiments, surprisingly a 'negative' spin-transfer torque from the cur-

rent flowing through the magnetic layer is the most likely explanation. However, though many additional experiments are performed in order to elucidate our findings (see Appendix D), drawing a definitive conclusion on the mechanism behind our observations would be premature. Future experiments should therefore first rule out that the observed motion is driven by the SHE with certainty. These experiments should include an additional measurement of the DMI (preferably via an other method than the one used in Appendix D) to exclude an unexpected change of sign in D. Also, a direct measurement of either the spin Hall angle from the top and bottom Pt layer as a function of layer thickness or the total spin-orbit torque for all investigated layer thickness combinations would be highly desirable. Further, additional evidence for the existence of a negative STT in our material stack should be obtained. Following the work that unambiguously demonstrated that such a torque affects a DW in a similar material stack, this can be achieved by determining the spin polarization in our samples by GMR measurements in a current perpendicular to the plane geometry.

In Chapter 10 we focus on confining the skyrmion bubbles to small geometrical shapes. From simulations, compact skyrmions are known to be repelled by the physical edge of a sample, because of the DMI-induced canted magnetic state at the edge. However, our skyrmion bubbles turn out to always keep a distance of at least 1 µm from the edge, and repulsion over such a large distance cannot be explained by the same mechanism. We show that dipolar stray fields are the most likely explanation for our observations. The preferential positions of skyrmion bubbles calculated based on dipolar interactions only, matches the experimental data well. Next, we fabricated a sample starting from a film that is uniformly and perpendicularly magnetized. Subsequently, FIB is used to locally reduce the magnetic anisotropy and hence create conditions in which skyrmion bubbles can be stabilized. We demonstrate that skyrmion bubbles can indeed be stabilized in samples fabricated via this approach. An essential difference with the earlier samples is that the small geometries containing the skyrmion bubbles are now imbedded in a magnetic film. By independently controlling the magnetization outside the skyrmion-containing geometries, it can be selected whether or not the skyrmion bubbles are repelled from the edge by dipolar stray fields. Our results regarding the FIB-fabricated samples yield new possibilities in device design. A next step in

this line of research would be to use FIB to stabilize compact skyrmions, that are technologically more relevant. In order to achieve this, we should switch to a material stack more suitable for hosting compact skyrmions, for instance multilayers with many repeats. Characterizing the anisotropy and DMI as a function of the irradiation dose for multiple layer thicknesses and repeats will be a considerable task, but would be an important contribution to this field of research.

A

Experimental methods

Due to the experimental nature of the work presented in this thesis, tools for sample fabrication and measuring equipment are essential. The experimental methods that we use are well-established: sputter deposition for the growth of ultrathin metallic layers, electron beam lithography (EBL) for lateral patterning and device fabrication, focussed ion beam irradiation (FIB) for local manipulation of the material properties, and magneto optical Kerr effect (MOKE) microscopy for the imaging of magnetic domains. Each of these techniques is introduced in this appendix: both the basic principles behind the technique and the specifics for our particular experiments are discussed.

A.1 Sputter deposition

In this section, the procedure we follow to create our thin film samples is described. The procedure involves several cleaning steps, but the essential step is the actual growth of the thin layers. For this, we employ a technique called *sputtering* [174], which is widely used to controllably and reproducibly deposit layers with a sub-nanometer thickness control.

For all samples, a substrate of Si capped with a 100 nm thick layer of thermally oxidized SiO_2 is used. First, the substrate is thoroughly cleaned: it is immersed subsequently into beakers containing ammonia, acetone and isopropanol, and each beaker is put into an ultrasonic bath for several minutes. After this, the substrate

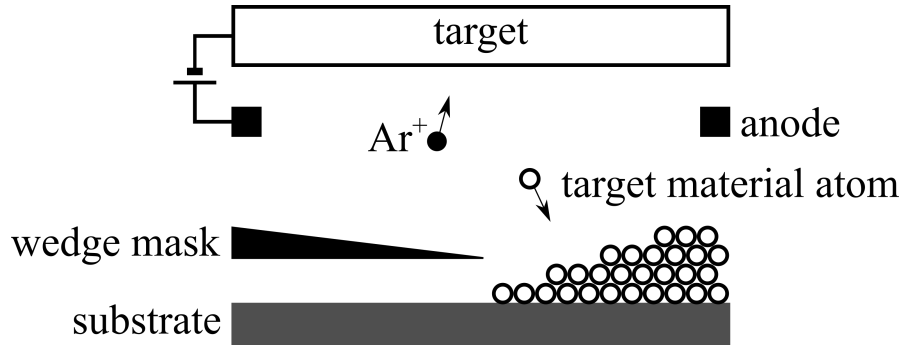

Figure A.1: Schematic view of the inside of a sputter deposition facility.

is loaded into the deposition facility *, in which an ultra high vacuum is maintained (typically the base pressure is in the order of 10^{-8} mbar). Inside the facility, the substrate is subjected to an oxygen plasma inside a separate, dedicated oxidation chamber for 10 minutes in order to burn away any residual chemicals from the previous cleaning step.

After this, the sample is transported to the deposition chamber and positioned beneath a target consisting of the desired material. Then the actual deposition can start, as schematically depicted in Fig. A.1. Argon gas is lead into the deposition chamber, increasing the pressure to $\sim 10^{-2}$ mbar, and is ionized by a voltage applied between the target and an anode ring. The Ar^+ ions are accelerated towards the target and knock out material fragments. This material condenses on the substrate with a growth rate of typically $0.1\,\mathrm{nm\,s^{-1}}$, allowing for the growth of ultrathin layers with sub-nanometer thickness control.

There are several parameters affecting the material growth: the argon pressure during deposition, the distance between material and substrate, and the power used to sustain the argon plasma. These parameters do not only influence the growth rate, but also the quality of the interfaces between layers of different material. This in turn influences the strength of the magnetic anisotropy and DMI, which is exploited in Chapter 5. Further, for some experiments, for instance those presented in Chapter 9, films of varying thickness instead of constant thickness

*Two facilities are available, the *Caruso* and the *NanoFilm* [175]. At the end of each chapter it is indicated in the method section which of these is used for that project. The working principle of the two facilities is the same, but the Nanofilm rotates the sample during deposition and has the sample positioned above the target instead of below it.

are desired. For this, the so-called wedge mask is used: a sharp piece of metal, positioned close to the sample surface, which can be set to gradually (un)cover the substrate during deposition. The sputter deposition facility offers various other options (other masks, or the possibility to co-sputter materials), but these are not used for the work presented in this thesis.

A.2 Electron beam lithography

Often a more complex device is necessary for an experiment instead of a homogeneous film. A flexible and high-resolution technique for lateral patterning is electron beam lithography (EBL). For this technique the sample is coated with a resist on which the desired pattern is subsequently written by an electron beam (e-beam).

For the samples presented in Chapter 3, 4, 5, and 9 polymethyl methacrylate (PMMA) is used as a positive resist, meaning that the resist becomes more soluble after irradiation with the e-beam. PMMA consists of long polymer chains, which break when exposed to the e-beam. We use a bilayer of PMMA: the bottom layer consists of chains of 495 000 monomers on average, while the top layer has chains of 950 000 repetitions. These layers are affected slightly different by the e-beam, leading to the formation of an overhanging structure. The creation of this overhang is intentional, as it should results in a better quality of the edge of the final structure. Both layers of resist are put onto the substrate by spin coating: the liquid disperses over the surface while the sample is rotated at 3000 rotations per minute for 60 seconds. After this, the sample is place on a 150 °C hotplate for 1 minute to evaporate the solvent (in our case anisole). For the writing step with the e-beam a *FEI Nova dualbeam* system is used [176], with a beam energy of 30 keV and a dose of 250 $\mu C\,cm^{-2}$. Subsequently, the sample is immersed into a developer, a (1:3) MIBK IPA mixture, for 45 seconds to remove the exposed parts of the resist. After deposition of the desired material stack, the remaining resist is removed using acetone (lift off). The whole process is schematically depicted in Fig. A.2(a).

In Chapter 10, we focus on the interaction between skyrmion bubbles and the lithographical edge of a structure. For this study, the quality of the edge is of

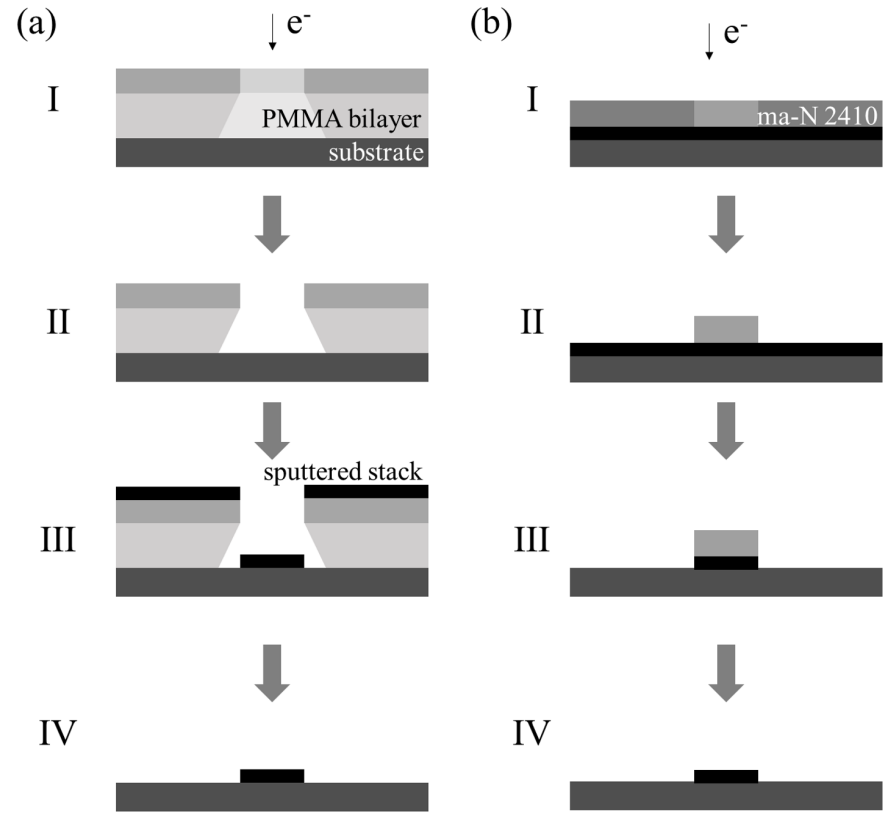

Figure A.2: (a) Lithography procedure using a positive resist: I e-beam exposure, II development, III material stack deposition, and IV lift-off. (b) Lithography procedure using a negative resist: I e-beam exposure, II development, III ion beam milling, and IV resist removal.

utmost importance, and an alternative fabrication procedure is followed to ensure this quality. The structures are now created using the negative resist ma-N 2410 and the dedicated EBL facitlity *Raith EBPG 5150* [177]. During this procedure, the substrate is first fully covered with the desired material stack by sputter deposition. Then the resist is spin coated on top of the material stack at 3000 rotations per minute for 30 seconds. The sample is then baked at a hot plate at 90 °C for 2.5 minutes. A beam energy of 100 keV and a dose of 400 µC cm^{-2} are used during the e-beam exposure. The sample is then submersed into the developer ma-D 332s for 80 seconds, resulting in the removal of only the unexposed resist. Subsequently, all the sputter deposited material that is not covered with resist anymore is removed by ion beam milling. A *Roth & Rau Ion Beam Etcher* is used for

this procedure [178]. Lastly, the remaining resist is removed with acetone. This process is schematically depicted in Fig. A.2(b).

A.3 Focused ion beam irradiation

Focused ion beam irradiation (FIB) can be used to locally mill away material, or to locally deposit material when used in the presence of specific precursor gasses [179]. In this work, only small doses of ions are used, such that no material is removed, but the structure of the material is altered. In ultrathin magnetic layer stacks, interactions at the interfaces determine certain material properties, in particular the perpendicular magnetic anisotropy and the DMI. The effect of FIB on the DMI unexplored, but the anisotropy is known to change because of the induced intermixing at the interfaces and release of tensile stress [26, 73, 180].

The FIB employed in this work is part of a *FEI Nova dualbeam* system in which gallium ions with an energy of 30 keV are used [176]. In Chapter 3 and 4 parts of the lithographically created magnetic strips are irradiated with ions, hence decreasing the anisotropy locally. In Chapter 10 FIB is used to locally create a delicate balance of material parameters suitable for skyrmion bubble stabilization.

A.4 Kerr microscopy

All experiments presented in this thesis are based on the optical detection and visualization of the magnetic state. Other techniques, like vibrating sample magnetometry [181], giant magnetoresistance measurements [7], and object oriented micromagnetic framework simulations [182], are sporadically used in support of the main measurements. Background on these techniques can be found in the referenced literature, but in this section we will exclusively discuss our primary measurement technique: Kerr microscopy.

Throughout this thesis several schematic images have been shown visualizing magnetic structures by arrows or colour coding. This is done to conveniently illustrate certain principles, but in reality magnetism cannot be 'seen'. Fortunately, there is an interaction between light and magnetic materials, enabling us to visualize magnetic domains directly, which is the topic of this section.

In 1845 Michael Faraday demonstrated the existence of an interaction between light and magnetism for the first time: the polarization plane of light traveling through a medium was rotated by an angle depending on the strength of the applied magnetic field. Later, in 1877, John Kerr discovered an intimately related effect: a change in polarization of light reflected off a magnetic pole. This last effect was named the magneto optical Kerr effect (MOKE) and can be exploited to probe the magnetization in thin films (as the ones studied in this thesis) optically, which is illustrated in Fig. A.3(a). If a beam of light is passed through a polarizer, no light will be able to pass through a second, crossed polarizer (commonly referred to as an analyser). However, if the the light reflects from a magnetic surface before reaching the analyser, it will have a slight change in rotation, allowing some light to pass through. Therefore, the light intensity measured after the analyser is a qualitative measure for the magnetization of the probed surface. Because of the simplicity of this technique, and because of its flexibility (any desired component of the magnetization can be probed, by choosing the appropriate angle of incidence) it has been widely used in studies on magnetic thin films.

We will now describe the physics behind MOKE, but for a more formal and detailed treatment the reader is referred to Ref. [183]. The optical properties of a material follow from its dielectric tensor, which in turn follows from the motion of its electrons. In order for the magnetization to be revealed by light, it should therefore influence the motion of the electrons in the material. This influence indeed exists in the form of spin-orbit coupling, which couples the spin of an electron to its orbital motion. Spin-orbit coupling is the microscopic origin of MOKE, and quantum theory is necessary to describe this correctly. However, considering the classical motion of electrons and treating the magnetization as an effective field experienced by the electrons provides a more intuitive description.

The light that reaches the material surface is linearly polarized, which can be seen as a superposition of right-handed and left-handed circularly polarized light. When light travels through a medium, the electrons there will follow the electric field of the light. The right- and left-handed components will both force the electrons to move in circles, though in the opposite direction. When the material has a magnetization, which we treat as an effective magnetic field, the electrons now experience a Lorentz force, making the electrons with the one sense of rotation

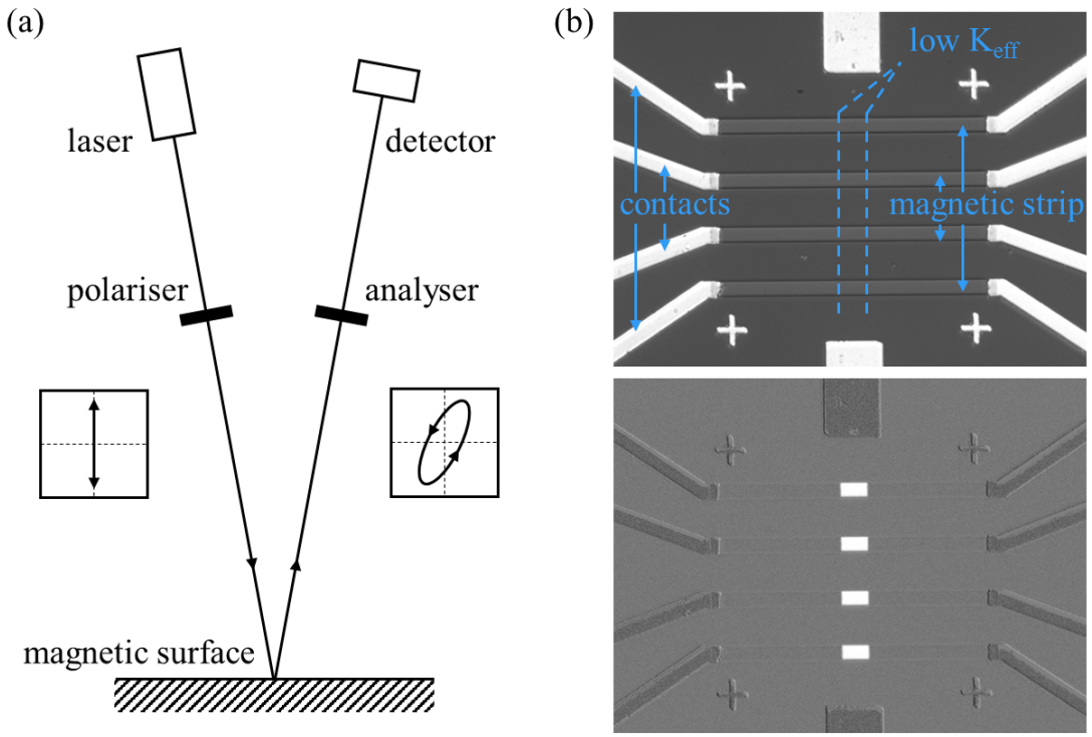

Figure A.3: (a) The magneto optical Kerr effect: light undergoes a change in rotation and ellipticity when reflected of a magnetic surface. (b) Example of a Kerr microscope image of four magnetic strips containing a low anisotropy region where a reversed domain can be nucleated controllably. After background subtraction (bottom image) these domains become clearly visible.

move in circles with a larger radius, while for the other sense of rotation that radius will be decreased. These different radii correspond to different electric dipole moments, and hence different dielectric constants. The final result is a reflected beam with a changed polarization and elipticity.

Up to now, a single beam of light has been discussed, which is adequate to probe the magnetization, but not to 'see' magnetic domains on the sample. This visualization can be achieved by equipping an optical microscope with additional components for polarization analysis. Such an apparatus is referred to as a Kerr microscope, and for the measurements presented in this thesis a model from *Evico magnetics* is used [164]. The light is collected by a CCD camera and in the resulting image the various magnetic domains can recognized by an additional intensity in the image. In the setup it is possible to apply magnetic fields in all desired di-

rections up to strengths of ~ 50 mT and send electrical currents through a sample. The time resolution is limited by the CCD camera, and typically 16 frames per second can be recorded. A sub-micrometer spacial resolution can be reached. Fig. A.3(b) shows an example of an image obtained by Kerr microscopy. It shows four contacted magnetic strips in which the middle parts are irradiated and have their magnetization pointing in an other direction than the pristine parts of the strips. In the bottom image a background image taken at saturation is subtracted, and the additional contrast between the magnetic domains induced by MOKE becomes apparent.

B

Supplementary information on Chapter 4

B.1 Analysis procedure

Converting the Kerr microscope data in the experiments presented in Chapter 4 to DW positions is not trivial. In this section this analysis procedure is discussed in detail.

The Kerr intensity is measured along the 70 µm long, 1 µm wide strips by dividing them into 70 adjacent 1 µm long (or 100 adjacent 0.7 µm long) regions of interest (ROI)*, see Fig. B.1(a). Next, it is determined in which ROIs the magnetization points up and in which it points down. Due to the random creation of domains during the nucleation step, this cannot be done by simply checking whether the Kerr intensity is above or below the average value. The up and down domains are not necessarily equal in size, or the strip may even be entirely up (or down). To solve this, a histogram of the intensity measured in the different ROIs is made. This is fitted with a mixture of two normal distributions see Fig. B.1(b). If the difference in the central value of the two normals exceeds a certain empirically chosen value, and both normals contribute at least 3 percent to the total fit function, we conclude that both up and down domains are present. Whether a certain ROI is up or down is determined by checking whether its intensity is above or below the average of the two normal central values.

The DW positions along the strip after every field step have now been identified.

*For smaller regions of interest the signal to noise ratio becomes unworkable small.

However, it is not trivial which DWs observed at different steps correspond to each other. We cannot simply say that the most left DW after the nucleation step is the same as the most left DW after the first propagation step. This is because DWs can disappear when they reach the end of the strip, DWs can annihilate when an UD and an DU wall meet, and new domains can be nucleated if large H_z fields are used. In our analysis, we start with a DW in the initial configuration, and then assume after a cycle that the DW that is closest by and of the same type (an UD wall cannot be changed to an DU wall) is that same DW. This solves the mentioned problems in most cases, as shown in Fig. B.1(c), but can still lead to a some errors, especially when large magnetic fields are used.

Now we have data on how the individual DWs move through the strip in time. To analyse the performance of the device, it should be determined whether a DW stays pinned when it is supposed to and whether it is propagated when it is supposed to. The locations of the anisotropy barriers are known as they are purposely constructed during the sample fabrication. For every propagation step, the closest barrier to the DW is identified, and in the next step it is checked whether the DW has past this barrier or not. There is no additional inspection of whether a DW has passed one barrier or more. This is no problem at the moment, but should be addressed in a later stage of the development of the device. If multiple barriers are passed within one cycle the device still functions, but the space required to store one bit of information increases, which is undesirable for data storage applications.

Last, the Kerr microscope measurements take several hours, so a small drift in the sample position can occur. Therefore the first and last ROI sometimes come to cover not only the magnetic strip, but also (partially) the substrate, for which the measured intensity is completely different. For the software, this resembles a DW that stays at the same position throughout all cycles, which changes the measured pinning/depinning probability. Therefore the first and last ROI are not included in the analysis.

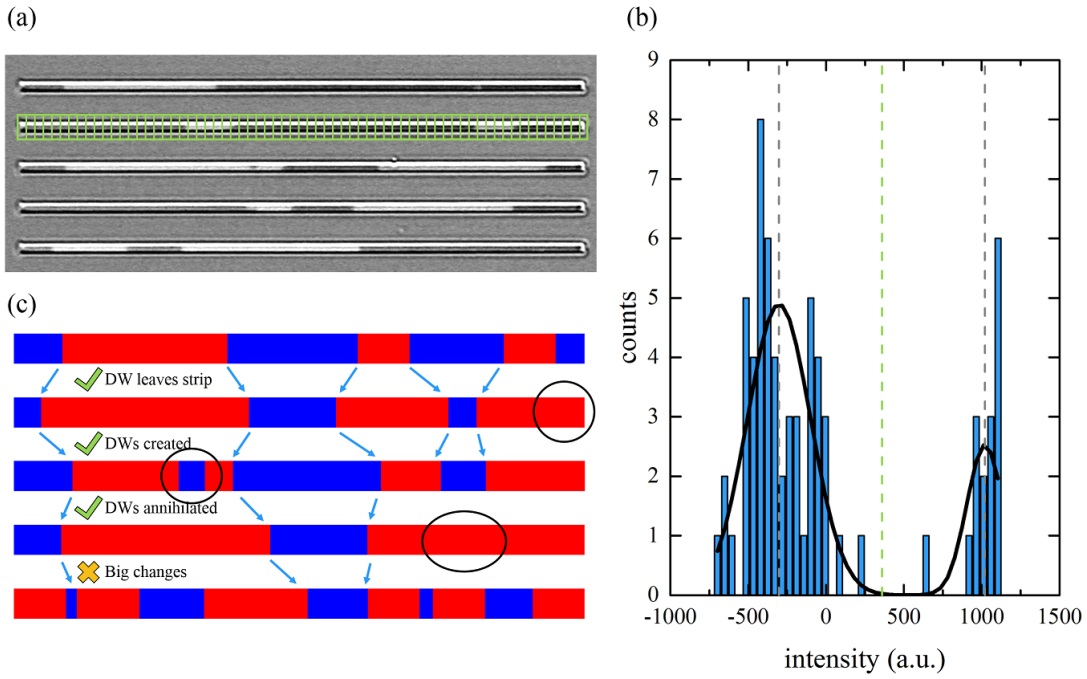

Figure B.1: Extracting DW positions and displacements from Kerr microscope images. (a) Typical Kerr microscope image of 5 devices with several DWs. The strips are divided into small regions of interest (ROI), typically 1.0 µm or 0.7 µm wide, as is schematically shown for the second strip. (b) For each ROI the intensity is measured and a histogram can be made of how often certain ranges of intensities occur. This is fitted with a mix of two normal distributions such that the average values corresponding to up and down domains (grey dashed lines) can be identified. The mean of these two (green dashed line) can be used to select which ROIs are identified as up and down. (c) Schematic example of how the software follows DWs through different cycles. In most cases, creation and annihilation of DWs or DWs moving to the edge of the strip do not cause problems. When large fields are used and many of these events occur within one cycle the process becomes unreliable.

B.2 Influence of irradiation on Pt/Co/Ir

In Chapter 4 it was observed that a Pt/Co/Ir strip could show directional DW motion using our propagation scheme, even without anisotropy barriers engineered by ion irradiation. In this section, the influence of additional ion irradiation on the functionality of this device is investigated.

One difference between the Pt/Co/Pt and Pt/Co/Ir samples is the thickness of the Co layer; for Pt/Co/Pt a thickness of 0.6 nm was used, while for Pt/Co/Ir a

thickness of 0.8 nm was used. The choice for 0.6 nm in Pt/Co/Pt was a practical one, as for this particular material stack measurements of the anisotropy as a function of the ion irradiation dose were already available. On the choice for 0.8 nm in Pt/Co/Ir, we will elaborate here, as the behaviour of this material stack is central in this section.

The main motivation for the study of Pt/Co/Ir is to see how the devices behave if the DMI is large. Because the DMI in these samples is an interfacial effect, its energy contribution per area of a DW becomes larger for thinner layers, so making the Co layer as thin as possible would be preferable. It turns out that, for samples grown in our sputtering facility, the range of thicknesses for which a sample has PMA is different for Pt/Co/Pt and Pt/Co/Ir; for Pt/Co/Ir the minimum Co thickness to obtain PMA is larger. We speculate that this is related to the formation of a magnetically dead layer. Within the range where Pt/Co/Ir shows PMA, the smallest Co thickness is chosen, but at a safe interval from the transition where the PMA disappears. This interval is required to still have PMA after ion irradiation.

Domain-wall motion in Pt/Co/Pt films grown in our sputtering facility was extensively studied before [46], whereas in Pt/Co/Ir it was not. Therefore first DW velocity, v, measurements as a function of H_z are performed in absence of any in-plane field. Both a pristine strip and a homogenously irradiated strip (dose $0.2\,\mu\mathrm{C\,cm^{-2}}$) are investigated. In Fig. B.2 the natural logarithm of the measured velocity is plotted against $\mu_0 H_z^{-1/4}$. This results in a straight line (for both the pristine sample, Fig. B.2(a) and the irradiated sample, Fig. B.2(b)) indicating that the DW motion follows the creep law, $v = v_0 \exp\left(-\chi(\mu_0 H_z)^{-1/4}\right)$. In this equation v_0 is the characteristic speed and χ is a scaling constant. The results are similar as for Pt/Co/Pt, which also shows creep behaviour for the field strengths used in this experiment. Interestingly, there is no significant difference between the fit parameters obtained for the pristine sample ($\chi = -5.6 \pm 0.2$, $\ln v_0 = 13.4 \pm 0.5$) and the homogeneously irradiated sample ($\chi = -5.6 \pm 0.3$, $\ln v_0 = 13 \pm 1$), implying that the DW motion is not affected by the irradiation.

Next the data shown in Fig. 4.3(e+f) is analysed further by examining the pinning and propagation chances separately instead of the total success chance. Figure

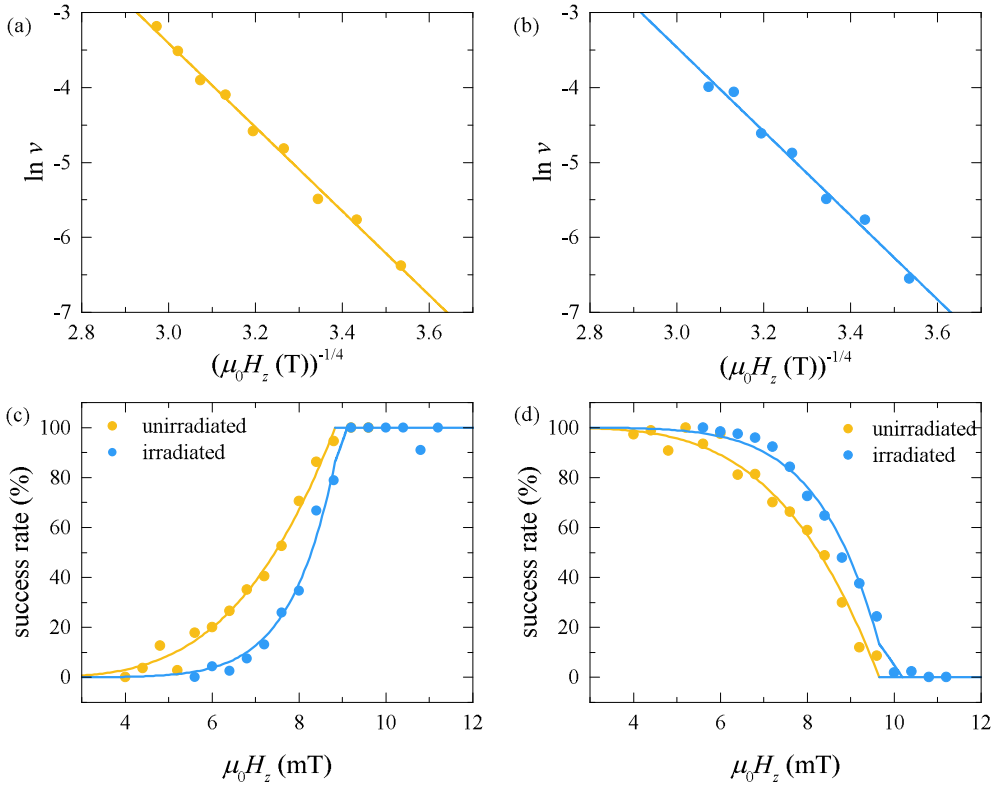

Figure B.2: Investigation of the influence of irradiation on Pt/Co/Ir samples. Velocity versus $\mu_0 H_z$ measurement of an (a) unirradiated Pt/Co/Ir strip (b) homogeneously irradiated Pt/Co/Ir strip using a dose of $0.2\,\mu\mathrm{C\,cm^{-2}}$. Quantities on the axes are chosen such that behaviour according to the creep law results in a linear relation. Points indicate the measured values, the line shows a linear fit. Chance that a DW (c) moves when it is supposed to move (d) stays pinned when it is supposed to stay pinned as a function of $\mu_0 H_z$, with an in-plane field strength of 50 mT. The yellow points are measurements on an unirradiated strip, the blue points on a strip with an anisotropy profile created by irradiation. Curves are fits using the model described in the text.

B.2(c) shows the chance that a DW moves over the closest barrier when it is supposed to. Figure B.2(d) shows the chance that chance that a DW does not move over the barrier when it is supposed to remain pinned. Data for both an unirradiated sample (yellow points) and a sample with a block-shaped anisotropy profile created by irradiation (blue points) are shown. First, an expectation for the pinning chance as a function of H_z for the unirradiated strips is formulated. Because there are no anisotropy barriers, the success chance simply is computed by checking whether the DW passes the point where there would be a barrier in an irradiated sample. We assume that the distance between a DW and the

nearest barrier it has to pass is a random distance between 0 and 4 µm (because the distance between two neighbouring barriers is 4 µm). The used pulse duration is 500 µs (though the effective time will be less, because of the finite rise time), so the measured propagation chance should be proportional to the DW velocity (which dependence on H_z as given by the creep law), until a velocity is reached for which more than 4 µm is travelled during one pulse. Fits using this model are shown in Fig. B.2(c+d) as the yellow curves.

For the sample in which a block-shaped anisotropy profile is created by irradiation, this model describes the data less accurately (fit is not shown). This is because besides the chance that the DW reaches the barrier, now there is also a chance that the DW cannot overcome the barrier, which is not yet taken into account. The model is now improved in the following way: we assume that the chance, p, that the anisotropy barrier is overcome follows an Arrhenius law, $p = p_0 \exp(-\frac{E_\mathrm{b}}{k_\mathrm{B}T})$ [184]. Here p_0 is a parameter related to the attempt frequency and E_b is the height of the energy barrier. Now the chance that a DW moves past the barrier is a product of the chance that the barrier is reached and and the chance that the barrier is overcome. For the first contribution, the χ and $\ln v_0$ from the unirradiated sample can be used, because the study of the homogeneous irradiated strip showed that the irradiation did not chance these values significantly. For the chance that the barrier is overcome p_0 and E_b are left as fit parameters. Examples of fits with this product of these two probabilities is shown in Fig. B.2(c+d) as the blue curves. This improved model now turns out to be able to describe the measured points satisfactorily.

Please note that the analysis presented here is specific for the case in which the initial positions of the DWs are random. This is indeed the case in the experiments presented in the Chapter 4, but one could envision that in future devices it would be desirable to controllably write domains at a specific location. In that case, the chance that a DW reaches a pinning barrier is no longer given by $(velocity \times pulse\,time)/4\,\mu\mathrm{m} \times 100\%$ and the analysis would have to be reworked. However, as this is not applicable for the experiments shown in this work, an alternative analysis is beyond the scope of this work and will not be given here.

When comparing the data of the unirradiated and the irradiated samples in Fig.

B.2(c) and (d) two differences stand out. First, the H_z field at which a DW moves (or fails to pin) is shifted towards higher values for the irradiated samples. This is expected, because the introduction of anisotropy barriers makes it more difficult for the DWs to move and this result is in agreement with Fig. 4.4. The other difference is that the transition from pinning to moving is less gradual in the irradiated sample. This makes it possible to reach a higher total success rate, which explains the difference between Fig. 4.3(e) and (f). In conclusion, the irradiation on the Pt/Co/Ir does not create an additional asymmetry with in-plane field due to an asymmetry in the depinning field, but it influences the success rate by making the transition from pinning to moving more abrupt.

B.3 OOMMF results

One advantage of our device concept is that the DWs can be located at discrete positions, namely the anisotropy barriers, but this is not trivial. DWs that are pinned end up at a barrier, but the ones that are moved can end up at any position, depending on the duration of the field pulse. This problem can be solved by pulsing the H_x instead of the H_z field. This way the DWs can only depin during the short H_x pulse, but they will keep moving (driven by H_z) until they reach the next anisotropy barrier. Using our setup this would be a tedious experiment, as the coil used to generate the H_z field is integrated in the sample stage. If this field is not pulsed but applied continuously, heating causes the sample stage to expand and bring the sample out of the focus of the microscope. So instead we investigate this alternative scheme by object oriented micromagnetic framework (OOMMF) simulations [182]. Also, OOMMF simulations enable us to study the DW motion in the absence of random pinning sites or thermal fluctuations. This means that the DW motion in the simulations is in the flow regime per definition, allowing us to investigate the device concept also in this regime. Last, the simulations make it possible to study the device on time and length scales that are not accessible in our proof-of-principle experimental setup.

The cell size in the simulations is chosen to be 4×4 nm; simulations with larger cell sizes would be unreliable because the cell size would then exceed the typical DW width. The geometry is a 2100 nm long, 156 nm wide and 1 nm thick strip, with

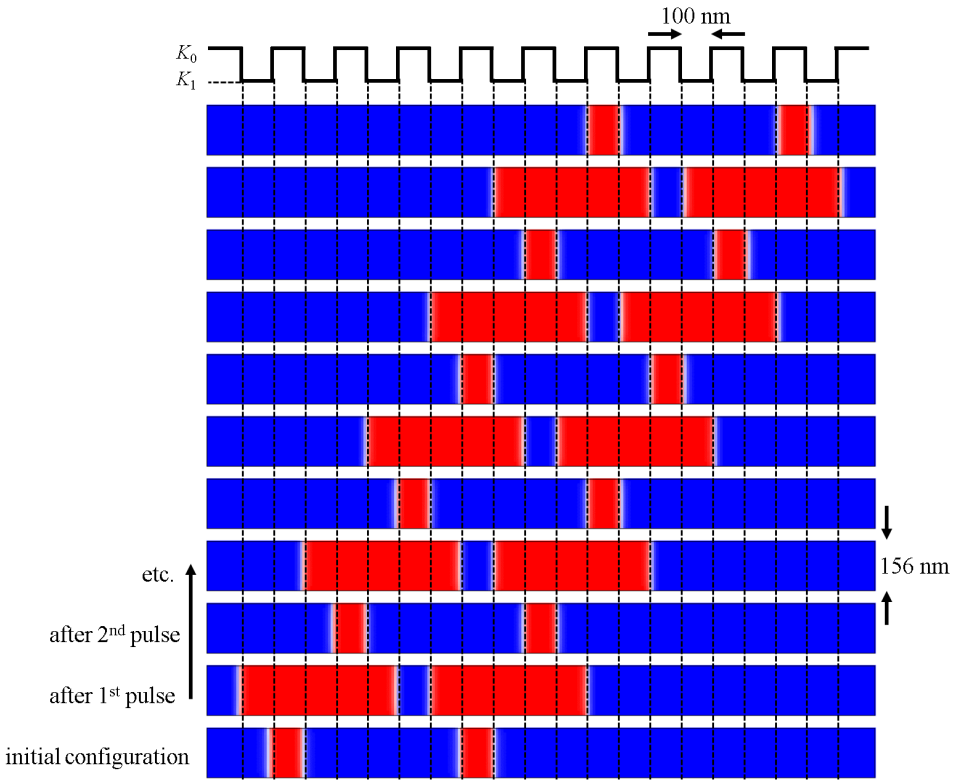

Figure B.3: Magnetic configurations obtained by OOMMF simulations. The bottom picture shows the initial configuration, configurations after subsequent field pulses are shown from bottom to top. The schematic block profile shows the anisotropy variation along the strip.

regions of lower anisotropy that are 100 nm wide and 100 nm separated from each other. This is considerably smaller than the experimental strips (70 µm long) and this decided both to reduce computing time and to explore these small dimensions that are more interesting for applications. The material parameters used are $M_S = 1.4 \times 10^6\,\mathrm{A\,m^{-1}}$ (bulk value for Co), $K_{\mathrm{eff}} = 1.5 \times 10^6\,\mathrm{J\,m^{-3}}$, $A = 1.6 \times 10^{-11}$ $\mathrm{J\,m^{-1}}$, $D = 0.2\,\mathrm{mJ\,m^{-2}}$, and in the irradiated regions K and D are reduced by 10% and 100%, respectively. In preparatory simulations, in which the depinning field was determined, also other parameters were investigated. The anisotropy in in the irradiated area was reduced by 5, 10, 15 and 20 percent. The DMI constant of the pristine region was set to $0\,\mathrm{mJ\,m^{-2}}$, $0.2\,\mathrm{mJ\,m^{-2}}$ or $0.5\,\mathrm{mJ\,m^{-2}}$, which are moderate value in order to mimic our symmetric Pt/Co/Pt stack. Also, reductions of the DMI of 0, 15 and 100 percent in the irradiated region were investigated. Which of

these is most realistic is unclear at this moment, and further experimental studies are required to clear this up. In almost all cases a difference between the depinning field of UD and DU walls could be created using an in-plane magnetic field, the exceptions are simulations in which there is no DMI in both the pristine and irradiated regions. We take one typical combination of parameters to show that this difference can be used to create unidirectional DW motion in the simulation. To investigate a large parameter space and create a phase diagram is beyond the scope of this paper.

During one propagation step a magnetic field $\mu_0 H_z = 45\,\mathrm{mT}$ is applied for 7 ns, during which a magnetic field pulse $\mu_0 H_x = 50\,\mathrm{mT}$ is applied for 2 ns. Figure B.3 shows the evolution of the magnetic domain structure together with the anisotropy profile. The DW motion is 100% reliable in these pinning- and noise-free simulations. Also note that the DWs now always end up at the anisotropy transitions after each step, as is desired. This result shows the working principle of the device using H_x pulses, and shows the theoretical possibility of operating these devices in the flow regime of DW motion.

C

Supplementary information on Chapter 5

C.1 Deposition conditions

The material stack studied in this work is deposited using DC sputter deposition, a technique that provides various parameters (e.g. distance between substrate and target, deposition pressure, and magnetron power) that can be tuned to change the deposition rate and quality. In previous work, it has been shown that the interface quality, and hence the anisotropy and DMI, can be controlled by varying the argon pressure during the deposition of the Pt layers [46]. We have taken deposition parameters from that work and used the same deposition facility, in order to obtain the desired material parameters. In particular, the bottom Pt layer is deposited at an Ar pressure of 0.29 Pa, and the top Pt layer at 1.12 Pa, which is expected to lead a large asymmetry in DW velocity under the influence of an in-plane field and an effective anisotropy constant of K_{eff}, of 1.3 MJ m^{-3}. We have also investigated two other growth pressure combinations for which a smaller anisotropy constant was reported (not shown here), but for these samples the field range for which a DW could be studied was more limited, because nucleation of inverted domains occurs more easily.

C.2 Fit functions

To describe the measured DW velocity, v, versus H_z curves, we use functions that have been derived in literature [97, 98]. For the creep regime, we use

$$v(H_z, T) = v(H_\mathrm{d}, T) \exp\left(-\frac{\Delta E}{k_\mathrm{B} T}\right) \tag{C.1}$$

with

$$\Delta E = k_\mathrm{B} T_\mathrm{d} \left(\left(\frac{H_z}{H_\mathrm{d}} \right)^{\mu} - 1 \right), \tag{C.2}$$

where T is the temperature, H_d the depinning field, k_B the Boltzmann constant, T_d the depinning temperature, and μ is the universal creep exponent.

For the depinning regime we use

$$v(H_z, T \ll T_\mathrm{d}) = v_H \left(\frac{H_z - H_\mathrm{d}}{H_\mathrm{d}} \right)^{\beta}, \tag{C.3}$$

where v_H is the depinning velocity and β is the depinning exponent.

C.3 Derivation of domain wall curvature as a function of field

In literature it is described how the competition between the gain in Zeeman energy and the cost of increasing the domain wall (DW) length results in a circle arc shaped domain expansion when a DW reaches a Hall cross and is pinned there [101]. Also it has been reported that for DW motion in a strip, edge roughness leads to DW pinning caused by the same mechanism [102]. Here we extend this model to describe how the radius of the circle arc that a DW forms when propagation through a strip depends on the applied out-of-plane magnetic field.

The difference in energy, dE, between two DW configurations can be calculated in the following way:

$$dE = \sigma t dL - 2\mu_0 M_\mathrm{S} H_z t dA. \tag{C.4}$$

The first term is the DW energy per unit area (σ) times the layer thickness (t) times the difference in DW length (dL). The second term is the difference in in Zeeman energy, which can be calculated by multiplying the vacuum permeability (μ_0), the saturation magnetization (M_S), the magnetic field strength (H_z), t, the

difference in area in which the magnetization is aligned with the magnetic field, dA, and a factor 2 (because by increasing the area with magnetization aligned parallel to the field, an equal area with magnetization antiparallel to the field is removed). When we assume that the DW is fixed at the edges, the energy associated with the circular expansion can be calculated as a function of applied field. The increase in area aligned with the magnetic field, compared to the straight configuration, is calculated in the following way:

$$dA = \int_{-\frac{w}{2}}^{+\frac{w}{2}} R\cos\theta dy - wR\cos\theta_c. \tag{C.5}$$

Here R is the radius of the circle arc, w the width of the strip, y the position along the cross section of the strip, θ the angle between the line from a point on the circle arc to the centre and the line along the centre of the strip and θ_c the θ value at the strip edge. See Fig. C.1(a) for a visual representation of these symbols. The integral of equation C.5 is worked out step by step in equation C.6 to C.9:

$$dA = \int_{-\frac{w}{2}}^{+\frac{w}{2}} R\cos\left(\arcsin\left(\frac{y}{R}\right)\right)dy - wR\cos\left(\arcsin\left(\frac{w}{2R}\right)\right), \tag{C.6}$$

$$dA = \int_{-\frac{w}{2}}^{+\frac{w}{2}} R\sqrt{1-\left(\frac{y}{R}\right)^2}dy - wR\sqrt{1-\frac{w}{2R}^2}, \tag{C.7}$$

$$dA = \frac{y}{2}\sqrt{R^2-y^2} + \frac{R^2}{2}\arcsin\left(\frac{y}{R}\right)|_{-\frac{w}{2}}^{+\frac{w}{2}} - wR\sqrt{1-\left(\frac{w}{2R}\right)^2}, \tag{C.8}$$

and

$$dA = R^2\arcsin\left(\frac{w}{2R}\right) - \frac{w}{2}\sqrt{R^2-\frac{w^2}{4}}. \tag{C.9}$$

The increase in DW length can be calculated by:

$$dL = 2R\theta_c - w, \tag{C.10}$$

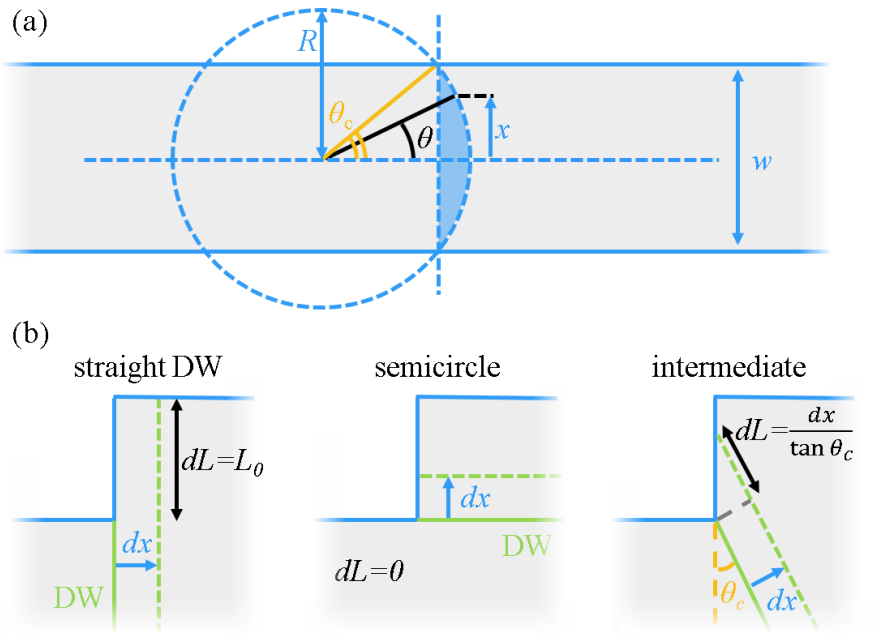

Figure C.1: (a) Definition of geometrical quantities for the calculation of the DW curvature. (b) Schematic depiction of how the increase in DW length depends on the DW angle at the edge of a strip.

and

$$dL = 2R \arcsin\left(\frac{w}{2R}\right) - w. \tag{C.11}$$

Inserting the equation C.9 and C.11 into equation C.4 makes it possible to calculate R as a function of H_z. Intuitively it would be expected that for $H_z = 0$ R becomes infinite, because curving will only result in the cost of having a longer DW without any gain in Zeeman energy, and when H_z goes to infinity R should approach $w/2$ (the minimum value), the situation with the largest area gain. When using realistic material parameters, it is found that from $\mu_0 H_z = 0.2\,\mathrm{mT}$ onward R is very close to $w/2$. This is in contrast with the experimental results: we only studied fields significantly larger than 0.2 mT, and the DW configuration is somewhere in between straight and a semi circle. Moreover, the DW becomes straighter for higher fields instead of rounder.

The problem in this analysis is that DW is not fixed at the edges in reality.

Therefore, what we actually need to calculate is the curvature at which the DW depins. This will then be the observed curvature of the DW, because the following process takes place: the DW starts out straight, then it will get pinned at some position, the curvature will start to increase, and (as just calculated) for the fields used here the balance between gain in Zeeman energy and cost of the increase in DW length will allow the DW to grow towards maximum curvature. When a critical curvature is reached the DW depins and can move further. Because it is a circular arc that grows with the same velocity in all directions, the radius will increase, and the curvature will decrease again. This will continue up to the point that the DW gets pinned again at the next pinning site, where the curvature will increase again up to the critical curvature where the DW depins and so on. Because many of these pinning sites are expected at the edge of the strips, we expect that the measured curvature will be approximately the curvature necessary for depinning.

The critical angle for which the DW depins can again be calculated using equation C.4. For a straight DW that reaches an antinotch (or leaves a notch), the increase in DW length when it would move further over a distance dx would be the size of the (anti)notch, L_0. This means that at very abrupt notches, $\frac{dE}{dx}$ scales with $\frac{L_0}{dx}$, suggesting an infinitely high pinning strength. However, when the DW is at a certain angle at the edge θ_c, the increase in length will be $\frac{dx}{\tan\theta_c}$ when it moves over a distance dx, and $\frac{dE}{dx}$ is reduced. This is depicted in the cartoons of Fig. C.1(b). Therefore the energy required to depin decreases as θ_c increases. Next, the decrease in Zeeman energy that has to compensate for this increase in DW length is calculated, which in the simplest view the associated area difference should be $dA = wdx$.

Inserting the expressions for dA and dL into equation C.4 leads to the following expression for the circle arc radius:

$$R = \frac{w}{2\sin\left(\arctan\left(\frac{\sigma}{2\mu_0 M_S H_z w}\right)\right)}. \tag{C.12}$$

Equation C.12 predicts an increase in radius (so a decrease in curvature) when H_z

increases, which is in accordance with the observations. A detailed comparison between equation C.12 and the experimental data is given in Chapter 5.

C.4 Incorrect explanations for Hx influence on curvature

The dependence of the DW curvature on H_x is an exciting observation that is most likely intimately related to the DMI. In Chapter 5 it is mentioned that we explored various approaches to describe the observed phenomenon, but no satisfactory results were obtained. In this section we present the details and results of these efforts.

According to the DW curvature model that was worked out in the previous section, the DW curvature is determined by the balance between the energy gain when increasing the area in which the magnetization is aligned with H_z and the energy cost of an increase in DW length. This last term is determined by the DW energy, σ, which is more complicated than the $\sigma_0 = 4\sqrt{AK_{\text{eff}}}$ when DMI and in-plane magnetic fields are considered [30]:

$$\sigma = \begin{cases} \sigma_0 + \lambda\mu_0 M_S \left(H_K + \pi\left(H_{\text{DMI}} + H_x\right)\right) & : H_x < -\frac{2}{\pi}H_K - H_{\text{DMI}} \\ \sigma_0 - \lambda\mu_0 M_S \frac{\pi^2 (H_{\text{DMI}} + H_x)^2}{4H_K} & : -\frac{2}{\pi}H_K - H_{\text{DMI}} \leq H_x \leq +\frac{2}{\pi}H_K - H_{\text{DMI}} \\ \sigma_0 + \lambda\mu_0 M_S \left(H_K - \pi\left(H_{\text{DMI}} + H_x\right)\right) & : H_x > +\frac{2}{\pi}H_K - H_{\text{DMI}} \ . \end{cases} \tag{C.13}$$

Here H_{DMI} is the effective field the DW experiences as a result of the DMI, H_x is the in-plane field applied perpendicular the the DW, $\lambda = \sqrt{A/K_{\text{eff}}}$ which is a measure for the DW width, and H_K is an effective field following from dipolar interactions which favors a Bloch wall configuration.

The DW curvature model can now be extended to include the effect of in-plane field by inserting this in-plane field dependent DW energy density in equation 5.1. Fig. C.2 shows the curvature extracted from the Kerr microscope images (black points) as a function of H_x together with predictions by the extended model (yellow curve). Realistic parameters were used for the calculation of this curve: $K_{\text{eff}} = 1.3\,\text{MJ}\,\text{m}^{-3}$, $|\mu_0 H_{\text{DMI}}| = 50\,\text{mT}$, and $\mu_0 H_z = 20\,\text{mT}$. This curve

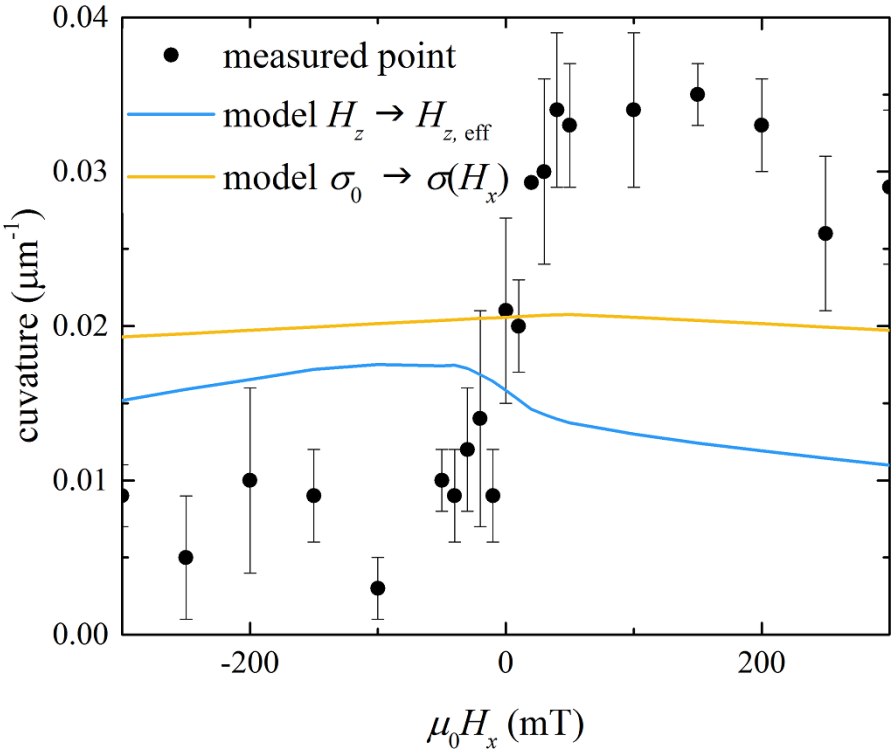

Figure C.2: Influence of of longitudinal in-plane magnetic fields on the DW configuration. Curvature as extracted from Kerr microscopy images as a function of in-plane field strength, together with theoretical curves.

clearly does not match the experimental data: the influence of H_x is much smaller in the calculation than in the experiment. This is not surprising when looking at equation C.13: the terms containing H_x are small compared to σ_0, because the magnetic anisotropy is relatively large in the investigated material stack.

Next, we present an alternative interpretation based on the DW velocity dependence on the in-plane field. A change in DW velocity suggests that the balance between the driving force an the pinning strength has changed. Regardless of the physical reason for this, it can be incorporated in the model by introducing an effective driving field, $H_{z,\text{eff}}$. We define this as the H_z field that would lead to the same DW velocity as the combination of H_z and H_x that is used. These $H_{z,\text{eff}}$ values can be put into equation 5.1 instead of the regular H_z to calculate the DW curvature. The results are represented by the blue line in Fig. C.2 (for the calculation the same material parameters are used as for the blue curve in Fig. C.2).The the shape of the calculated curve resembles the experimental data, but

rotated 180° around the vertical axis. This suggests that a DW gets more curved when the in-plane field is applied such that it moves slower. However, after careful experimental checking, it turns out that the DW becomes more curved when the in-plane field is applied such that it moves faster. This contradiction rules out the last explanation for the influence of H_x on the curvature with certainty.

Up to now, it is assumed in the model that the DW expansion is circular, which is not true in samples with DMI under the influence of an in-plane magnetic field. So the third approach to understand the relation between the DW curvature and H_x concerns the precise geometrical shape of the DW. The expected equilibrium shape of a bubble in our material stack is calculated following the approach of Lau *et al.* [105], which uses Wulff construction.

The following equation is used for the DW energy density:

$$\sigma(\phi,\eta) = \sigma_0 - \pi\lambda\mu_0 H_x M_S \cos(\phi+\eta) - \pi\lambda\mu_0 H_{\mathrm{DMI}} M_S \sin\phi + 2\lambda K_D \sin^2\phi, \quad \text{(C.14)}$$

where K_D is the DW anisotropy originating from dipolar interactions, ϕ is the angle between the DW and in-plane part of the magnetization inside the DW, and η is the angle between the DW and the in-plane field, H_x.

For every η, from 1° to 360° in steps of 1°, the angle ϕ for which the energy is minimal and the corresponding minimal energy density are found. The energy density is now plotted as a function of η, and a Wulff construction is performed (through each point on the curve, a line that is perpendicular to the line connecting that point to the origin is drawn).

The material parameters that are used are $M_S = 1.4\,\mathrm{MA\,m^{-1}}$, $K_{\mathrm{eff}} = 1.3\,\mathrm{MJ\,m^{-3}}$, $K_D = 48\,\mathrm{kJ\,m^{-3}}$, $A = 1.5\,\mathrm{pJ\,m^{-1}}$, and $|\mu_0 H_{\mathrm{DMI}}| = 50\,\mathrm{mT}$. Three different values for the applied in-plane field are used: $-100\,\mathrm{mT}$, $0\,\mathrm{mT}$, and $+100\,\mathrm{mT}$, which are typical values for which significantly different DW curvatures are observed in Chapter 5. The results are shown in Fig. C.3.

The deviation from a circular shape turns out to be marginal. This is because the H_x dependent terms in eq. C.14 are small compared to σ_0. So though according

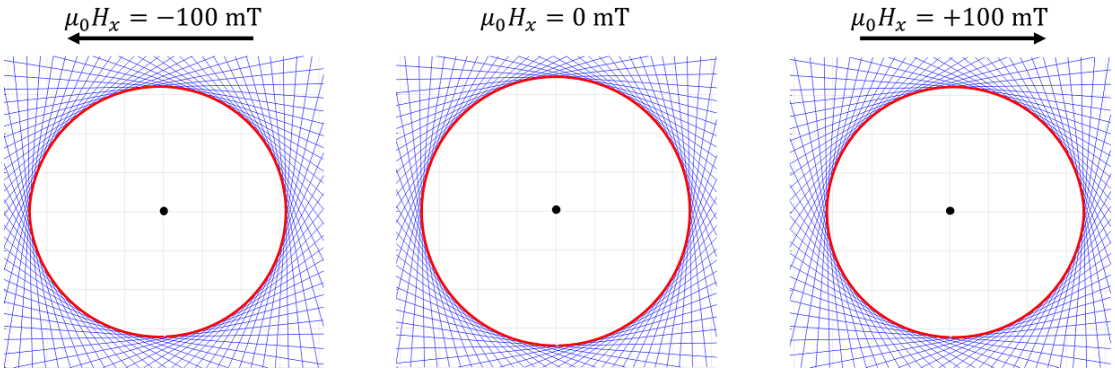

Figure C.3: Wulff construction to find the equilibrium bubble shape for the material parameters relevant to this study. The three plots show the results for three different values of the applied in-plane field. The black dots indicate the origin, the red curves the found equilibrium shapes.

to this view point a small dependence of the DW curvature on H_x should exist, it is insufficient to describe the large influence that is observed experimentally. A possible problem with this description is that the influence of edge pinning is not included.

C.5 Influence of the strip width

In Chapter 5, the DW velocity was measured as a function of H_z in 25 µm wide strips. However, in some of the subsequent experiments concerning the geometrical configuration of the DW, 50 µm wide wire where used. In literature it has been shown that the width of a strip can significantly influence the DW velocity [102]. This raises the question whether these results in Chapter 5 can be combined.

In Fig. C.4 measurements of the DW velocity in both 25 µm and 50 µm wide strips are compared. For this measurement, three strips hosting DWs were imaged simultaneously in order to obtain the DW velocities under exactly the same conditions. There are data points that deviate from the smooth creep curve, and this deviation seems to be correlated for the three wires investigated. This suggests that the dominant source of uncertainty in these measurements lies either in the magnetic field strength or in the pulse duration. The differences between the wires of different width is smaller than these experimental errors. We therefore conclude

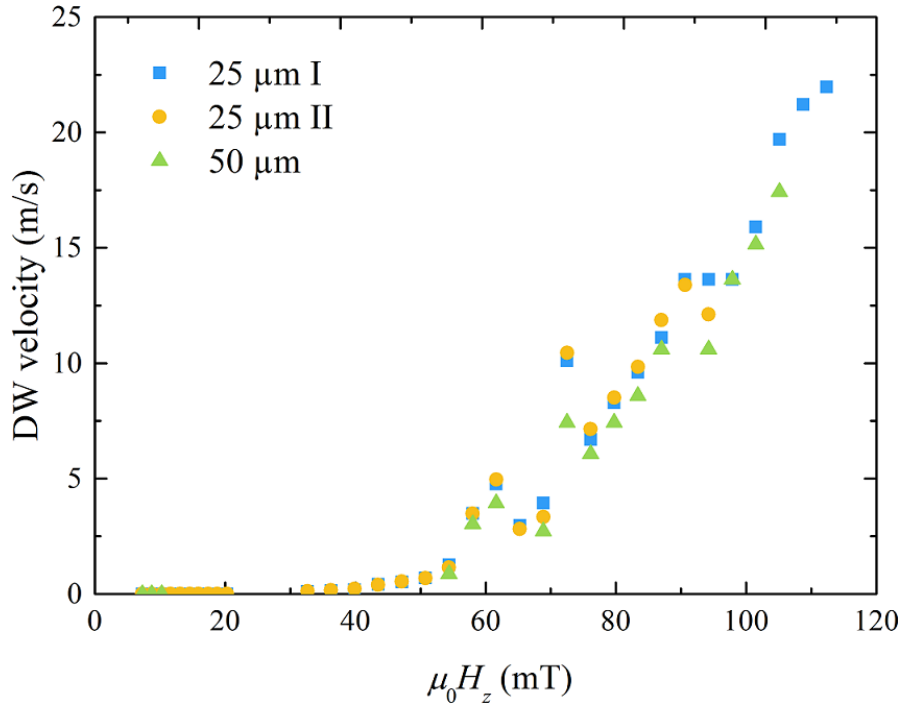

Figure C.4: DW velocity as a function of H_z for 25 µm and 50 µm wide wires.

that for the strip widths and edge roughnesses studied here, there is no significant influence of the wire width on the DW velocity.

C.6 Influence of the initial state

Figure 5.5(b) shows measured DW tilt angles as a function of H_y. Remarkably, the data point taken at $H_x = 0\,\mathrm{mT}$ does not correspond to a tilt angel of zero degrees within the margin of error. This is surprising, because both the energy minimization as shown in Fig. 4(c) as the interpretation based on asymmetric DW velocities predict a zero tilt angle under these conditions. We therefore investigate whether the configuration of the DW prior to this measurement could have influenced these results. The experiment is repeated two times with two well defined, different initial conditions, and the recordings are shown in supplementary video 3 and 4, which are available online [159]. In video 3, the DW is prepared while $H_y = +100\,\mathrm{mT}$ and in video 4 while $H_y = -100\,\mathrm{mT}$, leading to opposite tilt angles. Subsequently, H_y is set to zero, and the DW is propagated by a perpendicular field only. In both videos, the same non-zero tilt arises, so independent of

the initial state. The physical origin of this non-zero tilt angle in absence of an in-plane field is unclear to us, and warrants further investigation.

D

Supplementary information on Chapter 9

D.1 Material properties

The samples studied in Chapter 9 contain a Co layer that varies in thickness, and in this section important material parameters, in particular the effective perpendicular anisotropy constant, K_{eff}, and the saturation magnetization, M_{S}, are determined as a function of Co thickness, as well as the DMI constant, D, at the skyrmion bubble transition.

For a full sheet Ta (4 nm) / Pt (4 nm) / Co (0.6 nm) / Pt (4 nm) sample grown with the same deposition equipment and using the same growth parameter settings, M_{S} was found to be 1.3 MA m^{-1} by VSM SQUID measurement [46]. We assume that in our wedge geometry sample, M_{S} will also have this value at the position where the Co thickness is equal to 0.6 nm. Using polar MOKE measurements while magnetic fields are applied perpendicular to the sample surface, magnetic hysteresis loops along the wedge can be obtained. The size of the signal obtained at saturation is proportional to the amount of magnetic material, in the limit that the layer thickness is small compared to the light penetration depth [185]. If this value is proportional $M_{\text{S}} \times t$, than M_{S} should be proportional to the saturation value divided by the Co layer thickness. The M_{S} value at 0.6 nm is known, from which M_{S} for the rest of the wedge can be derived, see Fig. D.1(a). When the magnetic signal is too low, the fit of the hysteresis curves becomes unreliable, resulting in nonphysical values for M_{S}. These measurement points are shown as open points.

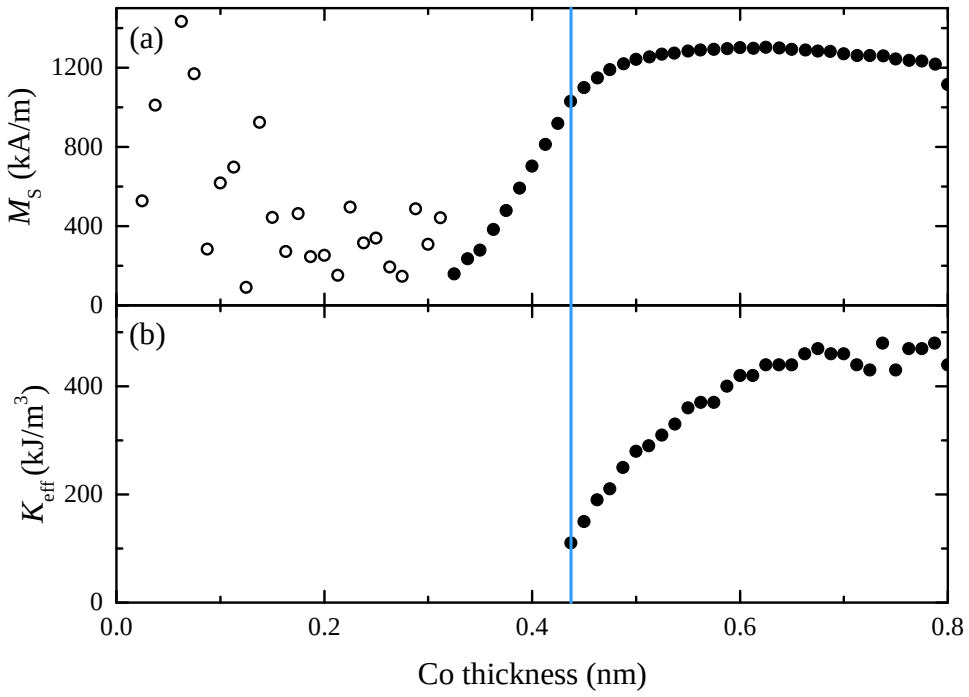

Figure D.1: MOKE measurements on a Ta (4 nm) / Pt (4 nm) / Co (t_{Co}) / Pt (4 nm) sample. (a) Saturation magnetization as a function of Co thickness. Unreliable values are indicated by open points. (b) Effective anisotropy constant as a function of Co thickness. The skyrmion bubble transition is indicated by the blue, vertical line.

For the determination of K_{eff} along the wedge, hysteresis loops obtained by polar MOKE are used as well, only now the magnetic field is applied in the plane of the sample surface. K_{eff} can be extracted from these loops by Stoner Wohlfarth fits [186]. For these fits the thickness dependent M_S values that were determined earlier are used. Also, data points for which M_z is less than 80 percent of M_S are disregarded to prevent the formation of a multidomain state to influence the fit. The obtained K_{eff} as a function of Co is shown in Fig. D.1(b).

Last, for the determination of the DMI strength at the skyrmion bubble transition, Kerr microscope images of the labyrinth state are analysed in detail. Kaplan and Gehring [187] have shown that the domain size, L, that is observed is related to the DW energy, σ, via

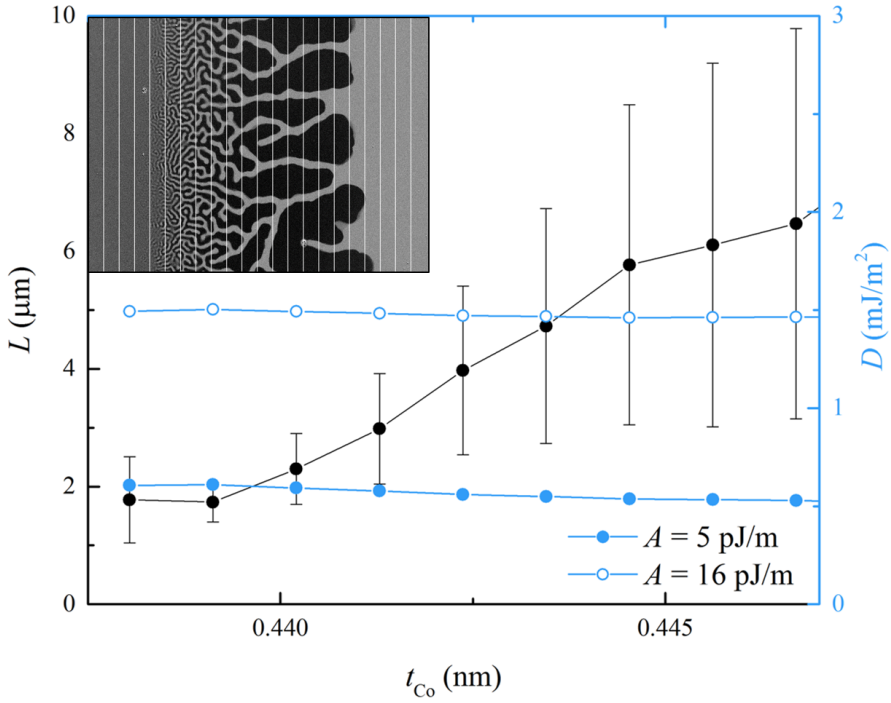

Figure D.2: Typical domain size in the labyrinth state as a function of the Co thickness, together with the corresponding DMI constants. Inset shows the Kerr microscope image of the labyrinth state divided into 22 µm wide strips.

$$L = \alpha t_{\mathrm{Co}} \exp\left(\frac{\pi L_0}{2t_{\mathrm{Co}}}\right), \tag{D.1}$$

where $\alpha \approx 0.955$ is a numerical constant [145, 187], and $L_0 = \frac{\sigma}{\mu_0 M_{\mathrm{S}}^2}$. Images of the labyrinth structure on the wedge sample are divided into 22 µm wide strips, as shown in the inset of Fig. D.2, such that the material parameters are approximately constant within a strip. For each strip, the domain size and standard deviation are determined using Fourier analysis, resulting in a typical domain size as a function of the position in the image. The position in the image can be converted to the Co thickness. The result is shown in Fig. D.2. Via $\sigma = 4\sqrt{AK_{\mathrm{eff}}} - \pi D$ the DMI constant can then be obtained. This results in $|D| = 0.6$ - $1.4\,\mathrm{mJ\,m^{-2}}$, when $A = 5$ - $16\,\mathrm{pJ\,m^{-1}}$ is used. Here $16\,\mathrm{pJ\,m^{-1}}$ is the commonly used value for Co, but because extremely thin layers are considered A might be reduced [188].

D.2 Characterisation of skyrmion bubbles

Chapter 9 focusses on the current-induced motion of skyrmion bubbles, but their static properties are only briefly mentioned. However, these properties are essential for those wanting to reproduce our results. In this section, more details on the observed skyrmion bubbles are presented. In particular, we will pay attention to the size of the skyrmion bubbles, in which magnetic field range they are stable, and the effect of changing the material of the top layer of the stack (Ta (5 nm) / Pt (4 nm) / Co (t_{Co}) / X (4 nm) stacks are investigated, where X is Pt, Ta or Ir). The method to extract these properties from our data is discussed as well.

Kerr microscope images of the skyrmion bubbles are subjected to an averaging filter and converted to black-and-white images. From the domains present in these images only the ones with a minimal size (to prevent noise from single pixels obscuring the data) and with a limited deviation from a circular shape are selected. From these results the average size of the skyrmion bubbles can be found, and if the procedure is repeated for various $\mu_0 H_z$, the field at which skyrmion bubbles are nucleated and stabilized can be found.

Fig. D.3(a) shows the number of bubbles that are identified in images as a function of $\mu_0 H_z$ for all material stacks investigated. All images are analysed twice: one time to identify dark circular domains on a light background (which will be referred to as 'dark bubbles') and one time to identify light circular domains on a dark background (which will be referred to as 'light bubbles'), of which the results are represented by the closed and open symbols, respectively. For all samples, two peaks in the number of detected bubbles are found, one for the dark bubbles and one for the light bubbles. The peaks occur for magnetic field strengths slightly below 0.1 mT. There is no significant difference in the fields at which the bubbles occur for the different material stacks.

One interesting observation is that for all samples investigated a larger number of light bubbles than dark bubbles is found. Though the exact number of bubbles found using this method is prone to errors and is only meant to identify the field stability range, this seems to be a clear trend. The data presented in Fig. D.3 were obtained starting at the most negative $\mu_0 H_z$ value and gradually increasing $\mu_0 H_z$

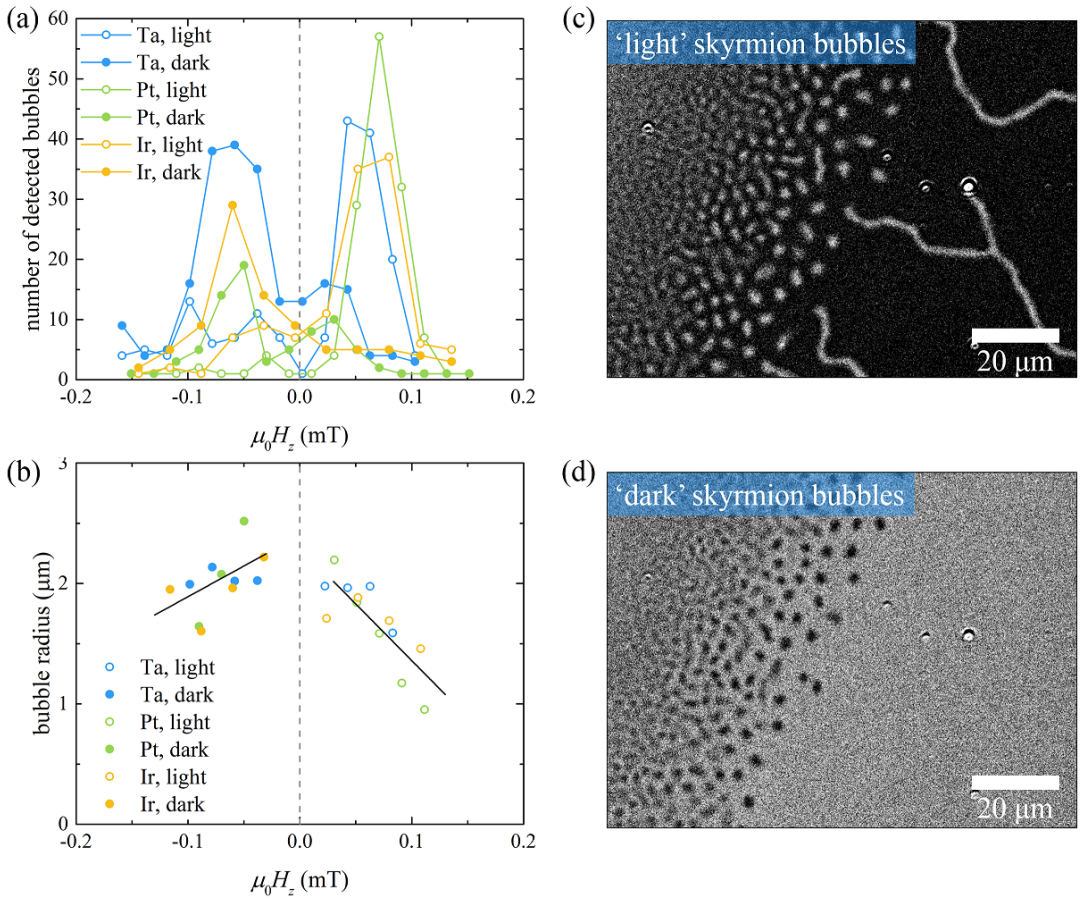

Figure D.3: (a) Number of detected skyrmion bubbles as a function of $\mu_0 H_z$, showing for which fields skyrmion bubbles occur for all investigated material stacks. (b) The average radius of the detected bubbles as a function of $\mu_0 H_z$ for all investigated material stacks. The points represent the measured data, the lines are a guide to the eye. 'Light' refers to light bubbles in a dark background and 'dark' refers to dark bubbles in a light background, as illustrated in (c) and (d), respectively.

from there. The measurements are repeated starting from the most positive $\mu_0 H_z$ value (these results are not shown here). In that measurement series, more light than dark bubbles were found (but still at the same values of H_z as before). This indicates that the number of bubbles depends on whether the stabilization field is reached coming from the saturated state or from the labyrinth state. The time between two measured points is in the order of 20 s. Because we observe thermally activated movement, nucleation and annihilation of the bubbles, we expect that

the importance of the field history will disappear when the system is allowed to settle at the investigated $\mu_0 H_z$ fields for a longer time.

The magnetic field is applied using an air coil, which is calibrated by measuring the magnetic field as a function of the current through the coil using a Hall probe, prior to the actual experiment. At the field exactly in between the fields for which the dark and light bubbles appear, a labyrinth domain structure is observed. Because of the symmetry of the situation, the fact that for the labyrinth structure the areas covered by up and down domains are equally large, and observations from literature [169], we believe that this labyrinth state occurs when the $\mu_0 H_z$ is exactly 0 mT. However, experimentally it is found that the labyrinth structure appears at a field close to, but not equal to, zero. We believe that this is due to experimental artifacts (like a small field present in the surrounding of the setup, the earth magnetic field, a remanent field in the magnet or other part of the setup or an imperfect calibration of the magnet) rather than that this deviation from zero is real. Therefore we have corrected for this for every field value that is shown, both in this Appendix and in Chapter 9.

Next, the size of the skyrmion bubbles is investigated. The areas of the domains that are identified as bubbles are divided by π and the square root of the result is taken. This gives the bubble radius in pixels, which is subsequently converted to micrometers. The size of the bubbles is similar for all material stacks investigated, and in the order of 2 µm. The following trend is observed: the bubbles become smaller when the applied field is stronger (see the black lines in Fig. D.3(b)), which is in agreement with observations in literature [56].

In the pictures used for analysis a certain range of bubble sizes is present, which can for instance be seen in Fig. D.3(c) and (d), because of the fast change of material parameters at the skyrmion bubble transition. One should note that the values in Fig. D.3 are averages that mainly represent the larger bubbles. This is because the smaller bubbles are at the limit of what is possible to distinguish in the used microscope, and their thermal motion is larger, making it very difficult for our analysis program to identify them.

D.3 spin Hall effect direction check

In Chapter 9 it is argued that it should be possible to reverse the direction of the net spin Hall current in Pt/Co/Pt samples by changing the thickness of both Pt layers. However, no change in direction of skyrmion bubble motion by manipulating the Pt layer thicknesses was observed. A possible reason for this could be that the two Pt/Co interfaces ar not equally transparent for spins. It is known that though the same materials are present at these interfaces, they do not have to be identical, which is for instance illustrated by their different contributions to the perpendicular magnetic anisotropy or to the total Dzyaloshinskii-Moriya interaction. Suppose that, for example, the bottom interface would be much more transparent for spins than the top interface, then it would be expected that the spin current coming from the bottom Pt layer always gives the dominant contribution, irrespective of the Pt layer thicknesses. In this section we explore this explanation for the experimental results.

In samples with perpendicular magnetic anisotropy, the spin current generated by the spin Hall effect does not only exert a torque on the DWs, but also on the spins inside the uniform domains. When the symmetry is broken by a magnetic field directed along the current direction, this torque can even switch the magnetization, when the spin current is sufficiently large. We will now use this effect to identify the direction of the net spin current injected into the Co layer in our samples. These experiments are more straightforward to interpret than DW motion based measurements, because the strength and direction of the DMI do not have to be considered and also effects like the bulk spin transfer torque do not play a role.

Using standard lithography and lift off techniques, 5 µm wide strips are created and contacted. For the strips material stacks of Pt (4 nm) / Co (0.6 nm) / Pt (2 nm) and Pt (2 nm) / Co (0.6 nm) / Pt (4 nm) are used, for which an opposite net spin current is expected. For this experiment it is necessary that the magnetization is uniform and out-of-plane at remanence, and therefore a slightly thicker Co thickness is chosen compared to the Co thickness at the skyrmion transition. The following measurement routine is then performed: using a magnetic field in the $-z$ direction, the magnetization in the strips is saturated. This field is turned off again, and next a magnetic field of 30 mT, which is sustained throughout the remainder of the

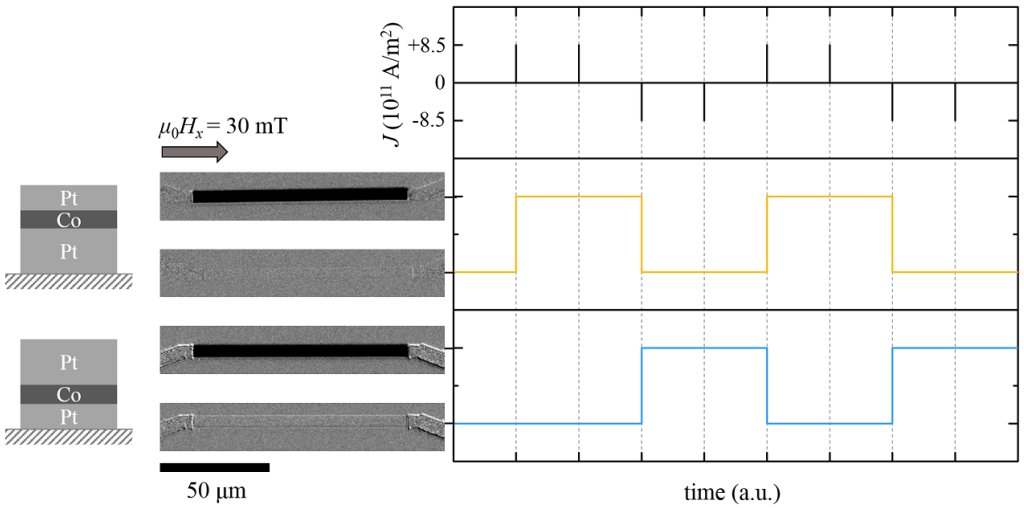

Figure D.4: Reaction of both a Pt (4 nm) / Co (0.6 nm) / Pt (2 nm) and a Pt (2 nm) / Co (0.6 nm) / Pt (4 nm) strip to current pulses in the presence of a 30 mT magnetic field along the strips. Note that the graphs are merely a schematic representation of the observed behaviour: the "values" on the vertical axes are two typical states that are distinguished by eye, and because the current pulses are triggered manually the time between the pulses is not constant as may be suggested on the horizontal axis.

measurement, is applied along the x direction. Then current pulses are applied through the strips, resulting in a current density, J, of 8.5×10^{11} A m^{-2} for a duration of 10 ms. After each two pulses, the current direction is reversed, as schematically indicated in the black graph of Fig. D.4. The whole process is monitored using a Kerr microscope, and two distinct states of the magnetic strips are observed: dark and light, corresponding to an up or down magnetization, respectively. The yellow and blue graphs in Fig. D.4 show in which state the strips are after each pulse for the Pt (4 nm) / Co (0.6 nm) / Pt (2 nm) and Pt (2 nm) / Co (0.6 nm) / Pt (4 nm) stack, respectively.

The results are in agreement with the principle of spin Hall effect induced switching. The magnetization can clearly be switched back and forth without problems, and the fact that a second current pulse in the same direction does not change the state excludes heat induced toggling. The direction in which the magnetization ends up depends on the combination of the current direction and the in-plane field direction, so it was also verified that this direction reverses when the in-plane field is inverted (not shown here). The most important observation is that the favoured

magnetization direction for the same in-plane field and current directions is opposite for the two material stacks. This is a clear indication that for one stack it is the bottom Pt layer that provides the dominant contribution to the spin current, while for the other stack it is the top Pt layer. This is in agreement with observations by Haazen *et al.* [72, 189]. In that work also measurements on samples with top and bottom Pt layers of equal thickness are performed, in which no significant effect of the SHE was found. This makes it plausible that the spin Hall angles for both Pt layers are comparable. As the samples studied here are fabricated using the same setup and the same growth parameters as the samples in the Chapter 9, it is highly unlikely that the direction of the net spin Hall current is not inverted within the Pt thickness range studied in Chapter 9. However, we must exercise some restraint, as the Co layer in the experiment presented here is slightly thicker than the skyrmion transition thickness.

D.4 Analysis procedure

In Chapter 9 skyrmion bubble velocities are shown, and in this section we show how these velocities have been extracted from the raw data. In this case the raw data are Kerr microscope movies, in which a large number of skyrmion bubbles are moving around. Because it turned out to be unfeasible to reliably identify all bubbles and track them through the different frames, we took the following approach: the first frame of a movie is divided into narrow vertical strips. Such a strip is then slid over the next frame, and at each position it is checked how well the image underneath matches the original strip, an schematic example is shown in Fig. D.5. This way it can be found how far the bubbles (though it would work for other shapes of domains as well) have moved during the time between two frames, and from this the velocity can be calculated. Because this can be done for every strip of the first frame, a position dependent velocity can be measured.

When examining the movies, it can be seen by eye that not all bubbles move at the same velocity. This is caused by the change in material parameters along the Co wedge: typically it is observed that the small bubbles that are formed in the region where the Co is a bit thinner, move faster than the larger bubbles in the thicker Co regions. This also follows from the analysis, but for the scope of this

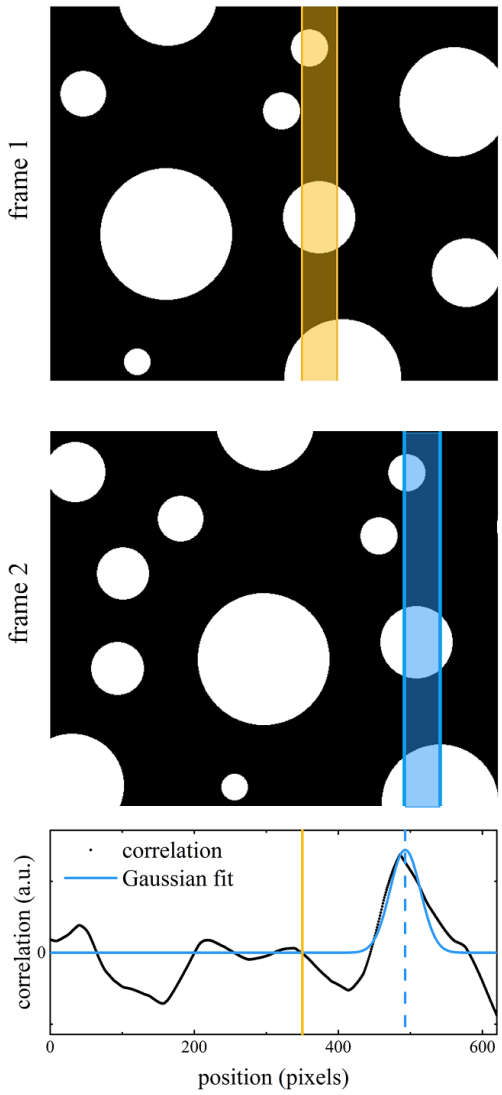

Figure D.5: Illustration of the principle behind the script used to extract the bubble velocity from Kerr microscope movies. A small vertical strip from frame 1 selected, and the position in frame 2 that matches this original strip best is identified. The position of the strip in the first frame is indicated in yellow, and the best matching position in the second frame is indicated in blue.

thesis is it more useful to work with a typical velocity and see how this depends on the current. Therefore, the velocities for all positions are averaged to find a mean value, and the position dependence of the velocity causes a relatively large standard deviation, as can be seen in Fig. 9.3(b).

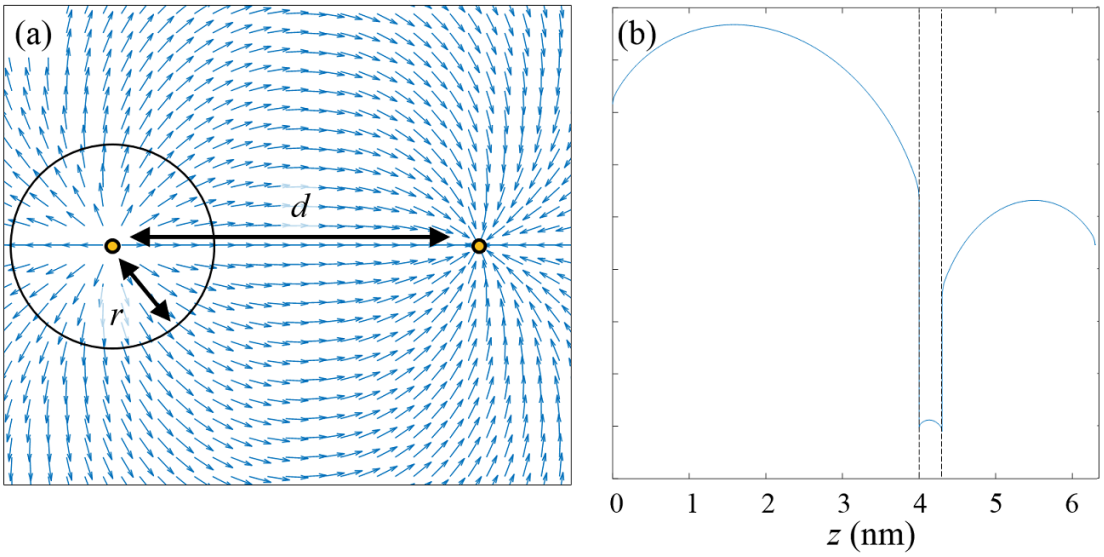

Figure D.6: (a) Current distribution (indicated by blue arrows) when current is applied via probes. The locations of the probes are marked in yellow, and r and d, which are used in Eq. D.2 and D.3, are defined graphically. (b) Calculated current distribution as a function of the z position in the material stack for a Pt (4 nm) / Co (0.3 nm) / Pt (2 nm) stack. The same material parameters as in Ref. [157] are used.

D.5 current density calculations

The current density used to drive the skyrmions is an important parameter in Chapter 9. In this section it is discussed how this parameter is calculated.

On the double wedged samples studied in Chapter 9, probes are used that can be landed in the measurement region so a current can be applied locally, see Fig. D.6(a). The current distribution is inhomogeneous, but can be estimated reasonably well, provided that the following conditions are fullfiled: the probes act as point contacts (which is reasonable because the diameter of their contact area ($\sim 2\,\mu$m) is much smaller than the distance between the probes ($\sim 200\,\mu$m)), the sample is homogeneous (which is justifiable, as the measurements are on a scale of $\sim 200\,\mu$m, while the variation in thickness is 10 nm over 15 mm), the sample is infinitely large in the x and y direction (which is reasonable considering the scale on which we measure ($\sim 200\,\mu$m) and the size of the sample (~ 2 cm)), and that the conducting layer is infinitely thin (which is reasonable considering total stack thickness (~ 10 nm) compared to the measurement scale ($\sim 200\,\mu$m)).

When all these conditions are fulfilled, the current density can be calculated in the following way: consider only one contact point from which the total current I flows into the sample. Because of the assumption of homogeneity and infinity of the sample, this current flow will be radially outward. When drawing an imaginary circle around the contact, the current density at points located at this circle, J_{av} can be calculated by the conservation of current:

$$J_{\mathrm{av}} = \frac{I}{2\pi r t}, \tag{D.2}$$

where r is the circle radius. When a second contact is added (but now one where the current flows out of the sample) at a distance d from the first, the current density and direction at every position can be calculated by adding the contributions of both contacts. Most relevant is the current density at the line connecting both contacts at equal distance to both contacts, as this corresponds to where the skyrmion bubble velocity is measured experimentally.

In the experiments videos are made of an 436 µm times 331 µm area in which the skyrmion transition is visible as well as the probes landed around it. In this region the current distribution is highly inhomogeneous (which is also apparent in the observed skyrmion motion), so for the determination of the velocity a smaller region (approximately 50 µm times 50 µm) around the point of symmetry is manually selected. The current density at the point of symmetry can be calculated by

$$J_{\mathrm{av}} = \frac{2I}{2\pi (d/2) t}. \tag{D.3}$$

Up to now the average current density through the whole material stack was considered. However, in practice the current density will be dependent on the z position within the material stack. It depends not only on the resistivities of the different materials used, but also on the proximity to the surfaces and interfaces where additional scattering takes place. In this study this is very relevant: the STT contribution to the skyrmion motion scales with the current density in the magnetic layer, while the SHE depends on the current density in and thickness of

the adjacent heavy metal layers. In our experiment where measurements are done for different thicknesses of the top Pt layer, how large J_{Co} and J_{Pt} are compared to the J_{av} can be different per measured point, making it impossible to disentangle the two contributions. Therefore the z dependent current density is required, which can be calculated using the Fuchs-Sondheimer model. For the calculations parameters from Ref. [157] are used. Typical results of such calculations are shown in Fig. D.6(b). From data like these, J_{Co} and J_{Pt} compared to the J_{av} can be estimated, which resulted in the curves of Fig. 9.4(b) and (d).

Although the calculated curves in Fig. 9.4(b) and (d) reproduce the experimentally observed behaviour qualitatively, the match with the experimental data is not perfect. One explanation for this mismatch is the use of an incorrect value for the spin diffusion length in Pt, λ_{sf}, a parameter that strongly affect the shape of the SHE contribution curve. We have taken this value to be 1.2 nm, based on [160], but several different values have been reported in literature. The parameter has even been shown to be dependent on the Pt thickness [190], an effect that is not taken into account in our calculations. Careful determination of λ_{sf} in our sample stack might be an important ingredient for future improvement of our calculations.

D.6 Skyrmion bubble motion for homogeneous currents

In Chapter 9 closely spaced probes are used for current injection, which results in an inhomogeneous current distribution through the sample, as was discussed in section D.5. To rule out that the observed skyrmion bubble motion is caused by temperature gradients or inhomogeneous Oersted fields, we also perform measurements using a homogeneous current density. For this, samples with a single wedge geometry are used, where the Co layer has a wedge shape, but the Pt capping layer thickness is constant. Using silver paint, large contacts are created at the outer ends of these wedges. The contacts are several mm large, and approximately 2 cm apart. This results in a current density that is nearly homogeneous within the measurement field of view of 300 µm wide. The average current density, J_{av}, can now simply be calculated as:

$$J_{\mathrm{av}} = \frac{I}{wt}, \tag{D.4}$$

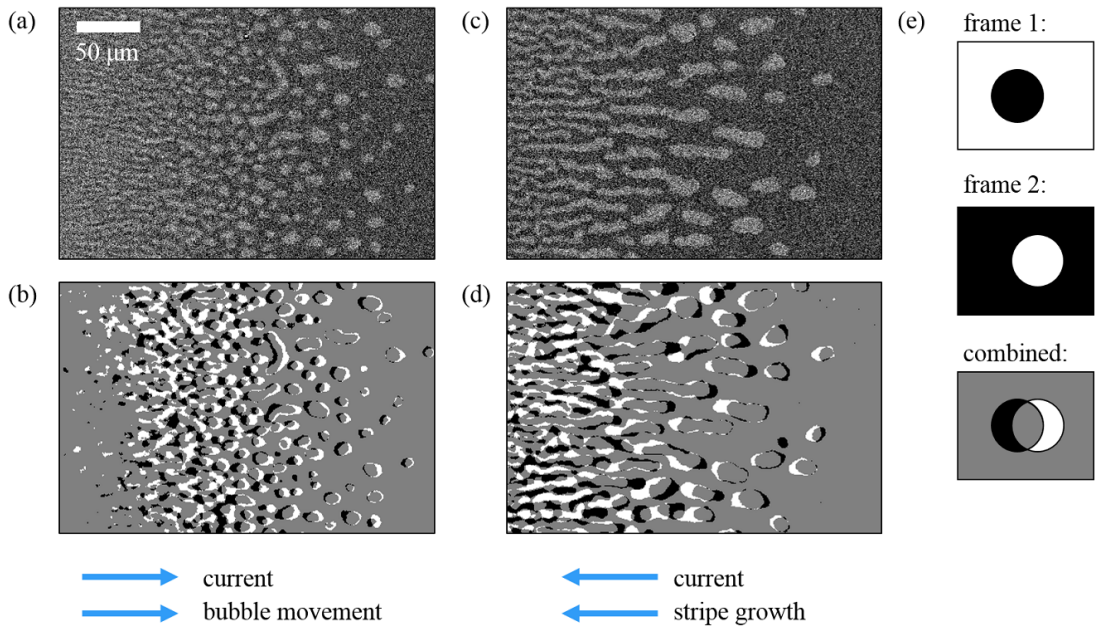

Figure D.7: Kerr microscope images of the domain structures in the Ta/Pt/Co/Ir sample while applying current (a) in the direction towards the thicker part of the wedge (towards the right of the image) (c) in the direction towards the thinner part of the wedge (towards the left of the image). (b) and (d) show the difference between filtered, black-and-white frames from the movies from which the images in (a) and (c) are taken. In (e) the color coding in (b) and (d) is illustrated.

with I the total curent, w the width of the sample and t the thickness of the material stack.

Fig. D.7 shows typical Kerr microscopy images from videos taken during this experiment. Fig. D.7(a) shows the result of sending current ($6.7 \times 10^8\,\mathrm{A\,m^{-2}}$) in the direction towards the thicker end of the wedge and Fig. D.7(c) shows the result when the current is reversed and flows towards the thinner end of the wedge ($3.4 \times 10^8\,\mathrm{A\,m^{-2}}$). Figure D.7(b) and (d) show differential image of the situations in figures (a) and (c), respectively, visualizing the bubble motion and deformation. The colour coding is explained by the schematic example in D.7(e). Grey represents the areas in which the magnetization in consecutive frames is identical, and the black and white indicates the regions where the magnetization is different. Larger black and white areas indicate a larger difference between the frames en therefore a higher velocity. Also the direction of motion can be seen from these

differential images: in the colour definition used here, bubble shapes with a white edge on their right and a black edge on their left are moving towards the right.

For the situation in Fig. D.7(a) and (c), the skyrmion bubbles are moved along with the current, until they reach a region where they are no longer stable and collapse. In Fig. D.7(b) and (d), the magnetic domains again follow the direction of the current flow, but now the circular shapes are not preserved. Elongated domains, oriented along the current flow, are formed. We explain this observation in the following way: the observed velocity is larger at the thinner part of the wedge, as was discussed in section D.4. When a skyrmion bubble is moved to the left, its left side will move faster than its right side, elongating the skyrmion bubble. The more elongated it becomes, the larger the velocity difference becomes, and soon it is transformed into a long stripe.

Following this reasoning, one might expect annihilation of skyrmion bubbles in case the current flows towards the thicker region, as was the case in Fig. D.7(a). The left side of the bubble would move faster than the right side, so if the bubble moves to the right, at a certain point its two sides would meet, and the bubble would disappear. However, this is not what is observed experimentally, indicating that there is some force preventing the skyrmion bubble from collapsing. This could be its topological protection or the result of dipole-dipole interactions [191].

For the experiments presented in Chapter 9, the current always flows from the thinner part of the Co wedge to the thicker part of the Co wedge. This way the velocity can be obtained and averaged over a large portion of the region in which the skyrmion bubbles are stable. The system is extremely sensitive to changes in the Co thickness, which results in variations in skyrmion bubbles size over short distances, and it is observed that the skyrmion bubble velocity depends on the size. Therefore, for measurements with current flowing along constant Co thickness, the size and hence the velocity of the skyrmion bubbles would strongly depend on the exact positioning of the probes, which would make it impossible to compare measurements taken at various Pt thicknesses.

D.7 One dimensional model

In Chapter 9 it is proposed that both the SHE and a negative bulk STT contribute to the observed skyrmion motion. For the analysis it is assumed that the velocities that would result from these two contribution can simply be added together to obtain the resulting skyrmion velocity. In this section we verify this assumption using a one dimensional model for DW motion. We use the model as presented by Martinez *et al.* [192]. It is based on the Landau-Lifshitz Gilbert equation including spin-transfer torques ($\boldsymbol{\tau}_{\mathrm{ST}}$) and spin-orbit torques ($\boldsymbol{\tau}_{\mathrm{SO}}$):

$$\frac{\partial \mathbf{m}}{\partial t} = -\gamma\mu_0 \mathbf{m} \times \mathbf{H}_{\mathrm{eff}} + \alpha \left(\mathbf{m} \times \frac{\partial \mathbf{m}}{\partial t} \right) + \boldsymbol{\tau}_{\mathrm{ST}} + \boldsymbol{\tau}_{\mathrm{SO}}, \tag{D.5}$$

with $\mathbf{m}$ the normalized magnetization, γ is the gyromagnetic ratio, α the Gilbert damping parameter and $\mathbf{H}_{\mathrm{eff}}$ the effective field that includes external magnetic fields, exchange interaction, anisotropy, magnetostatic contributions, and the DMI. The spin-transfer torque is given by:

$$\boldsymbol{\tau}_{\mathrm{ST}} = (\mathbf{u} \cdot \nabla)\, \mathbf{m} + \beta \mathbf{m} \times (\mathbf{u} \cdot \nabla)\, \mathbf{m}, \quad \text{with} \quad |\mathbf{u}| = u = \frac{\mu_{\mathrm{B}} P J}{e M_{\mathrm{S}}}, \tag{D.6}$$

where the first term on the right hand side represents the adiabatic STT while the second term represents the nonadiabatic STT. The spin-orbit torque can include contributions from the spin Hall effect and the Rashba effect, but for the systems investigated here only the spin Hall effect is believed to be relevant [193]. J is the current density, and for simplicity this is assumed to be uniform, though it was shown in Section D.5 that the reality is more complex. Here β is the non-adiabatic parameter, P the spin polarization, and μ_{B} the Bohr magneton. The spin-orbit torque reads,

$$\boldsymbol{\tau}_{\mathrm{SO}} = \gamma\mu_0 \mathbf{m} \times (\mathbf{m} \times H_{\mathrm{SH}} \hat{\mathbf{y}}), \quad \text{with} \quad H_{\mathrm{SH}} = \frac{\hbar \theta_{\mathrm{SH}} J}{\mu_0 2 e M_{\mathrm{S}} t_{\mathrm{Co}}}. \tag{D.7}$$

When it is assumed that the the magnetization is constant in the z and y direction and that the shape of the DW profile is constant as well, two coupled differential equations that describe the behaviour of the DW can be derived:

$$\begin{aligned}\dot{q}/\lambda =& \frac{\alpha}{1+\alpha^2}\gamma\mu_0 H_z - \frac{1}{2}\frac{\mu_0\gamma}{1+\alpha^2}H_K \sin 2\varphi + \frac{(1+\alpha\beta)}{1+\alpha^2}\frac{u}{\lambda} \\ &+ \frac{\pi}{2}\frac{\gamma\mu_0}{1+\alpha^2}\left(\alpha H_{\mathrm{SH}} - H_y\right)\cos\varphi \\ &+ \frac{\pi}{2}\frac{\gamma\mu_0}{1+\alpha^2}\left(H_{\mathrm{DMI}} + H_x\right)\sin\varphi,\end{aligned} \tag{D.8}$$

$$\begin{aligned}\dot{\varphi} =& \frac{\gamma\mu_0}{1+\alpha^2}H_z - \frac{1}{2}\frac{\alpha\mu_0\gamma}{1+\alpha^2}H_K \sin 2\varphi + \frac{(\beta-\alpha)}{1+\alpha^2}\frac{u}{\lambda} \\ &+ \frac{\pi}{2}\frac{\gamma\mu_0}{1+\alpha^2}\left(H_{\mathrm{SH}} + \alpha H_y\right)\cos\varphi \\ &+ \frac{\pi}{2}\frac{\alpha\gamma\mu_0}{1+\alpha^2}\left(H_{\mathrm{DMI}} + H_x\right)\sin\varphi,\end{aligned} \tag{D.9}$$

where q is the DW position, φ the DW angle, and H_{DMI} is the effective DMI field defined as $H_{\mathrm{DMI}} = D/(\mu_0 M_{\mathrm{S}}\lambda)$. H_{K} is the magnetostatic field favoring a Bloch configuration calculated by $H_{\mathrm{K}} = NM_{\mathrm{S}}$, where N is the demagnetization factor which can be calculated by $N = t\ln 2/\pi\lambda$. These equations can be solved numerically to obtain the DW velocity as a function of current density. Using material parameters as determined in earlier sections and from Ref. [72], as listed in table D.1, the following procedure is followed: first the spin Hall effect is artificially switched off by setting the spin Hall angle to zero, so the DW velocity as a function of the current density, purely driven by spin-transfer torque, is calculated. After this, the spin Hall angle is restored to its realistic value, but instead the effect of the bulk spin-transfer torque is turned off by setting the spin polarization to zero. Now we have the velocity versus current density curve, both for purely STT and for the purely SHE driven situation. These two curves can be added together and compared to the calculation in which both contributions were included. The results are shown in Fig. D.8(a).

The curve for the calculation in which both the bulk STT and SHE are included overlaps perfectly with the curve representing the sum of the individual STT and SHE curves. This justifies the approach followed in Chapter 9, that is using $v = C_1 J_{\mathrm{Co}} + C_2 J_{\mathrm{S},net}$ to calculate the velocity when both the STT and SHE are relevant. This conclusion is not trivial: when larger current densities are considered φ may be altered by the SHE, which could complicate the situation.

Table D.1: Overview of the constants and parameters used for the calculations presented in Fig. D.8

Constant	**Value**
μ_0	$4\pi \times 10^{-7}$ T m A^{-1}
e	1.602×10^{-19} C
$\hbar$	1.055×10^{-34} J s
γ	1.76×10^{11} s^{-1} T^{-1}
μ_B	9.27×10^{-24} J T^{-1}
Quantity	**Value**
M_S	1.0×10^{6} A m^{-1}
K_{eff}	0.11×10^{6} J m^{-3}
A	1.6×10^{-11} J m^{-1}
θ_{SH}	0.076 [194]
D	-0.045 mJ m^{-2}
t_{Co}	0.44×10^{-9} m
P	0.4
α	0.1
β	0.13

However, experimentally only small current densities, similar to what is shown in Fig. D.8, are used, so this is not an issue.

Though DMI measurements were performed in previous sections, the results were inconclusive. Because we cannot guarantee that the investigated skyrmion bubbles have Néel walls, Bloch walls, or some intermediate configuration, it is addressed here how STT driven motion is influenced by the DW configuration. The SHE is again turned off artificially by setting $\theta_{SH} = 0$ and the calculations are repeated for various values of D. Fig. D.8 (b) shows the results, and its inset also shows φ as a function of J for all values of D investigated. $|D| = 0\,\mathrm{mJ\,m^{-2}}$ leads to a Bloch wall, $|D| = 1.5\,\mathrm{mJ\,m^{-2}}$ (the upper bound of D found experimentally in previous sections) leads to a Néel wall and $|D| = 0.045\,\mathrm{mJ\,m^{-2}}$ (which was also used in the calculations for Fig. D.8 (a)) leads to an intermediate form. It can be seen from the overlapping velocity vs J curves that these configurations do not influence the bulk STT driven DW motion.

The model in its present form is used to confirm that the contributions to the DW velocity from the STT and SHE can simply be added together, which is essential for the analysis in the presented in Chapter 9. However, quantitative predictions of

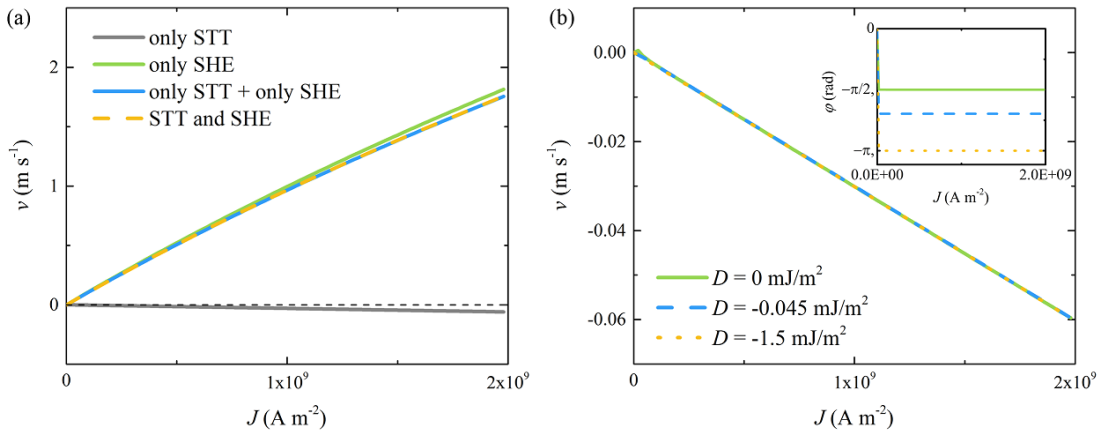

Figure D.8: Calculations with the one dimensional model using parameters from Table D.1 and experimentally relevant current densities. (a) Calculations including only bulk STTs, only SHE and both contributions are shown. (b) DW velocity versus J driven by STT only, for various DMI strengths. Inset shows the corresponding DW angle.

the DW velocity cannot be made. The bulk STT becomes relatively less important compared to the SHE when the magnetic layer becomes thinner. In fact, in Fig. D.8 it can be seen that for the material parameters and sample thickness we use, the SHE is expected to be the dominant contribution. So the possible increase in β when layers become atomically thin, or the change in sign of P or β are not included. If this solved in the future, quantitative predictions could be done. In that case it would also be advisable to account for pinning, add a thermal field and differentiate between the current density in the Co and Pt layer. A good match between these quantitative predictions and the experimental data would strengthen the claim that a negative STT is present in our system.

D.8 DMI direction check

In Chapter 9, the current-induced motion of the skyrmion bubbles is explained as an interplay between a negative bulk spin transfer torque, and the spin Hall effect. In Fig. 3(b) and (d) it can be seen that it is assumed that for a thin top Pt layer the SHE and STT work in concert, while for a thick top Pt layer they oppose each other, for both investigated samples. However, this comparison is only correct if the sign of the net DMI is the same for both samples, because the direction in which a skyrmion bubble is driven is not only determined by the direction of

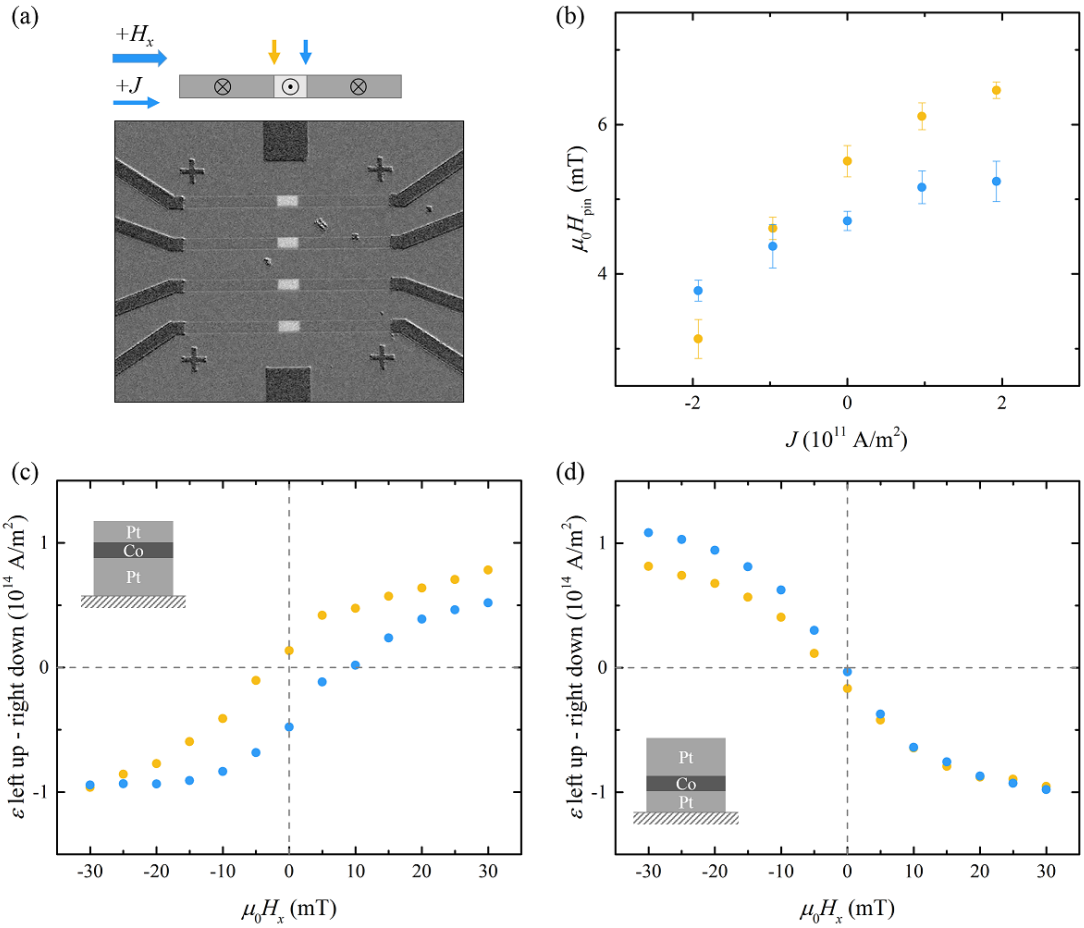

Figure D.9: (a) Kerr microscope image of strips whose middle region is irradiated with Ga^+ ions, and for which the magnetization in these irradiated regions is opposite to the rest of the strip. (b) Typical measurement of H_{pin} as a function of J while a 30 mT magnetic field is applied along the strip. The spin torque efficiencies as a function of magnetic field for Pt (4 nm) / Co (0.6 nm) / Pt (2 nm) and Pt (2 nm) / Co (0.6 nm) / Pt (4 nm) are shown in (c) and (d), respectively.

the spin current, but also by the internal spin structure of the skyrmion bubble wall. The difference between the two investigated samples is the thickness of the bottom Pt layer, which is 4 nm in the one case and 2 nm in the other. Because in a symmetric stack like Pt/Co/Pt the sign of the net DMI is determined by the structural situation at the interfaces, it is not self-evident that this sign will stay the same when the thickness of the bottom layer is changed. Therefore, the sign of the DMI for both cases is checked in this section.

For the DMI measurement, the method that was demonstrated by Haazen *et al.* is used: measurement of the spin torque efficiency. In this measurement a DW is created and pinned. The perpendicular magnetic field required to depin the DW, H_{pin}, is measured as a function of the applied current density and in-plane magnetic field. For this measurement, the strips from section D.3 are adapted. A region in the middle of each strip is irradiated with Ga^+ ions, which lowers the perpendicular magnetic anisotropy. This makes it possible to reliably create DWs that are pinned at the transition between the irradiated and pristine region. Fig. D.9(a) shows a Kerr microscope image of one of the samples. Fig. D.9(b) shows how H_{pin} varies as a function of J for both the left and right DW when H_z is swept from negative to positive while a constant $\mu_0 H_x$ of +30 mT is applied. In order to obtain a better signal to noise ratio, each measurement is repeated ten times, and the error bars show the standard deviation of the ten obtained values. We define the spin torque efficiency as $\epsilon = \mu_0 \frac{\mathrm{d}H_{\text{pin}}}{\mathrm{d}J}$, so the slope of a linear fit through these points*. This measurement is performed for various values of H_x, so that ϵ can be found as a function of H_x, which is shown in Fig. D.9(c) and (d) for the Pt (4 nm) / Co (0.6 nm) / Pt (2 nm) and Pt (2 nm) / Co (0.6 nm) / Pt (4 nm) samples, respectively.

The most striking difference between Fig. D.9(c) and (d) is that one shows an ascending curve and the other a descending curve. This means that the net spin Hall current direction is opposite for both samples, as was already shown in section D.3. To elucidate the sign of the DMI, the behaviour at small H_x has to be examined. For a DMI-free sample, an ϵ versus H_x curve is expected to go through the origin. In that case a Bloch DW is formed when $\mu_0 H_x = 0$ mT, which means that the spins in the wall are aligned with the injected spins by the spin Hall effect, so no torque is exerted. In Fig. D.9(c), this is clearly not the case. There is an opening between the curves for the left and right DW, indicating the presence of a net DMI. The curve for the left wall is shifted towards negative H_x and the curve for the right wall is shifted towards positive H_x. The zero crossings of the curves indicate the points where H_x exactly cancels the effective field induced by

*From the data in Fig. D.9(b) it can be seen that the relation is not exactly linear: there is a quadratic background present caused by Joule heating. The analysis was repeated while disregarding the data points taken at the highest current densities, to check if this Joule heating alters the resulting efficiency curves significantly, but this turned out not to be the case.

the DMI. If the DMI has the same sign for both samples, these zero crossings should be on the same side of the origin in both cases. In Fig. D.9(d) the curve for the left DW is shifted towards negative H_x values as well. However, the opening is much less pronounced in this figure, which is an indication of a smaller net DMI. In summary: the direction of the net spin Hall current is opposite for the Pt (4 nm) / Co (0.6 nm) / Pt (2 nm) and Pt (2 nm) / Co (0.6 nm) / Pt (4 nm) samples while the sign of the net DMI is the same (though the DMI for the Pt (2 nm) / Co (0.6 nm) / Pt (4 nm) sample is significantly smaller). This is all in agreement with the interpretation of current-driven bubble motion in Chapter 9.

The points where the curves intersect with the horizontal axis indicate the strength of the effective DMI field, H_{DMI}. Via $H_{\mathrm{DMI}} = \frac{D}{\mu_0 M_{\mathrm{S}} \lambda}$ this can be related to the DMI constant. From Fig. D.9(c) it can be seen that $\mu_0 H_{\mathrm{DMI}} \approx 10\,\mathrm{mT}$ for the Pt (4 nm) / Co (0.6 nm) / Pt (2 nm) sample, which corresponds to $|D| = 0.045$ - $0.081\,\mathrm{mJ\,m^{-2}}$ when assuming $A = 5$ - $16\,\mathrm{pJ\,m^{-1}}$, $M_{\mathrm{S}} = 1.3\,\mathrm{MA\,m^{-1}}$, and $K_{\mathrm{eff}} = 0.41\,\mathrm{MJ\,m^{-3}}$ (see section D.1). This value for $|D|$ is significantly lower than what was found based on the typical domain sizes at remanence as presented in section D.1. There are several possible explanations for this discrepancy. First, in the depinning efficiency measurements the DMI is actually measured for the part of the sample that is irradiated with Ga^+ ions, while the typical domain size method is applied to the pristine material stack. The effect of ion irradiation on the DMI is still an unexplored subject, but as it has a strong effect on the anisotropy, which is also an interface effect, it is not unlikely that it significantly alters the DMI. Secondly, the thickness of the Co layer is different in the two experiments. Because the DMI is an interface effect, and in the value of D this interaction is averaged over the magnetic layer thickness, D is expected to be larger for small layer thicknesses when the interfaces stay the same. However, the change in thickness is not large enough to account for a difference in D as large as we find. Also, a change in layer thickness could affect the quality of the interfaces themselves. However, because the change in thickness is very small (less than 2 Å) the change in interface quality is also expected to be small. Last, for both methods, the eventual calculation of D requires the value of the exchange constant, A. For this parameter the literature value was used, and the possibility that this value is reduced because the extremely small thickness of the magnetic layer is considered. However, it is possible that A

is reduced even further than we have accounted for. Both methods would result $|D| = 0.028\,\mathrm{mJ\,m^{-2}}$ if $A = 1.9 \times 10^{-12}\,\mathrm{J\,m^{-1}}$.

D.9 GMR measurements

As mentioned in Chapter 9, a negative STT-like effect, similar to our observations, was observed in a study on DW motion in a material system almost identical to ours [152]. In this work, the claim that the observed effect was a negative nonadiabatic bulk spin transfer torque was supported by the observation of a negative spin polarization in the ultrathin Co layer. This could be observed using giant magnetoresistance (GMR) measurements. The electrical resistance a system consisting of two magnetic layers separated by a non-magnetic spacer layer depends on the orientation of the magnetization in the layers. When both magnetic layers have a positive spin polarization, the resistance is lower in the case that magnetization directions are parallel to each other than in the antiparallel case. If one of the layers has a negative spin polarization, the opposite is expected: the resistance should then be higher in the parallel configuration. In this section, we present GMR measurements on our own samples to contribute to the discussion on the underlaying mechanism of the observed effect.

For the GMR measurements the following material stack is grown: Pt (4.0 nm) / Co (0 - 0.8 nm) / Pt (3.0 nm) / Co (1.0 nm) Pt (3.0 nm). The two bottom layers are identical to the ones used for the measurements Chapter 9. We have chosen the thickness of 3.0 nm for the Pt spacer layer, because Je *et al.* have successfully performed their measurements using this spacer layer thickness. The Co layer with constant thickness is chosen to be 1.0 nm. At this thickness the layer is expected to have PMA and to have a significantly different switching field from the bottom Co layer. We only expect a negative spin polarization in the thinnest Co layer, because both experimental observations that cannot be explained by the SHE or traditional STT (by us and by Je *et al.*) are made in the atomically thin regime. This expectation is supported by the theoretical prediction of a negative spin polarization in CoPt alloys with a large percentage of Pt [195].

The sample behaves as expected: the switch of the top Co layer is always visible in the MOKE signal, also when the bottom layer thickness is below the skyrmion

transition, see Fig. D.10(a). Around a thickness of 0.35 nm some additional curvature appears in the signal, which is caused by the bottom Co layer (Fig. D.10(b)). The contribution from this layer evolves via an 'S' shaped curve (Fig. D.10(c)), as was observed before at the skyrmion transition in single layers, to a sharp switch (Fig. D.10(d)). When the thickness of the bottom Co layer increases further, its switching field increases (Fig. D.10(e)) until it coincides with the switching of the top Co layer and the individual contributions cannot be distinguished anymore from the loops Fig. D.10(f).

Surprisingly, the 'S' shaped switch does not appear around 0 mT, but around 4 mT, contrary to what was observed earlier for a sample with only one magnetic layer. When measuring a full hysteresis curve, the bottom Co layer switch appears around +4 mT, in the up going curve and around −4 mT, in the down going curve. However, when a minor loop is taken (so the field sweep reverses before the top layer switches) the switch also appears at +4 mT, in the down going curve. This suggests that the deviation from 0 field is caused by coupling to the top Co layer. Given that the coupling is through 3 nm of Pt and that it is ferromagnetic, several mechanisms are possible: direct exchange via induced moments, RKKY coupling [196] or orange peel coupling [197]. Which of the these is dominant is not clear at this moment.

The sample is now examined by Kerr microscope. The skyrmion transition is observed, but instead of bubbles a more dendrite-like structure appears (Fig. D.10(g)). This seems to suggest that the aforementioned interlayer exchange coupling somehow destabilizes the skyrmion bubble state. Also the nature of the switches can be observed in the Kerr microscope. Above the skyrmion transition, the bottom Co layer switches by DW motion (Fig. D.10(h)). The top layer switches via nucleation (Fig. D.10(i)).

Next, the resistance of the sample is measured simultaneously with a hysteresis curve at several positions. The resistance measurement is performed in a current in-plane (CIP) geometry: contacts are put on the sample via wirebonding and an Agilent multimeter is used to measure the resistance. The thickest and thinnest investigated regions of the sample are approximately 0.5 cm apart, corresponding to a 0.2 nm difference in the bottom Co layer thickness (based on comparison to

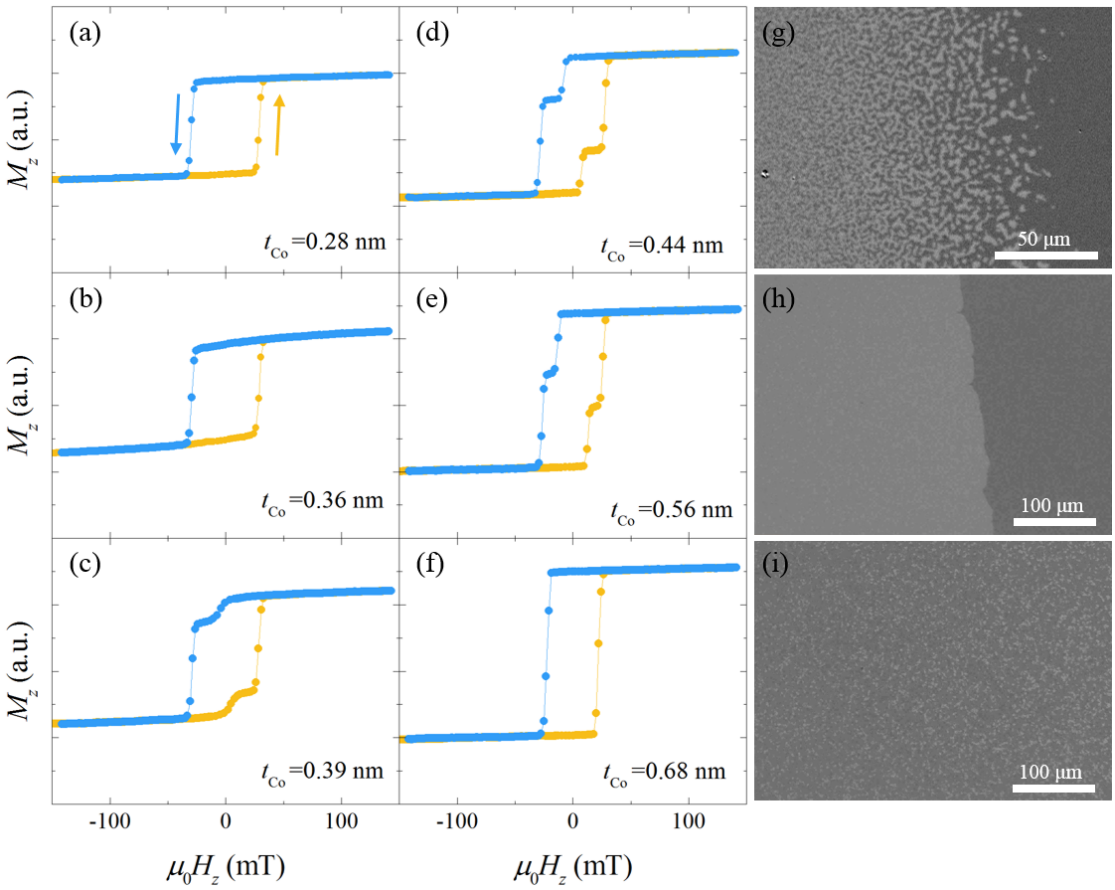

Figure D.10: (a-f) M_z versus H_z curves measured at various t_{Co} along the Pt (4.0 nm) / Co (t_{Co}) / Pt (3.0 nm) / Co (1.0 nm) / Pt (3.0 nm) sample. The yellow branches are measured while sweeping from negative to positive fields, while the blue branches are measured while sweeping from positive to negative fields, as indicated by the arrows. (g-i) Kerr microscope images of (g) the domain structure of the bottom Co layer at $t_{Co} \approx 0.4$ nm (h) the switching of the bottom Co layer at $t_{Co} \approx 0.5$ nm (i) the switching of the top Co layer.

the earlier presented MOKE measurements, corresponding to a range from 0.3 - 0.5 nm).

At the thickness for the curve in Fig. D.11(a) (approximately 0.5 nm), the bottom Co layer behaves like a normal ferromagnetic layer with PMA. Because its coercivity is lower than the top layer's, an antiparallel situation is found for certain fields. When changing between parallel and antiparallel magnetization, the resistance shows a clear response. The resistance is higher in the antiparallel situation, as it should be for two layers with a positive spin polarization.

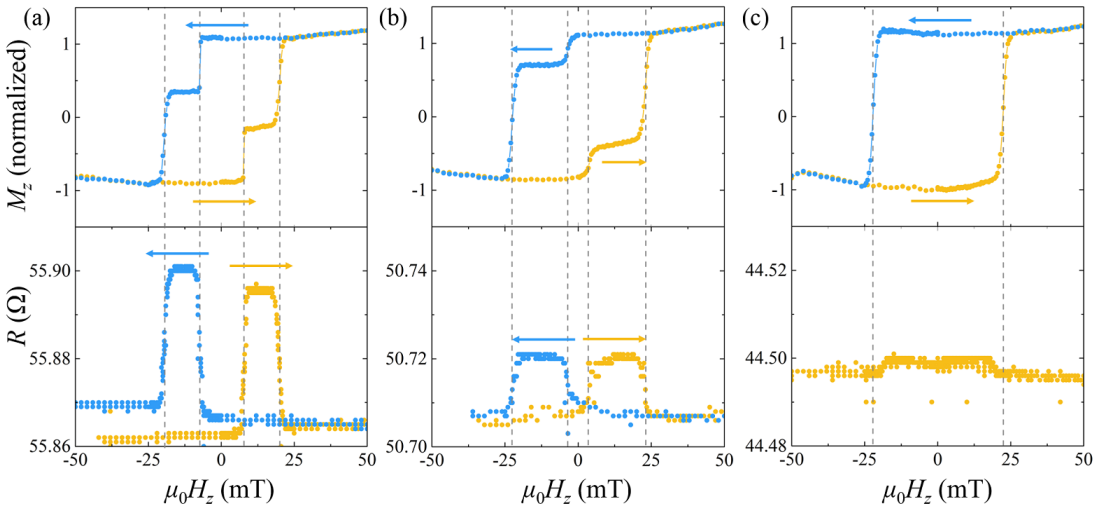

Figure D.11: M_z and R as a function of H_z. The arrows indicate the sweep direction. Measurements are taken on a Pt (4.0 nm) / Co (t_{Co}) / Pt (3.0 nm) / Co (1.0 nm) / Pt (3.0 nm) sample, with t_{Co} is (a) 0.5 nm (b) 0.4 nm (c) 0.3 nm.

At the thickness for the curve in Fig. D.11(b) (approximately 0.4 nm) the field of view comprises the skyrmion transition and a thinner part of the sample (so without PMA). The switching field for the bottom layer is decreased, and takes place around 4 mT. The switch looks less sharp. We still observe an increase in resistance for the antiparallel state, so again a GMR effect without any sign of a negative spin polarization.

Last, Fig. D.11(c) shows the results at about 0.3 nm, which is clearly thinner than the skyrmion transition thickness. The resistance curve is now an almost perfectly flat line.

In summary, we did not observe an inverse GMR for any of the investigated Co thicknesses, including the atomically thin regime. This seems to suggest that the spin polarization in the Co layer is always positive (which does not explain why there should be a negative STT) and to be in disagreement with the observations of Je *et al.* An important difference with the measurements of Je *et al.* is that they used a current perpendicular to the plane geometry (CPP), while we used a CIP geometry. Though there have been reports of negative GMR using CIP measurements [198, 199], it has also been reported that an inverse GMR was measured in CPP geometry, while a normal GMR was measured in CIP geometry in

the same sample [200]. This is explained by a weaker influence of spin dependent bulk scattering in the CIP geometry, caused by both the shorter scaling length in this geometry and the so-called channeling effect. This could be the explanation for the discrepancy between our measurements and those of Je *et al.* CPP measurements require a significant change in sample and experimental setup, and are therefore beyond the scope of this thesis.

D.10 Néel skyrmion bubbles?

Besides measurements discussed in section D.1 and section D.8, DW velocity measurements under the influence of in-plane magnetic fields and Brillouin light scattering measurements were performed on our material stack in order to determine the DMI constant. For the velocity measurements, the data could not be explained by current theories, and for Brillouin light scattering the DMI strength turned out to be below the sensitivity threshold. These issues and the different values for D found in previous sections demonstrate how the measurement of the DMI strength remains a non-trivial task to this day. In this section, we will discuss that it is possible that the walls of the skyrmion bubbles studied in Chapter 9 are not fully in a Néel configuration, and that this does not contradict the conclusions of Chapter 9.

It can be calculated what critical value of the DMI constant, D_c is required to force a DW to take on a Néel configuration by [57]

$$D_c = \frac{4\lambda K_{ip}}{\pi}, \tag{D.10}$$

where K_{ip} is the shape anisotropy constant of the DW, which can be calculated by $K_{ip} = \frac{N_x \mu_0 M_S^2}{2}$. In turn, N_x is a demagnetization factor, which can be calculated by $N_x = \frac{t_{Co} \ln 2}{\pi \lambda}$ [201]. For the material parameters measured at the skyrmion bubble transition ($t_{Co} = 0.44\,\mathrm{nm}$, $K_{eff} = 0.1\,\mathrm{MJ\,m^{-3}}$, and $M_S = 1.0\,\mathrm{MA\,m^{-1}}$) this results in $D = 0.1\,\mathrm{mJ\,m^{-2}}$. The DMI constant that followed from the domain size analysis is larger than this value, which implies that the DWs are in a Néel configuration. However, the DMI constant that followed from the depinning efficiency measurements is smaller than this value. For values of D between 0 and D_c there

is a gradual transition from the Bloch to the Néel configuration [57]. This means that based on the DMI measurements performed, we cannot be certain whether the observed skyrmions bubbles are in a complete or partial Néel configuration.

For SHE driven motion, the internal orientation of the magnetization inside the DW is of utmost importance: for a Bloch wall in a nanowire the injected spins are aligned parallel to the localized spins inside the DW, and no torque is exerted, while for a Néel wall these are oriented perpendicular to each other, leading to a maximum torque. For the bulk STT the situation is different: spins get polarized when flowing through an up or down domain, so they will never be aligned parallel to the spins inside the DW, regardless of whether it is a Bloch wall or a Néel wall. In section D.7 it was shown using a one dimensional model that no difference in velocity or direction of DW motion is expected when it is purely STT driven. In Chapter 9, the velocity as a result of the SHE and STT as a function of Pt thickness is calculated, but a phenomenological constant has to be used to make the ratio between the SHE and STT contributions match the experimental data. If the walls would only be partially in a Néel configuration, this could be part of the explanation of why the SHE is smaller than the negative STT, while it is usually the dominant contribution.

E

Supplementary information on Chapter 10

E.1 Material properties

In the thin wall model [27, 145] the energy of a cylindrical magnetic domain in a infinite film is calculated with respect to the uniformly magnetized situation. The magnetic material has perpendicular magnetic anisotropy, an external magnetic field is applied along the film normal, and it is assumed that the size of the domain is large compared to the width of the domain wall (DW) surrounding it. The size and stability of skyrmion bubbles can be calculated using this model, and is determined by the balance between the Zeeman energy (E_{Z}), the DW energy (E_{DW}) and the dipolar stray field energy (E_{dip}):

$$E_{\mathrm{sk}} = E_{\mathrm{Z}} + E_{\mathrm{DW}} + E_{\mathrm{dip}}. \tag{E.1}$$

These contributions can in turn be expressed in terms of the external magnetic field (H_z), the saturation magnetization (M_{S}), the magnetic film thickness (t), the skyrmion bubble radius (R), the DW energy per unit area (σ), and the vacuum permeability (μ_0):

$$E_{\mathrm{Z}} = 2\mu_0 H_z M_{\mathrm{S}} \pi R^2 t, \tag{E.2}$$

$$E_{\mathrm{DW}} = \sigma 2\pi R t, \tag{E.3}$$

$$E_{\mathrm{dip}} = \frac{2\mu_0}{3} t^3 M_{\mathrm{S}}^2 d \left[d^2 + \left(1 - d^2\right) \frac{E(u^2)}{u} - \frac{K(u^2)}{u} \right]. \tag{E.4}$$

Here $d = \frac{2R}{t}$ and $u^2 = \frac{d^2}{1+d^2}$ are defined for convenience, and $K(u^2)$ and $E(u^2)$ are the complete elliptical integrals of the first and second kind, respectively.

The material parameters occuring in these equations determine the skyrmion bubble size, and whether or not skyrmion bubbles are stable at all. Therefore, we determine these parameters experimentally in this section, using a full sheet sample of the material stack used for the structures created by electron beam lithography.

The magnetic layer thickness is determined simply by the growth rate and deposition time of the situation where skyrmion bubbles are stabilized, and was found to be $0.7 \pm 0.1\,\mathrm{nm}$. The external magnetic field can be determined by checking at what field skyrmion bubbles are found. This should be done with caution: because the used magnetic fields are extremely small, any field present in the surroundings is relevant. We therefore take the field relative to the field at which the labyrinth structure occurs, which should be at remanence. This way we circumvent possible deviations in the field calibration. The obtained stabilizing field is $0.08 \pm 0.01\,\mathrm{mT}$.

M_{S} and K_{eff} are extracted from the hysteresis curve obtained by SQUID VSM measurement, as shown in Fig. E.1. M_{S} follows from the magnetic moment measured at saturation and the sample surface and amounts to $0.43 \pm 0.08\,\mathrm{MA\,m^{-1}}$. Here, we have corrected the raw SQUID data for the shape and size of the sample[202]. Additionally, we have determined the magnetically dead layer in our sample using MOKE, see Fig. E.2(a), which is determined to be $1.1 \pm 0.2\,\mathrm{nm}$. Because the magnetic field is applied parallel to the sample surface, a hard axis loop is expected for a sample with perpendicular magnetic anisotropy, and the anisotropy constant can be deduced from the saturation field (B_K), via $B_K = \frac{2K_{\mathrm{eff}}}{M_{\mathrm{S}}}$. The result is $K_{\mathrm{eff}} = 5.0 \pm 0.7 \times 10^4\,\mathrm{J\,m^{-3}}$. However, note that the measured loop is not a perfect hard axis loop, and this result should be treated with caution. Based on this result, and assuming that the exchange constant, A ranges from $5\,\mathrm{pJ\,m^{-1}}$ to

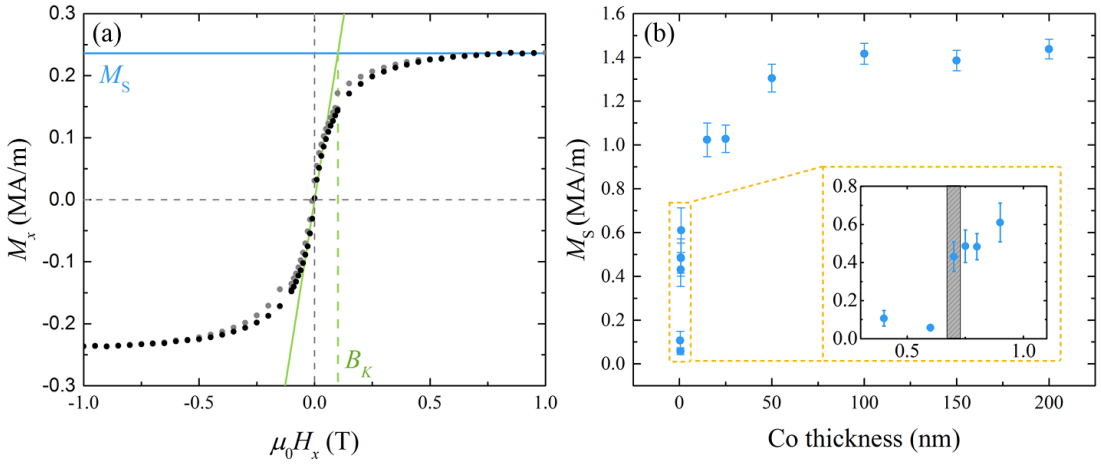

Figure E.1: (a) SQUID VSM measurement of a full sheet sample with a Co thickness suitable for skyrmion bubble stabilization. The magnetic field is applied along the sample plane. (b) Saturation magnetization as a function of Co thickness, measured using SQUID VSM. Inset shows a close-up of the region relevant for skyrmion bubble stabilization.

$16\,\mathrm{pJ\,m^{-1}}$, the DW width (λ) can be calculated using $\lambda = \sqrt{A/K_{\mathrm{eff}}}$. The result is $\lambda = 9\,\mathrm{nm}$ to $20\,\mathrm{nm}$, which is significantly smaller than the micrometer scaled domains, justifying the use of the thin model.

The DW energy can be extracted from the typical domain size (L) of the labyrinthine structure found at remanence, via:

$$L = \alpha t \exp \frac{\pi\sigma}{\mu_0 M_S^2 t}, \tag{E.5}$$

where $\alpha \approx 0.955$ is a constant [145]. To obtain this typical domain size, a two dimensional fast Fourier transform was performed on the images taken by Kerr microscope, as shown in Fig. E.1(b). The result is $\sigma = 0.41 \pm 0.05\,\mathrm{mJ\,m^{-2}}$. With these paremeters, the DMI constant D can be calculated using $\sigma = 4\sqrt{AK_{\mathrm{eff}}} - \pi D$, resulting in a D ranging from $0.6\,\mathrm{mJ\,m^{-2}}$ to $1.1\,\mathrm{mJ\,m^{-2}}$. This is smaller than values for similar stacks in literature [50, 145], which is related to the relatively low anisotropy in our samples. The low anisotropy is possibly caused by the fact that we grow very slowly to have optimal thickness control ($<0.01\,\mathrm{nm\,s^{-1}}$).

Now these values are combined in the energy equations. It turns out that the com-

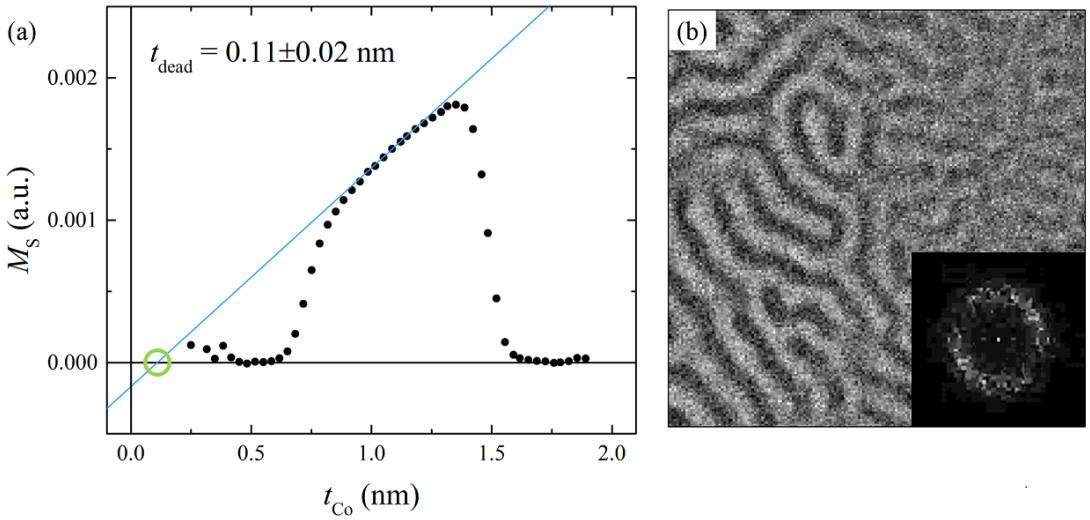

Figure E.2: (a) Magnetic MOKE signal as a function of Co thickness. The the intersection of the linear fit with the horizontal axis indicates the magnetically dead layer. (b) Typical Kerr image of the labyrinthine domain structure observed at remanence. Inset is the 2D FFT of the image.

bination of parameters needed for skyrmion bubble stabilization is delicate in the regime we are investigating: within the experimental uncertainty of the parameters both the situation that bubbles are stable as the situation in which they are not can be obtained. Therefore the typical radius of the bubbles is determined experimentally from the Kerr microscope images and was found to be $1.34 \pm 0.10\,\mu m$. The other parameters can now be tuned such (of course within their uncertainty range) to correspond with the existence of $1.34\,\mu m$ sized skyrmion bubbles. We expect this combination of parameters to correctly represents the experimental situation, and therefore these are the parameters that are subsequently used to calculate the effect of a decrease in the dipolar energy contribution. This is done by a adding a artificial factor p to equation E.1, resulting in

$$E_{sk} = E_Z + E_{DW} + pE_{dip}. \tag{E.6}$$

We find that for our material parameters, the minimum in the E_{sk} vs R curve disappears at $p = 0.93.4$ (see again Fig. E.3), indicating that skyrmion bubbles are no longer stable. In Chapter 10 this result is linked to a specific distance between skyrmion bubble and strucutre edge, and it can be checked experimentally that no

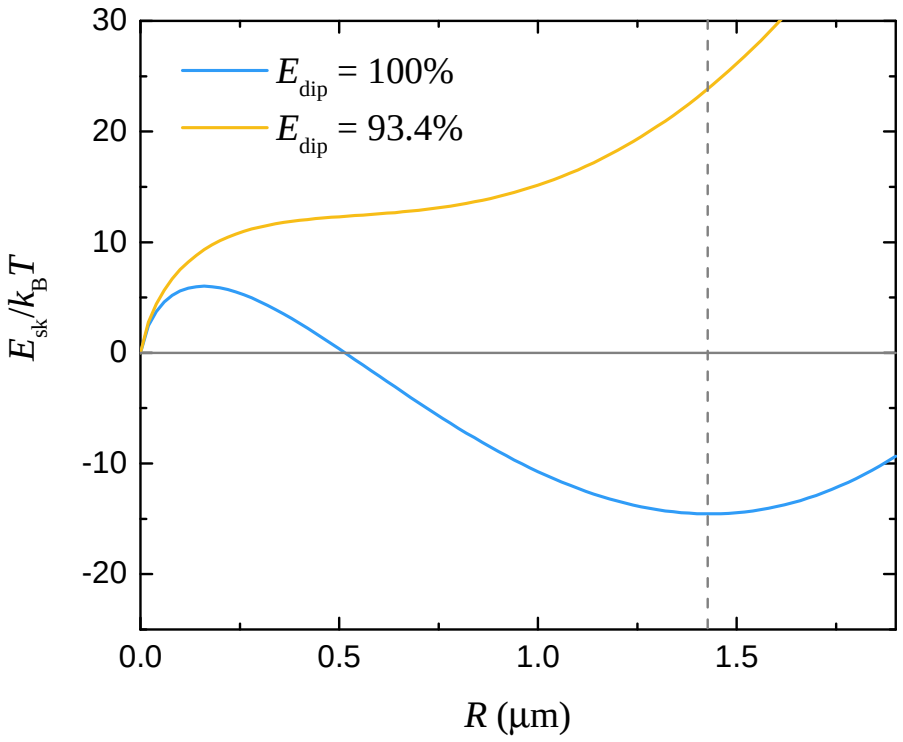

Figure E.3: Skyrmion bubble energy as a function of bubble radius, calculated by the thin wall model. The blue curve represents the standard result, while for the yellow curve the dipolar energy term is reduced by a factor 0.934. The used parameters are $t_{Co} = 0.7\,\mathrm{nm}$, $\mu_0 H_z = 0.07\,\mathrm{mT}$, $M_S = 0.43\,\mathrm{MA\,m^{-1}}$, and $\sigma = 0.41\,\mathrm{mJ\,m^{-2}}$.

skyrmion bubbles are stable anymore beyond this distance. However, please also note the assumptions that were made during this analysis. For the calculation of the boundary, the skyrmion bubble size as determined in an unpatterned film was used. However, because the bubble size depends on the dipolar stray fields, it is expected to be different in a confined geometry close to the edge. Because the skyrmion bubbles in confined structructures that were observed seem comparable in size to the bubbles in the unpatterned film, we choose to neglect this effect. Also, this analysis was performed using parameters that were determined for the structures produced by EBL. The FIB structures have slightly different material parameters, as indicated by the difference in bubble size, and the different in

the external field necessary for stabilization. Nevertheless, the experimentally observed skymrion bubbles seem to adhere to the calculated boundaries adequately.

E.2 Methods

All material stacks shown in this work are grown using sputter deposition. Using a deposition tool with a low base pressure of typically $< 10^{-8}$ mbar , fully automated growth sequences, and sample rotation during deposition, we reproducibly create full sheet samples in which skyrmion bubbles can be stabilized within areas of several square millimeters large. After deposition of the material stack, there are two ways to proceed, resulting in the two types of samples that are presented. For the first, a sample in which skyrmion bubbles are stable is selected and coated with ma-N 2410, which is a negative resist. The desired structures are written using EBL, and the exposed resist forms a hard mask. After development, ion-beam milling, and cleaning with acetone, a magnetic structure with a sharp edge remains. Alternatively, a region on the sample in which skyrmion bubbles are not stable can be selected, in particular where the perpendicular magnetic anisotropy is slightly too strong for skyrmion stabilization, and the material properties can be modified locally to create a small area in which they are stable. For the local modification of material properties, a Ga focussed ion beam (FIB) is used. This is an established technique to lower magnetic anisotropy [26, 73, 180], and the anisotropy gradient that is created at the boundary has been shown to be ± 22 nm wide for the fabrication tool we use [90]. Besides the work of Zhang *et al* in which FIB is used to create circular shapes with in-plane magnetization within an out-of-plane magnetized film to create an artificial skyrmion lattice [203], this is this to our knowledge the first time that this technique is employed to stabilize skyrmions. An energy of 30 keV and a dose of 1.25×10^{12} ions/cm^2 is used.

For the presented calculations in Fig. 10.4 on the dipole-dipole energy, a system of 10000 cells with dimensions of $450\,\text{nm} \times 450\,\text{nm} \times 0.7\,\text{nm}$ is defined. Because we consider a large range of bubble-edge distances, a relatively large cell size is used to reach acceptable calculation times. This leads to a bubble which is not entirely circular. The total area of the simulated bubble is 12% smaller, which is within the uncertainty range of the experimental determined average bubble

area. Due to relatively large variation of the bubble size and shape during the experiment, the imperfect bubble shape are not expected to significantly influence the qualitative behavior of the model. The direction of the magnetization for each cell is defined in such a way that the investigated structure, the skyrmion bubbles and the surrounding of the structure are mimicked. The energy resulting from dipolar interactions, E_{dip} between the cells can be calculated using the classical formula for two magnetic dipoles μ_{i} and μ_{j} whose positions are connected by a vector r_{ij}:

$$E_{\mathrm{dip}} = \frac{\mu_0}{4\pi}\left[\frac{\mu_i \cdot \mu_j}{r_{\mathrm{ij}}^3} - \frac{(\mu_i \cdot r_{\mathrm{ij}})\,(\mu_j \cdot r_{\mathrm{ij}})}{r_{\mathrm{ij}}^5}\right]. \tag{E.7}$$

For some geometries, it is possible to calculate the expected skyrmion bubble positions using the same type of calculations. It is experimentally determined how many skyrmion bubbles are present in a certain geometry at a certain external magnetic field, and E_{dip} is now calculated for various positions of these skyrmion bubbles (for these calculations lateral cell sizes ranging from 40 nm to 80 nm are used). This makes it possible to extract what would energetically the most favorable position of the bubbles when only dipolar interactions are considered, and these are marked in white in the data plots. We have performed this analysis only for those cases where there is already a clear expectation of the bubble possitions based on symmetry, which limits the number positions that needs to be investigated, and hence the computational time. In priciple, extending these simulations to a Monte Carlo method would enable the investigation of the geometries that contain more complex bubble configurations.

E.3 Overview shapes and sizes

In Chapter 10 only a selection of the investigated shapes and sizes is shown, in view of the legibility of the paper. In this section we show a more complete overview of the obtained results. Fig. E.4 shows the results for all shapes created by EBL in which skyrmion bubbles could be stabilized. The same analysis procedure and data representation as in Fig. 10.2 and Fig. 10.3 are used. When examining the complete collection of measurements, some general trends can be observed. Larger

structures can contain more skyrmion bubbles simultaneously. For the smallest structures, the bubbles are strongly confined to a preferential position. The larger the structures become, the smaller the influence of the edge becomes, and the more freely the bubbles can move around (though some preference for certain positions remains observable for all structure sizes investigated). The general observations agree well with our interpretation based on dipolar interactions, but in this section we will discuss some noteworthy individual cases.

First, there is the 8 µm sized circle, in which there are no distinct preferential positions visible, but a rather smeared out region. In the individual frames of the Kerr microscope movie, two individual skyrmion bubbles that occupy the structure simultaneously, can be identified. In the analysis of the complete movie, it can be seen that these bubbles have a preferred distance from the centre, but other than that they seem distributed randomly. The symmetric nature of the circle is well reflected in these results, in stark contrast with the results for the square and triangles. When examining the 15 µm sized circle, this symmetry is no longer present in the observations. Probably, there is an energy minimum caused by local variations in the material parameters that fixes the position of one skyrmion bubble, which in turn fixes the positions for the rest of the bubbles.

Just as in Chapter 10, the boundaries of the regime in which skyrmion bubbles are stable are indicated by the dashed lines. In most cases, these boundaries fit well with the observed bubble positions. The 8 µm sized circle and 8 µm sized square are exceptions: there are numerous observations of bubbles that seem to extend beyond the boundaries. Here we should realize that the software extracts only the bubble position, not its shape or size. The size of the red circles in Fig. E.4 is based on the average value for skyrmion bubbles in an unpatterned sample of the same material stack. In the thin wall model, as worked out in section E.1, the equilibrium size of a bubble is codetermined by the dipolar energy, and hence it will change in the proximity to another bubble or to the structure edge. Hitherto we have ignored the dependence of the bubble size on its distance to the edge and to other bubbles, to not overcomplicate our analysis. Also, it is conceivable that in an asymmetric environment (for example, when on the one side there is interaction with the structure edge, while on the other side there is interaction with another bubble) the equilibrium shape of a bubble can deviate from a circle,

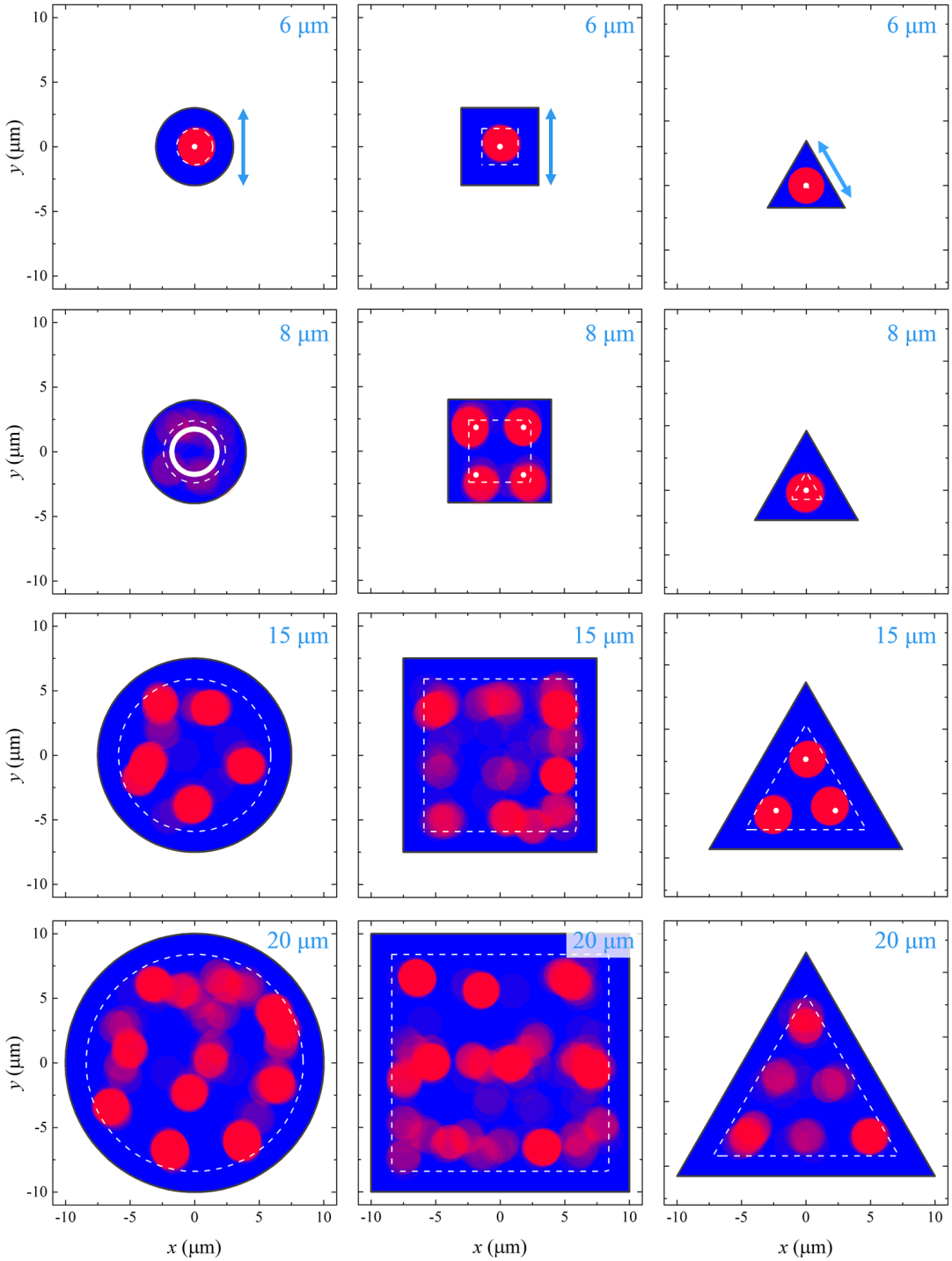

Figure E.4: Overview of the skyrmion bubbles detected in all investigated shapes and sizes created by EBL. The boundaries of the bubble stability regions are indicated by dashed lines, and for the straightforward configurations the calculated equibrium positions for the centres of the bubbles are indicated in white.

while the data is represented as perfect circles. Apparently, for the two mentioned structures, the ratio between the number of bubbles and the structure area is such that these additional effect become relevant, and a representation by average bubbles in infinite films is inaccurate.

For the 6 µm sized triangle, a bubble with the equilibrium size as found for the unpatterned film does not fit within the stability region. However, when processing the Kerr microscope images, our software consistently detects a skyrmion bubble at the centre of the triangle. Possibly the same complications as for the 8 µm sized circle and 8 µm sized square could play a role, and the bubble present in this structure is smaller than a bubble in an infinite film. However, there is also the possibilty that the inverted domain actually reaches the edges, and that it is not a bubble at all, but from the Kerr microscope footage it is not possible to conclude this with certainty.

Summary

Over the recent years researchers have been fascinated by the newly discovered interfacial Dzyaloshinskii-Moriya interaction (DMI) in thin film systems. This antisymmetric type of exchange interaction prefers a rotation of neighboring spins with respect to each other, which can lead to exotic magnetic structures like magnetic skyrmions: small, mobile whirls in the magnetization in which the spins rotate with a specific handiness. Also for magnetic domain walls (DWs), the narrow regions between uniform magnetic domains where the magnetization gradually rotates, the DMI has a strong influence on the dynamic properties. Besides the scientific interest, DMI is technologically relevant as both DWs and magnetic skyrmions are ideal candidates for encoding data in in the novel racetrack memory. In spite of all the attention and research efforts, DMI measurements remain cumbersome: the interpretation of the data is often non-trivial, most techniques pose specific requirements to the material and geometrical properties of the sample and there is a significant variation in reported DMI strengths literature even when the same materials are investigated. Part I of this thesis focusses on DWs in material stacks with non-zero DMI. Special attention is paid to observations directly related to the DMI with the potential to develop alternative DMI measurement techniques. In part II of this thesis magnetic skyrmions are investigated. Since these structures only recently became experimentally accessible, they pose many new experimental opportunities.

The samples studied in this thesis are produced by sputter deposition and standard electron beam lithography and lift-off techniques, in some cases followed by irradiation with a focused ion beam. This last technique allows for local control of the magnetic anisotropy. Part I starts with a study on magnetic micro wires which are partially irradiated with Ga ions, which causes the formation of pinning sites for DWs. The pinning strength is found to be controllable by a magnetic field di-

rected along the length of the wires, which is a direct consequence of the DMI. Also, we show that this effect can be exploited to move multiple DWs synchronously through a magnetic wire, results in a device that is basically a current-free race-track memory. We also theoretically investigated what happens when an in-plane magnetic field is applied to a domain wall pinned at an anisotropy barrier, and it turns out that on short time scales. Last, we studied DWs in magnetic wires that were not irradiated, so the DWs are free to take on any geometrical configuration that is energetically most favorable. The observed configurations where non-trivial and depended on the strength and direction of the applied magnetic field. Again, DMI is needed to explain the observed behavior.

In the second part of this thesis, we study an exotic magnetic structure: the magnetic skyrmion bubble. This is basically a large version of a 'normal' magnetic skyrmion. It is shown how these structures can be created and that they can be moved by an electrical current. The observed reaction to the electrical current turns out to be in contrast with the prevailing theories on skyrmion (bubble) motion. According to literature, skyrmion bubble motion is mainly governed by the spin Hall effect, but we demonstrate that reversing the dominant contribution of the spin Hall effect does not lead to a reversion in the direction of skyrmion bubble motion. This implies that there is an additional force driving the skyrmion bubble motion, which is both fundamentally and technologically of interest. Last, we study confinement of these skyrmion bubbles in small structures. A clear interaction between the skyrmion bubbles and the structure edge is observed. We conclude that the dominant mechanism for the bubble-edge interaction are dipolar interaction, which is different from what is the case for small skyrmions. We also explore ion irradiation as a means to create the parameter space in which skyrmion bubbles can be stabilized, which eliminates the need of a wedge shaped material stack, increasing the potential for industrial applications.

Curriculum Vitae

Franciska (Fanny) Chrétien Ummelen was born on November 17, 1990 in Roermond, the Netherlands. She went to high school at the 'Bisschoppelijk college Schöndeln' in Roermond, the Netherlands. Here she participated in the physics olympiad and qualified for the international competition, where she obtained an honorable mention. In 2009 she finished her high school education *cum laude*.

She then studied Applied Physics at Eindhoven University of Technology, where she obtained her Bachelor of Science degree *cum laude* in 2012, after completing her final project on growth and transport properties of multilayer graphene in the Molecular Materials and Nanosystems group under the supervision of dr.ir. Kees Flipse.

She continued her studies at Eindhoven University of technology to pursue a Masters degree. During her Master studies she visited the Thin Film Magnetism group of prof. Russell Cowburn at the University of Cambridge, United Kingdom, where she worked on canted states in magnetic bilayers under the supervision of dr. Amalio Fernández-Pacheco. She did her graduation project back in Eindhoven in the Physics of Nanostructures group of prof.dr. Bert Koopmans and prof.dr.ir. Henk Swagten on moving magnetic domain walls using a precesion torque, and obtained her Masters degree *cum laude* in 2014.

After this, she started her PhD research in that same group on the topic of spin-orbitronics. This lead to various publications and conference visits, and finally to this dissertation.

Publications

F.C. Ummelen, T. Lichtenberg, H.J.M. Swagten, and B. Koopmans, Controlling skyrmion bubble confinement by dipolar interactions, *Applied Physics Letters* **115**, 102402 (2019).

A. Fernández-Pacheco, E.Y. Vedmedenko, **F.C. Ummelen**, R. Mansell, D.C.M.C. Petit, and R.P. Cowburn, Symmetry-breaking interlayer Dzyaloshinskii–Moriya interactions in synthetic antiferromagnets *Nature Materials* **18**, 679–684 (2019).

F.C. Ummelen, H.J.M. Swagten, and B. Koopmans, Racetrack memory based on in-plane -field controlled domain-wall pinning *Scientific Reports* **7**, 833 (2017).

F.C. Ummelen,A. Fernández-Pacheco, R. Mansell, D. Petit, H.J.M. Swagten, and R.P. Cowburn, Controlling the canted state in antiferromagnetically coupled magnetic bilayers close to the spin reorientation transition *Applied Physics Letters* **110**, 102405 (2017).

M.J.G. Peeters, **F.C. Ummelen**, M.L.M. Lalieu, J.-S. Kim, H.J.M. Swagten, and B. Koopmans, Precession-torque-driven domain-wall motion in out-of-plane materials *AIP Advances* **7**, 055921 (2016).

F.C. Ummelen, D.-S. Han, J.-S. Kim, H.J.M. Swagten, and B. Koopmans, Asymmetric Domain-Wall Depinning Induced by Dzyaloshinskii–Moriya Interaction *IEEE Transactions on Magnetics* **51(11)**, 6000703 (2015).

A. Fernández-Pacheco, **F.C. Ummelen**, R. Mansell, D. Petit, J.H. Lee, H.J.M. Swagten, and R.P. Cowburn, Dynamic selective switching in antiferromagnetically-coupled bilayers close to the spin reorientation transition *Applied Physics Letters* **105**, 092408 (2014).

J.F.M. van Rens, J.T. Schoof, **F.C. Ummelen**, D.C. van Vugt, P.J. Bruggeman,

and E.M. van Veldhuizen, Induced Liquid Phase Flow by RF Ar Cold Atmospheric Pressure Plasma Jet *IEEE Transactions on Plasma Science* **42(10)**, 2622-2623 (2014).

Dankwoord

Mijn tijd bij FNA is een bijzondere periode in mijn leven geweest. Het is vreemd om te beseffen dat die nu echt voorbij is, en dat het daadwerkelijk gelukt is om dit boekje te schrijven, wat op sommige momenten als een onmogelijke opgave voelde. Ik weet zeker dat dit niet gelukt was zonder de hulp en steun van een heleboel mensen, die ik hier wil bedanken.

Ten eerste mijn promotor Henk. Ondanks jouw drukke schema heb je heel veel tijd voor mij vrijgemaakt. Inhoudelijk was je onmisbaar in het richting geven van mijn onderzoek, en zorgde je dat ik de big picture niet uit het oog verloor. Ik heb veel gehad aan jouw feedback, ook met betrekking tot het presenteren en excitement brengen in geschreven tekst. Ook wil ik je bedanken voor het luisteren naar mijn zorgen die niet direct met de natuurkunde te maken hadden.

Ten tweede mijn kamergenoten Mark en Reinoud. Niet alleen was het door hen gezellig en prettig werken op kantoor, maar ook hebben ze veel bijgedragen aan mijn werk. Reinoud jij bent door jouw ervaring een expert op het gebied van zo ongeveer alles binnen FNA (of het nou gaat om een opstelling, een theoretisch model, de literatuur of hoe de organisatie van de faculteit in elkaar zit), dus om jou zo laagdrempelig vragen te kunnen stellen heeft mijn werk een stuk makkelijker gemaakt. Mark, jij hebt mij vaak geholpen als ik tegen een probleem met mijn computer aanliep, en ook dat heeft me dagen van mijn leven gescheeld. Ook vond ik het heel fijn om te kunnen praten die in de zelfde fase van zijn PhD traject zat en daardoor tegen dezelfde dingen aanliep.

Ook aan alle studenten die ik heb mogen begeleiden ben ik veel dank verschuldigd. Marijn, Niek, Tijs, Irina en Vince: bedankt dat ik jullie heb mogen begeleiden tijdens jullie BEP. In het bijzonder wil ik Mark en Tom bedanken die ik een jaar lang heb mogen begeleiden tijdens hun afstudeer project. Dank jullie wel voor

jullie inzet en voor het leveren van werk dat van zulke hoge kwaliteit was dat ik het in mijn proefschrift heb kunnen gebruiken!

Eigenlijk ben ik iedereen binnen FNA dankbaar voor het creëren van een fijne sfeer. In het bijzonder Bert als groepshoofd. Vooral nadat ik een presentatie had gegeven of een PhD meeting had gehad gaf jij inhoudelijke feedback op mijn werk, en wel op zo'n manier dat ik er positieve energie van kreeg. Verder wil ik ook zeker Karin, Gerrie en Jeroen noemen: bedankt voor de praktische hulp en technische ondersteuning!

There are a number of people from outside the TU/e that I want to thank. Amalio, thank you for giving me the chance to participate in synchrotron measurements and involving me in the publications that followed from my traineeship. Nam-Hui, thanks for performing the time consuming the BLS measurements on my samples. Liza, thanks for the nice collaborations and performing the domain wall propagation measurements, I greatly appreciated our discussions over via email. And last, special thanks to the committee members for taking the time to read my thesis and attending my defense ceremony.

Ik heb het werken binnen FNA als heel prettig ervaren, en de professionaliteit en het enthousiasme van alle collega's vond ik zeker niet vanzelfsprekend. Echter nog veel minder vanzelfsprekend vind ik hoe goed men met mij is omgegaan in de periode dat het erg slecht met mij ging, want daar was niemand voor getraind of op voorbereid. Bijzonder dankbaar ben ik voor de flexibele houding van NWO-I waardoor ik toch het promotietraject heb kunnen afronden. Ook wil ik Mariëlle en Karin extra bedanken, omdat zij mij bij de groep zijn blijven betrekken. Henk wil ik bedanken voor zijn eindeloze geduld, respectvolle houding, en het doorstaan van mijn huilbuien. Ook mijn familie is een enorme steun geweest: mam, pap en Bartjan, ik kan jullie niet genoeg bedanken!

Bibliography

1. J. Ellis. "Antimatter matters". *Nature (London, U. K.)* **424,** 631–634 (2003).
2. J. S. Siegel. "Single-handed cooperation". *Nature (London, U. K.)* **409,** 777–778 (2001).
3. T. Solomons & C. Fryhle. *Organic chemistry* 8th ed. (Wiley India Pvt. Limited, 2006).
4. T. Thomson. *Magnetic properties of metallic thin films* (eds Barmak, K. & Coffey, K.) 454 –546 (Woodhead Publishing, 2014).
5. *Artistic sketch of a magnetic domain wall configuration*. Accessed: 2019-04-03.
6. I. Kézsmárki *et al.* "Néel-type skyrmion lattice with confined orientation in the polar magnetic semiconductor GaV_4S_8". *Nat. Mater.* **14,** 1116–1122 (2015).
7. M. N. Baibich *et al.* "Giant Magnetoresistance of (001)Fe/(001)Cr Magnetic Superlattices". *Phys. Rev. Lett.* **61,** 2472–2475 (Nov. 1988).
8. G. Binasch, P. Grünberg, F. Saurenbach & W. Zinn. "Enhanced magnetoresistance in layered magnetic structures with antiferromagnetic interlayer exchange". *Phys. Rev. B* **39,** 4828–4830 (Mar. 1989).
9. I. E. Agency. *IEA, Digitalization & Energy*. 2017.
10. N. Jones. "How to stop data centres from gobbling up the world's electricity". *Nature (London, U. K.)* **561,** 163–166 (2018).
11. A. Andrae, Edler & T. "On Global Electricity Usage of Communication Technology: Trends to 2030". *Challenges* **6,** 117–157 (2015).

12. J. Meena, S. Min Sze, U. Chand & T.-Y. Tseng. "Overview of Emerging Non-volatile Memory Technologies". *Nanoscale Res. Lett.* **9,** 1–33 (2014).

13. S. Zhang, A. A. Baker, S. Komineas & T Hesjedal. "Topological computation based on direct magnetic logic communication". *Sci. Rep.* **5,** 15773 (Oct. 2015).

14. S. Parkin & S.-H. Yang. "Memory on the racetrack". *Nat. Nanotechnol.* **10,** 195–198 (2015).

15. T. A. Moore *et al.* "High domain wall velocities induced by current in ultrathin Pt/Co/AlOx wires with perpendicular magnetic anisotropy". *Appl. Phys. Lett.* **93,** 262504 (2008).

16. S.-H. Yang, K.-S. Ryu & S. Parkin. "Domain-wall velocities of up to 750 ms^{-1} driven by exchange-coupling torque in synthetic antiferromagnets". *Nat. Nanotechnol.* **10,** 221–226 (Feb. 2015).

17. I. Dzyaloshinskii. "A thermodynamic theory of "weak" ferromagnetism of antiferromagnetics". *J. Phys. Chem. Solids* **4,** 241–255 (1958).

18. T. Moriya. "Anisotropic superexchange interaction and weak ferromagnetism". *Phys. Rev.* **120,** 91–98 (Oct. 1960).

19. A. Fert & P. M. Levy. "Role of Anisotropic Exchange Interactions in Determining the Properties of Spin-Glasses". *Phys. Rev. Lett.* **44,** 1538–1541 (June 1980).

20. D. Coffey, T. M. Rice & F. C. Zhang. "Dzyaloshinskii-Moriya interaction in the cuprates". *Phys. Rev. B* **44,** 10112–10116 (Nov. 1991).

21. H. De Raedt, S. Miyashita, K. Michielsen & M. Machida. "Dzyaloshinskii-Moriya interactions and adiabatic magnetization dynamics in molecular magnets". *Phys. Rev. B* **70,** 064401 (Aug. 2004).

22. I. A. Sergienko & E. Dagotto. "Role of the Dzyaloshinskii-Moriya interaction in multiferroic perovskites". *Phys. Rev. B* **73,** 094434 (Mar. 2006).

23. A. Fert. *Magnetic and Transport Properties of Metallic Multilayers*. in *Metallic Multilayers* **59** (Trans Tech Publications, Jan. 1991), 439–480.

24. H. Yang, A. Thiaville, S. Rohart, A. Fert & M. Chshiev. "Anatomy of Dzyaloshinskii-Moriya Interaction at Co/Pt Interfaces". *Phys. Rev. Lett.* **115,** 267210 (Dec. 2015).

25. M. D. DeJong & K. L. Livesey. "Analytic theory for the switch from Bloch to Néel domain wall in nanowires with perpendicular anisotropy". *Phys. Rev. B* **92,** 214420 (Dec. 2015).

26. J. Franken, M. Hoeijmakers, R. Lavrijsen & H. Swagten. "Domain-wall pinning by local control of anisotropy in Pt/Co/Pt strips". *J. Phys.: Condens. Matter* **24,** 024216 (2012).

27. A. P. Malozemoff & J. C. Slonczewski. *Magnetic domain walls in bubble materials* (Academic Press, New York, NY, 1979).

28. L. Landau & E. Lifshits. "On the Theory of the Dispersion of Magnetic Permeability in Ferromagnetic Bodies". *Phys. Zeitsch. der Sow.* **8,** 153–169 (1935).

29. M. Bode *et al.* "Chiral magnetic order at surfaces driven by inversion asymmetry". *Nature (London, U. K.)* **447,** 190–193 (2007).

30. S.-G. Je *et al.* "Asymmetric magnetic domain-wall motion by the Dzyaloshinskii-Moriya interaction". *Phys. Rev. B* **88,** 214401 (Dec. 2013).

31. S Pizzini *et al.* "Chirality-Induced Asymmetric Magnetic Nucleation in Pt/Co/AlO_x Ultrathin Microstructures". *Phys. Rev. Lett.* **113,** 047203 (July 2014).

32. D.-S. Han *et al.* "Asymmetric Hysteresis for Probing Dzyaloshinskii–Moriya Interaction". *Nano Lett.* **16,** 4438–4446 (2016).

33. K. Di *et al.* "Direct Observation of the Dzyaloshinskii-Moriya Interaction in a Pt/Co/Ni Film". *Phys. Rev. Lett.* **114,** 047201 (Jan. 2015).

34. I. Gross *et al.* "Direct measurement of interfacial Dzyaloshinskii-Moriya interaction in X|CoFeB|MgO heterostructures with a scanning NV magnetometer (X = Ta, TaN, and W)". *Phys. Rev. B* **94,** 064413 (Aug. 2016).

35. M. Baćani, M. A. Marioni, J. Schwenk & H. J. Hug. "How to measure the local Dzyaloshinskii-Moriya Interaction in Skyrmion Thin-Film Multilayers". *Sci. Rep.* **9,** 3114 (2019).

36. E. C. Corredor, S. Kuhrau, F. Kloodt-Twesten, R. Frömter & H. P. Oepen. "SEMPA investigation of the Dzyaloshinskii-Moriya interaction in the single, ideally grown Co/Pt(111) interface". *Phys. Rev. B* **96,** 060410 (Aug. 2017).

37. S. Kim *et al.* "Magnetic droplet nucleation with a homochiral Néel domain wall". *Phys. Rev. B* **95,** 220402 (June 2017).

38. S. Rohart & A. Thiaville. "Skyrmion confinement in ultrathin film nanostructures in the presence of Dzyaloshinskii-Moriya interaction". *Phys. Rev. B* **88,** 184422 (Nov. 2013).

39. H. T. Nembach, J. M. Shaw, M. Weiler, E. Jué & T. J. Silva. "Linear relation between Heisenberg exchange and interfacial Dzyaloshinskii–Moriya interaction in metal films". *Nat. Phys.* **11,** 825 (2015).

40. J. Cho *et al.* "Thickness dependence of the interfacial Dzyaloshinskii-Moriya interaction in inversion symmetry broken systems". *Nat. Commun.* **6,** 7635 (2015).

41. R. Soucaille *et al.* "Probing the Dzyaloshinskii-Moriya interaction in CoFeB ultrathin films using domain wall creep and Brillouin light spectroscopy". *Phys. Rev. B* **94,** 104431 (Sept. 2016).

42. K. Zakeri *et al.* "Asymmetric Spin-Wave Dispersion on Fe(110): Direct Evidence of the Dzyaloshinskii-Moriya Interaction". *Phys. Rev. Lett.* **104,** 137203 (Mar. 2010).

43. J. M. Lee *et al.* "All-Electrical Measurement of Interfacial Dzyaloshinskii-Moriya Interaction Using Collective Spin-Wave Dynamics". *Nano Lett.* **16.** PMID: 26653115, 62–67 (2016).

44. J. Franken, M. Herps, H. Swagten & B. Koopmans. "Tunable chiral spin texture in magnetic domain-walls". *Sci. Rep.* **4,** 5248 (2014).

45. S. Emori *et al.* "Spin Hall torque magnetometry of Dzyaloshinskii domain walls". *Phys. Rev. B* **90,** 184427 (Nov. 2014).

46. R. Lavrijsen *et al.* "Asymmetric magnetic bubble expansion under in-plane field in Pt/Co/Pt: Effect of interface engineering". *Phys. Rev. B* **91,** 104414 (Mar. 2015).

47. E. Jue *et al.* "Chiral damping of magnetic domain walls". *Nat. Mater.* **15,** 272–277 (2016).

48. N.-H. Kim *et al.* "Improvement of the interfacial Dzyaloshinskii-Moriya interaction by introducing a Ta buffer layer". *Appl. Phys. Lett.* **107,** 142408 (2015).

49. N.-H. Kim *et al.* "Interfacial Dzyaloshinskii-Moriya interaction, surface anisotropy energy, and spin pumping at spin orbit coupled Ir/Co interface". *Appl. Phys. Lett.* **108,** 142406 (2016).

50. A. Hrabec *et al.* "Measuring and tailoring the Dzyaloshinskii-Moriya interaction in perpendicularly magnetized thin films". *Phys. Rev. B* **90,** 020402 (July 2014).

51. A. Belabbes, G. Bihlmayer, F. Bechstedt, S. Blügel & A. Manchon. "Hund's Rule-Driven Dzyaloshinskii-Moriya Interaction at $3d$–$5d$ Interfaces". *Phys. Rev. Lett.* **117,** 247202 (Dec. 2016).

52. W. Peng, O. Keitel, R. H. Victoria, E. Koparal & J. H. Judy. "Co/Pt superlattices with ultra-thin Ta seed layer on NiFe underlayer for double-layer perpendicular magnetic recording media". *IEEE Transactions on Magnetics* **36,** 2390–2392 (Sept. 2000).

53. A. W. J. Wells, P. M. Shepley, C. H. Marrows & T. A. Moore. "Effect of interfacial intermixing on the Dzyaloshinskii-Moriya interaction in Pt/Co/Pt". *Phys. Rev. B* **95,** 054428 (Feb. 2017).

54. A. Fert, N. Reyren & V. Cros. "Magnetic skyrmions: advances in physics and potential applications". *Nat. Rev. Mater.* **2,** 17031 (2017).

55. K.-S. Ryu, S.-H. Yang, L. Thomas & S. S. P. Parkin. "Chiral spin torque arising from proximity-induced magnetization". *Nat. Commun.* **5,** 3910 (2014).

56. C.Moreau-Luchaire *et al.* "Additive interfacial chiral interaction in multilayers for stabilization of small individual skyrmions at room temperature". *Nat. Nanotechnol.* **11,** 444–448 (May 2016).

57. A. Thiaville, S. Rohart, E. Jué, V. Cros & A. Fert. "Dynamics of Dzyaloshinskii domain walls in ultrathin magnetic films". *Europhys. Lett.* **100,** 57002 (Dec. 2012).

58. Y. Yoshimura *et al.* "Soliton-like magnetic domain wall motion induced by the interfacial Dzyaloshinskii–Moriya interaction". *Nat. Phys.* **12,** 157–161 (2015).

59. K.-W. Moon *et al.* "magnetic bubblecade memory based on chiral domain walls". *Sci. Rep.* **5,** 9166 (Mar. 2015).

60. D. Petit, P. R. Seem, M. Tillette, R. Mansell & R. P. Cowburn. "Two-dimensional control of field-driven magnetic bubble movement using Dzyaloshinskii–Moriya interactions". *Appl. Phys. Lett.* **106,** 022402 (2015).

61. K.-W. Moon *et al.* "Domain wall motion driven by an oscillating magnetic field". *J. Phys. D: Appl. Phys.* **50,** 125003 (Feb. 2017).

62. F. C. Ummelen, D. S. Han, J. S. Kim, H. J. M. Swagten & B. Koopmans. "Asymmetric Domain-Wall Depinning Induced by Dzyaloshinskii Moriya Interaction". *IEEE Trans. Magn.* **51,** 1–3 (Nov. 2015).

63. K.-S. Ryu, L. Thomas, S.-H. Yang & S. Parkin. "Chiral spin torque at magnetic domain walls". *Nat. Nanotechnol.* **8,** 527–533 (2013).

64. S. Emori, U. Bauer, S. Ahn, E. Martinez & G. Beach. "Current-driven dynamics of chiral ferromagnetic domain walls". *Nat. Mater.* **12,** 611–616 (June 2013).

65. S. Mühlbauer *et al.* "Skyrmion lattice in a chiral magnet". *Science (Washington, DC, U. S.)* **323,** 915–919 (Feb. 2009).

66. A. Neubauer *et al.* "Topological Hall effect in the A phase of MnSi". *Phys. Rev. Lett.* **102** (May 2009).

67. C. Pappas *et al.* "Chiral paramagnetic skyrmion-like phase in MnSi". *Phys. Rev. Lett.* **102** (May 2009).

68. A. Fert, V. Cros & J. Sampaio. "Skyrmions on the track". *Nat. Nanotechnol.* **8,** 152–156 (2013).

69. J. Sampaio, V. Cros, S. Rohart, A. Thiaville & A. Fert. "Nucleation, stability and current-induced motion of isolated magnetic skyrmions in nanostructures". *Nat. Nanotechnol.* **8,** 839–844 (Nov. 2013).

70. K. Di *et al.* "Asymmetric spin-wave dispersion due to Dzyaloshinskii-Moriya interaction in an ultrathin Pt/CoFeB film". *Appl. Phys. Lett.* **106** (Feb. 2015).

71. J.-P. Tetienne *et al.* "The nature of domain walls in ultrathin ferromagnets revealed by scanning nanomagnetometry". *Nat. Commun.* **6** (2015).

72. P. Haazen *et al.* "Domain wall depinning governed by the spin Hall effect". *Nat. Mater.* **12,** 299–303 (2013).

73. T. Devolder. "Light ion irradiation of Co/Pt systems: Structural origin of the decrease in magnetic anisotropy". *Phys. Rev. B* **62,** 5794–5802 (Sept. 2000).

74. F. Ummelen, H. Swagten & B. Koopmans. "Racetrack memory based on in-plane-field controlled domain-wall pinning". *Sci. Rep.* **7** (2017).

75. S. Parkin, M. Hayashi & L. Thomas. "Magnetic Domain-Wall Racetrack Memory". *Science (Washington, DC, U. S.)* **320,** 190–194 (Apr. 2008).

76. Y. Zhang *et al.* "Perpendicular-magnetic-anisotropy CoFeB racetrack memory". *J. Appl. Phys. (Melville, NY, U. S.)* **111,** 093925 (2012).

77. D. Chiba *et al.* "Control of multiple magnetic domain walls by current in a Co/Ni nano-wire". *Appl. Phys. Express* **3,** 073004 (July 2010).

78. I. Miron *et al.* "Fast current-induced domain-wall motion controlled by the Rashba effect". *Nat. Mater.* **10,** 419–423 (May 2011).

79. C.-Y. You, I. M. Sung & B.-K. Joe. "Analytic expression for the temperature of the current-heated nanowire for the current-induced domain wall motion". *Appl. Phys. Lett.* **89,** 222513 (2006).

80. D. A. Allwood *et al.* "Magnetic Domain-Wall Logic". *Science (Washington, DC, U. S.)* **309,** 1688–1692 (2005).

81. D. Pierce & P. Brusius. "Electromigration: A review". *Microelectron. Reliab.* **37,** 1053 –1072 (1997).

82. J. Franken, H. Swagten & B. Koopmans. "Shift registers based on magnetic domain wall ratchets with perpendicular anisotropy". *Nat. Nanotechnol.* **7,** 499–503 (July 2012).

83. A. Himeno, S. Kasai & T. Ono. "Depinning fields of a magnetic domain wall from asymmetric notches". *J. Appl. Phys. (Melville, NY, U. S.)* **99,** 08G304 (2006).

84. J.-S. Kim *et al.* "Synchronous precessional motion of multiple domain walls in a ferromagnetic nanowire by perpendicular field pulses". *Nat. Commun.* **5,** 3429 (Mar. 2014).

85. M. J. G. Peeters *et al.* "Precession-torque-driven domain-wall motion in out-of-plane materials". *AIP Adv.* **7,** 055921 (2017).

86. Y. P. Kabanov *et al.* "In-Plane Field Effects on the Dynamics of Domain Walls in Ultrathin Co Films With Perpendicular Anisotropy". *IEEE Trans. Magn.* **46,** 2220–2223 (June 2010).

87. A. V. Khvalkovskiy *et al.* "Matching domain-wall configuration and spin-orbit torques for efficient domain-wall motion". *Phys. Rev. B* **87,** 020402 (Jan. 2013).

88. S. Heinze *et al.* "Spontaneous atomic-scale magnetic skyrmion lattice in two dimensions". *Nat. Phys.* **7,** 713–718 (July 2011).

89. G. Chen *et al.* "Tailoring the chirality of magnetic domain walls by interface engineering". *Nat. Commun.* **4,** 2671 (Oct. 2013).

90. J. H. Franken *et al.* "Precise control of domain wall injection and pinning using helium and gallium focused ion beams". *"J. Appl. Phys. (Melville, NY, U. S.)* **109,** 07D504 (2011).

91. M. Bauer *et al.* "Deroughening of Domain Wall Pairs by Dipolar Repulsion". *Phys. Rev. Lett.* **94,** 207211 (May 2005).

92. J. Zhang & C. A. Ross. "Domain wall configurations and interactions in perpendicular magnetic anisotropy nanowires". *IEEE Magn. Lett.* **7,** 1–5 (2016).

93. C. Chappert *et al.* "Planar Patterned Magnetic Media Obtained by Ion Irradiation". *Science (Washington, DC, U. S.)* **280,** 1919–1922 (1998).

94. T. Schulz *et al.* "Spin-orbit torques for current parallel and perpendicular to a domain wall". *Appl. Phys. Lett.* **107,** 122405 (2015).

95. I. Mihai Miron *et al.* "Current-driven spin torque induced by the Rashba effect in a ferromagnetic metal layer". *Nat. Mater.* **9,** 230–234 (2010).

96. M. Vaňatka *et al.* "Velocity asymmetry of Dzyaloshinskii domain walls in the creep and flow regimes". *J. Phys.: Condens. Matter* **27** (2015).

97. V. Jeudy *et al.* "Universal Pinning Energy Barrier for Driven Domain Walls in Thin Ferromagnetic Films". *Phys. Rev. Lett.* **117,** 057201 (July 2016).

98. R. Diaz Pardo, W. Savero Torres, A. B. Kolton, S. Bustingorry & V. Jeudy. "Universal depinning transition of domain walls in ultrathin ferromagnets". *Phys. Rev. B* **95,** 184434 (May 2017).

99. D.-Y. Kim, D.-H. Kim & S.-B. Choe. "Intrinsic asymmetry in chiral domain walls due to the Dzyaloshinskii-Moriya interaction". *Appl. Phys. Express* **9,** 053001 (2016).

100. D. M. Hartmann, R. A. Duine, M. J. Meijer, H. J. Swagten & L. Reinoud. *Creep of Chiral Domain Walls*. 2018. arXiv: 1812.09055.

101. J. Wunderlich *et al.* "Influence of geometry on domain wall propagation in a mesoscopic wire". *IEEE Trans. Magn.* **37,** 2104–2107 (2001).

102. F. Cayssol, D. Ravelosona, C. Chappert, J. Ferré & J. P. Jamet. "Domain Wall Creep in Magnetic Wires". *Phys. Rev. Lett.* **92,** 107202 (Mar. 2004).

103. V. Pratt. "Direct Least-squares Fitting of Algebraic Surfaces". *SIGGRAPH Comput. Graph.* **21,** 145–152 (Aug. 1987).

104. V. Mathet *et al.* "Morphology and magnetic properties of Pt/Co/Pt sandwiches grown by argon sputter deposition". *J. Magn. Magn. Mater.* **260,** 295 –304 (2003).

105. D. Lau, V. Sundar, J.-G. Zhu & V. Sokalski. "Energetic molding of chiral magnetic bubbles". *Phys. Rev. B* **94,** 060401 (Aug. 2016).

106. O. Boulle *et al.* "Domain Wall Tilting in the Presence of the Dzyaloshinskii-Moriya Interaction in Out-of-Plane Magnetized Magnetic Nanotracks". *Phys. Rev. Lett.* **111,** 217203 (Nov. 2013).

107. D.-Y. Kim *et al.* "Magnetic domain-wall tilting due to domain-wall speed asymmetry". *Phys. Rev. B* **97,** 134407 (Apr. 2018).

108. L. Herrera Diez *et al.* "Wire edge dependent magnetic domain wall creep". *Phys. Rev. B* **98,** 054417 (5 Aug. 2018).

109. A Mougin, M Cormier, J. P. Adam, P. J. Metaxas & J Ferré. "Domain wall mobility, stability and Walker breakdown in magnetic nanowires". *Europhys. Lett.* **78,** 57007 (2007).

110. T. Gilbert. "A Phenomenological Theory of Damping in Ferromagnetic Materials". *IEEE Trans. Magn.* **40,** 3443–3449 (Nov. 2004).

111. A. Thiaville, Y. Nakatani, J. Miltat & Y. Suzuki. "Micromagnetic understanding of current-driven domain wall motion in patterned nanowires". *Europhys. Lett.* **69,** 990 (2005).

112. A. J. Schellekens *et al.* "Determining the Gilbert damping in perpendicularly magnetized Pt/Co/AlOx films". *Appl. Phys. Lett.* **102** (2013).

113. L. H. Diez *et al.* "Enhancement of the Dzyaloshinskii-Moriya interaction and domain wall velocity through interface intermixing in Ta/CoFeB/MgO". *Phys. Rev. B* **99,** 054431 (5 Feb. 2019).

114. T. Skyrme. "A unified field theory of mesons and baryons". *Nucl. Phys.* **31,** 556 –569 (1962).

115. D. C. Wright & N. D. Mermin. "Crystalline liquids: the blue phases". *Rev. Mod. Phys.* **61,** 385–432 (Apr. 1989).

116. H.-B. Braun. "Topological effects in nanomagnetism: from superparamagnetism to chiral quantum solitons". *Adv. Phys.* **61,** 1–116 (2012).

117. A. Hubert & R. Schafer. *Magnetic Domains: The Analysis of Magnetic Microstructures Springer* (Jan. 1998).

118. T. Shinjo, T. Okuno, R. Hassdorf, †. K. Shigeto & T. Ono. "Magnetic Vortex Core Observation in Circular Dots of Permalloy". *Science (Washington, DC, U. S.)* **289,** 930–932 (2000).

119. *The synchronized dance of skyrmion spins*. Accessed: 2019-06-27.

120. C. Ma *et al.* "Electric Field-Induced Creation and Directional Motion of Domain Walls and Skyrmion Bubbles". *Nano Lett.* **19,** 353–361 (2019).

121. G. E. Volovik, J. Rysti, J. T. Mäkinen & V. B. Eltsov. "Spin, Orbital, Weyl and Other Glasses in Topological Superfluids". *J. Low Temp. Phys.* **196,** 82–101 (July 2019).

122. H.-B. Braun. *Solitons in Real Space: Domain Walls, Vortices, Hedgehogs, and Skyrmions* (eds Zang, J., Cros, V. & Hoffmann, A.) 1–40 (Springer International Publishing, Cham, 2018).

123. M. Hoffmann *et al.* "Antiskyrmions stabilized at interfaces by anisotropic Dzyaloshinskii-Moriya interactions". *Nat. Commun.* **8,** 308 (2017).

124. X. Z. Yu *et al.* "Biskyrmion states and their current-driven motion in a layered manganite". *Nat. Commun.* **5,** 3198 (2014).

125. L. Peng *et al.* "Real-Space Observation of Nonvolatile Zero-Field Biskyrmion Lattice Generation in MnNiGa Magnet". *Nano Lett.* **17.** PMID: 28990787, 7075–7079 (2017).

126. G. E. W. Bauer, E. Saitoh & B. J. van Wees. "Spin caloritronics". *Nat. Mater.* **11,** 391–399 (2012).

127. L. Berger. "Exchange interaction between ferromagnetic domain wall and electric current in very thin metallic films". *J. Appl. Phys. (Melville, NY, U. S.)* **55,** 1954–1956 (1984).

128. J. Slonczewski. "Current-driven excitation of magnetic multilayers". *J. Magn. Magn. Mater.* **159,** L1 –L7 (1996).

129. A. Thiaville, Y. Nakatani, J. Miltat & N. Vernier. "Domain wall motion by spin-polarized current: A micromagnetic study". *J. Appl. Phys. (Melville, NY, U. S.)* **95,** 7049–7051 (2004).

130. *Spin orbit electronics: From heavy metals to topological insulators*. Accessed: 2019-05-22.

131. A. van den Brink. *New directions for magnetic memory : alternative switching mechanisms for magnetic random-access memory*. English. Proefschrift. PhD thesis (Department of Applied Physics, Sept. 2016).

132. G. Vignale. "Ten Years of Spin Hall Effect". *J. Supercond. Novel Magn.* **23,** 3–10 (Oct. 2009).

133. T. Schulz *et al.* "Emergent electrodynamics of skyrmions in a chiral magnet". *Nat. Phys.* **8,** 301–304 (2012).

134. A. A. Thiele. "Steady-State Motion of Magnetic Domains". *Phys. Rev. Lett.* **30,** 230–233 (Feb. 1973).

135. W. Jiang *et al.* "Direct observation of the skyrmion Hall effect". *Nat. Phys.* **13,** 162–169 (2017).

136. A. Thiaville & J. Miltat. *Topology and Magnetic Domain Walls* (eds Zang, J., Cros, V. & Hoffmann, A.) 41–73 (Springer International Publishing, Cham, 2018).

137. J. Iwasaki, M. Mochizuki & N. Nagaosa. "Universal current-velocity relation of skyrmion motion in chiral magnets". *Nat. Commun.* **4,** 1463 (2013).

138. J. Iwasaki, M. Mochizuki & N. Nagaosa. "Current-induced skyrmion dynamics in constricted geometries". *Nat. Nanotechnol.* **8,** 742 (2013).

139. W. Legrand *et al.* "Room-Temperature Current-Induced Generation and Motion of sub-100 nm Skyrmions". *Nano Lett.* **17.** PMID: 28358984, 2703–2712 (2017).

140. S. Woo *et al.* "Observation of room-temperature magnetic skyrmions and their current-driven dynamics in ultrathin metallic ferromagnets". *Nat. Mater.* **15,** 501–506 (2016).

141. O. Boulle *et al.* "Room-temperature chiral magnetic skyrmions in ultrathin magnetic nanostructures". *Nat. Nanotechnol.* **11,** 449 (2016).

142. G. Yu *et al.* "Room-Temperature Creation and Spin–Orbit Torque Manipulation of Skyrmions in Thin Films with Engineered Asymmetry". *Nano Lett.* **16,** 1981–1988 (2016).

143. N. Romming *et al.* "Writing and Deleting Single Magnetic Skyrmions". *Science (Washington, DC, U. S.)* **341,** 636–639 (2013).

144. A. Soumyanarayanan *et al.* "Tunable room-temperature magnetic skyrmions in Ir/Fe/Co/Pt multilayers". *Nat. Mater.* **16,** 898–904 (2017).

145. M. Schott *et al.* "The Skyrmion Switch: Turning Magnetic Skyrmion Bubbles on and off with an Electric Field". *Nano Lett.* **17,** 3006–3012 (2017).

146. A. Hrabec *et al.* "Current-induced skyrmion generation and dynamics in symmetric bilayers". *Nat. Commun.* **8,** 15765 (2017).

147. W. Jiang *et al.* "Blowing magnetic skyrmion bubbles". *Science (Washington, DC, U. S.)* **349,** 283–286 (2015).

148. G. Berruto *et al.* "Laser-Induced Skyrmion Writing and Erasing in an Ultrafast Cryo-Lorentz Transmission Electron Microscope". *Phys. Rev. Lett.* **120,** 117201 (Mar. 2018).

149. S.-G. Je *et al.* "Creation of Magnetic Skyrmion Bubble Lattices by Ultrafast Laser in Ultrathin Films". *Nano Lett.* **18.** PMID: 30295499, 7362–7371 (2018).

150. D. A. Garanin, D. Capic, S. Zhang, X. Zhang & E. M. Chudnovsky. "Writing skyrmions with a magnetic dipole". *J. Appl. Phys. (Melville, NY, U. S.)* **124,** 113901 (2018).

151. T. A. Moore *et al.* "Erratum: "High domain wall velocities induced by current in ultrathin Pt/Co/AlOx wires with perpendicular magnetic anisotropy" [Appl. Phys. Lett. 93, 262504 (2008)]". *Appl. Phys. Lett.* **95,** 179902 (2009).

152. S.-G. Je *et al.* "Emergence of Huge Negative Spin-Transfer Torque in Atomically Thin Co layers". *Phys. Rev. Lett.* **118,** 167205 (Apr. 2017).

153. K. Ueda *et al.* "Transition in mechanism for current-driven magnetic domain wall dynamics". *Appl. Phys. Express* **7,** 053006 (2014).

154. K. Litzius *et al.* "Skyrmion Hall effect revealed by direct time-resolved X-ray microscopy". *Nat. Phys.* **13,** 170 (2016).

155. J. Slonczewski. "Current-driven excitation of magnetic multilayers". *J. Magn. Magn. Mater.* **159,** L1 –L7 (1996).

156. J. E. Hirsch. "Spin Hall Effect". *Phys. Rev. Lett.* **83,** 1834–1837 (Aug. 1999).

157. M. Cormier *et al.* "Effect of electrical current pulses on domain walls in Pt/Co/Pt nanotracks with out-of-plane anisotropy: Spin transfer torque versus Joule heating". *Phys. Rev. B* **81,** 024407 (Jan. 2010).

158. L. Liu, R. Buhrman & D. Ralph. *Review and Analysis of Measurements of the Spin Hall Effect in Platinum*. 2011. arXiv: 1111.3702.

159. *Supporting videos for this thesis.* Accessed: 2019-07-26.

160. W. Zhang *et al.* "Determination of the Pt spin diffusion length by spin-pumping and spin Hall effect". *Appl. Phys. Lett.* **103,** 242414 (2013).

161. G. Tatara & H. Kohno. "Theory of Current-Driven Domain Wall Motion: Spin Transfer versus Momentum Transfer". *Phys. Rev. Lett.* **92,** 086601 (Feb. 2004).

162. K. Gilmore, I. Garate, A. H. MacDonald & M. D. Stiles. "First-principles calculation of the nonadiabatic spin transfer torque in Ni and Fe". *Phys. Rev. B* **84,** 224412 (Dec. 2011).

163. F. Büttner, I. Lemesh & G. S. D. Beach. "Theory of isolated magnetic skyrmions: From fundamentals to room temperature applications". *Sci. Rep.* **8** (2018).

164. *Evico Magnetics GMBH*. Accessed: 2018-05-07.

165. F. Ummelen, T. Lichtenberg, H. Swagten & B. Koopmans. *Controlling skyrmion bubble confinement by dipolar interactions*. 2019. arXiv: 1905.10304.

166. R. Tomasello *et al.* "A strategy for the design of skyrmion racetrack memories". *Sci. Rep.* **4.** 25351135[pmid], 6784 (Oct. 2014).

167. H. Du *et al.* "Edge-mediated skyrmion chain and its collective dynamics in a confined geometry". *Nat. Commun.* **6,** 8504 (2015).

168. S. A. Meynell, M. N. Wilson, H. Fritzsche, A. N. Bogdanov & T. L. Monchesky. "Surface twist instabilities and skyrmion states in chiral ferromagnets". *Phys. Rev. B* **90,** 014406 (July 2014).

169. R. Tolley, S. A. Montoya & E. E. Fullerton. "Room-temperature observation and current control of skyrmions in Pt/Co/Os/Pt thin films". *Phys. Rev. Mater.* **2,** 044404 (Apr. 2018).

170. F. Ummelen *et al.* *Anomalous direction for skyrmion bubble motion*. 2018. arXiv: 1807.07365.

171. S. H. Lee, F. Q. Zhu, C. L. Chien. "Effect of geometry on magnetic domain structure in Ni wires with perpendicular anisotropy: A magnetic force microscopy study". *Phys. Rev. B* **77,** 132408 (Apr. 2008).

172. R. Juge *et al.* "Magnetic skyrmions in confined geometries: Effect of the magnetic field and the disorder". *J. Magn. Magn. Mater.* **455.** Magnetic skyrmions as future information carriers, 3 –8 (2018).

173. K. Zeissler *et al.* "Pinning and hysteresis in the field dependent diameter evolution of skyrmions in Pt/Co/Ir superlattice stacks". *Sci. Rep.* **7,** 15125 (2017).

174. J. Coey. *Magnetism and Magnetic Materials* (Cambridge University Press, 2010).

175. *NanoAccess: thin film engineering & in-situ nanolab*. Accessed: 2019-01-16.

176. *FEI Nova600i NanoLab*. Accessed: 2019-01-16.

177. *Raith EBPG 5150 Electron Beam Lithography*. Accessed: 2019-01-04.

178. *Roth & Rau Ion Beam Etcher*. Accessed: 2019-01-16.

179. S. Reyntjens & R. Puers. "A review of focused ion beam applications in microsystem technology". *J. Micromech. Microeng.* **11,** 287 (2001).

180. J Fassbender, D Ravelosona & Y Samson. "Tailoring magnetism by light-ion irradiation". *J. Phys. D: Appl. Phys.* **37,** R179 (2004).

181. S. Foner. "Versatile and Sensitive Vibrating Sample Magnetometer". *Rev. Sci. Instrum.* **30,** 548–557 (1959).

182. M. Donahue & D. Porter. *OOMMF User's Guide Version 1.0*. Tech. rep. (National Institute of Standards and Technology, Gaithersburg, MD, Sept. 1999).

183. Z. Q. Qiu & S. D. Bader. "Surface magneto-optic Kerr effect". *Rev. Sci. Instrum.* **71,** 1243–1255 (2000).

184. C. Burrowes *et al.* "Non-adiabatic spin-torques in narrow magnetic domain walls". *Nat. Phys.* **6,** 17–21 (Jan. 2010).

185. Z. Q. Qiu, J. Pearson & S. D. Bader. "Magneto-optic Kerr ellipticity of epitaxial Co/Cu overlayers and superlattices". *Phys. Rev. B* **46,** 8195–8200 (Oct. 1992).

186. C Tannous & J Gieraltowski. "The Stoner–Wohlfarth model of ferromagnetism". *Eur. J. Phys.* **29,** 475 (2008).

187. B. Kaplan & G. Gehring. "The domain structure in ultrathin magnetic films". *J. Magn. Magn. Mater.* **128,** 111 –116 (1993).

188. C. Eyrich *et al.* "Effects of substitution on the exchange stiffness and magnetization of Co films". *Phys. Rev. B* **90,** 235408 (Dec. 2014).

189. R. Lavrijsen *et al.* "Asymmetric Pt/Co/Pt-stack induced sign-control of current-induced magnetic domain-wall creep". *Appl. Phys. Lett.* **100** (2012).

190. M.-H. Nguyen, D. C. Ralph & R. A. Buhrman. "Spin Torque Study of the Spin Hall Conductivity and Spin Diffusion Length in Platinum Thin Films with Varying Resistivity". *Phys. Rev. Lett.* **116,** 126601 (Mar. 2016).

191. M. Ezawa. "Giant Skyrmions Stabilized by Dipole-Dipole Interactions in Thin Ferromagnetic Films". *Phys. Rev. Lett.* **105,** 197202 (Nov. 2010).

192. E. Martinez, S. Emori & G. S. D. Beach. "Current-driven domain wall motion along high perpendicular anisotropy multilayers: The role of the Rashba field, the spin Hall effect, and the Dzyaloshinskii-Moriya interaction". *Appl. Phys. Lett.* **103,** 072406 (2013).

193. L. Liu, O. J. Lee, T. J. Gudmundsen, D. C. Ralph & R. A. Buhrman. "Current-Induced Switching of Perpendicularly Magnetized Magnetic Layers Using Spin Torque from the Spin Hall Effect". *Phys. Rev. Lett.* **109,** 096602 (Aug. 2012).

194. L. Liu, T. Moriyama, D. C. Ralph & R. A. Buhrman. "Spin-Torque Ferromagnetic Resonance Induced by the Spin Hall Effect". *Phys. Rev. Lett.* **106,** 036601 (Jan. 2011).

195. O. Šipr, J. Minár, S. Mankovsky & H. Ebert. "Influence of composition, many-body effects, spin-orbit coupling, and disorder on magnetism of Co-Pt solid-state systems". *Phys. Rev. B* **78,** 144403 (14 Oct. 2008).

196. J. W. Knepper & F. Y. Yang. "Oscillatory interlayer coupling in Co/Pt multilayers with perpendicular anisotropy". *Phys. Rev. B* **71,** 224403 (June 2005).

197. J. Moritz, F. Garcia, J. C. Toussaint, B. Dieny & J. P. Nozières. "Orange peel coupling in multilayers with perpendicular magnetic anisotropy: Application to (Co/Pt)-based exchange-biased spin-valves". *Europhys. Lett.* **65,** 123 (2004).

198. J.-P. Renard *et al.* "Inverse magnetoresistance in the simple spin-valve system $Fe_{1-x}V_x$/Au/Co". *Phys. Rev. B* **51,** 12821–12824 (May 1995).

199. J. M. George *et al.* "Inverse spin-valve-type magnetoresistance in spin engineered multilayered structures". *Phys. Rev. Lett.* **72,** 408–411 (Jan. 1994).

200. S. Y. Hsu *et al.* "Towards a Unified Picture of Spin Dependent Transport in and Perpendicular Giant Magnetoresistance and Bulk Alloys". *Phys. Rev. Lett.* **78,** 2652–2655 (Mar. 1997).

201. S. Tarasenko, A. Stankiewicz, V. Tarasenko & J. Ferré. "Bloch wall dynamics in ultrathin ferromagnetic films". *J. Magn. Magn. Mater.* **189,** 19 –24 (1998).

202. *Accuracy of the Reported Moment: Sample Shape Effects*. Quantum Design SQUID VSM Application Note 1500-015.

203. S. Zhang, A. K. Petford-Long & C. Phatak. "Creation of artificial skyrmions and antiskyrmions by anisotropy engineering". *Sci. Rep.* **6,** 31248 (Aug. 2016).